



MONASH University

**FLEXIBLE NANOCELLULOSE – NANOPARTICLE
COMPOSITES: STRUCTURES AND PROPERTIES**

**Thesis in the fulfilment of the requirement for the degree of Doctor of
Philosophy in Chemical Engineering**

by

Uthpala Manavi Garusinghe

B. Eng. (Chem.)

Department of Chemical Engineering

Faculty of Engineering

MONASH UNIVERSITY

OCTOBER 2017

PREFACE

THIS PAGE HAS BEEN INTENTIONALLY LEFT BLANK

Dedicated to my parents

~ Amma & Appachchi ~

For their endless love, support and encouragement

PREFACE

THIS PAGE HAS BEEN INTENTIONALLY LEFT BLANK

COPYRIGHT NOTICE

© Uthpala Manavi Garusinghe, 2017. Except as provided in the Copyright Act 1968, this thesis may not be reproduced in any form without written permission of the author.

I certify that I have made all reasonable efforts to secure copyright permissions for third-party content included in this thesis and have not knowingly added copyright content to my work without the owner's permission.



.....

Uthpala Manavi Garusinghe

GENERAL DECLARATION

This thesis contains no material which has been accepted for the award of any other degree or diploma at any university or equivalent institution and that, to the best of my knowledge and belief, this thesis contains no material previously published or written by another person, except where due reference is made in the text of the thesis.

TABLE OF CONTENTS

Title page	i
Dedication	iii
Copyright notice	v
General declaration	vi
Table of contents	vii
Declaration of publication and authorship	ix
Acknowledgement	xiii
Abstract	xv
List of publications	xvii
List of figures	xix
List of tables	xxiv
List of abbreviations	xxv
List of nomenclature	xxviii
CHAPTER 1 Introduction and Literature Review	1
CHAPTER 2 Strong and thin Strong cellulose nanofibre-nanosilica composites with controllable pore structure	81
CHAPTER 3 Investigating silica nanoparticle-polyelectrolyte structures in microfibrillated cellulose films by scattering techniques	109
CHAPTER 4 Assembly of nanoparticle-polyelectrolyte complexes in nanofiber cellulose structures	131
CHAPTER 5 Nanocellulose-montmorillonite composites of low water vapour permeability	159
CHAPTER 6 Water resistant cellulose – titanium dioxide composites for photocatalysis	191
CHAPTER 7 Conclusion and Perspectives	227
APPENDIX I Supplementary Information	I-1
I (A) Strong and thin Strong cellulose nanofibre-nanosilica composites with controllable pore structure	I-3

PREFACE

I (B)	Assembly of nanoparticle-polyelectrolyte complexes in nanofiber cellulose structures	I-7
I (C)	Nanocellulose-montmorillonite composites of low water vapour permeability	I-13
I (D)	Water resistant cellulose – titanium dioxide composites for photocatalysis	I-19
APPENDIX II Publications included in thesis in their publication format		II-1
II (A)	Strong and thin Strong cellulose nanofibre-nanosilica composites with controllable pore structure	II-3
II (B)	Investigating silica nanoparticle-polyelectrolyte structures in microfibrillated cellulose films by scattering techniques	II-14
II (C)	Assembly of nanoparticle-polyelectrolyte complexes in nanofiber cellulose structures	II-21

Monash University

Thesis including published works declaration

I hereby declare that this thesis contains no material which has been accepted for the award of any other degree or diploma at any university or equivalent institution and that, to the best of my knowledge and belief, this thesis contains no material previously published or written by another person, except where due reference is made in the text of the thesis.

This thesis includes 3 original papers published in peer reviewed journals (Chapter 2, 3 and 4) and 2 submitted publications (Chapter 5 and 6). The core theme of the thesis is flexible nanocellulose – nanoparticle composites: structures and properties. The ideas, development and writing up of all the papers in the thesis were the principal responsibility of myself, the student, working within the Department of Chemical Engineering, Monash University, under the supervision of Associate Professor Warren Batchelor and Professor Gil Garnier.

(The inclusion of co-authors reflects the fact that the work came from active collaboration between researchers and acknowledges input into team-based research.)

In the case of Chapter 2 and 4 my contribution to the work involved the following:

Thesis Chapter	Publication Title	Status	Nature and % of student contribution
2	Strong cellulose nanofibre-nanosilica composites with controllable pore structure.	Published	Key ideas, experimental works, analysis or results, writing up.
4	Assembly of nanoparticle-polyelectrolyte complexes in nanofiber cellulose structures.	Published	Key ideas, experimental works, analysis or results, writing up.

I have renumbered sections of submitted or published papers in order to generate a consistent presentation within the thesis.

Student signature: 

Date: 12/10/2017

The undersigned hereby certify that the above declaration correctly reflects the nature and extent of the student's and co-authors' contributions to this work. In instances where I am not the responsible author I have consulted with the responsible author to agree on the respective contributions of the authors.

Main Supervisor signature: 

Date: 12/10/2017

PREFACE

THIS PAGE HAS BEEN INTENTIONALLY LEFT BLANK

Monash University

Traditional thesis declaration

I hereby declare that this thesis contains no material which has been accepted for the award of any other degree or diploma at any university or equivalent institution and that, to the best of my knowledge and belief, this thesis contains no material previously published or written by another person, except where due reference is made in the text of the thesis.

This thesis includes 3 original papers published in peer reviewed journals (Chapter 2, 3 and 4) and 2 submitted publications (Chapter 5 and 6). The core theme of the thesis is flexible nanocellulose – nanoparticle composites: structures and properties. The ideas, development and writing up of all the papers in the thesis were the principal responsibility of myself, the student, working within the Department of Chemical Engineering, Monash University, under the supervision of Associate Professor Warren Batchelor and Professor Gil Garnier.

(The inclusion of co-authors reflects the fact that the work came from active collaboration between researchers and acknowledges input into team-based research.)

In the case of Chapter 3, 5 and 6 my contribution to the work involved the following:

Thesis Chapter	Publication Title	Status	Nature and % of student contribution
3	Investigating silica nanoparticle-polyelectrolyte structures in microfibrillated cellulose films by scattering techniques	Published	Key ideas, experimental works, analysis or results, writing up.
5	Nanocellulose-montmorillonite composites of low water vapour permeability	Accepted	Key ideas, experimental works, analysis or results, writing up.
6	Water resistant cellulose – titanium dioxide composites for photocatalysis	Under final review	Key ideas, experimental works, analysis or results, writing up.

I have renumbered sections of submitted or published papers in order to generate a consistent presentation within the thesis.

Student signature:



Date: 12/10/2017

The undersigned hereby certify that the above declaration correctly reflects the nature and extent of the student's and co-authors' contributions to this work. In instances where I am not the responsible author I have consulted with the responsible author to agree on the respective contributions of the authors.

Main Supervisor signature:



Date: 12/10/2017

PREFACE

THIS PAGE HAS BEEN INTENTIONALLY LEFT BLANK

ACKNOWLEDGEMENTS

First and foremost, I would like to express my sincere gratitude and appreciation to my supervisors Associate Professor Warren Batchelor and Professor Gil Garnier for their constant support and guidance for the past three and a half years. My supervisors always had an open door for discussions. Without their constant reviews, comments and feedbacks, I would have not been able to achieve all my research goals to finish my thesis successfully. For that reason, and many more, thank you for making my PhD life an amazing one.

Next, I thank Dr. Swambabu Varanasi, Dr. Vikram Raghuvanshi and Dr. Joanne Tanner for their constant support, guidance, advice and mentorship over the years. Dr. Swambabu Varanasi, thank you for being there for me since the first day I started. You always helped me whenever I needed help. Dr. Vikram Raghuvanshi, thank you for your expertise, comments and advices which had enabled me to produce publications to complete this thesis. Also, thank you for taking me to mindfulness classes and giving me moral support when I needed it the most. Thank you Dr. Joanne Tanner for your help given to me during the last year of my PhD.

I would like to give my sincere gratitude for everybody who helped me at ANSTO and Australian Synchrotron with scattering. Without the beam time given by you all, I would not be able to complete my thesis. I also thank for the facilities provided at Monash Centre for Electron Microscopy.

I acknowledge the administrative and technical staff at BioPRIA and Department of Chemical Engineering. In particular, I am sincerely grateful for Janette Anthony for being there for me whenever I needed to talk, for organizing all the social events and making it enjoyable to work at BioPRIA. Also, I would like to acknowledge Scot Sharman for all the help he gave with equipment training and OHS information. Many thanks to Kim Phu, Lilyanne Price, Jill Crisfield for their assistance throughout my milestones.

I acknowledge the financial support given by Australian research council, Australian paper, Carter Holt Harvey, Circa, Orora, Norske Skog and Visy through the Industry Transformation Research Hub grant IH130100016. I am grateful for the FEIPRS and MGS scholarships given by the Faculty of Engineering and Monash University.

PREFACE

On a less formal note, a big shout out for all the people at Monash University, too big to list them all. Particularly a big shout out to my dearest friends at BioPRIA. We started off as colleagues but now you all have become my closest friends. Dr. Praveena Raj, Dr. Whui Lyn Then and Dr. Natasha Yeow, I really appreciate all the guidance you guys have given me as my seniors. Our monthly dinner meetups in the middle of my thesis completion period really helped me to clear my stress. I like to thank Thilina Gunawardhana, Llyza Mendoza, Aysu Onur, Dr. Windy Huang, Heather McLiesh, Janine Lodewyke, Anurag Parihar, Shaun Ang, Clare Henderson, Michael Hertaeg, Marek Bialkower and Julie Courgibet for being my buddies for coffee breaks, lunches, conferences, games and every other activity we did together. Because of you all, this PhD was rather a joyful one.

I would like to thank all my friends at Melbourne for making it feel like home. Living away from parents is difficult if not for you guys. Special thank goes to Dr. Suyog Mahajan, Meuni Imbulgoda, Rochini Wimalkantha, Naomi Gunasekara, Hansana Weerasooriya and Danushka Sooriyadasa.

To my best friend Lakma Godigamuwe, thank you for always been there for me. Your daily text messages, even from far away, have always brought a smile to my face. Thank you for always encouraging me and advising me to do the right thing.

To my little brother (malli), Yasas Bhanuka Garusinghe, I have not missed home as much as I thought I would because you have always been there for me in Australia. You have helped me so much in this journey, from taking care of me to making sure I am on track with my life goals. Thank you so much for the moral support and the encouragement, big or small, they meant so much to me. Malli, I could not have asked for a better brother and a better friend than you.

Saving the best for last. To my parents, Amma and Appachchi, first of all thank you for believing in me, for encouraging me, for giving me liberty to choose what I desired and for being there for me through good and bad times of this journey. Thank you for giving me the endless love, care and the strength to reach for the stars and chase my dreams. Thank you for the sacrifices you made to shape my life. You are truly my biggest strength and inspiration in life. Amma and Appachchi, I am grateful for everything you have done and everything to come. You are wonderful parents and wonderful friends. What I am today, I owe it to both of you. So this one is for both of you.

Cheers, everyone. It was so good to write my final words for the thesis. Stay in touch.

ABSTRACT

Nanocellulose fibres are a new class of material that has received a remarkable attention over the past decade. Nanocellulose is biodegradable, renewable, and sustainable and has many other attractive properties of technological interest. Such properties include excellent strength and stiffness, high thermal stability, low moisture adsorption, superior oxygen barrier properties and high optical transparency. Nanocellulose can be converted into nanocellulose thin films, which can then be used in wide range of applications because of the properties mentioned above. However, the property range achievable with nanocellulose by itself still has limitations. Therefore, this thesis focuses on the production of nanocellulose-inorganic nanoparticle (NP) composites to combine the advantage associated with both individual components together to extend the range of properties achievable. In the first part of the thesis, methods are developed to overcome the problems in composite production, characterization and optimization. Then the thesis focuses on engineering composites that can be used for high end applications by demonstrating two industrial applications with functional NPs.

Since the properties of the final composite, up to a certain extent, rely on the properties and the quantities of individual components in the composites, the unavailability of proper structure-property relationship data for nanocellulose-NP composites hinders the broader use of these composites. In this thesis, silicon dioxide (SiO_2) was used to make model composites that were used to measure the structure-property relationship. SiO_2 of two different NP sizes (small: ~ 50 nm, large: ~ 95 nm) were used. Since SiO_2 and nanocellulose are both negatively charged, cationic polyacrylamide (CPAM)-a type of polyelectrolyte- at a fixed ratio of CPAM mass to SiO_2 surface area was used to bridge between SiO_2 and nanocellulose. Using different SiO_2 NP loadings, and with a controlled preparation method, SiO_2 , CPAM and nanocellulose were combined together to produce the final composite. The outcome was that the composite structure can be controlled with the amount of NPs present in the composite and this changes the final film properties. For example, SiO_2 NP addition from 0 to 77 wt% reduced the pore size distribution from 100-1000 nm to 10-60 nm (narrow pore size range). It was also found that with careful mixing and preparation methods, heavily loaded NP composites with full retention of NPs can be achieved while maintaining the strength. This data is useful to develop structure-property relationships to better engineer composites.

Furthermore, another critical issue that hinders the broader use of composites is the lack of proper methods to characterize the internal structure of NP-CPAM complexes in the nanocellulose matrix. Understanding the structural assembly of NPs under the influence of CPAM or any polyelectrolyte is essential to engineer composites. Thus, this thesis explores the use of small angle X-ray scattering (SAXS) as a complementary scattering techniques to characterize the three dimensional (3D) internal structure of SiO₂-CPAM complexes. The radius of gyration of CPAM used in this work is ~37 nm (CPAM with 13 MDa and 40% charge). Therefore, two different NP sizes; 8 nm (smaller than size of CPAM) and 22 nm (closer to size of CPAM) was used to understand the effect of size and CPAM dosage on NP structural assembly. The SAXS measurements showed that the 8 nm SiO₂ data was best modelled with a bimodal distribution of single particles and agglomerates while 22 nm SiO₂ was best fitted with a combination of spherical core shell and spheres model. The results obtained from this part of the thesis show that different NP sizes arrange themselves differently when interacting with polyelectrolytes and varying the polyelectrolyte concentration can control the retention, arrangement and interactions of NPs. These results and the fundamental knowledge obtained about NP-polyelectrolyte complexes in nanocellulose matrices can be used to cater composites for specific industrial application.

The remainder of the thesis investigated specific industrial applications for MFC-NP composites. Nano-montmorillonite (MMT) and nano-titanium dioxide (TiO₂) were used to produce nanocellulose based composites targeted towards water barrier and photocatalytic applications, respectively. Preparation method of nanocellulose-MMT composites was optimised to maximise the available surface area by reducing the MMT stack size, thereby achieved the lowest water vapour permeability (WVP) for nanocellulose-clay composites ever published in literature. Nanocellulose – TiO₂ composites were prepared with polyamide-amine-epichlorohydrin (PAE) as a wet strengthening and a retention aid. The nanocellulose network combined with PAE strongly retains NPs and hinders their release in the environment. The composites are reusable and reproducible and gave remarkable photocatalytic activity by degrading methyl orange under UV light irradiation. The significance of the work are that both composites with MMT and TiO₂ were recyclable, portable, cheap, simple to produce and easy to scale up.

LIST OF PUBLICATIONS

Peer-Reviewed Journal papers

The following published and submitted papers are included in the body of this thesis as individual chapters. The sections of these published papers have been renumbered in order to generate a consistent presentation within the thesis. Papers in the published format are included as Appendix II.

1. **Uthpala M. Garusinghe**, Swambabu Varanasi, Gil Garnier, Warren Batchelor. Strong cellulose nanofibre–nanosilica composites with controllable pore structure. *Cellulose*, 2017. **24**(6): p. 2511-2521.
2. **Uthpala M. Garusinghe**, Vikram S. Raghuwanshi, Praveena Raj, Gil Garnier, Warren Batchelor. Investigating silica nanoparticle-polyelectrolyte structures in microfibrillated cellulose films by scattering techniques. *16th Fundamental Research Symposium, Oxford, September 2017*. **2**: p. 823-836.
3. **Uthpala M. Garusinghe***, Vikram S. Raghuwanshi*, Christopher J. Garvey, Swambabu Varanasi, Christopher R. Hutchinson, Warren Batchelor, Gil Garnier. Assembly of nanoparticles-polyelectrolyte complexes in nanofiber cellulose structures. *Colloids and Surfaces A: Physicochemical and Engineering Aspects*, 2017. **513**: p. 373-379.
4. **Uthpala M. Garusinghe**, Swambabu Varanasi, Vikram S. Raghuwanshi, Gil Garnier, Warren Batchelor. Nanocellulose-Montmorillonite Composites of Low Water Vapour Permeability. *Colloids and Surface A: Physicochemical and Engineering Aspects*, 2018.
5. **Uthpala M. Garusinghe**, Vikram S. Raghuwanshi, Warren Batchelor, Gil Garnier. Water resistant cellulose – titanium dioxide composites for photocatalysis. *Scientific Reports* 2018.

Related Co-Authored Journal papers

The following co-authored manuscripts that are published and in preparation are generated during this doctoral study. They are not included in the main body of this thesis.

1. Vikram S. Raghuwanshi, **Uthpala M. Garusinghe**, Jan Ilavsky, Warren Batchelor, Gil Garnier. Effect of nanoparticles size and polyelectrolyte on nanoparticles aggregation in a cellulose fibrous matrix. *Journal of Colloid and Interface Science*, 2018.**510**: p. 190-198.
2. Swambabu Varanasi, **Uthpala M. Garusinghe**, George Simon, Gil Garnier, Warren Batchelor. Novel in-situ precipitation concept for nanoparticle-nanocellulose composite films of very low oxygen and water vapour permeability. *Advanced Materials Interfaces*, 2017.
3. Melissa V. Werrett, Rajini Brammananth, Megan Herdman, **Uthpala M. Garusinghe**, Warren Batchelor, Paul K. Crellin, Ross L. Coppel, Philip C. Andrews. Bismuth Phosphinate Complexes as Additives for Antibacterial Materials. *Manuscript in preparation and to be submitted to Chemical Sciences*.

LIST OF FIGURES

Chapter 1

- Figure 1:** Repeating units of cellulose monomer (Obtained from Gilbert (1998) [1]).
- Figure 2:** Hierarchical break down of the wood from tree to the cellulose molecular structure (Obtained from Isogai [3]).
- Figure 3:** Overview of barrier materials indicating the oxygen permeability and water vapour permeability (Obtained from Aulin [79]).
- Figure 4:** Correlation between pore size and fibre diameter at a constant porosity in a fixed volume. Fibre diameter ratios of 1: 3: 10 (Obtained from Ma [87]).
- Figure 5:** 3D schematic of a pure fragment of silica structure (Obtained from Salh [134]).
- Figure 6:** Schematic representation of the MMT structure (Obtained from Nascimento [143]).
- Figure 7:** Tortuous path created by MMT (Obtained from Azeredo [147]).
- Figure 8:** Crystal structures of rutile, anatase and brookite titanium dioxide. Titanium atoms are in grey and oxygen atoms are in red (Obtained from Woodley [151]).
- Figure 9:** Schematic diagram of the photocatalysis process (Obtained from Gaya [160]).
- Figure 10:** Surface conformation of a polyelectrolyte indicating three segments; trains, loops and tails (Obtained from Sennerfors [194]).
- Figure 11:** Structure of CPAM (Obtained from [204]).
- Figure 12:** Schematic of the dissolution kinetic of CPAM (Obtained from Ngo [205]).
- Figure 13:** Structure of PAE (Obtained from Aoyama [212]).
- Figure 14:** Three constituents in the nanocellulose-inorganic composites with same length scale.
- Figure 15:** Nanoparticle aggregation based on (a) low CPAM concentration; (b) high CPAM concentration (Obtained from Ngo [213]).

Chapter 2

- Figure 1:** Preparation of nanocomposite. (a) Controlled Simultaneous Addition (CSA) method. (b) Preparation of composite sheet by filtration method. (c) Composite sheet processed using blotting papers. (d) Free standing 77 wt% V/S composite sheet. (e) Illustration of flexibility of 77 wt% V/S sheet.
- Figure 2:** Retention of nanofibres and NPs in the composite as a function of initial NP loading.
- Figure 3:** SEM images of nanofibre composite (V/S) with a) nanofibre sheet alone, b) 20 wt%, c) 30 wt%, d) 40 wt%, e) 50 wt%, f) 60 wt%, g) 77 wt% NPs, respectively at high magnification, h) 60 wt%, i) 77 wt% NPs, respectively at low magnifications.
- Figure 4:** Schematic mechanism of NP and CPAM hetero-coagulation with nanocellulose (not to scale). (a) No CPAM: NPs flow through the gap (indicated by the arrow) (b) With CPAM at low NP loading: CPAM bridges NPs with cellulose nanofibres (NPs retain in the gap). (c) With CPAM at high NP loading: Large NP-CPAM structure pushes nanofibres to fit the gap, creating a packed bed structure. Arrows indicate the movement of fibres from the initial position.
- Figure 5:** (a) Thickness and (b) fractional density of composites as a function of NP loading. Error bars in thickness graph are the standard deviations.
- Figure 6:** Pore size distribution for nanocellulose- SiO₂ composite sheets as a function of silica content. (a) V/S (smaller NPs), (b) V/L (larger NPs), (c) enlarged graph of V/L composite between 10-100 nm. The legend indicates the NP loading added in the suspension.
- Figure 7:** Composite pore volume as a function of NP loading. (a) Total pore volume for small pores (3-100nm). (b) Total pore volume for large pores (100-1000nm).
- Figure 8:** Tensile index based on nanofibre grammage on strain for V/S composite.

Chapter 3

- Figure 1:** Scanning electron microscopy (SEM) images (a) pure MFC sheet (b) MFC-22nm SiO₂-0.5mg/m² CPAM composite at high magnification.
- Figure 2:** (a) Auto correlation curves of Pure SiO₂ NPs and SiO₂ with CPAM concentration of 0.03 mg/m² and 0.05 mg/m².(b) Diameter distribution obtained from DLS for SiO₂ NPs with CPAM concentration of 0.03 mg/m², 0.05 mg/m² and 0.09 mg/m².
- Figure 3:** (a) SAXS curve for pure MFC sheet, (b) SAXS curves fitted with the core-shell and spherical models with different CPAM dosages.
- Figure 4:** (a) Electron density variation profile for the spherical core shell particle with SiO₂ core, CPAM shell and cellulose matrix, (b) Structure factor obtained after fitting of the SAXS curve for the CPAM dosages of 0.07 mg/m² and 0.5 mg/m².

Chapter 4

- Figure 1:** NP-CPAM complexes are first formed (step 1) and then mixed with a cellulose nanofiber suspension (step 2).
- Figure 2:** (a) SAXS curve of the pure MFC sheet. The solid line shows the modelled fit. Arrow shows the diameter of the sample for a peak obtained at a particular q value. (b) SEM image of the MFC sheet at 50,000 magnification.
- Figure 3:** (a) SAXS curves fitted with the bimodal distribution of the particles with different CPAM dosages; Sample H (High CPAM dosage), Sample M (Medium CPAM dosage), and Sample L (low CPAM dosage). The solid red line shows the fit and the arrows show the diameter obtained from the particular peak position. (b) Lognormal size distribution curves for the sample with the high dosage of CPAM (H).
- Figure 4:** TEM micrograph for the SiO₂ /CPAM complexes at high CPAM dosage prior to the addition of MFC suspension.
- Figure 5:** (a) Evaluated structure factor S(q) for the samples with different CPAM dosages; sample H has high CPAM, M medium and sample L has low CPAM. (b) Correlation length obtained from the SAXS data analysis.

Figure 6: SEM micrograph of the MFC sheet containing SiO₂ nanoparticles with (a) low (L) CPAM dosage and (b) high (H) CPAM dosage.

Chapter 5

Figure 1: TEM images of montmorillonite (MMT) platelets

Figure 2: EDX and SEM images of composite sheets with various MMT compositions. Line scan across 0 wt% and 33.3 wt% sheet cross sections are shown in (a and b). The cross-sectional image of the sheet with 28.6 wt% MMT shown in c) reveals a strong orientation of MMT platelets parallel to the substrate.

Figure 3: (a) XRD patterns of MMT, nanocellulose sheet and original composite sheets with different MMT loadings, (b) Area under the first XRD peak for original composite sheets and composite sheets with additional homogenization step, (c) 2 theta value of the first peak of the XRD graph with the loading of MMT for both sets of composites.

Figure 4: Mechanical properties obtained from tensile testing for original composite sheets with MMT loading. (a) maximum stress (blue), (b) elastic modulus (orange) and (c) strain to failure (grey). Deviations are based on 95% confidence level.

Figure 5: WVP of nanocellulose/MMT composites. Original composite sheets (blue dots), composite sheets with high pressure homogenization step (red triangles) and sonication step (yellow squares).

Figure 6: Mechanisms of MMT-stacking and arrangement of stacks in nanocellulose network (not to scale). (a) MMTs stack formation at high MMT loading; decrease the tortuous path; (b) MMT stacks are broken down using high pressure homogenization of nanocellulose/MMT suspension; increase the tortuous path for same amount of MMT.

Chapter 6

- Figure 1:** Experimental setup for photo catalytic degradation of methyl orange. The paper samples were cut to squares (2.5 cm x 2.5 cm).
- Figure 2:** UV-visible spectrum of a methyl orange aqueous solution indicating two absorption maxima. The inset illustrates the methyl orange solution colour change by photocatalysis before and after 3 hours UV exposure over TiO₂-MFC composite.
- Figure 3:** Photocatalytic activity of TiO₂-MFC composites with different TiO₂ loadings retained with (a) 10mg PAE/g MFC and (b) 50mg PAE/g MFC.
- Figure 4:** Photocatalytic repeatability and reproducibility for MO solution degradation over UV irradiated MFC-TiO₂ composites made with 10 mg PAE/g MFC and: (a) 2 wt% and (b) 5 wt% TiO₂; (c) Composite reusability for 3 full testing cycles (1wt% TiO₂ and 10 mg PAE/g).
- Figure 5:** Adsorption isotherm of PAE adsorbed on MFC as a function of PAE concentration in solution. The inset highlights the linear adsorption portion at low PAE concentrations. Error bars indicate the standard deviation.
- Figure 6:** Zeta potential of PAE-MFC suspensions as a function of PAE dosage (mg PAE/g MFC). The supernatant of PAE in a MFC suspension was analyzed after centrifugation according to [40].
- Figure 7:** Retention of TiO₂ nanoparticles as a function of initial TiO₂ loading for different dosages of PAE (10 mg/g and 50 mg/g).
- Figure 8:** SEM images of TiO₂ composites with 10 mg PAE/g MFC: (a) 1 wt%, (b) 2 wt%, (c) 5 wt%, (d) 10 wt%, (e) 40 wt% and (f) 80 wt% TiO₂.
- Figure 9:** SEM images of TiO₂ composites with 50 mg PAE/g MFC: (a) 2 wt%, (b) 5 wt%, (c) 20 wt%, and (d) 80 wt% TiO₂.
- Figure 10:** SAXS curves for the MFC/TiO₂ composites with 10 mg/g of PAE and different loading of NPs from 0.5 to 80 wt%.

Figure 11: Photocatalytic performance of the material represented by plotting the variation in rate constant as function of the TiO₂ amount retained in the composite.

LIST OF TABLES

Chapter 1

Table I: Mechanical properties of nanocellulose films from literature.

Table II: Functionality of some commonly used NPs.

Table III: Summary of strengths and weaknesses of nanocellulose and NPs.

Table IV: Some of the nanocellulose composites with different NPs published in literature. The abbreviations are entered below the table.

Chapter 2

Table I: Diameter distribution of NPs (full details in Appendix I Figure A1).

Chapter 4

Table I: Composition of SiO₂-nanocellulose composites, High (H), Medium (M) and Low (L) denote the CPAM concentration.

Chapter 5

Table I: Literature comparison of WVP for nanocellulose-clay based materials.

Chapter 6

Table I: Literature comparison of the material performances

LIST OF ABBREVIATIONS

AFM	Atomic force microscopy
ARC	Australian Research Council
BC	Bacterial cellulose
BEK	Bleached Eucalypt Kraft Pulp
CA	Cellulose acetate
CNC	cellulose nanocrystals
CNF	Cellulose nanofibre
CPAM	Cationic polyacrylamide
CSA	Controlled simultaneous addition
DA	Direct addition
DLS	Dynamic light scattering
LBL	Layer-by-layer
FBRM	Focussed beam reflectance measurements
FE-SEM	Field emission scanning electron microscopy
FTIR	Fourier transform infrared spectroscopy
EDS	Energy dispersive spectroscopy
LDPE	Low density polyethylene
MFC	Microfibrillated cellulose
MMT	Montmorillonite
MO	Methyl orange
NCC	Nanocrystalline cellulose
NFC	Nanofibrillated cellulose

PREFACE

NPs	Nanoparticles
OLEDs	Organic light-emitting diodes
OP	Oxygen permeability
PAA	Polyacrylic acid
PAE	Polyamide-amine-epichlorohydrin
PAH	Poly(allylamine hydrochloride)
PAN	Polyacrylonitrile
PDADMAC	Poly(diallyldimethylammonium chloride)
PDDA	Poly(dimethyldiallyl ammonium chloride)
PDMS	Polydimethylsiloxane
PE	Polyethylene
PEI	Branched polyethylenimine
PES	Polyethersulfone
PET	Polyethylene terephthalate
PP	Polypropylene
PSU	Polysulfone
PS	polystyrene
PSS	Poly(sodium 4-styrenesulfonate)
PVA	Poly(vinyl alcohol)
PVAm	Polyvinyl amine
PVC	Poly(vinyl chloride)
PVDC	Polyvinylidene
PVDF	Polyvinylidene fluoride

PREFACE

QCMD	Quartz crystal microbalance with dissipation
SAXS	Small angle X-ray scattering
SERS	Surface-enhanced Raman spectroscopy
SiO ₂	Silicon dioxide
TEM	Transmission electron microscopy
TEMPO	2,2,6,6,-tetra-methylpiperidine-1-oxyl radical
TFC	Thin film composites
TI	Tensile index
TiO ₂	Titanium dioxide
WAXS	Wide angle X-ray scattering
WVP	Water vapour permeability
WVTR	Water vapour transmission rate
XRD	X-ray diffraction
UV	Ultra-violet
ZVI	Zero-valent iron

LIST OF NOMENCLATURE

nm	nanometre
μm	micrometre
mm	millimetre
$^{\circ}$	degree
$^{\circ}\text{C}$	degrees Celcius
s	seconds
min	minutes
%	percentage
wt%	weight percentage
rpm	revolutions per minute
Da	Dalton
Gpa	Giga Pascal
MDa	Mega Dalton
mL	millilitre
mL/min	mililitre per minute
N	Netwon
kg	kilogram
kg/m^3	kilogram per metre cubed
m^2/g	metre squared per gram
gsm	gram per metre squared
mV	milli volts
keV	kilo electron volts

PREFACE

pA	pico Ampere
μ sec	ultra seconds
r	radius
Pa	Pascals

PREFACE

THIS PAGE HAS BEEN INTENTIONALLY LEFT BLANK

CHAPTER 1

INTRODUCTION & LITERATURE REVIEW

THIS PAGE HAS BEEN INTENTIONALLY LEFT BLANK

CHAPTER 1 INTRODUCTION AND LITERATURE REVIEW

1.1 INTRODUCTION5

1.2 LITERATURE REVIEW7

1.2.1 Nanocellulose7

 1.2.1.1 Definition7

 1.2.1.2 Different terminology8

 1.2.1.3 Sources of cellulose9

 1.2.1.4 Production methods of nanocellulose9

 1.2.1.5 Characterization11

 1.2.1.6 Nanocellulose film production11

 1.2.1.7 Nanocellulose film properties13

 1.2.1.7.1 Mechanical properties13

 1.2.1.7.2 Barrier properties17

 1.2.1.8 Nanocellulose film applications18

 1.2.1.8.1 Device substrates18

 1.2.1.8.2 Membranes19

 1.2.1.8.3 Packaging21

1.2.2 Inorganic nanoparticles22

 1.2.2.1 Properties of NPs23

 1.2.2.1.1 Silicon dioxide-model23

 1.2.2.1.2 Montmorillonite-barrier24

 1.2.2.1.3 Titanium dioxide-photocatalytic25

1.2.3 Nanocellulose – inorganic NP composites28

 1.2.3.1 Nanocellulose – inorganic NP composite production35

 1.2.3.1.1 Surface treatment35

 1.2.3.1.1.1 Layer-by-layer deposition35

 1.2.3.1.1.2 Size press treatment36

 1.2.3.1.1.3 Sol gel method36

 1.2.3.1.1.4 In situ precipitation36

CHAPTER 1

1.2.3.1.1.5 Spray deposition	37
1.2.3.1.2 Wet end addition	37
1.2.3.2 Polyelectrolytes	38
1.2.3.2.1 Cationic polyacrylamide	40
1.2.3.2.2 Polyamide-amine-epichlorohydrin	42
1.2.3.3 Interaction between polyelectrolyte-NP systems in nanocellulose matrix	43
1.2.4 Perspective and conclusion	46
1.2.4.1 Composite production	46
1.2.4.2 Composite characterization	47
1.3 GAPS IN KNOWLEDGE	49
1.4 RESEARCH OBJECTIVES	51
1.5 THESIS OUTLINE	53
1.6 REFERENCES	58

1.1 INTRODUCTION

Nanocellulose is a biodegradable, sustainable and recyclable material with excellent mechanical, optical and barrier properties. Therefore, nanocellulose has gained much attention over the last decade and research on nanocellulose based materials for various applications has drastically increased. For example, nanocellulose can be converted into nanocellulose thin films, which can be used in applications such as packaging, solar panels, flexible electronics and oil and water separation membranes.

However, the range of properties with nanocellulose by itself is limited. For example, nanocellulose provides a good oxygen permeability for a packaging material, but the water vapour permeability is high due to hydrophilic nature of cellulose. Therefore, pure nanocellulose based packaging materials are not ideal for moisture sensitive goods. The idea of nanocellulose based composites with inorganic nanoparticles (NPs), therefore, is promising because the advantages associated with the two individual materials can then be combined together to produce nanocellulose based composites for high end applications. NPs can be tailored for specific applications due to their surface properties, size, shape and chemical composition, but also require a good supporting matrix that is strong, flexible, durable and able to retain NPs while allowing the surface area of NPs to be readily available. Without a supporting matrix, NPs self-aggregate and may result in uncontrolled release to the environment. Therefore, the broad aim of this doctoral thesis is to address the limiting issues of nanocellulose-inorganic NP composites.

To address this, characterization of these composites with different NP loadings (low to extremely high) and sizes is crucial as the change in structure affect the final composite properties. While nanocellulose-inorganic NP composites are made and tested for specific applications, their structure-property relationships have not been explored, which limits the broader use of these composites. Therefore, the first objective of this thesis is to use silicon dioxide (SiO_2) as a model NP to quantify the effect of NP loading and sizes on the structure-property relationship of the composite.

Most of the available NPs and nanocellulose are anionic, therefore, retention aids such as cationic polyelectrolytes are used to fix NPs into the nanocellulose matrix. Proper methods to characterize the internal structure of the NP-polyelectrolyte complexes-structural assemblies of NPs- in the

nanocellulose matrix are lacking. Currently, scanning electron microscopy (SEM) is used to characterize the structure, but SEM is limited because the resolution is not high enough to accurately visualise small NPs, it only shows NPs on the two dimensional (2D) surface and the interaction and structural assembly of the NPs under the influence of polyelectrolytes is not shown. Therefore, the second objective of this thesis is to quantify the effect of polyelectrolytes on the structural assembly of NPs by adopting a complimentary scattering techniques, small angle X-ray scattering (SAXS). SAXS is a powerful tool that enables to analyse the bulk of the composite structures ranging in length scale from 1-100 nm. These characterizations will be invaluable for practical applications to tailor superior composites.

Using the knowledge obtained through composite preparation and characterization, the third objective is to prepare cheap and easily scalable composites that demonstrate two applications using two functional NPs; engineered nanocellulose-montmorillonite (MMT) composite as a material with excellent water vapour barrier properties, and nanocellulose-titanium dioxide (TiO₂) composite as a portable and green photocatalytic material.

Chapter 1 presents a critical review of nanocellulose-inorganic NP composites, which leads directly to the specific research objectives of this doctoral thesis. This chapter has four main parts (Section 1.2, 1.3, 1.4 and 1.5). In Section 1.2, the Literature Review, different sources of nanocellulose, production methods, characterization methods, nanocellulose film production, properties and applications is reviewed in Section 1.2.1. NPs and their role, properties and applications are reviewed in Section 1.2.2. Nanocellulose-NP composite production and polyelectrolytes are reviewed in Section 1.2.3. The final sub section gives the perspective of nanocellulose-NP composites, polyelectrolyte application and current problems with characterization of NP-polyelectrolyte systems (Section 1.2.4). Section 1.3 identifies the significant gaps in knowledge, which leads to specific research objectives in Section 1.4. The last section provides the organization of the thesis (Section 1.5).

1.2 LITERATURE REVIEW

The objective of this literature review is to critically review the development of nanocellulose-inorganic nanoparticle (NP) composites and identify the gaps in knowledge and opportunities. A brief overview of the properties of nanocellulose and inorganic NPs on their own are presented first, to provide a background to further discussion and the need for nanocellulose-NP composites. Three NPs, silicon dioxide (SiO₂), montmorillonite (MMT), titanium dioxide (TiO₂), have been selected in this thesis due to their wide usage, unique properties and functionality. This review then focuses on the deposition, characterization, production and applications of nanocellulose-NP composites.

1.2.1 Nanocellulose

1.2.1.1 Definition

Cellulose is the most abundant natural (bio)-polymer on earth, occurring in plant based materials. It is a high molecular weight linear homopolymer consisting repeating units of β -D-glucopyranosyl joined through (1 \rightarrow 4)-glycosidic linkages in different arrangements [1]. The basic chemical structure of cellulose is shown in Figure 1. Cellulose is the main reinforcing constituent in plant cell walls in combination with hemicellulose and lignin [2]. The hierarchical breakdown of the tree to produce cellulose bundles and fibrils are shown in Figure 2.

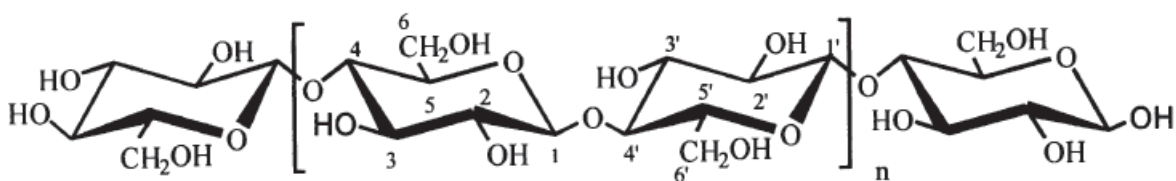


Figure 1: Repeating units of cellulose monomer (Obtained from Gilbert (1998) [1]).

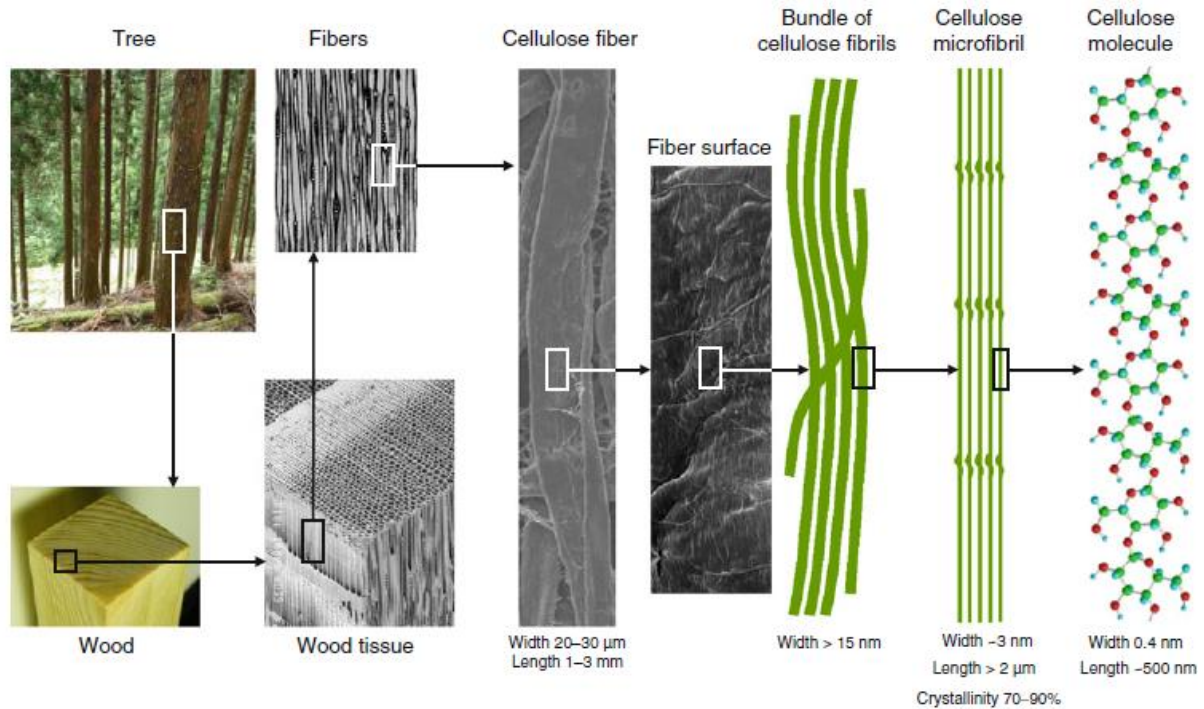


Figure 2: Hierarchical break down of the wood from tree to the cellulose molecular structure (Obtained from Isogai [3]).

Excellent characteristics of cellulose such as renewability, biodegradability, light weight, low cost, and nontoxicity make it a universally accepted resource [4-6]. Therefore, the development and interest on cellulose based fundamentals and applications research had been increased drastically in the past decades, and will continue to increase in coming ones.

1.2.1.2 Different terminology

Reduction in the diameter of cellulose fibres result in the production of nanocellulose (Figure 2). The term microfibrillated cellulose (MFC) was first introduced in 1980s by Turbak [7]. In literature, the term MFC, cellulose nanofibres and nanocellulose are all used to address fibres with diameters between 1-100 nm [7-9]. MFC should not be confused with the term “microfibrils”. MFC is composed of liberated semicrystalline microfibrils, produced through high pressure homogenization of wood pulp [10]. MFC is also termed “nanofibrils”, “nanofibre” and “nanofibrillated cellulose” in literature [11]. Nanocrystalline cellulose (NCC) is obtained by removing the amorphous sections of cellulose by acid hydrolysis, and are also termed “cellulose nanocrystals”, “crystallites”, “whiskers” and “rodlike cellulose microcrystals” in literature [12, 13].

In this thesis, we have used the term “nanocellulose” to address fibres with diameter ranging from 1-100 nm. This means MFC and nanocellulose essentially addresses the same fibre in this thesis.

1.2.1.3 Sources of cellulose

The main source of cellulose are plants. Despite the relative chemical simplicity, the physical and morphological structure of cellulose in higher plants are more complex and heterogeneous. The contents of cellulose in woods are about 40-50%, in bushes 30%, in bast plants 65-70% and in cotton fibres 90% [14]. Cellulose from wood is the primary and the most important industrial raw material for renewable energy sources, building materials, clothing, and pulp and paper industries [5]. The most widely used fibre for the production of MFC is bleached kraft pulp derived from wood [15]. The relatively high cost of the kraft pulp as a feedstock has driven interest towards the use of other sources of cellulose fibres from agricultural crops and by-products such as wheat and soy hulls [16], bagasse [17], rice straw [18], banana rachis [19] and sugar cane, etc. Agricultural crops have the processing advantages over wood because most cellulose is present in the primary cell wall that can be fibrillated easily compared to cellulose in secondary cell wall in wood. Also, non-wood plants generally have less lignin than wood, which makes the bleaching process much easier [20].

Cellulose fibres are also extracted from certain bacteria, denoted as bacterial cellulose (BC). *Acetobacter xylinum*, a gram-negative strain of acetic-acid-producing bacteria is the most efficient producer of BC [21, 22].

1.2.1.4 Production methods of nanocellulose

Due to strong hydrogen bonding between microfibrils, it is extremely difficult to fibrillate cellulose using refining. In early work, MFC was first produced using a high pressure homogenizer at 8000 psi and 80 °C, which required number of passes to break down the cell wall to delaminate fibres to give microfibrils. This causes a high demand for energy (approx. 25,000 kWh per tonne for the production of MFC) and impedes the commercial success. In addition, the frequent clogging of the homogenizer was a massive drawback [7, 23]. It was discovered later that the production of MFC using primary wall materials (e.g. sugar beet) are easier than the secondary wall materials (e.g. eucalyptus) [24]. However, for wood based cellulose fibres, chemical, mechanical and enzymatic

pre-treatment methods were developed to reduce the energy usage during homogenization and to improve the degree of nanofibrillation achievable [11].

Chemical pre-treatments involve introducing carboxylate groups in the form of sodium salts into cellulosic materials through various chemicals. Such groups swell the pulp, lower the cell wall cohesion and help the delamination. The energy requirement, after carboxymethylation treatment, to produce MFC has been reduced to approx. 500 kWh per tonne [25-27]. A novel way to introduce sodium carboxylate groups to cellulose is using 2,2,6,6-tetra-methylpiperidine-1-oxyl radical (TEMPO)-mediated oxidation in water. TEMPO catalyst can help to oxidize C6-primary hydroxyl groups of glucosyl units on the crystalline cellulose microfibril surfaces to C6-carboxyl groups of glucuronosyl units. When there are sufficient TEMPO treated aqueous cellulose fibres with C6-carboxylate content, the fibres can easily be converted to a highly viscous transparent gel using gentle mechanical disintegration. The sheet production with these fibres are limited to casting method due to high viscosity and gel behaviour. TEMPO oxidation does not change the morphology, crystal structure, crystallinity and crystal width of bleached wood cellulose. The TEMPO oxidation conditions and mechanical fibrillation can affect the length and the degree of polymerization of the treated fibres [28-31].

Mechanical pre-treatments involve subjecting cellulose fibres through various treatment processes to remove the primary cell wall, exposing secondary cell wall for further processing. The pre-treatment processes include disintegration in waring blenders, beating and refining in PFI mills, cryocrushing, and disk refiner, before nanocellulose production [16, 32-34]. For example, in refiners, the primary cell wall is damaged by being trapped between the rectangular bars in discs and cones in the rotors and refiners, separated by groove spaces.

Enzymatic hydrolysis pre-treatment partially cleaves the cellulose glycoside bonds present at the surface of fibres, making the fibrillation process easier when shearing using a high pressure homogenizer. Therefore, a combination of refining and enzymatic pre-treatment has opened up an economically viable method to reduce the energy usage from 12000-70000 kWh per tonne to 1500 kWh per tonne. Enzymes such as fungus isolated from infected Elm trees and endoglucanase are widely used [11, 35, 36].

The focus of this thesis is not optimize ways to save energy with pre-treatment methods. This thesis has focused on composite sheet preparation with nanocellulose fibres with combination of

different inorganic NPs and polyelectrolytes. The nanocellulose fibres used in this thesis is a commercially purchased product.

1.2.1.5 Characterization

The diameter and length distributions are significantly different between nanocelluloses, depending on its origin, pre-treatment conditions, production methods and other factors. Therefore, it is important to characterize nanocellulose since the properties are dependent on its structural parameters. Such properties include, for example, hydrodynamic properties which affects the rheological and interfacial properties [3, 37].

Scanning electron microscopy (SEM), transmission electron microscopy (TEM) and atomic force microscopy (AFM), combined with other imaging analysis, can be used to measure the diameter of nanocellulose. However, the high aspect ratio of nanocellulose prevents the precise estimation of their length because of entanglements and difficulties in identifying both ends of individual nanofibres [5, 38, 39].

In order to estimate the length of fibres, a sedimentation method was used in literature. This method allows to measure the gel point concentration, which is the lowest concentration at which fibres form a continuous network, also known as the connectivity threshold. Below the gel point concentration, the suspension does not have any mechanical strength because the fibres are not continuously in contact with each other. Martinez et al. (2001) first developed this method to calculate the aspect ratio on wood fibres [40]. Later, Zhang et al. (2012) adopted this method to measure the aspect ratio of nanocellulose [41]. Detailed description of theoretical equations used to calculate the aspect ratio through sedimentation method is given in [40, 42, 43]. Recently, this method was also adopted to investigate the relationship that gel point has on other processing parameters such as drainage time and final nanocellulose film properties, which has enabled the tailoring nanocellulose film production [44, 45]. In this thesis, this technique is used to obtain the aspect ratio of nanofibres.

1.2.1.6 Nanocellulose film production

Nanocellulose film production is hindered by the difficulty in producing simple and reproducible nanocellulose films both at laboratory and industrial scale. In laboratory scale, nanocellulose can be converted into nanocellulose thin films through casting, spraying or vacuum filtration. Casting

takes hours to several days, depending upon the evaporation of water used to disperse nanocellulose fibres and the air drying conditions (temperature and humidity). As such, casting is not a commercially scalable method [46-49]. Vacuum filtration and spraying are both considerably quicker processes compared to casting, however, these processes are still largely restricted to the lab scale.

During vacuum filtration, nanocellulose suspension is poured through a filtration column, where nanofibres settle down as the water drains through a filter, creating a wet film. A filter with smaller pore size improves the retention of nanocellulose, however, the drainage time then increases. Therefore, a range of different filter media have been tried. Some of these include; polyamide membrane filter with pore size 0.22 μm [50], hydrophilic polytetrafluoroethylene membrane with pore size 0.1 μm [51], woven filter fabrics with variety of pore sizes (55 μm , 109 μm and 150 μm) [41], Millipore filter membrane with pore size 0.65 μm [52], etc. When the wet film is formed, the film is taken out, and dried through various methods such as air drying [53], oven drying [52], hot pressing [54], sheet drier [55], etc. Also, if the water is removed through freeze-drying, then the wet film can be converted into “sponge-like” aerogels [56]. Laboratory nanocellulose film preparation time of a 60 g/m^2 basis weight sheet through vacuum filtration has been reduced from 3 to 4 hours [57] to 10 minutes [55]. This was done by increasing the solids content above the gel point and using polyelectrolytes to increase the strength of the flocs to improve filter resistance, while using commercial woven papermaking filters to minimise drainage resistance. With this method, however, there can still be significant issues regarding the handling of the wet film before drying.

Spraying nanocellulose to create films have recently been developed at laboratory scale as an alternative technique to filtration [58]. It can be done at higher solids content, reducing the amount of water to be removed during drying. Therefore, the basis weight achievable using spraying is much higher than that with filtration. Maximum basis weight pickup of 124 g/m^2 was achieved by spraying nanocellulose onto a nylon fabric running at a speed of 0.5 m/min [59]. Also, free standing nanocellulose films with basis weights ranging from 59 to 118 g/m^2 and thickness varying from 46 to 68 μm was recently prepared by Magnusson [60]. Furthermore, there are handful of publications on spraying nanocellulose to produce multilayer nanocomposites, suggesting that it is a promising method for rapid fabrication of large surface area composite

nanopapers [61, 62]. While spraying have advantages in terms of efficiency by reducing operator time, disadvantages of this method is the time taken for the water to evaporate to create a dry film and the formation of cracks in films. To avoid such cracks, extensive pretreatment methods prior to spraying needs to be done, which makes the production process difficult. However, very recently, Shanmugam et al. (2017) sprayed nanocellulose suspensions directly into a smooth steel plate, without any additional treatments, to produce nanocellulose films [63].

A further disadvantage of spraying, that is particularly relevant to NP composites is the occupational health risks that spraying may produce NP aerosols. Therefore, this thesis focuses on preparation of nanocellulose films and composites through vacuum filtration method. A sheet drier operating at 105 °C is used to dry nanocellulose and composite films, as it enables to dry the films in less than 10 minutes while avoiding any wrinkling or high moisture gradients. Two blotter papers sandwiching the film are passed through the moving belt in the sheet drier; the speed can be adjusted. The metal cylinder in the middle is heated to 105°C. When the moving belt goes around the metal cylinder, the film dries.

1.2.1.7 Nanocellulose film properties

There are number of reviews that detail many properties associated with nanocellulose films [9, 39, 64, 65]. For example, they include mechanical, optical, barrier and thermal properties. The two most important properties for the work in this thesis are strength and barrier properties.

1.2.1.7.1 Mechanical properties

Mechanical strength is one of the important parameters of nanocellulose films made from cellulosic materials. It is important when nanocellulose films are used in applications such as packaging, supporting matrix and membrane, to hold the structure while it provides its functions. The strength arise from the formation of hydrogen bonds between nanofibres due to tightly packed nanofibre network. Strength properties rely on number of critical factors such as aspect ratio of fibres, strength of individual fibres and bonds between fibres [66]. The tensile strength also varies based on nanocellulose origin, processing conditions and structural properties.

For most materials, the strength is expressed in Pascals (Pa) – breaking load per unit area, but this is difficult for a paper material because thickness is not very well defined. The thickness measured with a platen tester will depend significantly on the pressure. Therefore, tensile index (TI) is a good

indicator to measure and compare the strength of paper materials, as it is normalised by weight and not thickness. TI is the strength in N/m divided by grammage of the sheet. Mechanical properties of nanocellulose films prepared from different cellulose sources and by different production procedures are summarized in Table I. The reported strengths for the nanocellulose are strong, but highly variable due to reasons mentioned above.

Table I: Mechanical properties of nanocellulose films from literature.

Source of material	Pre-treatment/production of nanocellulose	Preparation	Thickness (μm)	Density (g/cm^3)	Grammage (g/m^2)	Maximum Strength (MPa)	Tensile Index (Nm/g)	Elastic Modulus (GPa)	Elongation (%)	Reference
Bleached spruce sulphite pulp	Homogenization	Vacuum filtration	21 \pm 1	0.81	17 \pm 1	104	129 \pm 16	15.7 \pm 1.3	5.3 \pm 1	[47]
			23 \pm 1	0.88	23 \pm 1	126	126 \pm 23	16.7 \pm 0.7	5.4 \pm 1.5	
			30 \pm 1	0.97	30 \pm 1	136	136 \pm 14	16.5 \pm 0.2	8 \pm 0.8	
			33 \pm 2	1.07	35 \pm 3	154	146 \pm 18	17.5 \pm 1	8.6 \pm 1.6	
Softwood	TEMPO	Suction filtration	20	1.46	29.2	233 \pm 44	159.6	6.9 \pm 1.4	7.6 \pm 0.2	[67]
Hardwood	TEMPO	Suction filtration	20	1.45	29	222 \pm 11	153.1	6.2 \pm 1.6	7 \pm 2.4	[67]
Commercial MFC	-	Spray coating	-	-	100.5	-	60.2 \pm 1.5	-	-	[63]
Commercial MFC	-	Vacuum filtration	-	0.75	60	-	71	-	-	[68]
Softwood sulphite pulp	Mechanical beating and Enzymatic treatment	Casting	40	1.4	56	180 \pm 10	128.5	10.3 \pm 0.16	5.9 \pm 0.8	[69]
		Filtration	45	1.4	63	211 \pm 26	150.7	12.1 \pm 0.29	6.6 \pm 1.5	
		Filtration	55	1.4	77	178 \pm 17	127.1	10.3 \pm 0.31	6.3 \pm 1.4	
		Semiautomatic sheet former	40	1.4	56	232 \pm 19	165.7	13.4 \pm 0.25	5.0 \pm 1.1	
Sugar beet pulp chip	Homogenization	Casting	-	-	-	104 \pm 8	-	9.3 \pm 0.9	3.2 \pm 0.8	[70]
Softwood	Enzymatic and Mechanical pre-treatment followed by homogenization	Vacuum filtration	60-80	1.14-1.2	68.4-96	129-214	113.2-178.3	10.4-13.7	3.3-10.1	[52]

CHAPTER 1

Wheat straw	Chemical treatment	Casting	-	0.8	-	30.2±1.3 4	-	7	1.8±0.1	[71]
Thermo-mechanical pulp	Mechanical beating and homogenization	Casting	58±3	0.514	29.81	28.27	55±2.9	5.13±0.83	-	[72]

Note: Test conditions are reported in the original references. Tensile index and grammage is usually calculated, if not specified, based on density, thickness and tensile strength reported.

1.2.1.7.2 Barrier properties

The most important barrier properties for all packaging materials are the oxygen permeability (OP) and the water vapour permeability (WVP). OP and WVP are derived from oxygen transmission rate (OTR) and water vapour transmission rate (WVTR) values, respectively, by incorporating the thickness and the pressure gradient [73]. Nanocellulose films have significantly lower OP values ($0.004 \text{ cm}^3 \cdot \mu\text{m} \cdot \text{m}^{-2} \cdot \text{day}^{-1} \cdot \text{kPa}^{-1}$) [67] compared to other petroleum based barrier materials such as polyvinylidene (PVDC) ($0.1\text{-}3 \text{ cm}^3 \cdot \mu\text{m} \cdot \text{m}^{-2} \cdot \text{day}^{-1} \cdot \text{kPa}^{-1}$) [74], poly(vinyl chloride) (PVC) ($20\text{-}80 \text{ cm}^3 \cdot \mu\text{m} \cdot \text{m}^{-2} \cdot \text{day}^{-1} \cdot \text{kPa}^{-1}$) [74], and low density polyethylene (LDPE) [75]. Although both OP and WVP values vary based on the nanocellulose source, chemical composition, physical structure and pre-treatment methods used to produce nanocellulose, nanocellulose films are seen as a good oxygen barrier material [64]. The main concern of nanocellulose films is the water barrier properties.

The influence of the type and the chemical composition of wood sources on WVTR was studied by producing MFC films from different wood pulp sources, using softwood and hardwood, both with and without lignin. MFC from bleached hardwood showed the highest WVTR ($200 \text{ g} \cdot \text{m}^{-2} \cdot \text{day}^{-1}$) [76]. However, regardless of the source, WVTR values are all higher than that of LDPE ($20 \text{ g} \cdot \text{m}^{-2} \cdot \text{day}^{-1}$) [76]. Upon the lignin content, WVTR increased from 300 to $500 \text{ g} \cdot \text{m}^{-2} \cdot \text{day}^{-1}$ and this could be due to the larger pores created in the film because of the low quality hydrogen bonds formation. Even though hydrophobicity increased with lignin content, the film structure is the most dominant factor affecting the water barrier properties [72, 77]. Therefore, the chemical composition in nanocellulose films play a major role in barrier properties than the type of wood source used to create the film.

Minelli et al. (2010) tested the effect of pretreatment on the production of MFC has on the WVTR by producing MFC via enzymatic pretreatment and carboxymethylation pretreatment [78]. The films were casted and dried using an incubator. At $35 \text{ }^\circ\text{C}$ and 0% relative humidity, WVTR of carboxymethylated MFC films gave a lower value ($10^{-4} \cdot \text{mol} \cdot \text{m} \cdot \text{m}^{-2} \cdot \text{s}^{-1} \cdot \text{Pa}^{-1}$) compared to an enzymatic treated MFC ($10^{-13} \cdot \text{mol} \cdot \text{m} \cdot \text{m}^{-2} \cdot \text{s}^{-1} \cdot \text{Pa}^{-1}$) [78]. The difference between the pretreated MFC films were not that significant. Therefore, the type of pretreatment applied on nanocellulose does not play a major role in water barrier properties.

Despite all of these treatments and production methods, WVTRs for 100% nanocellulose films still remain higher than the other polymer films, which is a significant barrier to use these as a barrier material. Figure 3 shows where nanocellulose films stand in the barrier sector. Production of nanocellulose based composites with fillers can reduce water barrier properties, but the type of filler that is used may interfere the film structure and porosity [64].

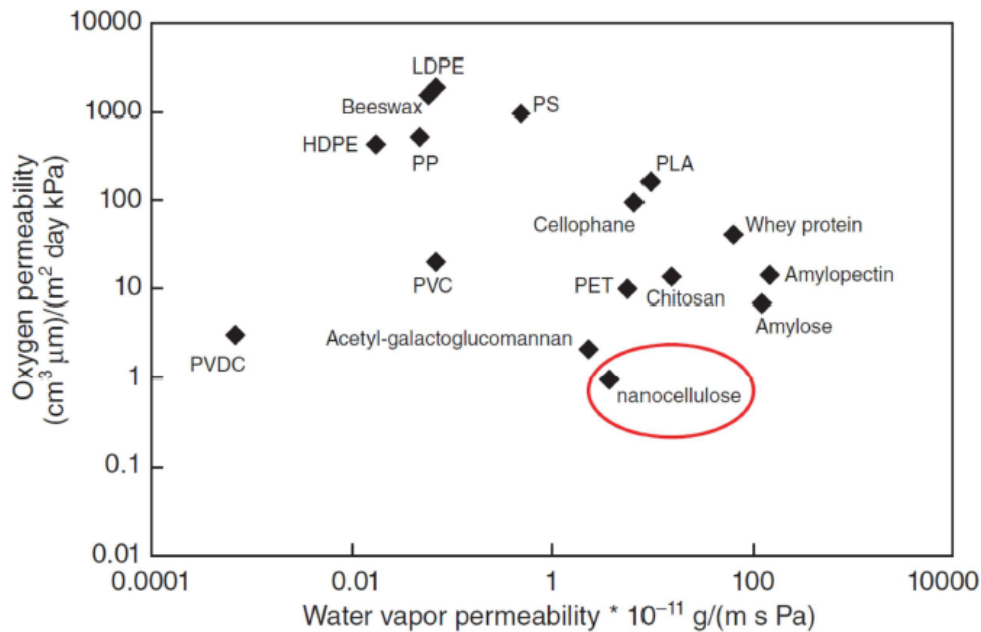


Figure 3: Overview of barrier materials indicating the oxygen permeability and water vapour permeability (Obtained from Aulin [79]).

1.2.1.8 Nanocellulose film applications

Due to excellent properties of nanocellulose, nanocellulose films are a promising candidate for many fields of applications, including device substrates-supporting matrix, membranes and packaging films.

1.2.1.8.1 Device substrates

Extremely low coefficient of thermal expansion, optical transparency and foldability in nanocellulose paper has led to the use of nanocellulose films, in lab scale, as substrates for numerous electronic applications, including highly sensitive antennas [80], organic light-emitting diodes (OLEDs) [81], chemical and biological sensors [82] and organic solar cells [83]. This is a promising step towards commercialization as these can be used to overcome various problems

arising from other available electronic devices. Fabrication of small subset devices for flexible electronics involve depositing conductive materials such as silver nanowires, graphene, carbon nanotubes and other conductive materials in the transparent substrate [84]. During this process, the transparent substrate must maintain their high optical transparency after high temperature heating. This is an issue for flexible polymer substrates. For example, polyimide films have high thermal durability, but their cost and yellow colour restrict them from use as a device substrate. Also, polyethylene terephthalate (PET) films are transparent and low cost, but they do not have enough thermal durability at high temperatures. Inorganic silicon or glass substrates, which have high thermal durability and low thermal expansion then can be used, but, these devices are heavy and inflexible [85, 86]. Therefore, nanocellulose films are a promising candidate for future electronic devices.

1.2.1.8.2 Membranes

Many organic and inorganic membranes are used for water filtration and waste water treatment applications. Commercially available organic membranes include, polypropylene (PP), polyethylene (PE), polyacrylonitrile (PAN), polysulfone (PSU), polyethersulfone (PES), polyvinylidene fluoride (PVDF) and cellulose acetate (CA) [87]. PAN, PSU, PES and PVDF are low cost and have good mechanical properties, but can cause oil, particle or biomacromolecule fouling [88]. CA membranes are sensitive to pH, thus can only be used in a narrow pH range. PP and PE have a good chemical resistance, cheap and good strength, however, they have poor resistance to weather, chlorine and oxidize easily and are flammable [87]. One major disadvantage in fabrication of above polymeric membranes is that volatile and toxic solvents have to be used, causing environmental concerns during solvent disposal [87-90]. While some new materials with excellent properties for water purification has been developed, their complex preparation process, cost and environmental concerns have made them difficult to implement on an industrial scale [91, 92]. A new material with excellent performances and minimal environmental impact is required. Hence, the next generation membranes should have excellent performances, be biodegradable, have low environmental impact during production and disposal and save energy. Nanocellulose films are a good candidate to be used to prepare such membranes.

There are two types of membranes: symmetric and asymmetric. Symmetric membranes are usually dense with thickness varying from 10 to 200 μm , while asymmetric membranes have a

dense top layer with thickness varying from 0.1 to 0.5 μm followed by a porous bottom layer with thickness varying from 50 to 150 μm [93]. Asymmetric membranes are more commercially used due to advantages such as low hydrodynamic resistance and high water flux which improves the performances [94]. Thin film composites (TFC) are similar to asymmetric membranes and typically consists of two to three layers. The bottom layer is generally tough and made from a non-woven material that provides mechanical strength to support subsequent layers. TFC made from combining organic and inorganic materials are attractive as nano-sized inorganic particles can fine tune the pore structure for different filtration categories [87].

There are three regimes of membrane filtration; particle filtration (yeast cells, pollens beach sand with particulate size is $\sim 1\text{-}1000\ \mu\text{m}$), microfiltration (paint pigments, bacteria with particulate size $\sim 0.1\text{-}1\ \mu\text{m}$) and ultrafiltration (virus, colloidal silica, albumin protein with particulate size $\sim 0.01\text{-}0.1\ \mu\text{m}$) [95]. The nanofibre diameter and the bulk porosity can be tailored to control the pore size in the film network. Figure 4 shows three dimensional (3D) simulated models with different fibre diameters to illustrate the relationship between fibre diameter and the pore size [87]. Thus, controlling the pore size allows to make nanocellulose membranes suitable for microfiltration and ultrafiltration applications. However, to filter the lowest particle sizes ($\sim 1\ \text{nm}$) in ultrafiltration applications may require the addition of inert NPs to control the pore size even further.

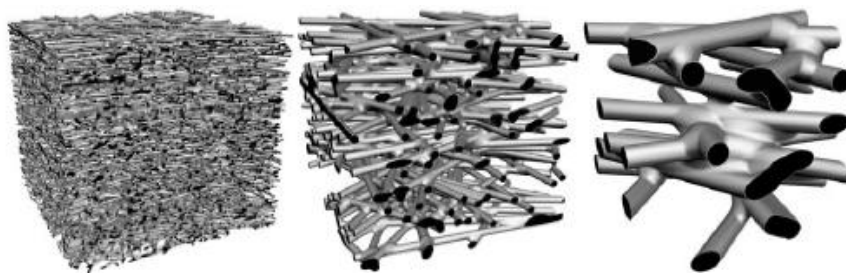


Figure 4: Correlation between pore size and fibre diameter at a constant porosity in a fixed volume. Fibre diameter ratios of 1: 3: 10 (Obtained from Ma [87]).

Varanasi produced TFC membrane by using the NIST hardwood sheet as a bottom layer followed by composite layer of SiO_2 NPs and nanocellulose (1:9 ratio) as the top layer. The flux (80 Litres per square meter per hour) and molecular weight cut off (200 KDa) was significantly improved to that of nanocellulose alone [96]. Pore size distribution indicates a low pore size range with the SiO_2 addition. However, the study only investigated one addition level of NPs and the resultant pore size distribution with high SiO_2 NP content is not reported. Nanocellulose films with better

controlled pore structures, using inorganic NPs are a promising candidate for ultrafiltration membrane applications.

1.2.1.8.3 Packaging

A common type of packaging involves the use of paperboard or cardboard as a support structure, with internal and/or external layers of other substances for improved barrier properties. An example of such laminated composite packaging can be seen in milk cartons, coffee cups, coffee bean bags, etc. These typically feature LDPE or similar materials lining the inner and outer surfaces of a cardboard structure [97]. The outer surface of the cardboard is thus protected from adsorption of moisture from the surroundings, while the inner surface is separated from direct contact with the milk. This protection is required due to the hydrophilicity of paperboard [98], and the damage associated with the extensive uptake of water.

While current packaging materials are effective in their primary purpose of protecting the encased products, there are still drawbacks and areas for improvement. The polyethylene layers of the laminate composites discussed above are not biodegradable. Recycling these packaging types are also difficult due to the need to separate the composite's components. Polyethylene itself is not an easily recyclable material even in its pure form, with an estimated 97.5% of all LDPE produced being sent to landfill, and just 2% being recycled [99]. This current lack of biodegradability and the poor recyclability of such composite packaging contribute to energy consumption and global warming. The production of polyethylene requires polymerisation reactions that take place at high temperature and pressure, up to 300 °C and 300 MPa respectively. Hence, this process requires a great energy usage, with roughly 77 MJ expended per kilogram of LDPE produced, while also requiring the input of 840 grams of crude oil. This production also releases greenhouse gases, specifically 1.7 kg of carbon dioxide and 16 g of methane per kilogram of LDPE [100].

Nanocellulose films can replace plastics in the packaging sector, as mentioned in Section 1.2.1.7.2, due to its biodegradability, recyclability and very low OP. However, WVP of nanocellulose is high due to hydrophilic nature of cellulose (as seen in Figure 3). This material characteristic weakens the strong bonds holding the two dimensional (2D) structure [101]. If WVP can be reduced in nanocellulose films, while maintaining the recyclability and biodegradability, then this material can potentially replace laminate layers in packaging materials mentioned above. Achieving a low WVP while keeping low OP is the key challenge to achieve packaging materials and membranes

with the required quality and ability to extend the shelf life of moisture sensitive foods, electronics and pharmaceuticals. Therefore, it is of interest to lower WVP of nanocellulose films, while maintaining its recyclability and biodegradability. This is one of the areas that have been addressed in this thesis.

1.2.2 Inorganic nanoparticles

Nanoparticles (NPs) are particles with at least one dimension between 1 and 100 nm. They show properties that are not found in the bulk samples of the same material. The advantages of NPs primarily come from the size reduction and the dramatic increase in surface area. The most important NP parameters affecting the structure and properties in a nanocellulose matrix is the particle composition, particle size and size distribution, shape and aspect ratio (spherical, cylindrical, plane) and surface properties (specific surface area, bonding type, charge distribution, surface chemistry) [102, 103]. Table II shows some commonly used NPs, their functionality and applications. Based on those, SiO₂, MMT and TiO₂ NPs are selected in this thesis to produce composites with nanocellulose. Therefore, this section reviews the properties of SiO₂, MMT and TiO₂ NPs.

Table II: Functionality of some commonly used NPs.

Nanoparticle	Functionality	Applications
SiO ₂	Inert fillers. With combination of other organic/inorganic materials, it can serve in many applications.	Coatings [104], Electronic and optical packaging materials [105], Ultra-permeable reverse-selective membranes [106], Sensors [107], Fillers to control pore structure [96, 108].
MMT	Serves as platelets to create tortuosity in a network	Barrier applications [73, 109, 110], Fire retardant [111].
TiO ₂	Photocatalytic Antimicrobial	Photodegradation of organic pollutants [112], Photocatalytic hydrogen production [113], Packaging [114, 115], Stain-proofing and self-cleaning [116].
Silver (Ag)	Antibacterial and antimicrobial Catalytic	Antimicrobial coatings [117], Wound dressings [118], Biomedical devices [119], Food packaging [120], Water treatment [121], Surface enhanced Raman scattering (SERS) [122].
Gold (Au)	Conductive Catalytic	Electronic devices [123], Drug and protein delivery [124, 125], Biosensors [126], SERS [127].

Copper (Cu)	Antimicrobial Catalytic	Biosensors [128], Electrochemical sensors [129], Catalytic applications [130].
Cobalt (Co)	Magnetic	Medical sensors [131], Coatings [132].

1.2.2.1 Properties of NPs

1.2.2.1.1 Silicon dioxide - model

Silicon dioxide (SiO_2) is a commonly occurring compound in nature and can also be synthesized. It has a three dimensional covalent structure as shown in Figure 5. Each silicon atom is covalently bonded to four oxygen atoms and each oxygen atom is covalently bonded to two silicon atoms. This means, there is a ratio of two oxygen atoms to one silicon atom, which gives the formula, SiO_2 [133]. Due to strong covalent bonding, SiO_2 is hard, does not dissolve in water and does not conduct electricity.

SiO_2 formed by the chemical reaction of silicon and oxygen, can be both amorphous and crystalline, depending on the surface differences. Depending upon the temperature, pressure and the cooling rate, SiO_2 can have different structures. Crystalline silica exists in seven different forms, of which four are rare. The three major forms are quartz, cristobalite and tridymite. All of them are chemically identical but the physical forms are different as their internal structures are different due to differences in Si-O bond length (d), the tetrahedral angle (ϕ), the inter-tetrahedral bond angle (α) and bond torsion angles (δ_1, δ_2) (Figure 5). The amorphous SiO_2 also takes the same chemical structure but then exhibits only short range ordering of atoms [133-135].

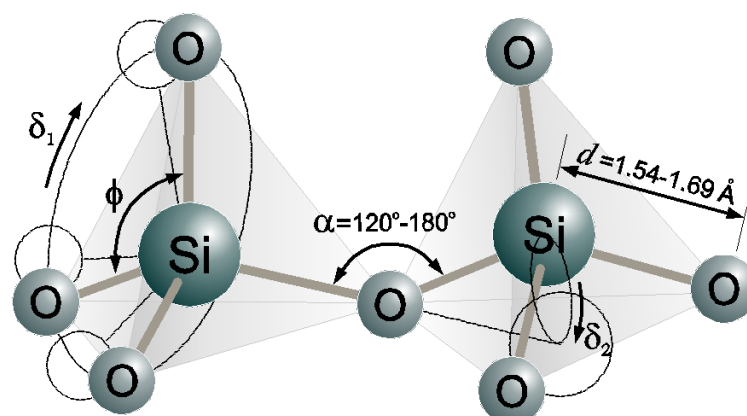


Figure 5: 3D schematic of a pure fragment of silica structure (Obtained from Salh [134]).

SiO_2 can be synthesized as non-porous silica spheres or micro-/mesoporous materials [136]. It has a good abrasion resistance, high thermal stability and electrical insulation. For these reasons, it is used as an inert, low expansion filler material for epoxy resins and electronic circuits [137, 138]. SiO_2 is also used with nanocellulose to produce separators for lithium-ion batteries [108].

Due to its spherical shape and the availability of a range of nanoscale sizes, SiO_2 is used as a model NP in this thesis to produce composites to characterize the structure.

1.2.2.1.2 Montmorillonite – barrier

Montmorillonite (MMT) is a type of nanoclay which composes of two tetrahedral layers sandwiching the central octahedral layer. In the tetrahedral layer, the silicon atom is surrounded by four oxygen atoms, and in the octahedral layer, metals such as aluminium or magnesium are surrounded by eight oxygen atoms. The tetrahedral and octahedral layers are bonded to each other by oxygen atoms [139, 140]. Schematic representation of the layered MMT structure is shown in Figure 6. The layers are arranged in a form of stacks which leads to a regular van der Waals gap between the layers called the interlayer or the gallery [141]. As the van der Waals forces are weak, the intercalation of the small molecules between layers is easier. Therefore, added to the low cost, the rich intercalation chemistry of the MMTs allow them to be chemically modified and makes them compatible with polymeric matrices [142].

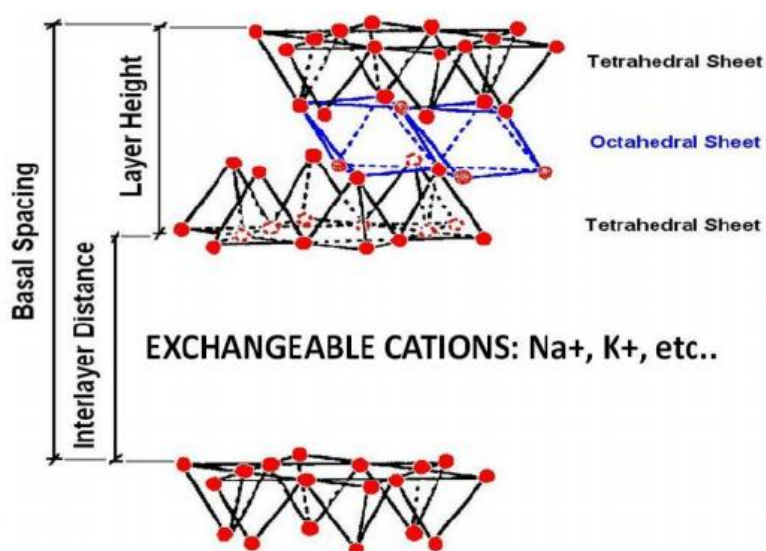


Figure 6: Schematic representation of the MMT structure (Obtained from Nascimento [143]).

Usually, the layer thickness of MMT is around 1 nm, and the lateral dimensions vary from 30 nm up to couple of microns, giving a high aspect ratio ranging from 100-1500 [144]. These disk shaped MMTs therefore when mixed with polymer, create a tortuous diffusive path for molecules to penetrate as shown in Figure 7. Therefore, MMT serve as an excellent additive in composites to create a barrier material for oxygen, water vapour and carbon dioxide [145, 146].

In the work of this thesis, MMT is used to create nanocellulose-MMT composites to improve the WVP of the composite material.

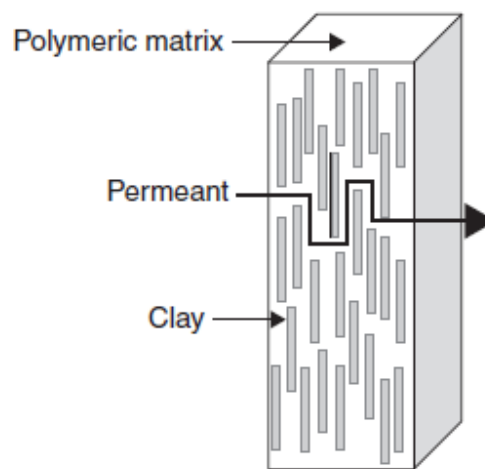


Figure 7: Tortuous path created by MMT (Obtained from Azeredo [147]).

1.2.2.1.3 Titanium dioxide – photocatalytic

Titanium dioxide (TiO_2) also known as Titania, is the naturally occurring oxide of Titanium. It is extensively used as a white pigment, for example in paints, because of its high brightness and high refractive index [148]. It is also used in wide range of other applications which includes addition to tiles, paints and cements to give material sterilizing, deodorising and anti-fouling properties, and added to sunscreens because it is a physical blocker of UVA (ultraviolet light with wavelength 315-400 nm) and UVB (wavelength 280-315 nm) [149].

TiO_2 naturally exists in three different forms: rutile (tetrahedral), anatase (tetrahedral) and brookite (orthorhombic). The most commonly used forms are rutile and anatase. Rutile is considered to be the most stable form, while anatase is considered metastable [150]. Different lattice system for rutile, anatase and brookite are shown in Figure 8.

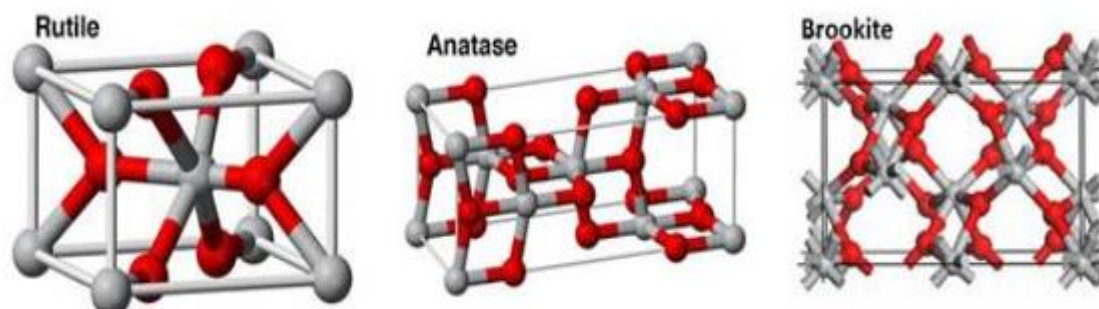


Figure 8: Crystal structures of rutile, anatase and brookite titanium dioxide. Titanium atoms are in grey and oxygen atoms are in red (Obtained from Woodley [151]).

TiO₂ is also a broad band gap semiconductor material with the size of the band gap dependent physiochemical and photoelectronic properties, which leads to applications in the field of photocatalysis. Fujishima and Honda discovered the photocatalysis with TiO₂ in 1972, and it has been reported that TiO₂ is low cost, gives high oxidizing power and has high chemical stability and low toxicity [152-154]. Rutile has a band gap of 3.05 eV and anatase has a band gap 3.26 eV [150]. Even though the band gap is larger, anatase gives a better photocatalytic activity than rutile, although physical causes are not yet completely understood. The first catalytic paper using TiO₂ was prepared by Matsubara in 1995 [155], since then, TiO₂ is widely been used in photocatalytic paper. First scientific study on photocatalytic paper application in water was by Fukahori in 2003 [156].

When TiO₂ absorb light energy greater than its band gap energy, an electron jumps from the valence band (VB) to the conduction band (CB), generating photoelectrons (e⁻) in the CB and holes (h⁺) in the VB. The photoelectrons travel to the surface of TiO₂ and react with oxygen (O₂) molecules to produce superoxide radical anions ($\cdot\text{O}_2^-$), while the holes react with the water (H₂O) to produce hydroxyl radicals ($\cdot\text{OH}$). Superoxide and hydroxyl radicals then work together to decompose organic compounds [157-159]. The process is illustrated in Figure 9. The recombination of the electrons and the holes must be prevented in order to favour the photocatalyzed reaction.

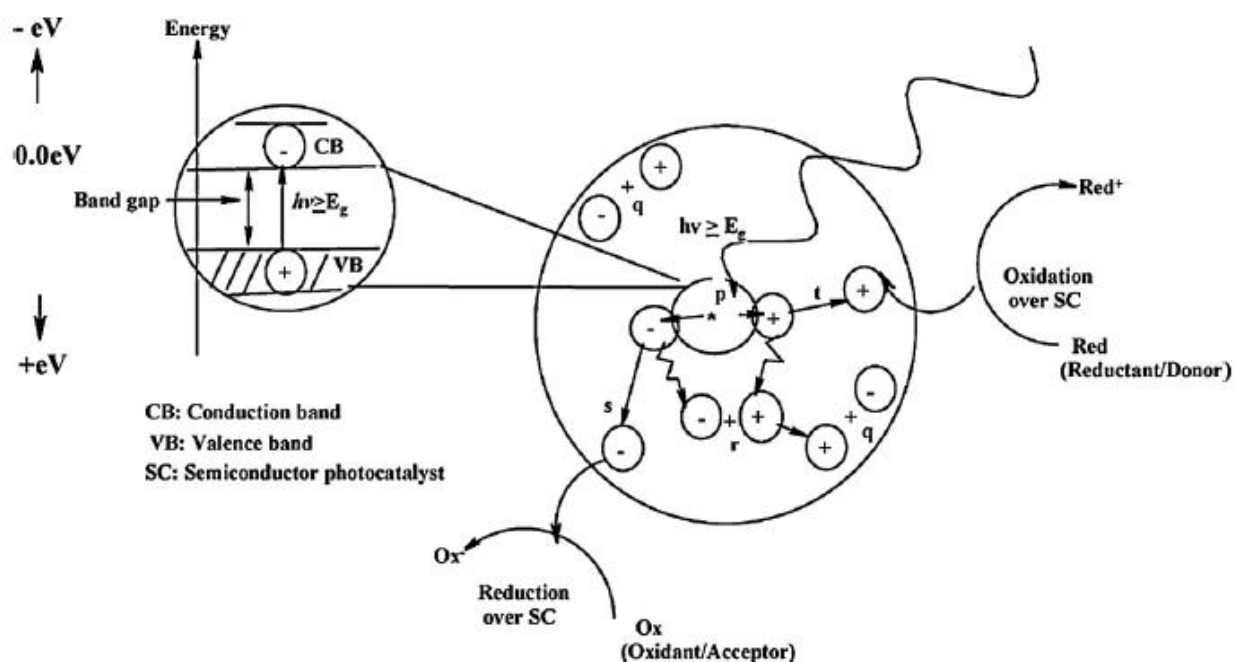


Figure 9: Schematic diagram of the photocatalysis process (Obtained from Gaya [160]).

The problem with the photocatalytic paper is the decomposition of paper substrate as the photocatalytic activity happens, reducing the strength and the immobilization of TiO_2 . In order to obtain a good photocatalytic paper, TiO_2 must be strongly bonded to the paper substrate while avoiding the deterioration of the paper. Also, a uniform distribution of TiO_2 , without any agglomeration, increases the available surface area and improves the photocatalytic activity [161]. It has been reported that TiO_2 should be distributed evenly through the thickness and in the plane of the paper to obtain a good photocatalytic activity. Moreover, the thickness and the porosity of the paper also affects the photocatalytic activity as light needs to pass through the paper to access TiO_2 [162].

In this thesis, nanocellulose- TiO_2 composites, incorporating a wet strengthening agent, is used to produce a portable photocatalytic paper with effective photocatalytic activity.

1.2.3 Nanocellulose-inorganic NP composites

Table III puts together some of the publications of nanocellulose-NP composites indicating their production method, application, the type of characterizations used to characterize the internal structure, NP loading achieved in the composite and the role of NP in the nanocellulose matrix. This was done in an attempt to identify the room for improvement, and perspectives are given in Section 1.2.4. Table IV analyses strengths and weaknesses of nanocellulose and NPs. The weaknesses of both components can be eliminated by combining the two. It is becoming more and more evident that nanocellulose's properties makes it a strong candidate for many applications, partially due to its green chemistry. However, the property range of nanocellulose film by itself is limited. The production of innovative nanocellulose based materials has not been fully explored, especially in the context of inorganic NP-nanocellulose composite research. Therefore, here the interest is to extend the property range of nanocellulose by incorporating inorganic NPs to produce nanocellulose based composites that are superior to either by itself.

Table III: Summary of strengths and weaknesses of nanocellulose and NPs.

	Strengths	Weaknesses
Nanocellulose films	<p>Nanocellulose films are flexible and strong materials that are biodegradable, recyclable and also have many other properties such as high thermal conductivity, high thermal resistance, high work of fracture and low oxygen barrier properties [67, 69, 163-165].</p> <p>Nanocellulose makes a semi-continuous network that gives high a porosity substrate, which enables fillers to use nanocellulose films as a supporting material, while still having filler surface area fully accessible [61, 96].</p> <p>Decrease in diameter of the cellulose fibres have a direct correlation with increase in film properties. Compared to cellulose films, properties of nanocellulose films have improved [2, 34, 87, 166].</p> <p>Membranes with excellent water filtration properties are available [91, 92], but their complex preparation process, cost and environmental concerns makes films made from nanocellulose an ideal candidate.</p>	<p>Pore size within nanocellulose films can be quite broad and it can only be fine-tuned up to a certain pore size on its own [96].</p> <p>Nanocellulose films can be an excellent material to replace everyday use non-recyclable plastic materials such as coffee cups, milk cartons and coffee bags, due to their recyclability, strength and low oxygen barrier properties [67]. However, moisture barrier properties of nanocellulose films by itself are high due to hydrophilic nature of cellulose [79, 101]. If moisture barrier properties could be improved, then this can be the next generation packaging material for everyday use.</p> <p>Unmodified cellulose by itself has limited functionality. They can only serve as an excellent supporting matrix/carrier for fillers [80-83].</p>
NPs	<p>NPs have a very high surface area [103]. NPs have properties that cannot be found in the bulk sample of the material [167].</p> <p>Different NPs consist of different functionalities such as antibacterial [168, 169], photocatalytic [170], barrier</p>	<p>On its own, NPs tend to agglomerate, diminishing the properties associated with the nanoscale material [149, 171].</p> <p>When functional NPs are used on their own, for example in water decontamination, it is extremely difficult to remove NPs</p>

	<p>additives [109], etc. NPs can be selected based on the end application.</p> <p>NPs can essentially be used as fillers to fine-tune a pore structure and increase the porosity of a material (mainly targeted as separators or membranes) [96, 108].</p> <p>NPs can be selected based on their shape, aspect ratio and surface properties such as type of bonding that can be engaged with the matrix [102].</p> <p>NPs have multifunctional properties, e.g. TiO₂ with photocatalytic and antibacterial properties [115], MMT as a barrier additive and fire-retardancy properties [111], MMT as both being a functional material for barrier properties and as a filler to control the pore structure.</p>	<p>from the contaminant medium after the reaction is completed [172].</p> <p>When NPs used in dry form, there is a risk of uncontrollable release of NPs to air, causing environmental and health problems [173].</p> <p>Maximising the surface area available can only be done with a support of another supporting matrix. However, the supporting matrix should enable the surface area of NPs to be readily available, while remaining strong and flexible.</p>
--	---	---

Table IV: Some of the nanocellulose composites with different NPs published in literature. The abbreviations are entered below the table.

NP type	Role of the NPs in the nanocellulose matrix	Production method	Applications	Methods used to characterize the internal structure of the composite	Maximum NP loading achieved	Reference
SiO₂ (5 nm) Negative charge	NP act as a filler in layers. The study was focused on the effect of number of layers on thickness and variation in mechanical properties.	NFC, polyvinyl amine and SiO ₂ fabricated on polydimethylsiloxane using LBL technique.	Potentially can be used these films as optical components for high performance devices, solar cells and biomedical devices.	AFM to observe the porous structure.	Since LBL deposition technique was used, no indication of amount of NPs coated.	[174]
SiO₂ (100 nm) Negative charge	NP act as a filler. The study was focused on the effect of low loading of NP on the ionic conductivity and electrolyte wettability properties	SiO ₂ was added to cellulose nanofibre and vigorously mixed, then subjected to vacuum filtration to produce composites.	Separators for use in lithium-ion-batteries.	SEM to observe the porous structure. The air permeability was measured using Gurley.	10 wt% (no information on retention efficiency of NPs)	[108]
SiO₂ (5-15 nm) Negative charge	NP act as a filler. The study was focused on introducing spraying as an alternative to filtration to produce	SiO ₂ powder was added to MFC hydrogel, stirred using a high speed mixer, sprayed MFC-SiO ₂ slurries into 25 cm diameter wet coated cardboard using in-house assembled spray coater .	Potentially can be used as a rapid production of separators for Li-ion batteries, overall, of large	SEM to observe the aggregation of SiO ₂ on MFC	33 wt% (complete retention of NPs)	[61]

CHAPTER 1

	large area composite paper.	(with this production method, large quantities of suspension is needed)	area composite nanopapers.			
MMT Both charges	NP act as a filler and a functional material. Study was done to prove that MMT gives a self-extinguishing properties and oxygen barrier properties to the paper.	NFC was added to MMT and stirred for 24 hours, then dispersed for 30 minutes using ultrasonic equipment. Composite was prepared using vacuum filtration.	Fire retardancy and gas barrier applications	SEM was used to observe the cross-sections of the composites. Orientation of MMT in NFC was measure using two dimensional XRD	89 wt% (no information on retention)	[111]
Mica R120 (clay) Both charges	NP act as a filler and a functional material. The study was focused on reducing WVP of the composite material in the presence of layered silicate.	Cationic NFC - mica R120 composites were prepared by high pressure homogenization followed by pressure filtration and vacuum hot-pressing.	Barrier material due to disk shaped clay to form a tortuous path to moisture transport.	SEM on top and cross sectional view	50 wt% (no information on retention)	[110]
MMT Both charges	NP act as a filler and a functional material. Amount of MMT content on oxygen and water vapour transmission properties were studied	MMT was mixed with PVA and sonicated first, NFC was then added to the mixture and the composite suspension was poured into a petri dish and casted.	Barrier material for oxygen and water vapour	SEM on cross sections of the composites	50 wt% (no information on retention)	[175]

TiO₂	NPs act as a functional material. Degradation of methylene blue was tested with composites with different TiO ₂ content.	TiO ₂ was mixed with CNF and the mixture was sonicated and poured into a petri dish for casting . Then dipped in Au or Ag solutions.	Photocatalytic paper. Degradation of organic molecules in natural water sources.	SEM to observe the dispersion of TiO ₂ .	NP loading or retention is unknown	[173]
TiO₂	NPs act as a functional material. Photocatalytic activity was tested on methyl orange. Antibacterial activity was tested against Gram negative bacteria <i>E. coli</i>	Single-step hydrothermal method was followed (refer to the original paper for detailed production). TiO ₂ and cellulose fibres were mixed together and then standard hand sheet making procedure was used to make composite sheets.	Antibacterial and photocatalytic properties. Potentially can be used as for household application where organic destruction is needed.	SEM to observe the presence of TiO ₂ in the composite.	10 wt% (no information on retention)	[115]
TiO₂	NPs act as a functional material. Degradation of red X-3B dye at different temperatures, pH and simultaneous photocatalytic-enzymatic conditions were tested.	Bacterial cellulose paper was dipped in TiO ₂ solution to prepare the composite. TiO ₂ was made in the laboratory (refer the original paper for detailed production).	Photocatalytic material.	SEM to observe the presence of TiO ₂ in the composite. AFM was used to analyse the arrangement of fibres on the surface.	NP loading onto the bacterial cellulose membrane was not calculated. Retention is unknown	[176]
Silver (Ag) NPs	NPs act as a functional material.	NFC produced by TEMPO oxidation of MFC and films were	Antibacterial material	Surface morphology was tested using	NP loading onto NFC substrate	[177]

	The antibacterial activity was tested against Gram negative bacteria <i>Escherichia coli</i> .	formed through filtration . Silver nitrate was then sprayed onto NFC film to fully wet the sheet until saturation. The in-situ growth of Ag NPs onto the porous film was done by chemical reduction of silver nitrate using sodium borohydride as a very strong reductant.		SEM. The amount of Ag NPs formed on the surface was related to the concentration sprayed. EDX was used to confirm the presence of Ag NPs on substrate. TEM was used to determine the size and size distribution of Ag NPs loaded to the substrate.	was not given. However, based on the Ag ⁺ concentration used, maximum loading achievable is around ~10-15 wt%. Actual retention or loading is known.	
Ag NPs	NPs act as a functional material. The composites were used to detect different concentrations of thiabendazole pesticides in apple.	CNF films were synthesized at the lab using PVA and glycerol in a glass flask at controlled a temperature, and pouring the suspension into petri dish for casting . Films were immersed into different concentrations of silver nitrate solutions first and then into sodium borohydride solution for chemical reduction and to impregnate Ag NPs.	SERS platform for detection of pesticides in apples	UV vis was used to detect Ag NPs prepared with different concentrations of sodium borohydride. TEM was used to get the size distribution of Ag NPs.	NP loading and retention is unknown.	[178]

LBL: layer-by-layer, NFC: Nanofibrillated cellulose, MMT: Montmorillonite, WVP: Water vapour permeability, XRD: X-ray diffraction, PVA: Poly(vinyl alcohol), CNF: cellulose nanofibre, EDX: Energy dispersive X-ray spectroscopy, SERS: surface-enhanced Raman spectroscopy.

1.2.3.1 Nanocellulose-inorganic NP composite production

There are mainly two approaches for adding/binding NPs to nanocellulose paper – “surface treatment” where dry nanocellulose sheet is impregnated with NPs, and “wet end addition” where NPs are added to nanocellulose before sheet forming. A brief review of main attachment methods are presented in this section.

1.2.3.1.1 Surface treatment

In surface treatment, NPs are more concentrated on the surface and the retention of NPs are generally higher compared to wet end addition. The extent of NP penetration into nanocellulose paper is controlled by the base paper’s roughness and porosity (paper structure) and hydrophobicity (sizing) [179]. There are many surface treatment methods, but here we only intend to briefly summarize the most used methods to impregnate NPs into nanocellulose paper. They are LBL, size press treatment, sol gel method, in-situ precipitation and spray deposition.

1.2.3.1.1.1 Layer-by-layer deposition

Layer-by-layer (LBL) involves the adsorption of different materials (mainly oppositely charged) onto a solid substrate to create multilayers. Number of layers required can be controlled with the properties of the material. Often, increase in thickness of the paper improves the properties of the composite. Eita et al. (2011) produced multilayer thin films composed of NFC, polyvinyl amine (PVAm) and SiO₂ fabricated on polydimethylsiloxane (PDMS) using LBL adsorption technique [174]. The multilayer build up and the film structure was characterized through quartz crystal microbalance with dissipation (QCM-D) analysis, ellipsometry and AFM. The thickness of the composite increased with the number of bilayers and this improved the Young’s modulus in the composite. Lu et al. (2007) used LBL to coat lignocellulose fibres with negatively charged Poly(styrenesulfonate) and positively charged TiO₂ [180]. The dry strength increased due to the electrostatic bonding between positive and negative polyelectrolyte-fibre-TiO₂ binding. Photocatalytic activity was tested upon layer assembly. Higher polyelectrolyte thickness improves the strength due to improved fibre interactions in the composite, however, lower photocatalytic activity was observed due to more TiO₂ on surface causing aggregates and self-shielding themselves from light and pollutant. Aggregation of NPs on the surface is a drawback with this technique.

1.2.3.1.1.2 Size press treatment

During the size press treatment, the dry nanocellulose paper is passed through a size press where the paper surface is exposed to NP suspensions combined with binders, which are mainly starch. The binders are required to have a relatively low viscosity to transport the NPs onto and within the paper surfaces. The main characteristics of the size press is that NPs are concentrated on and near the surface of nanocellulose paper [149]. At times the functionality of NPs could be hindered due to the coating created by the binder. There are number of examples where NPs are impregnated in non-woven matrices using a size press [168, 181, 182].

1.2.3.1.1.3 Sol gel method

Sol-gel method was used for several decades as a method to prepare ceramic precursors and inorganic glasses at relatively low temperatures. The main advantage of this process is that mild conditions such as low temperatures and pressures are used [135]. Uddin et al. (2007) produced photoactive TiO₂ films on cellulose fibres using sol-gel method. During the process, TiO₂ NPs are anchored to cellulose fibres through negatively charged functional groups [183]. Homogeneous distribution of TiO₂ on the surface gave an effective photocatalytic activity in degrading methylene blue dye. Small anatase TiO₂ crystallites of about 3-5 nm are strongly adhered to the underlying support and maintained the photocatalytic activity even after several cycles. TiO₂ deposited in this method protected the fibres from self-degrading. The retention of TiO₂ NPs or the loading of the NPs on the substrate, however, was not mentioned.

1.2.3.1.1.4 In-situ assembly

In situ assembly is usually done with the metal complex ions being attached to nanocellulose. Yan et al. (2016) achieved the in situ synthesis of Ag NPs in nanocellulose matrix through chemical reduction of silver nitrate (AgNO₃) solution [177]. The nanocellulose paper was sprayed with AgNO₃ solution until the paper was fully wet and saturated. Then the in situ growth of Ag NPs on nanocellulose paper was carried out through chemical reduction of AgNO₃ by using sodium borohydride as a strong reductant. The samples were characterized through SEM and TEM for morphology and NP size distribution, and were tested for antibacterial activity. AgNO₃ reduction using sodium borohydride was also done by Liou et al. (2017) to produce SERS substrate for pesticide detection in apples [178].

1.2.3.1.1.5 Spray deposition

Spray deposition is considered as an easy technique to produce large surface area composite papers in a relatively shorter period of time. Krol et al. (2015) produced MFC-SiO₂ nanopaper by a rapid spray deposition technique [61]. MFC slurries with different SiO₂ weight fractions were prepared in up to 2 kg batches and intensively stirred. The composites were then made by spraying MFC-silica slurries, using an in-house assembled spray coater, on a 25 cm diameter wet coated cardboard. The speed of the coater could be varied from 1 to 4 m/min and can spray at a mass flow of 0.75 kg/min. The excessive water in the sprayed slurries is removed through vacuum suction and composites are peeled off from the cardboard after vacuum drying. Results suggested that by changing the conveyer speed, the basis weight of the film could readily be manipulated. Some surface damage was observed during film manufacturing. With this method, progressive increase in SiO₂ content resulted in formation of large SiO₂ clusters embedded into MFC matrix. MFC was not detected inside SiO₂ clusters, indicating an incomplete dispersion of SiO₂ in the hydrogel. The Young's modulus and stress at break reduced from 6.7 to 2.2 GPa and 74 to 23 MPa, respectively, when SiO₂ mass fraction increased from 0 to 33% [61]. This could probably be due to large SiO₂ cluster formation. It is not clear if this effect would still hold if the NPs were adequately dispersed through the nanofibre matrix.

1.2.3.1.1.2 Wet end addition

Wet end addition provides distribution of NPs through the thickness of the nanocellulose paper, allowing NPs to be distributed in the 3D matrix. Kim et al. (2013) made SiO₂-cellulose nanofibre paper using wet-end addition method, where SiO₂ was added to nanocellulose suspension, vigorously mixed and then vacuum filtration was used to produce the composite [108]. Varanasi et al. (2015) also incorporated 5 nm SiO₂ NPs in MFC matrix using filtration [96]. Wang et al. (2013) produced photocatalytic paper, where first TiO₂ nanobelts undergoes a process of silver nitrate reduction to produce Ag/TiO₂ nanobelts, which were then mixed with cellulose nanofibres at different Ag/TiO₂ content after which vacuum filtration was used to produce photocatalytic paper [114]. The photocatalytic paper produced gave high photocatalytic activity by degrading methyl orange, and the activity increased with higher amount of Ag/TiO₂ in the composite.

The major challenge in wet end addition method is the retention of anionic NPs in the anionic nanocellulose matrix during filtration process against the drainage forces. With this method,

generally, water soluble cationic polyelectrolytes, called retention aids, are often used to bridge NPs tightly to nanocellulose network, to improve the retention [96, 149]. Cationic polyelectrolytes are also claimed to improve the flocculation characteristics of fillers and fines [184]. On the other hand, cationic polyelectrolytes can cause NPs to form large scale aggregations with themselves, therefore, care should be taken when cationic polyelectrolytes are incorporated into the composite [185].

Wet end addition is used in this thesis to incorporate NPs into nanocellulose matrix. NPs need to be distributed within the three dimensions of the nanocellulose matrix and aggregation of NPs need to be minimized. NPs chosen and nanocellulose are both anionic and will have some electrostatic repulsion, therefore, next section reviews the importance of polyelectrolytes as retention aids.

1.2.3.2 Polyelectrolytes

Polyelectrolytes are polymers bearing dissociated ionic groups that carries either positive or negative charges; produce cationic or anionic polyelectrolytes, respectively [186]. In polar solvents, these ionisable groups can dissociate, leaving charges on the polymer chains while releasing counterions in solutions [187].

Polyelectrolytes can be classified into natural, modified natural and synthetic polymers, and exist in linear, branched or cross-linked morphologies. Commercial synthetic polyelectrolytes are usually produced through polycondensation or polyaddition process [188]. They are macromolecules that exhibit various phenomena due to both their highly charged electrolytes and macromolecular chain molecules. Strong and weak polyelectrolytes with high and low charge densities are known based on the charge density and the acidity of the functional groups [189]. The chemical structure of polyelectrolytes can significantly vary depend on the different polymer backbone structures available.

Polyelectrolytes are generally characterized through their polydispersity index, which is the ratio of the weight average and number average molar masses. Most of the polyelectrolytes available have a polydispersity index greater than 1, which means that they have a broader molar mass distribution [190]. The charge density of polyelectrolytes, which is the total charge of the polyelectrolyte, are given in meg/g and measured using titration with an oppositely charged

polyelectrolyte until the zero charge is met [190]. This measures the total amount of charge in the polyelectrolyte. Also, if the polyelectrolytes are not linear, the general size of polyelectrolytes are characterized through the average radius of gyration (R_G) and the average end-to-end distance of the chain, which is dependent on both molecular weight of the polyelectrolyte and the condition of the solution [191, 192].

During polyelectrolyte adsorption onto opposite charged surfaces, following processes occur: transport of polyelectrolyte from the solution to the surface, the attachment of polyelectrolyte onto the surface and re-conformation of polyelectrolytes on the surface [193]. Figure 10 shows the conformation of the polyelectrolyte chain at a surface. The sections that touch the surface are referred to as trains, any part of the chain that extends to the solution and returns back to the surface are referred to as loops, and parts of the chain that does not return to the surface are referred to as tails [194, 195]. On non-porous surface, a highly charged polyelectrolyte has a low adsorption and is relatively independent of the molecular weight because the polyelectrolyte is adsorbed in a flat conformation. An intermediate charge polyelectrolyte has a higher adsorption and is dependent on the molecular weight because the polyelectrolyte is adsorbed in a much less compressed conformation [196].

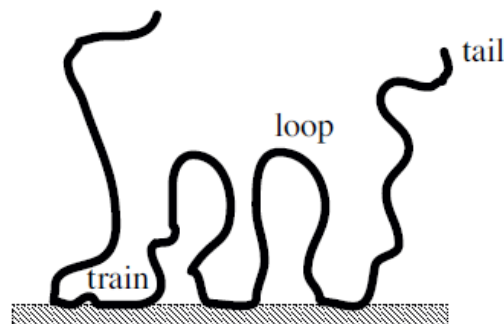


Figure 10: Surface conformation of a polyelectrolyte indicating three segments; trains, loops and tails (Obtained from Sennerfors [194]).

Cationic polyelectrolytes have been used for many years in the paper industry as a retention aid, and to control the paper structure and porosity. Because of that there is an extensive amount of work done on understanding the adsorption of cationic polyelectrolytes with cellulose fibres [26, 193, 197-200]. Generally, the primary factors affecting the flocculation of cellulose fibres with polyelectrolytes include the charge density, molecular weight, morphology, drainage time and the

dosage. Techniques such as AFM [201], neutron reflectometry [202], rheology measurements [203] and focussed beam reflectance measurements (FBRM) [8] have been used by researchers to understand the interaction between cellulose fibres and cationic polyelectrolytes.

It is not currently clear how all of this work translate to nanocellulose fibres, which have the diameter in the same order of magnitude as the radius of gyration as the cationic polyelectrolytes. Recently, Raj et al. (2015) worked with nanocellulose and cationic polyelectrolytes and quantified the effect of cationic polyacrylamide (CPAM) on the drainage of nanocellulose suspensions into films [44]. The floc strength and drainability was quantified through the gel point. The gel point was analysed with CPAM dosage, charge density and molecular weight. For all CPAM parameters, gel point went through a minimum with increasing dosage, and is independent of the CPAM charge density at constant molecular weight. Minimum gel point reduced with lower CPAM molecular weight at a constant addition rate. Drainage time to produce a nanocellulose film reduced by 2/3 by halving the gel point from 0.2 to 0.1 kg/m³. This is attributed to more flocculated suspensions facilitating drainage between flocs. Reducing the gel point also increased the porosity of the nanocellulose films. This study indicates that by manipulating polyelectrolyte addition to nanocellulose can change the final properties of the film. Incorporation of polyelectrolytes as retention aids to nanocellulose-NP composite production may affect the final composite structure and properties depending on the polyelectrolyte dosage.

In this thesis, two polyelectrolytes have been used as retention aids to produce composites; CPAM (13 MDa molecular weight and 40% charge density) and polyamide-amine-epichlorohydrin (PAE). Both of them are widely been used in paper industry.

1.2.3.2.1 Cationic polyacrylamide

Cationic polyacrylamide (CPAM) is a complex macromolecule available in both linear and branched forms (Figure 11). Polyacrylamide is cationized through either copolymerization of a cationic monomer with acrylamide or by modifying initial polyacrylamide chain. Understanding the preparation, structure and the interaction of CPAM is crucial to effectively incorporate CPAM in the nanocellulose-NP composites made in this thesis.

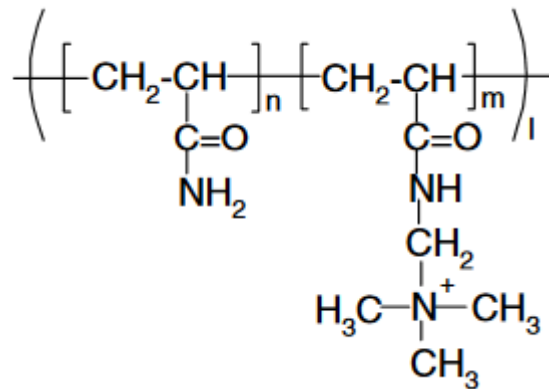


Figure 11: Structure of CPAM (Obtained from [204]).

CPAM normally comes in powder form and needs to be dispersed in water for longer period of time to expand the polymer and gain an equilibrium solution. Dissolution kinetics of CPAMs with 13 MDa molecular weight and different charge densities (5, 10 and 40 %), were studied by Ngo et al. (2013), who found that different charge densities affect the time required to completely dissolve CPAM powder in aqueous solutions [205]. The kinetics monitored by measuring macroscopic viscosity and hydrodynamic diameter indicated that both increased with time and reached a plateau after a critical time. CPAM with 40% charge density reached the plateau at 8 hours, while 5 and 10% charge density CPAM reached it after 12 hours. A two-step mechanism was proposed: an induction period where water diffuses into polymer powder (Figure 12a-b) and creates a swollen surface layer (Figure 12c), then the dissolution period where the interactions between the polymer-solvent and between charges overcome the polymer-polymer attraction forces, causing polymer chains to expand and absorb the solvent, increasing dimensions of its coils and the volume of the polymer matrix (Figure 12d-e) [206, 207].

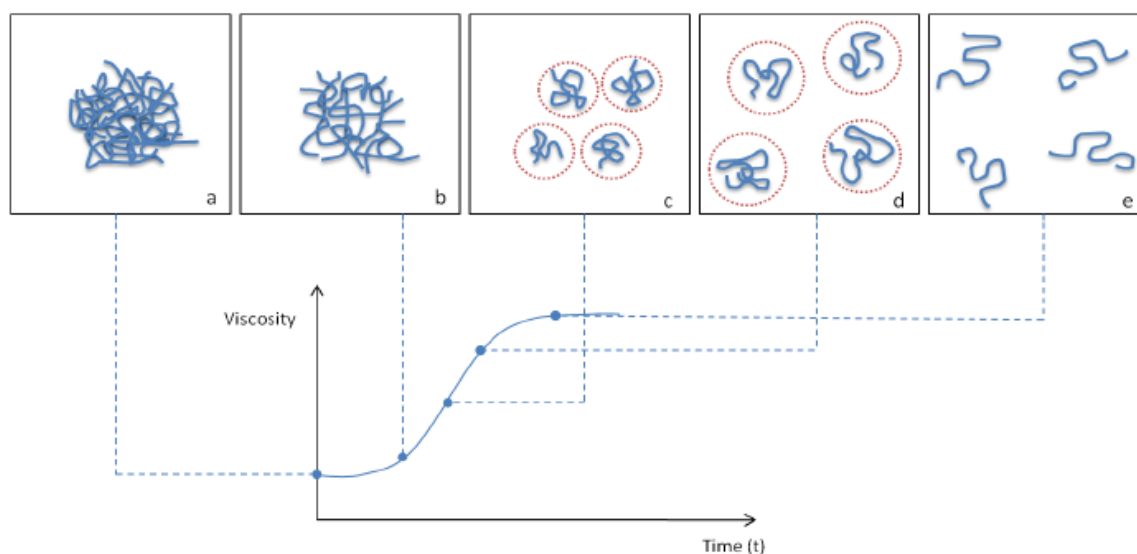


Figure 12: Schematic of the dissolution kinetic of CPAM (Obtained from Ngo [205]).

1.2.3.2.2 Polyamide-amine-epichlorohydrin

Polyamide-amine-epichlorohydrin (PAE) is commonly used as a wet strength agent for paper because of the cationic azetidinium groups present in the polymer that reacts with carboxyl groups on the anionic fibre surface during the curing process. Structure of PAE is shown in Figure 13. During the drying of the paper, PAE crosslinks under heating, forming a water insoluble three dimensional network that prevents the fibre bond detachment and provide wet strength to the paper [208, 209]. PAE is synthesized from polyamideamine chains by reacting with epichlorohydrin [210]. PAE molecules available commercially are highly dense polymers with average weight and number molecular mass values of 1,140,000 and 27,000, respectively, giving a polydispersity index of 42 [211].

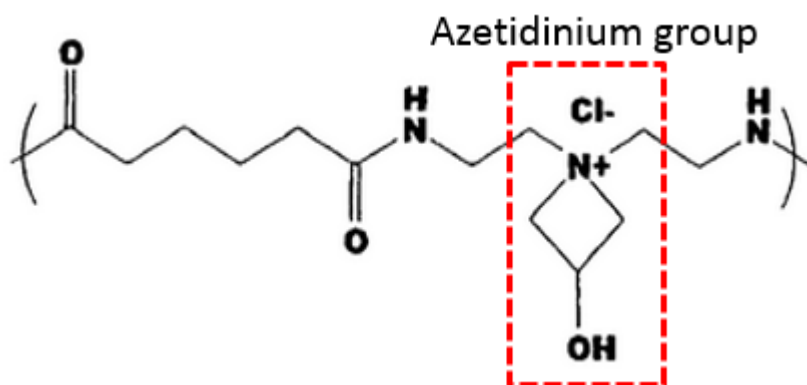


Figure 13: Structure of PAE (Obtained from Aoyama [212]).

1.2.3.3 Interaction between polyelectrolyte-NP systems in nanocellulose matrix

NPs can be added with polyelectrolyte into a nanocellulose matrix in many ways. Figure 14 shows a schematic representation of the three components with their charges. The key properties of nanocellulose-NP composite films are dictated by the NP structure embedded in the nanocellulose fibre matrix. Each addition method has a different arrangement and an interaction of NPs with the polyelectrolytes. This in turn means that understanding the interactions between NPs and polyelectrolytes are essential to tailor nanocomposite with optimized properties.

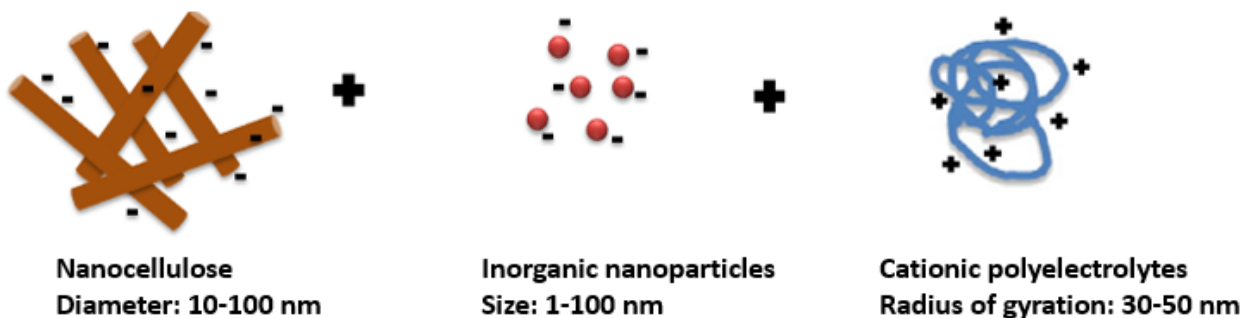


Figure 14: Three constituents in the nanocellulose-inorganic composites with same length scale.

Lu et al. (2007) coated lignocellulosic fibres with an organized multilayers of poly(dimethyldiallyl ammonium chloride) (PDDA) - polyelectrolyte and TiO_2 NPs using LBL assembly process [180] for photocatalytic activity. The fluorescent and SEM images indicated that there was a complete NP coating on the fibres. Thicker layers of polyelectrolyte increased the paper dry strength, however, it also caused TiO_2 NPs to agglomerate and pile up, covering them from light and reducing the photocatalytic activity [180].

Varanasi et al. (2015) used two methods to mix SiO_2 NPs, PAE and nanocellulose together to produce composites for ultrafiltration applications; direct addition (DA) and controlled simultaneous addition (CSA). DA is where PAE and SiO_2 NPs are directly added drop wisely to a mixture of nanocellulose (one step procedure). CSA is where PAE and SiO_2 NPs are added drop wisely first to facilitate a complete coverage of polyelectrolyte on NPs, and then PAE- SiO_2 suspension is mixed with nanocellulose suspension drop wisely again to get the final suspension (two step procedure). The two addition methods resulted in different NP distributions as indicated by SEM and pore size distribution analysis. Results revealed that CSA methods gave a uniform

dispersion of SiO₂ NPs coated PAE in the nanocellulose matrix whereas DA formed large agglomerates of SiO₂ NPs that effectively blocked the pores within the nanocellulose network [96]. The size of SiO₂ NP agglomerates and the assembly of SiO₂ NPs in the nanocellulose matrix with two preparation methods were not mentioned.

Ngo et al. (2013) treated cellulose paper with CPAMs of different concentrations, charges and molecular weights, and deposited Au NPs. The study quantified the effect of CPAM adsorption on paper on the aggregation and retention of Au NPs to enhance SERS. SERS performance increased for Au NP-CPAM paper than for untreated Au NP paper. SEM analysis revealed that depending on the concentration of CPAM, the aggregation state of Au NPs differ (Figure 15), however, aggregation size or assembly of Au NPs were not quantified [213].

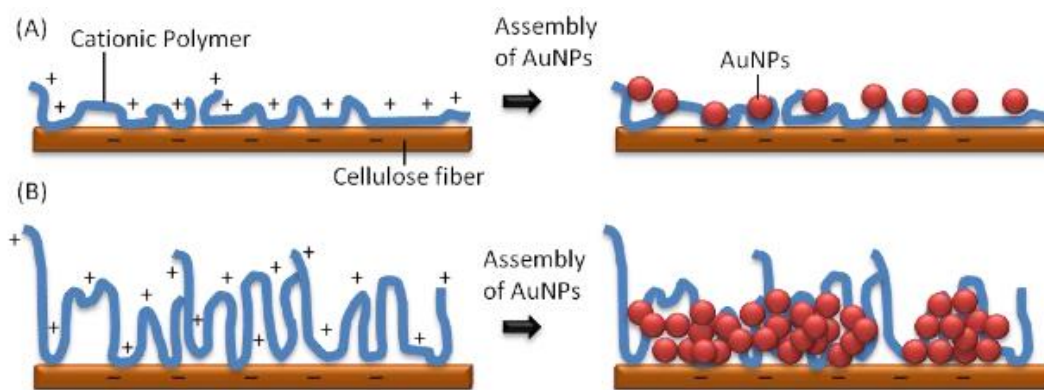


Figure 15: Nanoparticle aggregation based on (a) low CPAM concentration; (b) high CPAM concentration (Obtained from Ngo [213]).

Zhang et al. (2013) prepared cellulose based photocatalytic paper with TiO₂ loaded carbon fibres [214]. TiO₂ NPs were bonded to carbon fibres using sodium silicate or aluminium sulfate binders. As prepared TiO₂-loaded carbon fibres were then mixed with softwood pulp suspension and PAE, and hand sheets were made according to TAPPI test method T205. Photocatalytic activity was tested by degrading MO under UV light. PAE improved the wet strength of the paper and did not contribute to photocatalytic activity. This was the first study to evaluate the effect of wet strength resins on photocatalytic activity. Introduction of PAE slightly decreased the photocatalytic activity due to reduction in retention of TiO₂ NPs [214]. The TiO₂ in work may have been cationically charged since the charge of TiO₂ is dependent on pH of the solution [215]. No characterization was done on the internal structure of PAE and TiO₂ NPs on loading or retention.

Martins et al. (2012) produced an antibacterial paper with Ag NPs, nanocellulose and polyelectrolytes [168]. Effect of electrostatic assembly of Ag NPs with different polyelectrolytes were tested; PDDA, anionic poly(sodium 4-styrenesulfonate) (PSS), poly(allylamine hydrochloride) (PAH) and branched polyethylenimine (PEI). Nanocellulose was first treated with a cationic polyelectrolyte followed by an anionic polyelectrolyte and then again with a cationic polyelectrolyte. This promotes a charge homogeneity at the nanofibre surfaces that favours a good deposition of Ag NPs. Ag NPs-treated nanocellulose with polyelectrolytes were then mixed with starch binder and pressed into a bleached kraft pulp paper using a size press. The most efficient deposition of Ag NPs on to nanocellulose was with PDDA and PEI polyelectrolytes with anionic PSS. Composites were characterized through SEM indicating the presence of Ag NPs on the surface of nanocellulose. The antibacterial results were higher for composites with higher amount of Ag NPs deposited.

Xiao et al. (2009) used polyelectrolyte multilayer assembled electrospun polymer nanofibres to immobilize zero-valent iron (ZVI) NPs [216]. Negatively charged cellulose acetate nanofibres fabricated through electrospinning were assembled with multilayers of poly(diallyldimethylammonium chloride) (PDADMAC) and polyacrylic acid (PAA) through electrostatic LBL assembly. The treated cellulose acetate nanofibres were then used as a reactor for the formation of ZVI NPs by the reduction of Fe(II) ions through binding with free carboxyl groups of PAA. The composites were characterized through SEM, TEM, energy dispersive spectroscopy (EDS), Fourier transform infrared spectroscopy (FTIR), and thermogravimetry analysis. All techniques confirmed that ZVI NPs were successfully synthesized and uniformly distributed. Loading and size of ZVI NPs can be tuned with the polyelectrolyte and binding layers. The study suggested that when the size of ZVI NP clusters are bigger, the reactivity of ZVI NPs are poor in dye degradation. The influence of polyelectrolytes on the NP aggregation and assembly is therefore an important parameter to consider during fabrication of composites.

Salmi et al. (2009) studied the adsorption behavior of the layers formed by SiO₂ NPs and nanocellulose together with CPAM using QCM-D and AFM [217]. The composites were made using LBL technique. QCM-D was used to study the adsorption of the layer formed by SiO₂ and nanocellulose together with CPAM. AFM was used to study the interactions between cellulose surfaces. During the layer formation process, QCM-D indicated that nanocellulose formed a loose

and a thick layer containing excessive amount of water. SiO₂ NPs were able to penetrate the CPAM structure while nanocellulose formed individual layers between CPAM layers. Information on CPAM-SiO₂ NP internal structure characterization is not given.

Although, as summarized above, polyelectrolytes have been used in nanocellulose-NP composite production, proper techniques have not been used to characterize the internal structure of NP-polyelectrolyte complexes in nanocellulose matrix. It is believed that by understanding the interaction of polyelectrolytes in the composites, composites can be engineered better for high end applications.

1.2.4 Perspective and conclusion

The combination of inorganic NPs and nanocellulose uses the benefits of the properties of both components and simultaneously results in enhanced properties due to synergistic effect. The potential of these composites are promising and attracting. The major impact of applications penetrating to the market will at least be decades away. In an attempt to further understand the missing knowledge and improvements that can be done on nanocellulose-inorganic NP composites, a literature review was conducted to highlight some of the issues related to nanocomposite preparation and characterization. The performance of the final material depends greatly on the preparation methodologies employed in their production. It is believed that these nanocomposites' performances can further be improved by proper composite production and the application of better characterization techniques.

1.2.4.1 Composite production

As shown in Table IV (Section 1.2.3), even though a significant progress has been made on incorporating NPs into nanocellulose matrixes for different applications, a general understanding has yet to emerge. Methods to distribute NPs through the 3D of nanocellulose paper substrate were only developed recently. Therefore, a little attention is given to engineering the structure of nanocellulose-NP composites. Nanocellulose-NP composites are unusual because both the nanofibres and NPs are prone to agglomeration. With the pore structure of nanocellulose, the picture of individual NPs evenly distributed through a semi-continuous matrix does not hold up. Thus, more effort are needed to relate the internal structure to the macroscopic performance of the nanocomposites.

Table IV reveals that NPs can take up many roles in the nanocellulose matrix, as fillers, functional materials and as both fillers and functional materials. While the use of NPs to produce composites is targeted toward specific applications, the effect that NPs in the nanocellulose matrix has on the final properties of the composite in terms of variation in the structure is not properly explored. The method used to characterize the structure of the composite is mainly limited to SEM which only gives information about the morphology of the surface. Also, Table IV shows that while NP loadings have gone up to >50% for NPs such as MMT (which are platelets with both positive and negative charges), anionic and spherical NPs have only been used at low levels of loading without any indication of their retention.

All these information indicate that there is room for improvement in these nanocellulose-NP composites. The major challenge in developing such composites for high end applications is the lack of structure-property relationship data and the challenge of dispersing the NPs in nanocellulose substrate while the retention and agglomeration is controlled. Establishing such models require answering the following questions:

- Can the nanocomposite structure be controlled/changed with systematic loading of NPs, and how does that affect the final properties (strength, pore size distribution)?
- What is the maximum NP loading achievable while maintaining the retention and uniform distribution in the 3D network?

Therefore, quantifying the effect of NP loadings and sizes on structure and properties of the nanocomposite is a critical area that will be addressed in this thesis.

As shown in Table IV, most of the publications have complicated and expensive methods to produce nanocomposites which hinder the commercialization of such composites. Functional nanocellulose based composite production using MMT and TiO₂, using cheap and easily scalable methods, which gives improved water vapour barrier performance and photocatalytic activity, respectively, will therefore be addressed in this thesis.

1.2.4.2 Composite characterization

Although there are many publications on the use of polyelectrolytes to fix NPs, the characterization of the composite is mainly limited to imaging techniques such as SEM. Such techniques could be used to get a basic idea of the structural variation with the preparation

method, but, it cannot be used to get a complete picture of the nanoscale interactions between polyelectrolytes and NPs. Generally, SEM is a limited tool because 1) SEM only use a selected area and does not provide information about local distribution of NPs in the matrix; 2) SEM only shows the NPs appearing on the surface (2D-imaging); 3) the interaction between polyelectrolytes with NPs is not visible; 4) when the colloidal size is reduced from micro- to nanoscale, the structure is very complex and less well understood and the resolution of SEM to characterize the structure may be insufficient.

As discussed in Section 1.2.3.3, the order and the procedure of mixing three nanoscale materials (nanocellulose, NP and polyelectrolyte) changes the aggregation of NPs in the composites. The interactions between polyelectrolytes and NP systems, without a matrix, has been studied extensively. For example, Pandav et al. (2015) presented a computational study of the interactions, phase behaviour and aggregation characteristics of positively charged spherical particles with negatively charged polyelectrolytes [218]. Pryamitsyn et al. (2014) presented a depletion and electrostatic interaction between uncharged and charged particles in a polyelectrolyte system [219]. While there have been studies conducted on the use of polyelectrolytes and interactions between polyelectrolytes and NPs systems, the structural assembly of different NP sizes under the influence of different polyelectrolyte dosages and the interaction of NPs in the presence of a nanocellulose matrix is poorly understood. So there remains a clear gap in utilizing proper characterization techniques to characterize the internal structure of NP-polyelectrolyte complexes in nanocellulose matrix, thus this gap will be addressed in this thesis.

1.3 GAPS IN KNOWLEDGE

This critical review of nanocellulose, inorganic nanoparticles (NPs), production of nanocellulose-NP composites and use of polyelectrolytes as retention aids/binders has shown the path to developing new materials. Nanocellulose is an emerging class of material with many potential applications. It is recyclable, eco-friendly, biodegradable material that possesses excellent properties such as very high mechanical strength, good barrier and optical properties. This review highlights that the property range achievable with nanocellulose by itself is limited, and that nanocellulose-inorganic NP composites can combine the advantages of the two individual constituents, and is a promising candidate to tailor composites for high end applications.

Although there are nanocellulose-inorganic NP based composites available, the effect of three critical nanoscale materials; nanocellulose, NPs and polyelectrolytes on the structure and the effect of changing structure on the final composite properties has not been properly explored. Also, how these nanoscale materials should be added, and the effect of addition process on the retention and NP arrangement in the nanostructure is poorly understood in literature. Moreover, the interaction of polyelectrolytes with NPs in a nanocellulose matrix has been poorly characterized previously. It is extremely crucial to characterize such systems properly to obtain the structural assembly of these NPs with polyelectrolytes to effectively bring out the functionality of the NPs.

The critical questions left unanswered include:

1. Characterizing the nanocellulose-NP composites and its properties.
 - How can NPs be incorporated into the nanocellulose matrix without reducing the retention of NPs?
 - What is the maximum loading of NPs achievable?
 - Can the structure of the composite be controlled by varying NP loading and different sizes? Does that affect the final composite properties?
 - Can a structure-property model be developed for nanocellulose-inorganic NP composites?

2. Development of proper characterization techniques to characterize the internal structure of NP-polyelectrolyte complexes in nanocellulose matrix
 - What is the structural assembly of NPs under the influence of cationic polyelectrolytes?
 - Does the structural assembly change with NP sizes and different dosages of cationic polyelectrolyte?

1.4 RESEARCH OBJECTIVES

This doctoral thesis has three main objectives. First objective is to produce nanocellulose-NP composites with different NP sizes and NP loading varying from low to extremely high. This is done to understand the effect of NP loading has on structure and property of the composite. The second objective is to characterize the internal structure of NP-polyelectrolyte complexes in nanocellulose. The third objective is to produce and engineer composites in laboratory scale with nanocellulose and functional NPs for specific applications.

The specific research aims are:

1. Quantify the effect of NP loadings and sizes on structure and properties of the final composites and the maximum loading of NPs achievable in the matrix.
2. Quantify the effect of NP sizes and polyelectrolyte dosages on the structural assemblies of NP-polyelectrolyte systems in nanocellulose matrix.
3. Production of montmorillonite (MMT)-nanocellulose composites as a strong, fine-tuned material for water vapour barrier applications.
4. Production of titanium dioxide (TiO₂)-nanocellulose composites as a portable, green material for effective photocatalytic degradation of toxic substances.

THIS PAGE HAS BEEN INTENTIONALLY LEFT BLANK

1.5 THESIS OUTLINE

This thesis is presented in the format of “Thesis with publications” based on the Monash University guidelines for Doctor and MPhil Degrees 2016 and the Thesis with Publications guidelines. It consists of five experimental chapters of which three of them are already published and two are submitted. All published papers are reformatted for a consistent presentation whilst the content remains unchanged. The original publications are provided in Appendix II.

A chapter-by-chapter outline based on the research aims, the conducted research studies and the successful outcome is presented.

- **Chapter 1 – Introduction and Literature Review**

This chapter reviews nanocellulose and inorganic nanoparticles as materials including their individual properties and applications. The limitations of nanocellulose and nanoparticles on their own is identified and the review on nanocellulose-inorganic nanoparticle composites is done. Gaps in knowledge were identified from the literature reviews. In order to address these issues of concern, the main objectives were raised to guide the experimental work required.

- **Chapter 2 - Strong cellulose nanofibre – nanosilica composites with controllable pore structure**

Uthpala M. Garusinghe, Swambabu Varanasi, Gil Garnier, Warren Batchelor. Strong cellulose nanofibre–nanosilica composites with controllable pore structure. Cellulose, 2017. 24(6): p. 2511-2521.

Impact factor: 3.417

This chapter explores the production of flexible nanocellulose-SiO₂ nanoparticle (NP) composites with two different SiO₂ NP sizes and varying SiO₂ loading from 5 to 77 wt%. The aim of this work was to understand and quantify how changing NP size and loading can change the composite structure, and how change in structure affect the final film properties. Composites were prepared by complexing SiO₂ NPs with cationic polyacrylamide (CPAM), followed by retaining SiO₂-CPAM complex on nanocellulose fibre network. Preparation method allowed a NP retention above 90%.

Film thickness was approximately constant at low loading, indicating that NPs are just filling the gaps created by the nanocellulose network. Thickness drastically increased beyond a certain loading, indicating that the structure of the composite changes from a thin film to a packed bed structure. At this point the NP-CPAM complexes are too large to accommodate into the pores of the fibres, therefore, embedding into the matrix pushed fibres apart. Much tighter controlled pore size distribution was achieved at this point. The resultant composites have a controllable pore structure (100-1000 nm to 10-60 nm). The tensile index of nanocellulose mass basis was maintained for the entire range of loadings, indicating that NPs do not interfere with the bonding between nanocellulose fibres. This study proves that structures and properties of the composites can tremendously be varied with the addition and retention of NPs in nanocellulose based composites. The model prepared in this work can be used to engineer materials that requires the flexibility, controlled pore structure and high surface area.

- **Chapter 3 – Investigating silica nanoparticle – polyelectrolyte structures in microfibrillated cellulose films by scattering techniques**

Uthpala M. Garusinghe, Vikram S. Raghuwanshi, Praveena Raj, Gil Garnier, Warren Batchelor. Investigating silica nanoparticle-polyelectrolyte structures in microfibrillated cellulose films by scattering techniques. 16th Fundamental Research Symposium, Oxford, September 2017. 2: p. 823-836.

This chapter explores the use of different scattering techniques to characterize the NP-polyelectrolyte interactions in suspension and in nanocellulose fibre matrix using dynamic light scattering (DLS) and small angle X-ray scattering (SAXS), respectively. Composites with varying CPAM dosage were prepared by firstly complexing SiO₂ NPs and CPAM together, secondly SiO₂-CPAM suspension is mixed with nanocellulose suspension and thirdly final composite sheet production through standard papermaking procedure. DLS revealed that higher CPAM dosage creates larger sized CPAM-SiO₂ NP aggregates due to more NPs are picked up by stretched CPAM chains. SAXS study revealed that the structural assembly of 22 nm SiO₂ under the influence of CPAM fits well with a spherical core shell model (with SiO₂ partially covered with CPAM) and sphere model (SiO₂ alone) combined together. Use of scattering techniques to characterize NP-polyelectrolyte systems enable us to better engineer composites for high end applications.

- **Chapter 4 – Assembly of nanoparticle – polyelectrolyte complexes in nanofiber cellulose structures**

*Uthpala M. Garusinghe**, *Vikram S. Raghuwanshi**, *Christopher J. Garvey*, *Swambabu Varanasi*, *Christopher R. Hutchinson*, *Warren Batchelor*, *Gil Garnier*. *Assembly of nanoparticles-polyelectrolyte complexes in nanofiber cellulose structures. Colloids and Surfaces A: Physicochemical and Engineering Aspects*, 2017. **513**: p. 373-379.

**Both authors have contributed equally*

Impact factor: 2.714

This chapter explores the use of SEM, TEM and SAXS techniques to characterize the structural assembly of 8 nm SiO₂ NP under the influence of different dosages of CPAM. The composite suspensions were made by complexing SiO₂ NPs and CPAM together, and then mixing CPAM-SiO₂ suspensions with nanocellulose suspensions to get the final suspension. Composite sheets were then made using a standard paper making procedure. SEM indicates that NP-CPAM complexes are filling the gaps created by the nanofibre network. Data fitting and analysis allows to understand the interparticle interaction within assemblies of SiO₂ NPs at the nanometer scale with respect to different CPAM concentrations. 8 nm NPs in the composite shows a lognormal bimodal distribution of NP sizes. Higher CPAM dosage increased retention of NPs within nanocellulose matrix, creating a stronger interparticle interactions and result in composites with smaller pores. With CPAM dosage increased from 16.5 to 330 mg/g NPs, the correlation length increased from 30 to 70 nm. Correlation length indicates the size of NP clusters. This study concludes that understanding the effect of CPAM concentration on various NP sizes and composite structural conformations enable to engineer novel hierarchically and functional nanocellulose based inorganic NP composites.

-
- **Chapter 5 –Nanocellulose – montmorillonite composites of low water vapour permeability**

Uthpala M. Garusinghe, Swambabu Varanasi, Vikram S. Raghuwanshi, Gil Garnier, Warren Batchelor. Nanocellulose-Montmorillonite Composites of Low Water Vapour Permeability. Accepted by Colloids and Surface A: Physicochemical and Engineering Aspects, 2018.

Impact factor: 2.714

This chapter explores the production of montmorillonite (MMT)-nanocellulose composites as a barrier material. The objective was to use a simple technique to develop a novel MMT (9.1-37.5 wt%)-nanocellulose composites of low water vapour permeability (WVP) by testing three different processing methodologies; 1) MMT and nanocellulose mixed together followed by composite sheet formation through paper making process, 2) MMT-nanocellulose suspension was sonicated before composite sheet formation 3) MMT-nanocellulose suspension was homogenized before composite sheet formation. The composites remained very strong (strength-110 MPa), stiff (modulus-11 GPa) yet flexible. SEM proved that MMT is uniformly distributed across and within the composite sheet. WVP worsened with the sonication step (methodology 2) as sonication breaks MMT platelets into smaller particles which then decrease the tortuosity in the membrane. With methodology 1, WVP decreased by half to $13.3 \pm 2.0 \text{ g} \cdot \mu\text{m}/\text{m}^2 \cdot \text{day} \cdot \text{kPa}$ with 16.7 wt% MMT content. Further increasing MMT content increased WVP and this was assumed because of the aggregate formation of MMT at high loading. With the homogenization step (methodology 3), the WVP increased even further, achieving lowest of $6.33 \pm 1.5 \text{ g} \cdot \mu\text{m}/\text{m}^2 \cdot \text{day} \cdot \text{kPa}$ with 23.1 wt% MMT. This is the lowest achieved for the nanocellulose-clay composites published in literature. With homogenization, MMT aggregates are broken down to smaller sizes, maximizing the available surface area that creates a better tortuous path for permeating molecules. This study proves that processing methodology is important to create a good barrier material. The composite produced in this work is recyclable and biodegradable. These thin, inexpensive, strong and flexible composites present a new and attractive option as a recyclable/compostable packaging material for applications where water vapour protection is crucial.

- **Chapter 6 – Water resistant cellulose – titanium dioxide composites for photocatalysis**

Uthpala M. Garusinghe, Vikram S. Raghuwanshi, Warren Batchelor, Gil Garnier. Water resistant cellulose – titanium dioxide composites for photocatalysis. Under final review by Scientific Reports, 2018.

Impact factor: 4.259

This chapter explores the production of titanium dioxide (TiO₂)-nanocellulose composites for photocatalytic contaminant removal by using methyl orange (MO) as a model dye pollutant. Photocatalytic composites consisting of nanocellulose – polyamide-amine-epichlorohydrin (PAE) – TiO₂ were prepared by a papermaking technique with TiO₂ loading from 0.5-80 wt% and two different PAE dosages (10 and 50 mg/g MFC). Composites were prepared using a simple two step procedure – PAE added to nanocellulose to coat a monolayer of polymer on fibre, followed by addition of TiO₂. In addition to holding nanocellulose structure, higher PAE dosage helped retaining more TiO₂ in the matrix. The composites exhibit a remarkable photocatalytic activity by degrading MO to 95% in 150 minutes for the composite with best combination of TiO₂ and PAE. SEM confirmed that TiO₂ is located on the surface of nanocellulose rather than in between pores created by nanocellulose, and TiO₂ is uniformly distributed in the matrix. SEM also confirmed that at higher TiO₂ loadings, aggregations of TiO₂ NPs were seen. This composite leads to an important application in photodegradation of organic pollutant. The composites were repeatable, reproducible and reusable – no reduction in photocatalytic activity or destroyed nanocellulose structure even after repeats of 3 cycles. The material can readily be removed from the pollutant medium once used. The composites therefore are durable, cheap, green, can easily scale up and portable. The two stage mixing procedure of TiO₂ composite making is promising for a simple manufacture of high performance photocatalytic paper. This material has a good potential in the field of waste water treatment applications.

- **Chapter 7 – Conclusion and Perspective**

1.6 REFERENCES

- [1] R. Gilbert, J. Kadla, *Polysaccharides—cellulose*, in: *Biopolymers from renewable resources*, Springer, 1998, pp. 47-95.
- [2] W. Stelte, A.R. Sanadi, *Preparation and characterization of cellulose nanofibers from two commercial hardwood and softwood pulps*, *Industrial & engineering chemistry research*, **48** (2009) 11211-11219.
- [3] A. Isogai, *Wood nanocelluloses: fundamentals and applications as new bio-based nanomaterials*, *Journal of wood science*, **59** (2013) 449-459.
- [4] D. Klemm, B. Heublein, H.P. Fink, A. Bohn, *Cellulose: fascinating biopolymer and sustainable raw material*, *Angewandte Chemie International Edition*, **44** (2005) 3358-3393.
- [5] D. Klemm, F. Kramer, S. Moritz, T. Lindström, M. Ankerfors, D. Gray, A. Dorris, *Nanocelluloses: A new family of nature - based materials*, *Angewandte Chemie International Edition*, **50** (2011) 5438-5466.
- [6] J.N. BeMiller, *Carbohydrate chemistry for food scientists*, American Association of Cereal Chemists, Inc (AACC), 2007.
- [7] F.W. Herrick, R.L. Casebier, J.K. Hamilton, K.R. Sandberg, *Microfibrillated cellulose: morphology and accessibility*, in: *J. Appl. Polym. Sci.: Appl. Polym. Symp.:(United States)*, ITT Rayonier Inc., Shelton, WA, 1983.
- [8] P. Raj, W. Batchelor, A. Blanco, E. de la Fuente, C. Negro, G. Garnier, *Effect of polyelectrolyte morphology and adsorption on the mechanism of nanocellulose flocculation*, *Journal of colloid and interface science*, **481** (2016) 158-167.
- [9] D. Sandquist, *New horizons for microfibrillated cellulose*, *Appita Journal: Journal of the Technical Association of the Australian and New Zealand Pulp and Paper Industry*, **66** (2013) 156.
- [10] L. Wågberg, G. Decher, M. Norgren, T. Lindström, M. Ankerfors, K. Axnäs, *The build-up of polyelectrolyte multilayers of microfibrillated cellulose and cationic polyelectrolytes*, *Langmuir*, **24** (2008) 784-795.

-
- [11] M. Pääkkö, M. Ankerfors, H. Kosonen, A. Nykänen, S. Ahola, M. Österberg, J. Ruokolainen, J. Laine, P.T. Larsson, O. Ikkala, *Enzymatic hydrolysis combined with mechanical shearing and high-pressure homogenization for nanoscale cellulose fibrils and strong gels*, *Biomacromolecules*, **8** (2007) 1934-1941.
- [12] S. Beck-Candanedo, M. Roman, D.G. Gray, *Effect of reaction conditions on the properties and behavior of wood cellulose nanocrystal suspensions*, *Biomacromolecules*, **6** (2005) 1048-1054.
- [13] V. Favier, H. Chanzy, J. Cavaille, *Polymer nanocomposites reinforced by cellulose whiskers*, *Macromolecules*, **28** (1995) 6365-6367.
- [14] M. Ioelovich, *Cellulose as a nanostructured polymer: a short review*, *BioResources*, **3** (2008) 1403-1418.
- [15] A. Bhatnagar, M. Sain, *Processing of cellulose nanofiber-reinforced composites*, *Journal of Reinforced Plastics and Composites*, **24** (2005) 1259-1268.
- [16] A. Alemdar, M. Sain, *Isolation and characterization of nanofibers from agricultural residues—Wheat straw and soy hulls*, *Bioresource technology*, **99** (2008) 1664-1671.
- [17] J. Li, X. Wei, Q. Wang, J. Chen, G. Chang, L. Kong, J. Su, Y. Liu, *Homogeneous isolation of nanocellulose from sugarcane bagasse by high pressure homogenization*, *Carbohydrate Polymers*, **90** (2012) 1609-1613.
- [18] M.L. Hassan, A.P. Mathew, E.A. Hassan, N.A. El-Wakil, K. Oksman, *Nanofibers from bagasse and rice straw: process optimization and properties*, *Wood science and technology*, **46** (2012) 193-205.
- [19] R. Zuluaga, J.L. Putaux, J. Cruz, J. Vélez, I. Mondragon, P. Gañán, *Cellulose microfibrils from banana rachis: Effect of alkaline treatments on structural and morphological features*, *Carbohydrate Polymers*, **76** (2009) 51-59.
- [20] E. Dinand, H. Chanzy, M. Vignon, *Parenchymal cell cellulose from sugar beet pulp: preparation and properties*, *Cellulose*, **3** (1996) 183-188.
-

-
- [21] S. Yano, H. Maeda, M. Nakajima, T. Hagiwara, T. Sawaguchi, *Preparation and mechanical properties of bacterial cellulose nanocomposites loaded with silica nanoparticles*, *Cellulose*, **15** (2008) 111-120.
- [22] R. Kose, I. Mitani, W. Kasai, T. Kondo, "*Nanocellulose*" as a single nanofiber prepared from pellicle secreted by *gluconacetobacter xylinus* using aqueous counter collision, *Biomacromolecules*, **12** (2011) 716-720.
- [23] A.F. Turbak, F.W. Snyder, K.R. Sandberg, *Microfibrillated cellulose*, in, Google Patents, 1984.
- [24] E. Dinand, H. Chanzy, R. Vignon, *Suspensions of cellulose microfibrils from sugar beet pulp*, *Food Hydrocolloids*, **13** (1999) 275-283.
- [25] J.A. Walecka, *An investigation of low degree of substitution carboxymethylcelluloses*, in, Georgia Institute of Technology, 1956.
- [26] L. Wågberg, L. Winter, L. Ödberg, T. Lindström, *On the charge stoichiometry upon adsorption of a cationic polyelectrolyte on cellulosic materials*, *Colloids and surfaces*, **27** (1987) 163-173.
- [27] G. Carlsson, P. Kolseth, T. Lindström, *Polyelectrolyte swelling behavior of chlorite delignified spruce wood fibers*, *Wood Science and Technology*, **17** (1983) 69-73.
- [28] T. Saito, S. Kimura, Y. Nishiyama, A. Isogai, *Cellulose nanofibers prepared by TEMPO-mediated oxidation of native cellulose*, *Biomacromolecules*, **8** (2007) 2485-2491.
- [29] A. Isogai, *Preparation and characterization of TEMPO-oxidized cellulose nanofibers*, *Bulletin of the Tokyo University Forests*, (2012) 1-43.
- [30] M. Hirota, K. Furihata, T. Saito, T. Kawada, A. Isogai, *Glucose/Glucuronic Acid Alternating Co - polysaccharides Prepared from TEMPO - Oxidized Native Celluloses by Surface Peeling*, *Angewandte Chemie International Edition*, **49** (2010) 7670-7672.
- [31] R. Shinoda, T. Saito, Y. Okita, A. Isogai, *Relationship between length and degree of polymerization of TEMPO-oxidized cellulose nanofibrils*, *Biomacromolecules*, **13** (2012) 842-849.
-

-
- [32] M.E. Malainine, M. Mahrouz, A. Dufresne, *Thermoplastic nanocomposites based on cellulose microfibrils from Opuntia ficus-indica parenchyma cell*, Composites Science and Technology, **65** (2005) 1520-1526.
- [33] B. Wang, M. Sain, *Isolation of nanofibers from soybean source and their reinforcing capability on synthetic polymers*, Composites Science and Technology, **67** (2007) 2521-2527.
- [34] S. Iwamoto, A. Nakagaito, H. Yano, *Nano-fibrillation of pulp fibers for the processing of transparent nanocomposites*, Applied Physics A: Materials Science & Processing, **89** (2007) 461-466.
- [35] M. Henriksson, G. Henriksson, L. Berglund, T. Lindström, *An environmentally friendly method for enzyme-assisted preparation of microfibrillated cellulose (MFC) nanofibers*, European Polymer Journal, **43** (2007) 3434-3441.
- [36] S. Janardhnan, M.M. Sain, *Isolation of cellulose microfibrils—an enzymatic approach*, Bioresources, **1** (2007) 176-188.
- [37] D. Ishii, T. Saito, A. Isogai, *Viscoelastic evaluation of average length of cellulose nanofibers prepared by TEMPO-mediated oxidation*, Biomacromolecules, **12** (2011) 548-550.
- [38] S. Elazzouzi-Hafraoui, Y. Nishiyama, J.-L. Putaux, L. Heux, F. Dubreuil, C. Rochas, *The shape and size distribution of crystalline nanoparticles prepared by acid hydrolysis of native cellulose*, Biomacromolecules, **9** (2007) 57-65.
- [39] I. Siró, D. Plackett, *Microfibrillated cellulose and new nanocomposite materials: a review*, Cellulose, **17** (2010) 459-494.
- [40] D. Martinez, K. Buckley, S. Jivan, A. Lindstrom, R. Thiruvengadaswamy, J. Olson, T. Ruth, R. Kerekes, *Characterizing the mobility of papermaking fibres during sedimentation*, in: Proceedings of the Transactions of 12th fundamental Research Symposium, Oxford, 2001, pp. 225-254.
- [41] L. Zhang, W. Batchelor, S. Varanasi, T. Tsuzuki, X. Wang, *Effect of cellulose nanofiber dimensions on sheet forming through filtration*, Cellulose, **19** (2012) 561-574.
-

-
- [42] A. Celzard, V. Fierro, A. Pizzi, *Flocculation of cellulose fibre suspensions: the contribution of percolation and effective-medium theories*, *Cellulose*, **15** (2008) 803.
- [43] S. Varanasi, R. He, W. Batchelor, *Estimation of cellulose nanofibre aspect ratio from measurements of fibre suspension gel point*, *Cellulose*, **20** (2013) 1885-1896.
- [44] P. Raj, S. Varanasi, W. Batchelor, G. Garnier, *Effect of cationic polyacrylamide on the processing and properties of nanocellulose films*, *Journal of colloid and interface science*, **447** (2015) 113-119.
- [45] Q. Li, P. Raj, F.A. Husain, S. Varanasi, T. Rainey, G. Garnier, W. Batchelor, *Engineering cellulose nanofibre suspensions to control filtration resistance and sheet permeability*, *Cellulose*, **23** (2016) 391-402.
- [46] A. Dufresne, D. Dupeyre, M.R. Vignon, *Cellulose microfibrils from potato tuber cells: processing and characterization of starch–cellulose microfibril composites*, *Journal of Applied Polymer Science*, **76** (2000) 2080-2092.
- [47] K. Syverud, P. Stenius, *Strength and barrier properties of MFC films*, *Cellulose*, **16** (2009) 75.
- [48] A. Dufresne, J.-Y. Cavaille, M.R. Vignon, *Mechanical behavior of sheets prepared from sugar beet cellulose microfibrils*, *Journal of applied polymer science*, **64** (1997) 1185-1194.
- [49] S. Iwamoto, A.N. Nakagaito, H. Yano, M. Nogi, *Optically transparent composites reinforced with plant fiber-based nanofibers*, *Applied Physics A: Materials Science & Processing*, **81** (2005) 1109-1112.
- [50] Z.D. Chen, D.G. Li, L. Xu, Y.M. Wang, D.L. Lin, *Research on preparation and properties of cellulose nanofibers and its polymethylmethacrylate (PMMA) based nanocomposites*, in: *Applied Mechanics and Materials*, Trans Tech Publ, 2012, pp. 893-899.
- [51] L.Y. Zhang, T. Tsuzuki, X.G. Wang, *Preparation and characterization on cellulose nanofiber film*, in: *Materials science forum*, Trans Tech Publ, 2010, pp. 1760-1763.
- [52] M. Henriksson, L.A. Berglund, P. Isaksson, T. Lindstrom, T. Nishino, *Cellulose nanopaper structures of high toughness*, *Biomacromolecules*, **9** (2008) 1579-1585.
-

-
- [53] T. Taniguchi, K. Okamura, *New films produced from microfibrillated natural fibres*, Polymer International, **47** (1998) 291-294.
- [54] A. Nakagaito, H. Yano, *The effect of morphological changes from pulp fiber towards nano-scale fibrillated cellulose on the mechanical properties of high-strength plant fiber based composites*, Applied Physics A, **78** (2004) 547-552.
- [55] S. Varanasi, W.J. Batchelor, *Rapid preparation of cellulose nanofibre sheet*, Cellulose, **20** (2013) 211-215.
- [56] M. Pääkkö, J. Vapaavuori, R. Silvennoinen, H. Kosonen, M. Ankerfors, T. Lindström, L.A. Berglund, O. Ikkala, *Long and entangled native cellulose I nanofibers allow flexible aerogels and hierarchically porous templates for functionalities*, Soft Matter, **4** (2008) 2492-2499.
- [57] M. Nogi, S. Iwamoto, A.N. Nakagaito, H. Yano, *Optically transparent nanofiber paper*, Advanced materials, **21** (2009) 1595-1598.
- [58] D. Beneventi, D. Chaussy, D. Curtil, L. Zolin, C. Gerbaldi, N. Penazzi, *Highly porous paper loading with microfibrillated cellulose by spray coating on wet substrates*, Industrial & Engineering Chemistry Research, **53** (2014) 10982-10989.
- [59] D. Beneventi, E. Zeno, D. Chaussy, *Rapid nanopaper production by spray deposition of concentrated microfibrillated cellulose slurries*, Industrial Crops and Products, **72** (2015) 200-205.
- [60] J. Magnusson, *Method for spraying of free standing 3D structures with MFC: Creation and development of a method*, in, 2016.
- [61] L.F. Krol, D. Beneventi, F. Alloin, D. Chaussy, *Microfibrillated cellulose-SiO₂ composite nanopapers produced by spray deposition*, Journal of Materials Science, **50** (2015) 4095-4103.
- [62] L. Zolin, *Electrode preparation exploiting the spray coating technique*, in: *Large-scale Production of Paper-based Li-ion Cells*, Springer, 2017, pp. 77-94.
- [63] K. Shanmugam, S. Varanasi, G. Garnier, W. Batchelor, *Rapid preparation of smooth nanocellulose films using spray coating*, Cellulose, (2017) 1-8.
-

-
- [64] N. Lavoine, I. Desloges, A. Dufresne, J. Bras, *Microfibrillated cellulose—its barrier properties and applications in cellulosic materials: A review*, Carbohydrate polymers, **90** (2012) 735-764.
- [65] S. Mondal, *Preparation, properties and applications of nanocellulosic materials*, Carbohydrate polymers, **163** (2017) 301-316.
- [66] L. Neimo, *Papermaking chemistry (Book 4)*, Papermaking science and technology, (1999).
- [67] H. Fukuzumi, T. Saito, T. Iwata, Y. Kumamoto, A. Isogai, *Transparent and high gas barrier films of cellulose nanofibers prepared by TEMPO-mediated oxidation*, Biomacromolecules, **10** (2008) 162-165.
- [68] S. Varanasi, W. Batchelor, *Superior non-woven sheet forming characteristics of low-density cationic polymer-cellulose nanofibre colloids*, Cellulose, **21** (2014) 3541-3550.
- [69] H. Sehaqui, A. Liu, Q. Zhou, L.A. Berglund, *Fast preparation procedure for large, flat cellulose and cellulose/inorganic nanopaper structures*, Biomacromolecules, **11** (2010) 2195-2198.
- [70] J. Leitner, B. Hinterstoisser, M. Wastyn, J. Keckes, W. Gindl, *Sugar beet cellulose nanofibril-reinforced composites*, Cellulose, **14** (2007) 419-425.
- [71] V. Barbash, O. Yaschenko, O. Shniruk, *Preparation and Properties of Nanocellulose from Organosolv Straw Pulp*, Nanoscale Research Letters, **12** (2017) 241.
- [72] K.L. Spence, R.A. Venditti, Y. Habibi, O.J. Rojas, J.J. Pawlak, *The effect of chemical composition on microfibrillar cellulose films from wood pulps: mechanical processing and physical properties*, Bioresource technology, **101** (2010) 5961-5968.
- [73] C. Aulin, G. Salazar-Alvarez, T. Lindström, *High strength, flexible and transparent nanofibrillated cellulose–nanoclay biohybrid films with tunable oxygen and water vapor permeability*, Nanoscale, **4** (2012) 6622-6628.
- [74] J. Lange, Y. Wyser, *Recent innovations in barrier technologies for plastic packaging—a review*, Packaging Technology and Science, **16** (2003) 149-158.
-

-
- [75] J.M. Krochta, E. Baldwin, M. Nisperos-Carriedo, *Permeability properties of edible films*, Edible Coatings and Films to Improve Food Quality, (1994) 139.
- [76] K.L. Spence, R.A. Venditti, O.J. Rojas, Y. Habibi, J.J. Pawlak, *The effect of chemical composition on microfibrillar cellulose films from wood pulps: water interactions and physical properties for packaging applications*, Cellulose, **17** (2010) 835-848.
- [77] S. Belbekhouche, J. Bras, G. Siqueira, C. Chappey, L. Lebrun, B. Khelifi, S. Marais, A. Dufresne, *Water sorption behavior and gas barrier properties of cellulose whiskers and microfibrils films*, Carbohydrate Polymers, **83** (2011) 1740-1748.
- [78] M. Minelli, M.G. Baschetti, F. Doghieri, M. Ankerfors, T. Lindström, I. Siró, D. Plackett, *Investigation of mass transport properties of microfibrillated cellulose (MFC) films*, Journal of Membrane Science, **358** (2010) 67-75.
- [79] C. Aulin, T. Lindström, *Biopolymer coatings for paper and paperboard*, Biopolymers-New Materials for Sustainable Films and Coatings, (2011) 255-276.
- [80] M. Nogi, N. Komoda, K. Otsuka, K. Suganuma, *Foldable nanopaper antennas for origami electronics*, Nanoscale, **5** (2013) 4395-4399.
- [81] S. Ummartyotin, J. Juntaro, M. Sain, H. Manuspiya, *Development of transparent bacterial cellulose nanocomposite film as substrate for flexible organic light emitting diode (OLED) display*, Industrial Crops and Products, **35** (2012) 92-97.
- [82] J.-W. Han, B. Kim, J. Li, M. Meyyappan, *Carbon nanotube based humidity sensor on cellulose paper*, The Journal of Physical Chemistry C, **116** (2012) 22094-22097.
- [83] B. Lamprecht, R. Thünauer, M. Ostermann, G. Jakopic, G. Leising, *Organic photodiodes on newspaper*, physica status solidi (a), **202** (2005).
- [84] D.S. Hecht, L. Hu, G. Irvin, *Emerging transparent electrodes based on thin films of carbon nanotubes, graphene, and metallic nanostructures*, Advanced materials, **23** (2011) 1482-1513.
-

-
- [85] M. Nogi, 能木雅也, C. Kim, 金昌宰, T. Sugahara, 菅原徹, T. Inui, 乾哲治, T. Takahashi, 高橋司, *High thermal stability of optical transparency in cellulose nanofiber paper*, Applied Physics Letters, **102** (2013) 181911.
- [86] M.-C. Hsieh, C. Kim, M. Nogi, K. Suganuma, *Electrically conductive lines on cellulose nanopaper for flexible electrical devices*, Nanoscale, **5** (2013) 9289-9295.
- [87] H. Ma, C. Burger, B.S. Hsiao, B. Chu, *Ultra-fine cellulose nanofibers: new nano-scale materials for water purification*, Journal of Materials Chemistry, **21** (2011) 7507-7510.
- [88] H. Ma, K. Yoon, L. Rong, Y. Mao, Z. Mo, D. Fang, Z. Hollander, J. Gaiteri, B.S. Hsiao, B. Chu, *High-flux thin-film nanofibrous composite ultrafiltration membranes containing cellulose barrier layer*, Journal of Materials Chemistry, **20** (2010) 4692-4704.
- [89] H. Ma, K. Yoon, L. Rong, M. Shokralla, A. Kopot, X. Wang, D. Fang, B.S. Hsiao, B. Chu, *Thin-film nanofibrous composite ultrafiltration membranes based on polyvinyl alcohol barrier layer containing directional water channels*, Industrial & Engineering Chemistry Research, **49** (2010) 11978-11984.
- [90] M. Ulbricht, *Advanced functional polymer membranes*, Polymer, **47** (2006) 2217-2262.
- [91] M. Zhou, P.R. Nemade, X. Lu, X. Zeng, E.S. Hatakeyama, R.D. Noble, D.L. Gin, *New type of membrane material for water desalination based on a cross-linked bicontinuous cubic lyotropic liquid crystal assembly*, Journal of the American Chemical Society, **129** (2007) 9574-9575.
- [92] X. Peng, J. Jin, Y. Nakamura, T. Ohno, I. Ichinose, *Ultrafast permeation of water through protein-based membranes*, Nature nanotechnology, **4** (2009) 353-357.
- [93] J. Mulder, *Basic principles of membrane technology*, Springer Science & Business Media, 2012.
- [94] S.P. Nunes, K.-V. Peinemann, *Membrane technology*, Wiley Online Library, 2001.
- [95] G. Pearce, *Introduction to membranes: Filtration for water and wastewater treatment*, Filtration & separation, **44** (2007) 24-27.
-

-
- [96] S. Varanasi, Z.-X. Low, W. Batchelor, *Cellulose nanofibre composite membranes—Biodegradable and recyclable UF membranes*, *Chemical Engineering Journal*, **265** (2015) 138-146.
- [97] M. Bertolini, E. Bottani, G. Vignali, A. Volpi, *Comparative Life Cycle Assessment of Packaging Systems for Extended Shelf Life Milk*, *Packaging Technology and Science*, **29** (2016) 525-546.
- [98] L. Yang, A. Paulson, *Mechanical and water vapour barrier properties of edible gellan films*, *Food Research International*, **33** (2000) 563-570.
- [99] L. Shen, M.K. Patel, *Life cycle assessment of polysaccharide materials: a review*, *Journal of Polymers and the Environment*, **16** (2008) 154.
- [100] Boustead, *Low density polyethylene (LDPE)*, in, *Eco-profiles of the European Plastic Industry 2005*, pp. 1-19.
- [101] D. Twede, S. Selke, *Cartons, Crates and Corrugated Board: Handbook of Paper and Wood Packaging Technology*, 2005, Lancaster: Destech Pubns Inc, (2014).
- [102] H. Kausch, G. Michler, *Effect of nanoparticle size and size - distribution on mechanical behavior of filled amorphous thermoplastic polymers*, *Journal of Applied Polymer Science*, **105** (2007) 2577-2587.
- [103] K.I. Winey, R.A. Vaia, *Polymer nanocomposites*, *MRS bulletin*, **32** (2007) 314-322.
- [104] F. Li, S. Zhou, L. Wu, *Preparation and characterization of UV - curable MPS - modified silica nanocomposite coats*, *Journal of applied polymer science*, **98** (2005) 2274-2281.
- [105] Y. Sun, Z. Zhang, C. Wong, *Influence of interphase and moisture on the dielectric spectroscopy of epoxy/silica composites*, *Polymer*, **46** (2005) 2297-2305.
- [106] T. Merkel, B. Freeman, R. Spontak, Z. He, I. Pinnau, P. Meakin, A. Hill, *Sorption, transport, and structural evidence for enhanced free volume in poly (4-methyl-2-pentyne)/fumed silica nanocomposite membranes*, *Chemistry of Materials*, **15** (2003) 109-123.
- [107] J. Jang, J. Ha, B. Lim, *Synthesis and characterization of monodisperse silica–polyaniline core–shell nanoparticles*, *Chemical Communications*, (2006) 1622-1624.
-

-
- [108] J.-H. Kim, J.-H. Kim, E.-S. Choi, H.K. Yu, J.H. Kim, Q. Wu, S.-J. Chun, S.-Y. Lee, S.-Y. Lee, *Colloidal silica nanoparticle-assisted structural control of cellulose nanofiber paper separators for lithium-ion batteries*, Journal of Power Sources, **242** (2013) 533-540.
- [109] I. Algar, C. Garcia-Astrain, A. Gonzalez, L. Martin, N. Gabilondo, A. Retegi, A. Eceiza, *Improved Permeability Properties for Bacterial Cellulose/Montmorillonite Hybrid Bionanocomposite Membranes by In-Situ Assembling*, Journal of Renewable Materials, **4** (2016) 57-65.
- [110] T.T. Ho, T. Zimmermann, S. Ohr, W.R. Caseri, *Composites of cationic nanofibrillated cellulose and layered silicates: water vapor barrier and mechanical properties*, ACS applied materials & interfaces, **4** (2012) 4832-4840.
- [111] A. Liu, A. Walther, O. Ikkala, L. Belova, L.A. Berglund, *Clay nanopaper with tough cellulose nanofiber matrix for fire retardancy and gas barrier functions*, Biomacromolecules, **12** (2011) 633-641.
- [112] Y. Iguchi, H. Ichiura, T. Kitaoka, H. Tanaka, *Preparation and characteristics of high performance paper containing titanium dioxide photocatalyst supported on inorganic fiber matrix*, Chemosphere, **53** (2003) 1193-1199.
- [113] X. An, D. Cheng, L. Dai, B. Wang, H.J. Ocampo, J. Nasrallah, X. Jia, J. Zou, Y. Long, Y. Ni, *Synthesis of nano-fibrillated cellulose/magnetite/titanium dioxide (NFC@ Fe₃O₄@ TNP) nanocomposites and their application in the photocatalytic hydrogen generation*, Applied Catalysis B: Environmental, **206** (2017) 53-64.
- [114] J. Wang, W. Liu, H. Li, H. Wang, Z. Wang, W. Zhou, H. Liu, *Preparation of cellulose fiber–TiO₂ nanobelt–silver nanoparticle hierarchically structured hybrid paper and its photocatalytic and antibacterial properties*, Chemical engineering journal, **228** (2013) 272-280.
- [115] I. Chauhan, P. Mohanty, *In situ decoration of TiO₂ nanoparticles on the surface of cellulose fibers and study of their photocatalytic and antibacterial activities*, Cellulose, **22** (2014) 507-519.
-

-
- [116] A. Fujishima, T.N. Rao, D.A. Tryk, *Titanium dioxide photocatalysis*, Journal of Photochemistry and Photobiology C: Photochemistry Reviews, **1** (2000) 1-21.
- [117] C. Kang, D. Ahn, C. Roh, S.S. Kim, J. Lee, *Development of Synergistic Antimicrobial Coating of p-Aramid Fibers Using Ag Nanoparticles and Glycidyltrimethylammonium Chloride (GTAC) without the Aid of a Cross-Linking Agent*, Polymers, **9** (2017) 357.
- [118] T. Maneerung, S. Tokura, R. Rujiravanit, *Impregnation of silver nanoparticles into bacterial cellulose for antimicrobial wound dressing*, Carbohydrate polymers, **72** (2008) 43-51.
- [119] V. Dal Lago, L.F. de Oliveira, K. de Almeida Gonçalves, J. Kobarg, M.B. Cardoso, *Size-selective silver nanoparticles: future of biomedical devices with enhanced bactericidal properties*, Journal of Materials Chemistry, **21** (2011) 12267-12273.
- [120] M. Singh, T. Sahareen, *Investigation of cellulosic packets impregnated with silver nanoparticles for enhancing shelf-life of vegetables*, LWT-Food Science and Technology, **86** (2017) 116-122.
- [121] Q.L. Shimabuku, F.S. Arakawa, M. Fernandes Silva, P. Ferri Coldebella, T. Ueda-Nakamura, M.R. Fagundes-Klen, R. Bergamasco, *Water treatment with exceptional virus inactivation using activated carbon modified with silver (Ag) and copper oxide (CuO) nanoparticles*, Environmental technology, **38** (2017) 2058-2069.
- [122] P.A. Marques, H.I. Nogueira, R.J. Pinto, C.P. Neto, T. Trindade, *Silver - bacterial cellulosic sponges as active SERS substrates*, Journal of Raman Spectroscopy, **39** (2008) 439-443.
- [123] H.M. Osorio, P. Cea, L.M. Ballesteros, I. Gascón, S. Marqués-González, R.J. Nichols, F. Pérez-Murano, P.J. Low, S. Martín, *Preparation of nascent molecular electronic devices from gold nanoparticles and terminal alkyne functionalised monolayer films*, Journal of Materials Chemistry C, **2** (2014) 7348-7355.
- [124] M. Pérez-Ortiz, C. Zapata-Urzuúa, G.A. Acosta, A. Álvarez-Lueje, F. Albericio, M.J. Kogan, *Gold nanoparticles as an efficient drug delivery system for GLP-1 peptides*, Colloids and Surfaces B: Biointerfaces, **158** (2017) 25-32.
- [125] X. Sun, G. Zhang, R.S. Keynton, M.G. O'Toole, D. Patel, A.M. Gobin, *Enhanced drug delivery via hyperthermal membrane disruption using targeted gold nanoparticles with PEGylated*
-

-
- Protein-G as a cofactor*, *Nanomedicine: Nanotechnology, Biology and Medicine*, **9** (2013) 1214-1222.
- [126] O. Parlak, A. İncel, L. Uzun, A.P. Turner, A. Tiwari, *Structuring Au nanoparticles on two-dimensional MoS₂ nanosheets for electrochemical glucose biosensors*, *Biosensors and Bioelectronics*, **89** (2017) 545-550.
- [127] Y.H. Ngo, D. Li, G.P. Simon, G. Garnier, *Gold nanoparticle–paper as a three-dimensional surface enhanced raman scattering substrate*, *Langmuir*, **28** (2012) 8782-8790.
- [128] R.-m. Yuan, H.-j. Li, X.-m. Yin, J.-h. Lu, L.-l. Zhang, *3D CuO nanosheet wrapped nanofilm grown on Cu foil for high-performance non-enzymatic glucose biosensor electrode*, *Talanta*, **174** (2017) 514-520.
- [129] E. Flores, J. Pizarro, F. Godoy, R. Segura, A. Gómez, N. Agurto, P. Sepúlveda, *An electrochemical sensor for the determination of Cu (II) using a modified electrode with ferrocenyl crown ether compound by square wave anodic stripping voltammetry*, *Sensors and Actuators B: Chemical*, **251** (2017) 433-439.
- [130] M.B. Gawande, A. Goswami, F.-X. Felpin, T. Asefa, X. Huang, R. Silva, X. Zou, R. Zboril, R.S. Varma, *Cu and Cu-based nanoparticles: synthesis and applications in catalysis*, *Chemical reviews*, **116** (2016) 3722-3811.
- [131] S. Gupta, S.M. Nalawade, S. Hatamie, H. Thakur, S. Kale, *Sensitive, Weak Magnetic Field Sensor Based on Cobalt Nanoparticles Deposited in Micro - Tunnels of PM - PCF Optical Fiber*, in: *AIP Conference Proceedings*, AIP, 2011, pp. 437-439.
- [132] V. Krishnamoorthy, S. Rajiv, *Potential Seed Coatings Fabricated from Electrospinning Hexaaminocyclotriphosphazene and Cobalt Nanoparticles Incorporated Polyvinylpyrrolidone for Sustainable Agriculture*, *ACS Sustainable Chemistry & Engineering*, **5** (2016) 146-152.
- [133] O.W. Flörke, H.A. Graetsch, F. Brunk, L. Benda, S. Paschen, H.E. Bergna, W.O. Roberts, W.A. Welsh, C. Libanati, M. Ettlinger, D. Kerner, M. Maier, W. Meon, R. Schmoll, H. Gies, D. Schiffmann, *Silica*, in: *Ullmann's Encyclopedia of Industrial Chemistry*, Wiley-VCH Verlag GmbH & Co. KGaA, 2000.
-

-
- [134] R. Salh, *Defect related luminescence in silicon dioxide network: a review*, in: Crystalline Silicon-Properties and Uses, InTech, 2011.
- [135] H. Zou, S. Wu, J. Shen, *Polymer/silica nanocomposites: preparation, characterization, properties, and applications*, Chem. Rev, **108** (2008) 3893-3957.
- [136] A. Ahmed, R. Clowes, E. Willneff, P. Myers, H. Zhang, *Porous silica spheres in macroporous structures and on nanofibres*, Philosophical Transactions of the Royal Society of London A: Mathematical, Physical and Engineering Sciences, **368** (2010) 4351-4370.
- [137] M.G. Burzo, P.L. Komarov, P.E. Raad, *Thermal transport properties of gold-covered thin-film silicon dioxide*, IEEE Transactions on Components and Packaging Technologies, **26** (2003) 80-88.
- [138] S.H. Kim, S.H. Ahn, T. Hirai, *Crystallization kinetics and nucleation activity of silica nanoparticle-filled poly (ethylene 2, 6-naphthalate)*, Polymer, **44** (2003) 5625-5634.
- [139] R. Prasanth, P.S. Owuor, R. Shankar, J. Joyner, S. Kosolwattana, S.P. Jose, P. Dong, V.K. Thakur, J.H. Cho, M. Shelke, *Eco-Friendly Polymer-Layered Silicate Nanocomposite-Preparation, Chemistry, Properties, and Applications*, in: Eco-friendly Polymer Nanocomposites, Springer, 2015, pp. 1-42.
- [140] P. Hall, *Clays: their significance, properties, origins and uses*, A Handbook of Determinative Methods in Clay Mineralogy, **1** (1987) 1-25.
- [141] S.S. Ray, M. Bousmina, *Biodegradable polymers and their layered silicate nanocomposites: in greening the 21st century materials world*, Progress in materials science, **50** (2005) 962-1079.
- [142] L. Ludueña, J. Morán, V. Alvarez, *Biodegradable Polymer/Clay Nanocomposites*, in: Eco-friendly Polymer Nanocomposites, Springer, 2015, pp. 109-135.
- [143] G.M. Do Nascimento, *Structure of Clays and Polymer-Clay Composites Studied by X-ray Absorption Spectroscopies*, in: Clays, Clay Minerals and Ceramic Materials Based on Clay Minerals, InTech, 2016.
-

-
- [144] S.G. Jahromi, B. Andalibizade, S. Vossough, *Engineering properties of nanoclay modified asphalt concrete mixtures*, Arabian Journal for Science & Engineering (Springer Science & Business Media BV), **35** (2010).
- [145] R. Bharadwaj, A. Mehrabi, C. Hamilton, C. Trujillo, M. Murga, R. Fan, A. Chavira, A. Thompson, *Structure–property relationships in cross-linked polyester–clay nanocomposites*, Polymer, **43** (2002) 3699-3705.
- [146] L.s. Cabedo, E. Giménez, J.M. Lagaron, R. Gavara, J.J. Saura, *Development of EVOH-kaolinite nanocomposites*, Polymer, **45** (2004) 5233-5238.
- [147] H.M. De Azeredo, *Nanocomposites for food packaging applications*, Food research international, **42** (2009) 1240-1253.
- [148] J.H. Braun, A. Baidins, R.E. Marganski, *TiO₂ pigment technology: a review*, Progress in organic coatings, **20** (1992) 105-138.
- [149] R. Pelton, X. Geng, M. Brook, *Photocatalytic paper from colloidal TiO₂—fact or fantasy*, Advances in colloid and interface science, **127** (2006) 43-53.
- [150] A. Wold, *Photocatalytic properties of titanium dioxide (TiO₂)*, Chemistry of Materials, **5** (1993) 280-283.
- [151] S. Woodley, C. Catlow, *Structure prediction of titania phases: implementation of Darwinian versus Lamarckian concepts in an evolutionary algorithm*, Computational Materials Science, **45** (2009) 84-95.
- [152] K. Hashimoto, K. Wasada, M. Osaki, E. Shono, K. Adachi, N. Toukai, H. Kominami, Y. Kera, *Photocatalytic oxidation of nitrogen oxide over titania–zeolite composite catalyst to remove nitrogen oxides in the atmosphere*, Applied Catalysis B: Environmental, **30** (2001) 429-436.
- [153] J. Manassah, *Treatment of highly polluted paper mill waste water by solar photocatalytic oxidation with synthesized nano TiO₂*, in: Green Technology and Environmental Conservation (GTEC 2011), 2011 International Conference on, IEEE, 2011, pp. 356-361.
-

-
- [154] A. Fujishima, *Electrochemical photolysis of water at a semiconductor electrode*, *nature*, **238** (1972) 37-38.
- [155] H. Matsubara, M. Takada, S. Koyama, K. Hashimoto, A. Fujishima, *Photoactive TiO₂ containing paper: preparation and its photocatalytic activity under weak UV light illumination*, *Chemistry Letters*, **24** (1995) 767-768.
- [156] S. Fukahori, H. Ichiura, T. Kitaoka, H. Tanaka, *Photocatalytic decomposition of bisphenol A in water using composite TiO₂-zeolite sheets prepared by a papermaking technique*, *Environmental science & technology*, **37** (2003) 1048-1051.
- [157] I.K. Konstantinou, T.A. Albanis, *TiO₂-assisted photocatalytic degradation of azo dyes in aqueous solution: kinetic and mechanistic investigations: a review*, *Applied Catalysis B: Environmental*, **49** (2004) 1-14.
- [158] N.M. Mahmoodi, M. Arami, N.Y. Limaee, N.S. Tabrizi, *Kinetics of heterogeneous photocatalytic degradation of reactive dyes in an immobilized TiO₂ photocatalytic reactor*, *Journal of colloid and interface Science*, **295** (2006) 159-164.
- [159] R.W. Matthews, *Photooxidative degradation of coloured organics in water using supported catalysts. TiO₂ on sand*, *Water research*, **25** (1991) 1169-1176.
- [160] U.I. Gaya, A.H. Abdullah, *Heterogeneous photocatalytic degradation of organic contaminants over titanium dioxide: a review of fundamentals, progress and problems*, *Journal of Photochemistry and Photobiology C: Photochemistry Reviews*, **9** (2008) 1-12.
- [161] N. Mandzy, E. Grulke, T. Druffel, *Breakage of TiO₂ agglomerates in electrostatically stabilized aqueous dispersions*, *Powder technology*, **160** (2005) 121-126.
- [162] Y.H. Ngo, D. Li, G.P. Simon, G. Garnier, *Paper surfaces functionalized by nanoparticles*, *Advances in colloid and interface science*, **163** (2011) 23-38.
- [163] J. Kim, S. Yun, Z. Ounaies, *Discovery of cellulose as a smart material*, *Macromolecules*, **39** (2006) 4202-4206.
-

-
- [164] K. Oksman, A. Mathew, D. Bondeson, I. Kvien, Manufacturing process of cellulose whiskers/polylactic acid nanocomposites, *Composites science and technology*, 66 (2006) 2776-2784.
- [165] D. Klemm, D. Schumann, F. Kramer, N. Heßler, M. Hornung, H.-P. Schmauder, S. Marsch, Nanocelluloses as innovative polymers in research and application, in: *Polysaccharides II*, Springer, 2006, pp. 49-96.
- [166] H. Yano, J. Sugiyama, A.N. Nakagaito, M. Nogi, T. Matsuura, M. Hikita, K. Handa, Optically transparent composites reinforced with networks of bacterial nanofibers, *Advanced Materials*, 17 (2005) 153-155.
- [167] F. Hussan, M. Hojjayi, M. Okamoto, R.E. Gorga, Review article: Polymer-matrix Nanocomposites, Processing, Manufacturing and Application, *J. comp. mat.*, 40 (2006).
- [168] N.C. Martins, C.S. Freire, R.J. Pinto, S.C. Fernandes, C.P. Neto, A.J. Silvestre, J. Causio, G. Baldi, P. Sadocco, T. Trindade, Electrostatic assembly of Ag nanoparticles onto nanofibrillated cellulose for antibacterial paper products, *Cellulose*, 19 (2012) 1425-1436.
- [169] R.J. Pinto, P.A. Marques, C.P. Neto, T. Trindade, S. Daina, P. Sadocco, Antibacterial activity of nanocomposites of silver and bacterial or vegetable cellulosic fibers, *Acta Biomaterialia*, 5 (2009) 2279-2289.
- [170] X. An, Y. Wen, A. Almuji, D. Cheng, J. Li, X. Jia, J. Zou, Y. Ni, Nano-fibrillated cellulose (NFC) as versatile carriers of TiO₂ nanoparticles (TNPs) for photocatalytic hydrogen generation, *RSC Advances*, 6 (2016) 89457-89466.
- [171] R.J. Pinto, M.C. Neves, C.P. Neto, T. Trindade, Composites of cellulose and metal nanoparticles, in: *Nanocomposites-New Trends and Developments*, InTech, 2012.
- [172] M.A. Mohamed, W. Salleh, J. Jaafar, A. Ismail, M.A. Mutalib, S.M. Jamil, Incorporation of N-doped TiO₂ nanorods in regenerated cellulose thin films fabricated from recycled newspaper as a green portable photocatalyst, *Carbohydrate polymers*, 133 (2015) 429-437.
- [173] A. Snyder, Z. Bo, R. Moon, J.-C. Rochet, L. Stanciu, *Reusable photocatalytic titanium dioxide-cellulose nanofiber films*, *Journal of colloid and interface science*, **399** (2013) 92-98.
-

-
- [174] M. Eita, H. Arwin, H. Granberg, L. Wågberg, *Addition of silica nanoparticles to tailor the mechanical properties of nanofibrillated cellulose thin films*, Journal of colloid and interface science, **363** (2011) 566-572.
- [175] S. Spoljaric, A. Salminen, N. Dang Luong, P. Lahtinen, J. Vartiainen, T. Tammelin, J. Seppälä, *Nanofibrillated cellulose, poly (vinyl alcohol), montmorillonite clay hybrid nanocomposites with superior barrier and thermomechanical properties*, Polymer Composites, **35** (2014) 1117-1131.
- [176] G. Li, A.G. Nandgaonkar, Q. Wang, J. Zhang, W.E. Krause, Q. Wei, L.A. Lucia, *Laccase-immobilized bacterial cellulose/TiO₂ functionalized composite membranes: Evaluation for photo-and bio-catalytic dye degradation*, Journal of Membrane Science, **525** (2017) 89-98.
- [177] J. Yan, A.M. Abdelgawad, M.E. El-Naggar, O.J. Rojas, *Antibacterial activity of silver nanoparticles synthesized In-situ by solution spraying onto cellulose*, Carbohydrate polymers, **147** (2016) 500-508.
- [178] P. Liou, F.X. Nayigiziki, F. Kong, A. Mustapha, M. Lin, *Cellulose nanofibers coated with silver nanoparticles as a SERS platform for detection of pesticides in apples*, Carbohydrate polymers, **157** (2017) 643-650.
- [179] T. Nypelo, M. Osterberg, J. Laine, *Tailoring surface properties of paper using nanosized precipitated calcium carbonate particles*, ACS applied materials & interfaces, **3** (2011) 3725-3731.
- [180] Z. Lu, S. Eadula, Z. Zheng, K. Xu, G. Grozdits, Y. Lvov, *Layer-by-layer nanoparticle coatings on lignocellulose wood microfibrils*, Colloids and Surfaces A: Physicochemical and Engineering Aspects, **292** (2007) 56-62.
- [181] A. Aguedach, S. Brosillon, J. Morvan, E.K. Lhadi, *Photocatalytic degradation of azo-dyes reactive black 5 and reactive yellow 145 in water over a newly deposited titanium dioxide*, Applied Catalysis B: Environmental, **57** (2005) 55-62.
- [182] C. Raillard, V. Hequet, P. Le Cloirec, J. Legrand, *Kinetic study of ketones photocatalytic oxidation in gas phase using TiO₂-containing paper: effect of water vapor*, Journal of Photochemistry and Photobiology A: Chemistry, **163** (2004) 425-431.
-

-
- [183] M. Uddin, F. Cesano, F. Bonino, S. Bordiga, G. Spoto, D. Scarano, A. Zecchina, *Photoactive TiO₂ films on cellulose fibres: synthesis and characterization*, Journal of Photochemistry and Photobiology A: Chemistry, **189** (2007) 286-294.
- [184] L. Wagberg, M. Bjorklund, I. Asell, A. Swerin, *On the mechanism of flocculation by microparticle retention-aid systems*, Tappi journal (USA), (1996).
- [185] J.F. Bringley, A. Wunder, A.M. Howe, R.D. Wesley, T.A. Qiao, N.B. Liebert, B. Kelley, J. Minter, B. Antalek, J.M. Hewitt, *Controlled, simultaneous assembly of polyethylenimine onto nanoparticle silica colloids*, Langmuir, **22** (2006) 4198-4207.
- [186] F. Oosawa, *Polyelectrolytes*, in: Polyelectrolytes, Marcel Dekker, 1971.
- [187] A.V. Dobrynin, M. Rubinstein, *Theory of polyelectrolytes in solutions and at surfaces*, Progress in Polymer Science, **30** (2005) 1049-1118.
- [188] H. Dautzenberg, W. Jaeger, J. Kötzt, B. Philipp, C. Seidel, D. Stscherbina, *Polyelectrolytes: formation, characterization and application*, (1994).
- [189] J. Koetz, S. Kosmella, *Polyelectrolytes and nanoparticles*, Springer Science & Business Media, 2007.
- [190] M. Rubinstein, R.H. Colby, *Polymer physics*, Oxford University Press New York, 2003.
- [191] D. Evans, H. Wennerström, *The colloidal domain—where physics, chemistry, biology and technology meet*, ch. 2, New York, NY: Wiley-VCH, (1999) 45-98.
- [192] G. Fleer, M. Cohen Stuart, J. Scheutjens, T. Cosgrove, B. Vincent, *Polymers at interfaces*, Ch 7, in, Chapman & Hall, London, 1993.
- [193] L. Wågberg, R. Hägglund, *Kinetics of polyelectrolyte adsorption on cellulosic fibers*, Langmuir, **17** (2001) 1096-1103.
- [194] T. Sennerfors, *Interfacial Behaviour of Polyelectrolyte-Nanoparticle Systems*, in, Kemi, 2002.
- [195] B. Abu-Sharkh, *Structure and mechanism of the deposition of multilayers of polyelectrolytes and nanoparticles*, Langmuir, **22** (2006) 3028-3034.
-

-
- [196] H. Tanaka, L. Ödberg, L. Wågberg, T. Lindström, *Adsorption of cationic polyacrylamides onto monodisperse polystyrene latices and cellulose fiber: effect of molecular weight and charge density of cationic polyacrylamides*, Journal of colloid and interface science, **134** (1990) 219-228.
- [197] L. Winter, L. Wågberg, L. Ödberg, T. Lindström, *Polyelectrolytes adsorbed on the surface of cellulosic materials*, Journal of colloid and interface science, **111** (1986) 537-543.
- [198] L. Wågberg, L. Ödberg, T. Lindström, R. Aksberg, *Kinetics of adsorption and ion-exchange reactions during adsorption of cationic polyelectrolytes onto cellulosic fibers*, Journal of colloid and interface science, **123** (1988) 287-295.
- [199] M.A. Hubbe, H. Nanko, M.R. McNeal, *Retention and polymer interactions with cellulosic surfaces and suspensions: A review*, BioResources, **4** (2009) 850-906.
- [200] M.A. Hubbe, *Flocculation and redispersion of cellulosic fiber suspensions: A review of effects of hydrodynamic shear and polyelectrolytes*, BioResources, **2** (2007) 296-331.
- [201] J. Lefebvre, D.G. Gray, *AFM of adsorbed polyelectrolytes on cellulose I surfaces spin-coated on silicon wafers*, Cellulose, **12** (2005) 127-134.
- [202] J. Su, C.J. Garvey, S. Holt, R.F. Tabor, B. Winther-Jensen, W. Batchelor, G. Garnier, *Adsorption of cationic polyacrylamide at the cellulose-liquid interface: A neutron reflectometry study*, Journal of colloid and interface science, **448** (2015) 88-99.
- [203] W.K. Mosse, D.V. Boger, G.P. Simon, G. Garnier, *Effect of cationic polyacrylamides on the interactions between cellulose fibers*, Langmuir, **28** (2012) 3641-3649.
- [204] G. Liu, H. Zhong, Y. Hu, S. Zhao, L. Xia, *The role of cationic polyacrylamide in the reverse flotation of diasporic bauxite*, Minerals Engineering, **20** (2007) 1191-1199.
- [205] Y.H. Ngo, D. Li, G.P. Simon, G. Garnier, *Effect of cationic polyacrylamide dissolution on the adsorption state of gold nanoparticles on paper and their Surface Enhanced Raman Scattering properties*, Colloids and Surfaces A: Physicochemical and Engineering Aspects, **420** (2013) 46-52.
-

-
- [206] B.A. Miller-Chou, J.L. Koenig, *A review of polymer dissolution*, Progress in Polymer Science, **28** (2003) 1223-1270.
- [207] F.W. Billmeyer, *Textbook of Polymer Science*, John Wiley & Sons, Inc. New York, (1984).
- [208] H.H. Espy, *The mechanism of wet-strength development in paper: a review*, Tappi journal (USA), (1995).
- [209] T. Lindström, L. Wågberg, T. Larsson, *On the nature of joint strength in paper-A review of dry and wet strength resins used in paper manufacturing*, in: 13th fundamental research symposium, The Pulp and Paper Fundamental Research Society Cambridge, UK, 2005, pp. 457-562.
- [210] T. Obokata, A. Isogai, *¹H - and ¹³C - NMR analyses of aqueous polyamideamine - epichlorohydrin resin solutions*, Journal of applied polymer science, **92** (2004) 1847-1854.
- [211] T. Obokata, M. Yanagisawa, A. Isogai, *Characterization of polyamideamine - epichlorohydrin (PAE) resin: Roles of azetidinium groups and molecular mass of PAE in wet strength development of paper prepared with PAE*, Journal of applied polymer science, **97** (2005) 2249-2255.
- [212] M. Aoyama, K. Sawa, *Water soluble resin composition, gas barrier film and packaging material employing it*, in, Google Patents, 2005.
- [213] Y.H. Ngo, D. Li, G.P. Simon, G. Garnier, *Effect of cationic polyacrylamides on the aggregation and SERS performance of gold nanoparticles-treated paper*, Journal of colloid and interface science, **392** (2013) 237-246.
- [214] J. Zhang, W. Liu, P. Wang, K. Qian, *Photocatalytic behavior of cellulose-based paper with TiO₂ loaded on carbon fibers*, Journal of Environmental Chemical Engineering, **1** (2013) 175-182.
- [215] K. Bourikas, T. Hiemstra, W. Van Riemsdijk, *Ion pair formation and primary charging behavior of titanium oxide (anatase and rutile)*, Langmuir, **17** (2001) 749-756.
- [216] S. Xiao, S. Wu, M. Shen, R. Guo, Q. Huang, S. Wang, X. Shi, *Polyelectrolyte multilayer-assisted immobilization of zero-valent iron nanoparticles onto polymer nanofibers for*
-

- potential environmental applications*, ACS applied materials & interfaces, **1** (2009) 2848-2855.
- [217] J. Salmi, T. Nypelö, M. Österberg, J. Laine, *Layer structures formed by silica nanoparticles and cellulose nanofibrils with cationic polyacrylamide (C-PAM) on cellulose surface and their influence on interactions*, BioResources, **4** (2009) 602-625.
- [218] G. Pandav, V. Pryamitsyn, J. Errington, V. Ganesan, *Multibody Interactions, Phase Behavior, and Clustering in Nanoparticle–Polyelectrolyte Mixtures*, The Journal of Physical Chemistry B, **119** (2015) 14536-14550.
- [219] V. Pryamitsyn, V. Ganesan, *Interplay between Depletion and Electrostatic Interactions in Polyelectrolyte–Nanoparticle Systems*, Macromolecules, **47** (2014) 6095-6112.

THIS PAGE HAS BEEN INTENTIONALLY LEFT BLANK

CHAPTER 2

STRONG CELLULOSE NANOFIBRE-NANOSILICA COMPOSITES WITH CONTROLLABLE PORE STRUCTURE

THIS PAGE HAS BEEN INTENTIONALLY LEFT BLANK

PREFACE

Property range of nanocellulose by itself is limited and there is a need to explore new possibilities by combining nanocellulose with inorganic nanoparticles (NPs). Also, NPs have versatile properties and can be selected for their chemical composition, but also can be tailored for their size, shape and surface area and chemistry properties. However, on its own NPs agglomerate and diminish the properties associate with the nanoscale, and also NPs on its own can cause uncontrolled release of NPs to air. Therefore, combining NPs in a nanocellulose matrix can be used to develop new functional materials. In literature, there is a poor understanding of the role played by NPs in the nanocellulose composite structure, and how structure changes with systematic loading of NPs. This chapter presents the effect of NP loading and different NP sizes on the structure and its properties. Two different silicon dioxide (SiO_2) NP sizes were chosen. Cationic polyacrylamide (CPAM) was used to retain SiO_2 NPs in the microfibrillated cellulose (MFC) structure. Variation in retention, thickness, fractional density, morphology, pore size distribution and strength was quantified.

This chapter follows the first objective.

THIS PAGE HAS BEEN INTENTIONALLY LEFT BLANK

**CHAPTER 2 STRONG CELLULOSE NANOFIBRE - NANOSILICA
COMPOSITES WITH CONTROLLABLE PORE STRUCTURE**

2.1 Abstract89

2.2 Keywords90

2.3 Introduction90

2.4 Experimental91

 2.4.1 Material91

 2.4.2 Method92

 2.4.2.1 Preparation of MFC, CPAM and NP suspensions92

 2.4.2.2 MFC sheet preparation92

 2.4.2.3 MFC-NP composite preparation92

 2.4.3 Characterization94

 2.4.3.1 Structure and morphology study94

 2.4.3.2 Thickness and density measurements94

 2.4.3.3 Pore size distribution measurements94

 2.4.3.4 Particle and colloid charge95

 2.4.3.5 Mechanical strength95

2.5 Results and discussion95

2.6 Conclusion105

2.7 Acknowledgement105

2.8 References106

THIS PAGE HAS BEEN INTENTIONALLY LEFT BLANK

Monash University
Declaration for Thesis Chapter 2

In the case of Chapter 2, my contribution to the work involved the following:

Nature of contribution	Extent of contribution (%)
Initiation, key ideas, experimental works, analysis of results, writing up	70

The following co-authors contributed to the work. If co-authors are students at Monash University, the extent of their contributions in percentage must be stated:

Co-author name (s)	Nature of contribution
Swambabu Varanasi	Key ideas, paper reviewing and editing
Gil Garnier	Key ideas, paper reviewing and editing
Warren Batchelor	Key ideas, paper reviewing and editing

The undersigned hereby certify that the above declaration correctly reflects the nature and extent of the candidate's and co-authors' contributions to this work.

Student signature:



Date: 12/10/2017

The undersigned hereby certify that the above declaration correctly reflects the nature and extent of the student's and co-authors' contributions to this work. In instances where I am not the responsible author I have consulted with the responsible author to agree on the respective contributions of the authors.

Main Supervisor signature:



Date: 12/10/2017

THIS PAGE HAS BEEN INTENTIONALLY LEFT BLANK

STRONG CELLULOSE NANOFIBRE-NANOSILICA COMPOSITES WITH CONTROLLABLE PORE STRUCTURE

Uthpala M. Garusinghe, Swambabu Varanasi, Gil Garnier, Warren Batchelor*

BioResource Processing Research Institute of Australia (BioPRIA), Department of Chemical Engineering, Monash University, Clayton 3800, VIC, Australia.

Corresponding author: 

2.1 ABSTRACT

Flexible Nanocellulose composites with silica nanoparticle loadings ranging from 5 to 77 wt% and tuneable pore size were made and characterized. The new composites have a pore structure that can be controlled (100-1000 nm to 10-60 nm) by adjusting the silica nanoparticle content. Composites were prepared by first complexing nanoparticles with a cationic dimethylamino-ethyl-methacrylate polyacrylamide, followed by retaining this complex into a nanocellulose fibre network. High retention of nanoparticles resulted. The structural changes and pore size distribution of the composites were characterised through scanning electron microscopy (SEM) and mercury porosimetry analysis, respectively. The heavily loaded composites formed packed bed structures of nanoparticles. Film thickness was approximately constant for low loading composites indicating that nanoparticles are filling the gaps created by nanocellulose fibres without altering the structure. Film thickness increased drastically for high loading because of the new packed bed structure. Unexpectedly, within the spectrum of loadings, the tensile index on a nanocellulose mass basis was maintained, showing that the silica nanoparticles did not significantly interfere with the bonding between the cellulose nanofibres. This hierarchically engineered material remains flexible at all loadings and its unique packing can be used in nanocellulose composites applications that requires a controlled pore structure and high surface area.

2.2 KEYWORDS

Nanocellulose; Nanoparticles; Composites; Porosity; Structure; Strength

2.3 INTRODUCTION

The pursuit for novel structures with nanoparticles (NPs) is ever increasing because of their excellent properties, such as providing large surface area. NPs can be selected for their chemical composition, but also tailored for size (scale), shape (cylindrical, plane, spherical) and surface properties (surface area, bonding type, charge distribution) [1-3]. Although NPs have versatile properties and can self-aggregate, their use raises important issues concerning their uncontrolled release to air when dry which might limit applications. To prevent release, NPs can be dispersed in a supporting matrix or sintered to form films. Embedding NPs in a continuous polymer matrix limits the availability of NPs' surface. Sintering retains NPs together by forming a composite film typically brittle and weak, also limiting applications. Ideally, the NP embedding matrix is strong, flexible and durable, able to retain NPs while allowing the surface area of NPs to be readily available; combining these requirements has remained a significant challenge.

Using nanocellulose as the structural component/binder to hold NPs in the matrix opens up a new path to tailor performant nanoparticulate composites. The porous fibre structure allows access to NPs in the material. Nanocellulose is a renewable and sustainable nanomaterial which is biodegradable, recyclable and readily available [4, 5]. Nanocellulose has great potential in many applications for its high mechanical strength, low thermal expansion, large surface area, and broad capacity of chemical modifications and flexibility [6, 7]. While the diameter of nanocellulose ranges from 1 to 100 nm [8], the lengths are in micron scale, which gives nanocellulose fibres a high aspect ratio, allowing for a highly entangled network when transformed into a nonwoven material [9]. As a result, nanocellulose can form aerogels [10], strong films [6], membranes [11], bio-composites [12], hydrogels, etc. Each of these substrates with high porosity can serve as a flexible template or carrier for NPs, enabling the production of nanocomposites that combine the advantage of two constituents [13, 14].

Even though progress has been made on developing nanocellulose-NP composites, there is a poor understanding of the role played by NPs in the composite structure. In particular, the performance of the material at very high NP loadings and the variation in performance, surface area and pore

size with NP loading is not well understood. Nanocomposites with very high NP loading have been created with mixing cellulose nanofibrils and montmorillonite together achieved 90 wt% clay loadings which helped improve the tortuosity in the composite to lower the oxygen permeability [15]. However, factors such as shape of clay, size and the cationic charge altogether makes it easier for clay to bind to nanofibril network. On the other hand, anionic and spherical NPs such as SiO₂ with dimensions in the same range as nanofibre diameters are far more difficult to retain within a cellulose fibrous matrix.

In this paper, we have focussed on composites made of nanocellulose and silica NPs. Materials from silica NPs have widespread application in drug delivery [16, 17], serve as separators in Li-ion batteries [14, 18], and while silica NPs have been used at low levels in nanocellulose membranes [13, 19], there has been no systematic study of silica NP-nanocellulose composites across the range of composition. Therefore, the aim of this work is to produce flexible, strong and pore size controllable nanocellulose composites from a solution/filtration process providing high retention of NPs in the structure while retaining the availability of NPs surface.

2.4 EXPERIMENTAL

2.4.1 Material

Micro fibrillated cellulose (MFC) was purchased from DAICEL Chemical Industries Limited, Japan (grade Celish KY-100G). MFC was supplied at 25% solids content and stored at 5°C as received. MFC has a mean diameter of 73 nm and an aspect ratio between 100 to 150 [20].

Cationic dimethylamino-ethyl-methacrylate polyacrylamide (CPAM) polymer of high molecular weight (13 MDa) and a charge density of 40 wt% (F1, SnowFlake Cationics) was kindly supplied by AQUA+TECH, Switzerland. This CPAM can flocculate nanofibres [21] and NPs.

NexSil 85-40 and NexSil 125-40 Aqueous Colloidal Silica with surface area of 55 m²/g and 35 m²/g respectively were provided by IMCD Australia Ltd as 40 wt% suspensions. Diameter distributions are summarized in Table 1.

Table I: Diameter distribution of NPs (full details in Appendix I Figure A1).

	Image J using SEM images	Dynamic light scattering (DLS)
NexSil 85-40 (Small)	30 nm and 70 nm	35 nm and 78 nm
NexSil 125-40 (Large)	60 nm and 130 nm	46 nm and 113 nm

2.4.2 Method

2.4.2.1 Preparation of MFC, CPAM and NP suspensions

A 3L Mavis Engineering (Model No. 8522) disintegrator was used to disperse 0.2 wt% nanofibres in deionized water uniformly using 15,000 propeller revolutions. 0.01 wt% CPAM solutions were prepared by mixing CPAM powder in deionized water using a magnetic stirrer for 8 hours prior to the experiment to ensure full solubilisation [22]. 0.1 wt% of Silica NP suspensions were prepared by diluting 40 wt% silica NP suspension using deionized water and mixing using a magnetic stirrer for 10 minutes prior to use. All suspensions were prepared at room temperature.

2.4.2.2 MFC sheet preparation

Nanofibre sheets were prepared using a standard British hand sheet maker (model T205). The hand sheet maker was equipped with a woven filter with average openings of 74 microns. 0.2 wt% solids MFC suspension was poured into the hand sheet maker and allowed to drain under gravity. After the water drained, film formed was removed from the filter using blotting papers and then dried at 105°C using a sheet drier.

2.4.2.3 MFC-NP composite preparation

Preparation of composite suspension involved mixing nanofibres (0.2 wt%), colloidal silica (0.1 wt%) and CPAM (0.01 wt%) suspensions together (Figure 1a) by double controlled simultaneous addition method (CSA) [13, 23]. Firstly, CPAM and NP suspensions were mixed together; secondly, the NP-CPAM and nanofibre suspensions were mixed to obtain the final suspension of 0.15 wt%. To facilitate the mixing in both stages, a small amount of deionized water (50 mL) was initially added to both beakers. In the composite suspensions preparation, silica weight fraction varied from 5-77 wt%. As composites with higher NP content have more solution to be mixed, flowrates were varied. CPAM flowrate ranged from 2.1 to 165 mL/min, NP suspension flowrate varied from

5.2 to 397 mL/min while nanofibres were mixed at 75 mL/min. Flowrates were adjusted to keep the mixing time in each step at 8 minutes. Final suspension was poured into the British hand sheet maker for composite processing as described above. The NP - CPAM ratio was kept constant at 0.5mg CPAM / 1m² NP for all composites because a complete retention was achieved at this ratio. Nanofibre mass was fixed to 1.2 g while NPs were added as a percentage of nanofibre mass. Therefore, composite's final mass varied. Two sets of composites were prepared for two different NP sizes. The notations given were "Composite V/S" for variable total grammage and small NP size, and "Composite V/L" for variable total grammage and large NP size.

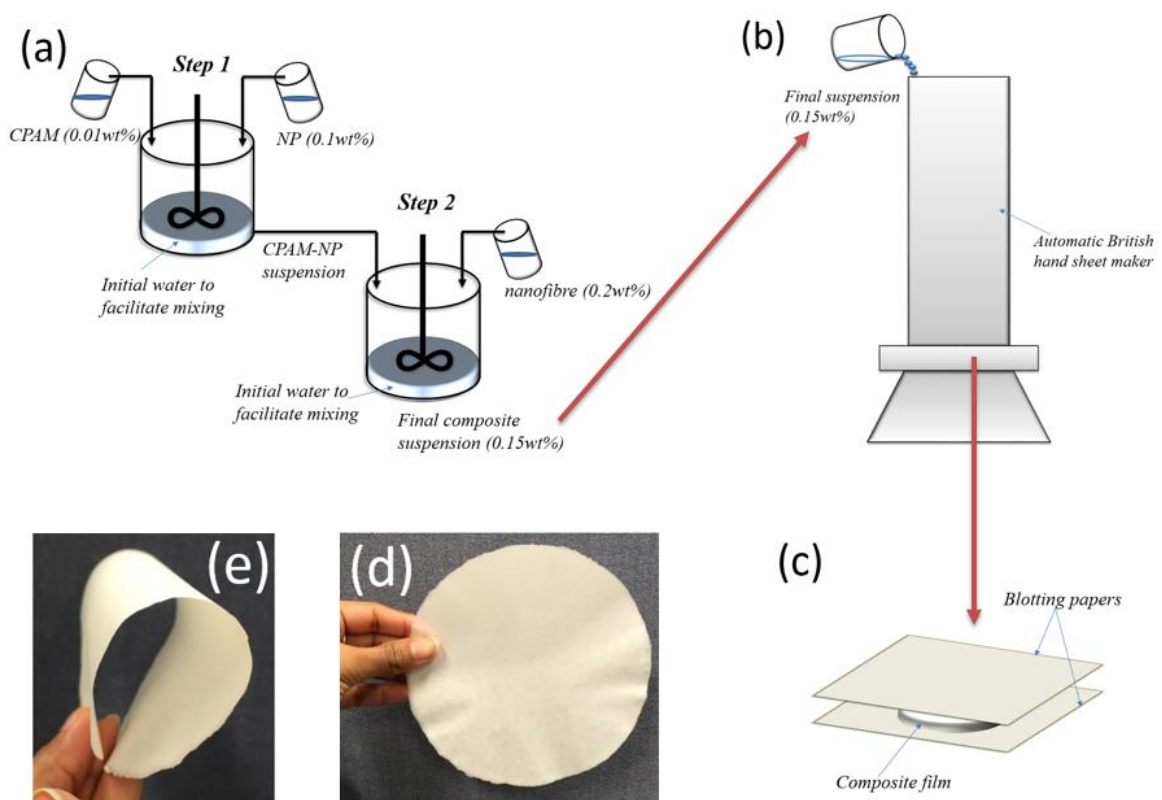


Figure 1: Preparation of nanocomposite. (a) Controlled Simultaneous Addition (CSA) method. (b) Preparation of composite sheet by filtration method. (c) Composite sheet processed using blotting papers. (d) Free standing 77 wt% V/S composite sheet. (e) Illustration of flexibility of 77 wt% V/S sheet.

2.4.3 Characterization

2.4.3.1 Structure and morphology study

SEM was performed using a FEI Nova NanoSEM 450 FEG SEM on nanofibres, composites and casted silica NPs to quantify structure and morphology. To prepare samples for SEM study, a 3 mm by 3 mm sample square was mounted onto a metal substrate using carbon tape and coated with a thin layer of Iridium.

2.4.3.2 Thickness and density measurements

Thickness of the composites was measured using L&W thickness tester (model no 222); the average thickness of ten points was used. Theoretical density of silica NPs and nanofibres are taken as 2400 kg/m³ and 1500 kg/m³ respectively [20]. Composite density was calculated after the sample was oven dried for 4 hours at 105°C; volume was calculated from the area and thickness of the composite after oven drying. The minimum thickness, t_m was calculated as:

$$t_m = \frac{g_f}{\rho_f} + \frac{g_s}{\rho_s} \quad \text{Equation 1}$$

Where g_f and g_s are grammage (g/m²) of nanofibres and NPs respectively, and ρ_f and ρ_s are the densities of nanofibres and NPs, respectively. The maximum density of the composites was calculated with:

$$\rho_m = \frac{g_f + g_s}{t_m} \quad \text{Equation 2}$$

Fractional density ratio is the density of composite divided by theoretical maximum density.

2.4.3.3 Pore size distribution measurements

Pore size distribution and surface area of composites were measured using a mercury porosimetry (Micromeritics' AutoPore IV 9500 Series). The sheets were cut into 5 mm by 5 mm pieces and placed in the sample holder, then degassed overnight at 105°C. Samples were then transferred into a penetrometer (0.412 stem, solid) and used for analysis. The minimum size of pore that can be measured using mercury porosimetry is 3 nm.

2.4.3.4 Particle and colloid charge

The zeta potential measurements for MFC and SiO₂ NPs were performed with a Nanobrook Omni (Brookhaven Instruments) in a cuvette cell at 25°C. Using the supplied software, zeta potential was calculated by determining electrophoretic mobility from an electrophoresis experiment using laser Doppler velocimetry and applying the Smoluchowski equation. 0.2 wt% MFC suspension was centrifuged at 4400 rpm for 20 minutes to remove big aggregates and the supernatant containing colloidal nanocellulose was then used to measure the zeta potential. 0.1 wt% SiO₂ suspension was used as it is for the measurements.

2.4.3.5 Mechanical strength

An Instron tensile tester (model 5566) was used to record the tensile strength based on Australian/New Zealand Standard Methods 448s and 437s. Composites were cut into 120 mm x 15 mm strips and equilibrated at 23°C and 50% relative humidity for a minimum of 24 hours prior to dry tensile testing. The span tested was 100 mm and the elongation was 10mm/min. For each sample, a mean value was obtained from 20 valid tests.

2.5 RESULTS AND DISCUSSION

Two series of composites, V/S and V/L, were prepared with small (S) and large (L) NPs, respectively. Nanofibre grammage was fixed at 60 gsm to allow a good retention of NPs in the nanocellulose matrix at all NP loadings in both composites. Basis weight of films vary as the NP loading increases- denoted variable (V). Composite properties are evaluated in terms of SiO₂ loading and discussed in terms of composite structure. Retention efficiency in composite of both small and large NPs with and without CPAM are given in Figure 2. Retention efficiency is the ratio of the total solid content retained after the filtration process over the initial solid content added to the suspension. The sheet preparation technique used resulted in high retention efficiency for both series. Nanofibre sheets alone have 98% fibre retention with 0.2 wt% fibre concentration because highly entangled network of fibres prevented fibres loss during the filtering process. The composites achieved high loadings (up to 77 wt%) as the majority of the NPs are strongly bounded to interconnecting cellulose fibres which provide a flexible material (Figure 1e).

Both MFC and SiO₂ are negatively charged with zeta potential of -26 mV and -29 mV, respectively. Retention of SiO₂ in an anionic matrix is unfavourable, particularly through filtration method. However, some methods such as spray coating [14] or layer-by-layer techniques [24] can force the adhesion of NPs onto the cellulose surface irrespective to charges. In such cases, retention is not an issue. Without a retention aid such as CPAM, the retention is very low (Figure 2 triangles), however still maintained around 20% at 77 wt% loading.

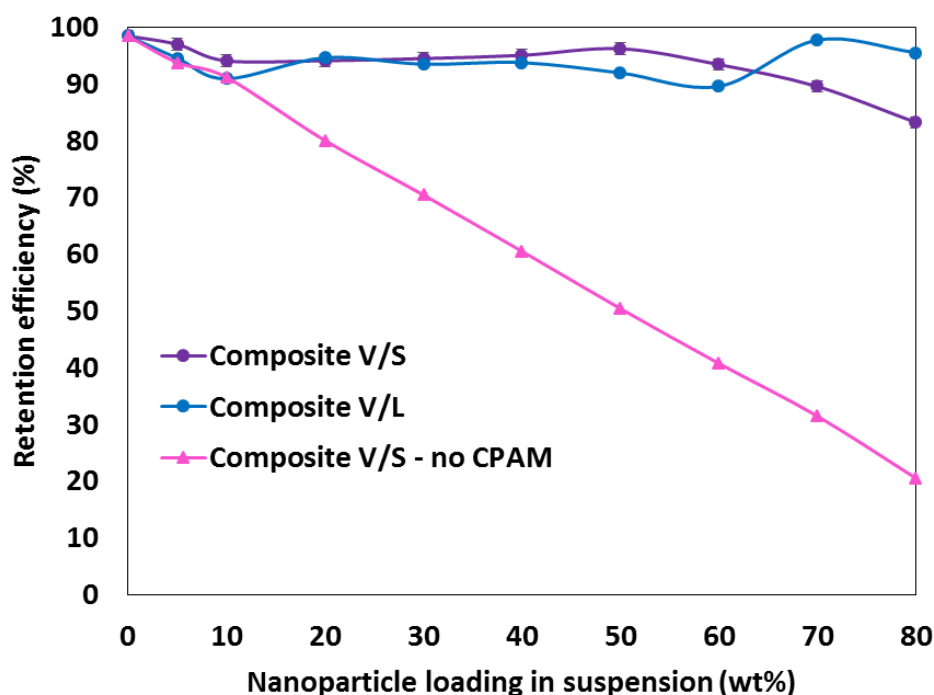


Figure 2: Retention of nanofibres and NPs in the composite as a function of initial NP loading.

SEM images of V/S composites with progressive increase of SiO₂ content are shown in Figure 3. SEM indicates that in the absence of NPs, nanofibres formed a highly interconnected, reasonably dense film with pores of irregular shapes (Figure 3a). The density without NP addition was 750 kg/m³ which is consistent with the previous data obtained on sheets from these fibres of 783 kg/m³ [25]. As the NP content progressively increased, the nanofibre's porous structure gets filled up by the NPs (Figure 3b-d). High NP content formed large NP-CPAM clusters which remained intact since there were no nanofibres seen in between clusters (Figure 3e). The aggregates are distributed uniformly in the nanofibre matrix. Beyond a certain NP content, the aggregates became larger than the inter-fibrous pores, thus embedding into nanofibre matrix caused

nanofibres to push apart, de-structuring the nanofibre matrix into a packed bed structure. Hence, NP content between 5-40 wt% (low loading) gives one regime where the role of NPs is to fill the gaps in the nanofibre network. NP content between 50-77 wt% (high loading) represents another regime where NP clusters form a much tighter controlled pore structure (Figure 3e-g). This behaviour is schematically illustrated in Figure 4. Figure 3h-i shows SEM images of 60 wt% and 77 wt% respectively at low magnifications. SEM images for V/L composites can be found in Appendix I Figure A2. The transition point from one regime to the other varied for V/S and V/L composite, probably due to the size difference in NPs. These images are significant as they show a new packing arrangement of SiO₂ in the nanofibre matrix. SEM demonstrates that incorporation of silica NPs as complexes is an effective way of controlling the pore structure and achieving high surface area from the NPs. At very high NP content, the surface area of the composite obtained from mercury porosimetry analysis almost doubled (33 m²/g for pure nanofibre sheet, 80 m²/g and 70 m²/g at 70 wt% V/S and V/L composites, respectively).

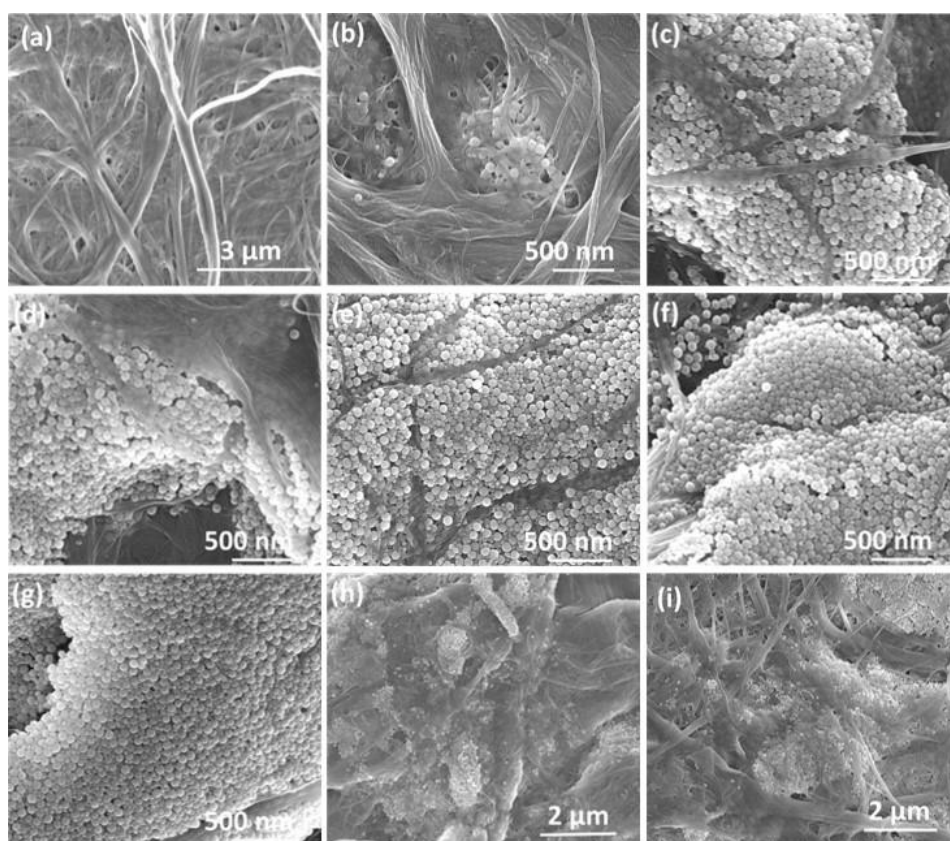


Figure 3: SEM images of nanofibre composite (V/S) with a) nanofibre sheet alone, b) 20 wt%, c) 30 wt%, d) 40 wt%, e) 50 wt%, f) 60 wt%, g) 77 wt% NPs, respectively at high magnification, h) 60 wt%, i) 77 wt% NPs, respectively at low magnifications.

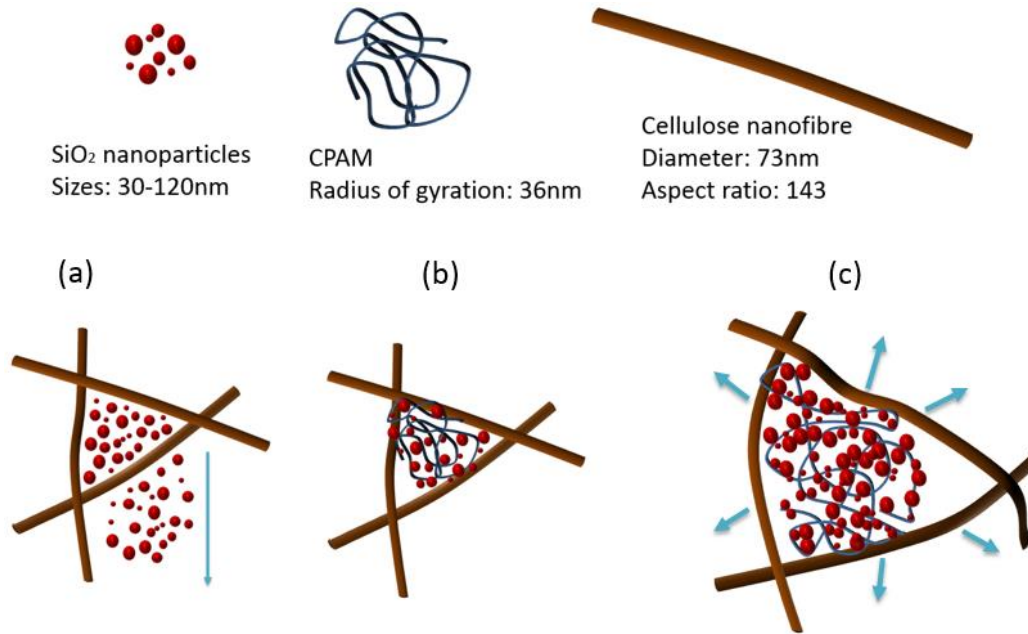


Figure 4: Schematic mechanism of NP and CPAM hetero-coagulation with nanocellulose (not to scale). (a) No CPAM: NPs flow through the gap (indicated by the arrow) (b) With CPAM at low NP loading: CPAM bridges NPs with cellulose nanofibres (NPs retain in the gap). (c) With CPAM at high NP loading: Large NP-CPAM structure pushes nanofibres to fit the gap, creating a packed bed structure. Arrows indicate the movement of fibres from the initial position.

Thickness variation also supports the de-structuring described through SEM images (Figure 5a). Initially, the thickness increased slowly for V/S and V/L with NP addition level, but both series showed a transition point where the slope of the data increased. This happened at 50 wt% for V/L and 60 wt% for V/S composites by deforming the structure. Previous work published by us used small angle X-ray scattering (SAXS) to quantify the structure of silica NP/MFC/CPAM system which gives statistical measurements on the structure [26]. The paper explains that the higher CPAM dosage gives bigger/bulk NP clusters. Therefore, high dosage of CPAM (0.5 mg/m²) was used in this study and as a result, SiO₂ NPs formed big clusters and retained in the structure, which contributed to almost double increase in thickness compared to a pure nanofibre sheet. The fractional density data is shown in (Figure 5b). The fractional density is the fraction of the maximum density achievable if all the pores are removed. Constant fractional density throughout the NP loading indicates the structure has a constant void volume; however, the nature of the volume changes.

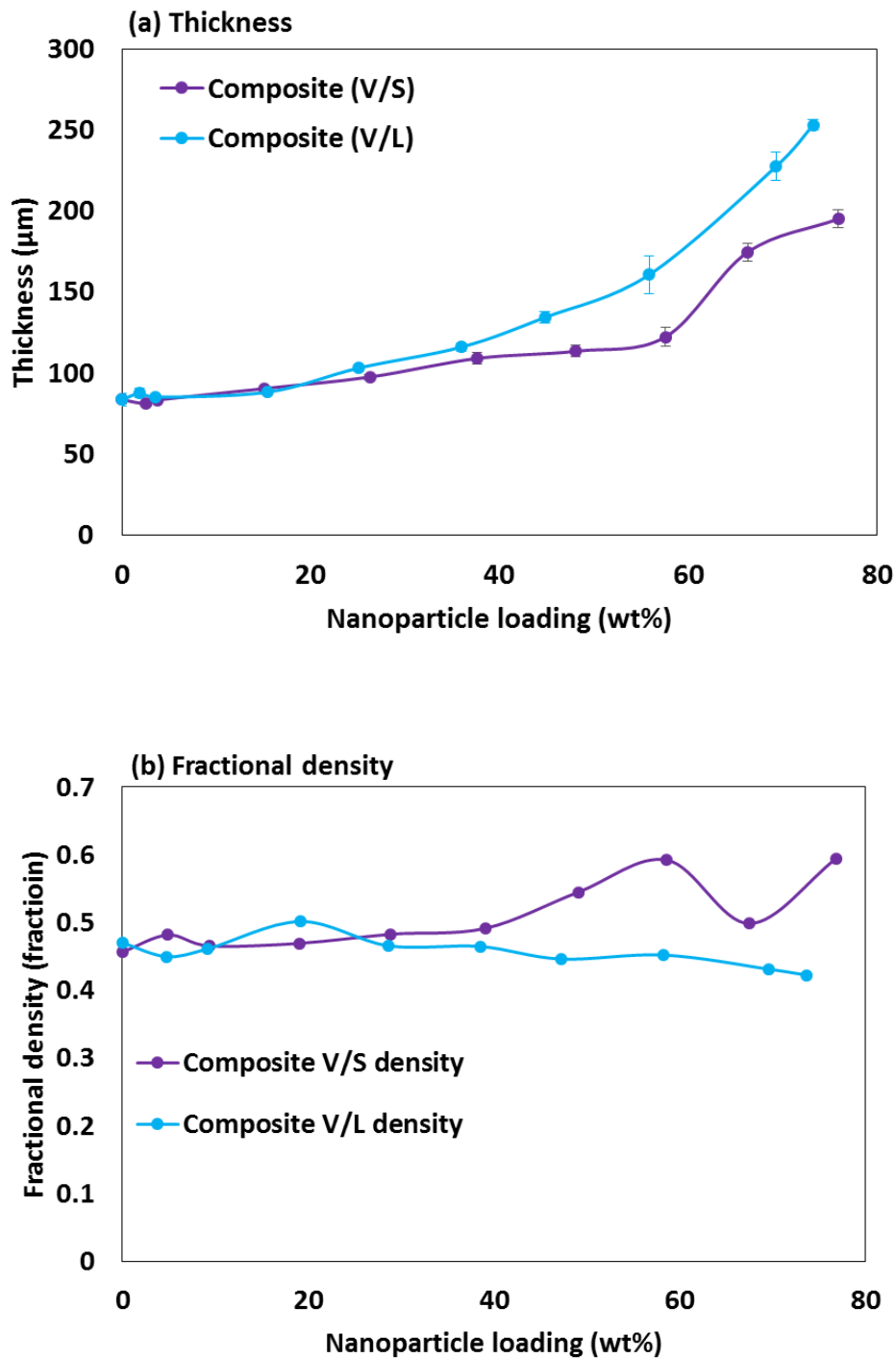
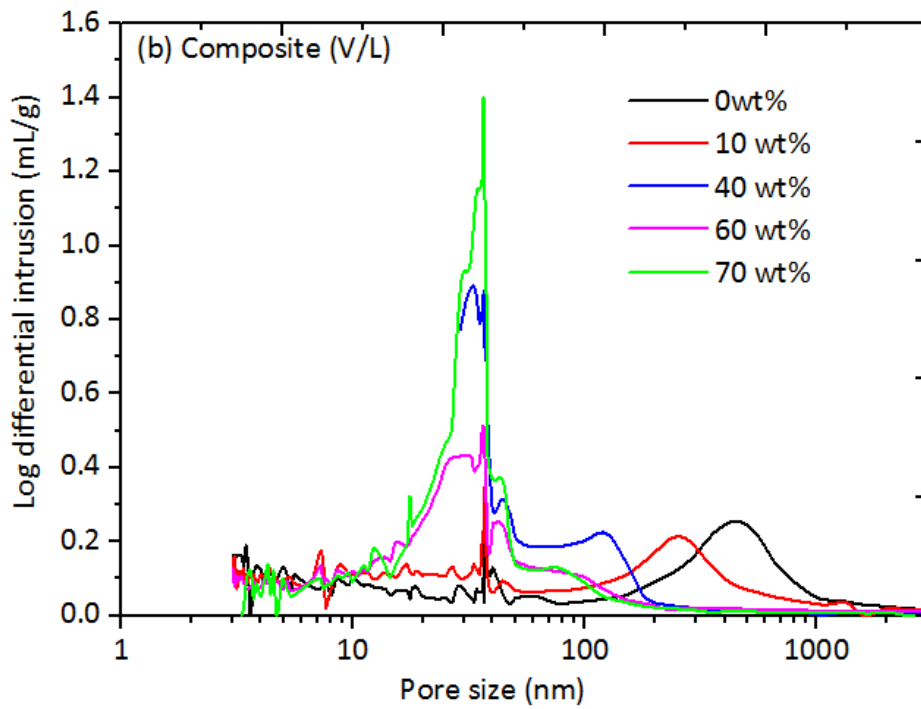
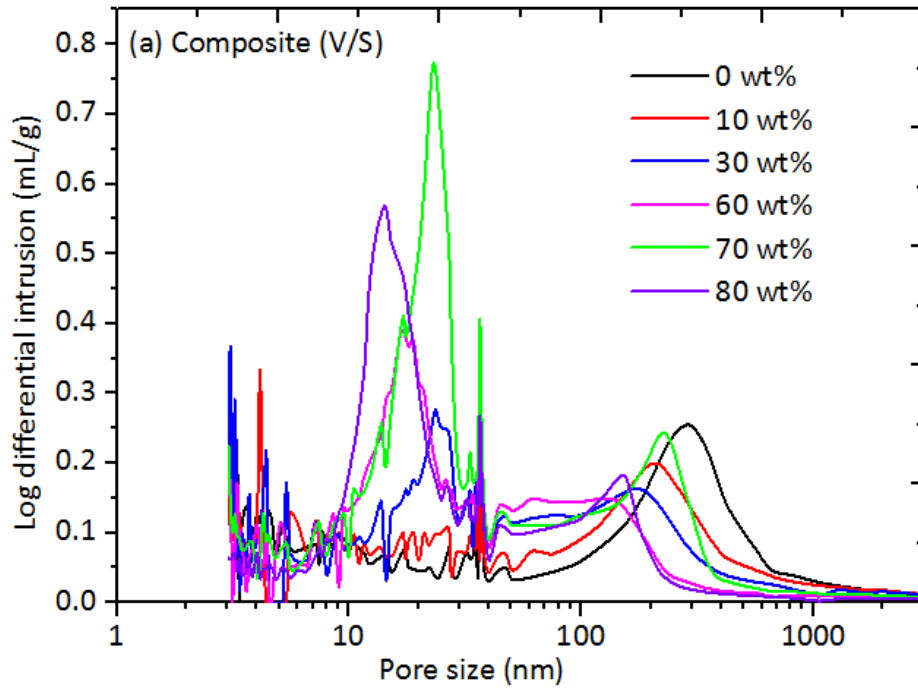


Figure 5: (a) Thickness and (b) fractional density of composites as a function of NP loading. Error bars in thickness graph are the standard deviations.

Pore structure quantified through mercury porosimetry shows that pure nanofibre sheet has a broad pore range between 100-1000 nm, which arises from the pores between the nonwoven fibre structure (Figure 6). A significant change in pore structure was then observed with SiO_2 NP

addition. With the subsequent increase in NP content, not only the broad peak from nanofibres reduced in width, but also the pore size range shifted to smaller range. In addition, a new peak is observed between 10-60 nm, which continuously increased in size with NP content because these represents the pores present within NP clusters and number of clusters increased with NP content. The pore volume inside the graph represents the number of pores present with the same pore diameter. Plotting that for lower (3-100 nm) and higher (100-1000 nm) diameter range indicates that the number of pores in smaller pore range increases with SiO₂ loading while the number of pores in larger pore range decreases (Figure 7). This signifies that large pore size range is controlled by SiO₂. SiO₂ addition in nanocellulose composites creates a more developed pore structure.

Pore size distribution pattern for V/L (Figure 6b) differs from V/S (Figure 6a). At low loadings for V/L series (SiO₂ = 10 wt%), the overall pore structure does not deviate much from that of pure nanofibres. However, at high loadings V/L series reduced the pore size by almost a magnitude compared to V/S. Bimodal structure changed to a single peak with low pore size, indicating a more compact and much tighter control of pore size distribution. It is not clear why these two composites behave differently; this is possibly due to NP size difference. A drawback of the mercury porosimetry method is that it only measures pores of size larger than 3 nm. However, this is of little consequence as the applications targeted for these composites is in the separation of larger particles – especially bacteria and food based colloids- which are orders of magnitude larger than the 3 nm detection limit.



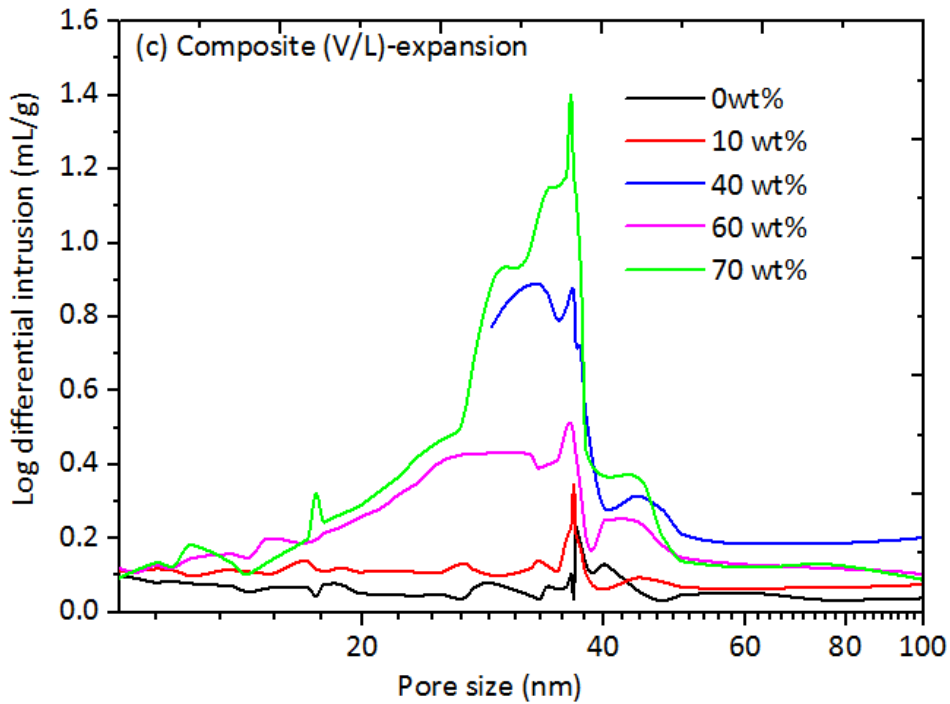
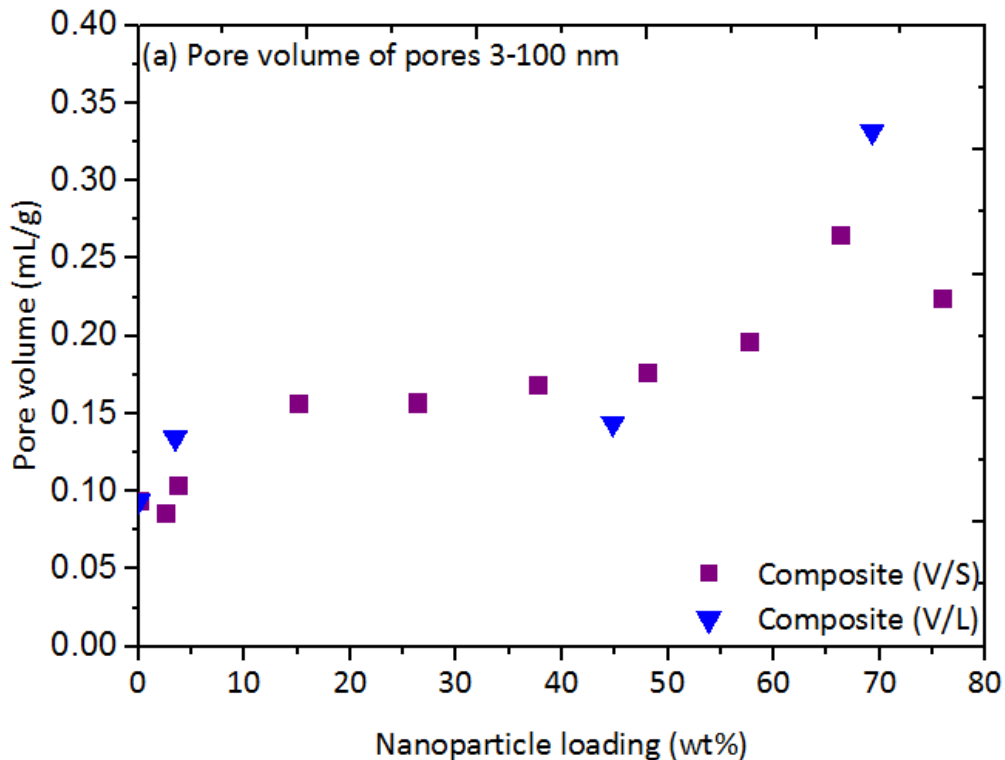


Figure 6: Pore size distribution for nanocellulose- SiO₂ composite sheets as a function of silica content. (a) V/S (smaller NPs), (b) V/L (larger NPs), (c) enlarged graph of V/L composite between 10-100 nm. The legend indicates the NP loading added in the suspension.



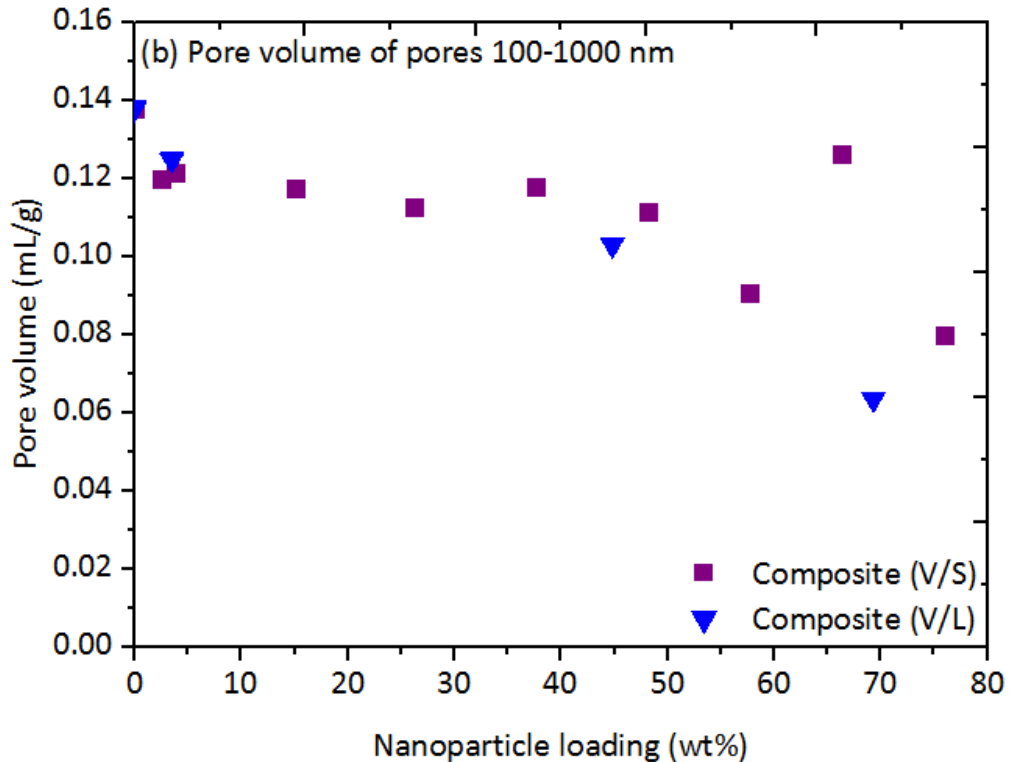


Figure 7: Composite pore volume as a function of NP loading. (a) Total pore volume for small pores (3-100nm). (b) Total pore volume for large pores (100-1000nm).

The strength is significantly important in composites because a composite with very high loading and retention becomes redundant if the strength of the material is poor. The silica NPs are not expected to contribute significantly to strength. Indeed, for sheets made from conventional cellulose fibres, the addition of inorganic filler particles significantly reduces strength, as the inorganic particles interfere with the bonding between the fibres.

Figure 8 shows the curves of tensile index (TI) versus strain based on nanofibre grammage for V/S composites. Tensile index here is calculated as $TI = F / (w \cdot G)$, where F is the breaking force, w is the test specimen width of 15 mm and G is the nanofibre grammage in g/m^2 . Since mass of nanofibres used is same in all composites (1.2 g, $60 g/m^2$), the force versus strain graph is identical outside a scaling factor.

The results in Figure 8 are extremely interesting. While the strain at break reduced from 5.8% for the unloaded sample to 2.8% at 77 wt% loading, there was very little change in the tensile index based on nanofibres grammage, which was maintained in the range of 70-80 Nm/g.

It is likely that the strain at break is reduced because at high loadings the fibres are completely surrounded by NPs and are not free to rearrange themselves to accommodate an applied load, thus significantly reducing the plastic deformation occurring just before fracture. The same breaking load for all composites indicates that firstly, that the NPs do not contribute to the strength and they are only filling the gaps in the fibres, but surprisingly, the NPs do not interfere with the bonding between the fibres. This is an extremely interesting finding and the mechanisms should be explored further. The initial slope, in the elastic region, is similar for all the loadings except for 60 wt% onwards. This is at the point where the fibre structure changed as mentioned above. The measured mean elastic modulus and tensile stiffness index for nanofibre sheet alone was 4.8 GPa and 4582 Nm/g respectively, while 77 wt% sheet was 3.8 GPa and 6130 Nm/g respectively. Thus, novel composite maintain the strength even at high loadings, highlights promising mechanical properties.

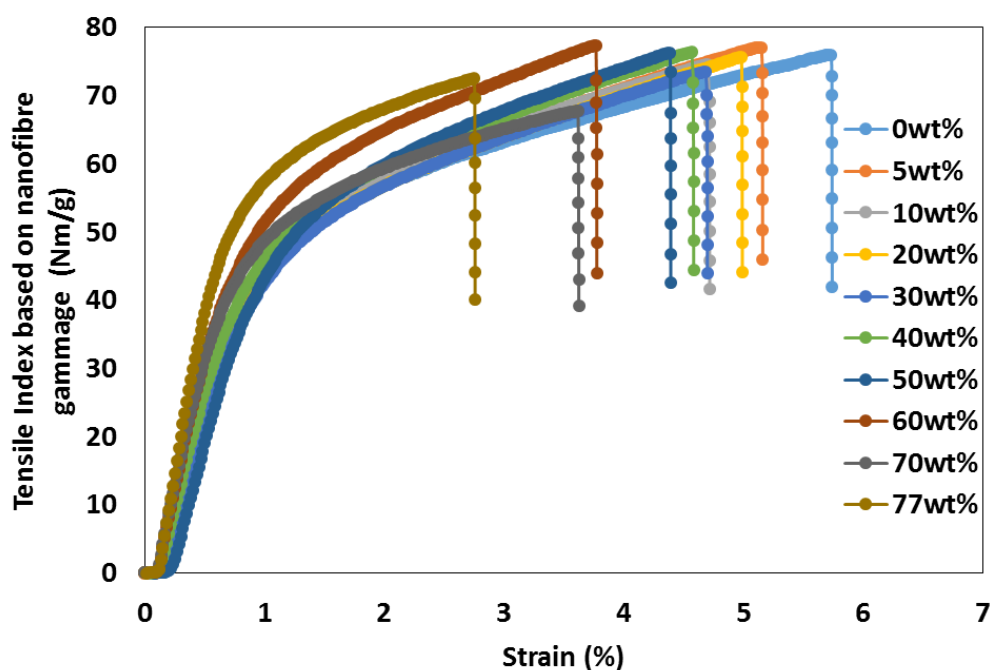


Figure 8: Tensile index based on nanofibre grammage on strain for V/S composite.

SEM and structure analysis demonstrated that the MFC-SiO₂ composites produced to be a new type of fibrous composites of very high NP loading and unique packing arrangement. With their good strength, flexibility and tuneable pore structure, this new material is promising as membrane

in applications such as pasteurization and other food processing, separators in batteries [14, 18], water treatment [13].

2.6 CONCLUSION

New MFC-SiO₂ flexible composite films with high surface area and tuneable pore structure were developed using a process combining controlled simultaneous addition (CSA) with standard filtration. This process is easily scalable for industrial applications. Anionic NP loading up to 77 wt% was achieved at high nanoparticle (NP) retention by forming NP-polyelectrolyte complexes. For the low levels of NP loading, the NP clusters simply filled the gaps created by the nanofibre porous structure. At this point, there was no significant change in composite film thickness observed. At high levels of NP loading, the NP clusters become too large for the available pores and the nanofibre matrix de-structured while accommodating these clusters by pushing fibres apart. This results in composites having a packed bed type structure. Composite film thickness at higher NP loadings therefore increased significantly. Composite pore size distribution analysis reveals that the material has a tuneable pore structure (100-1000 microns to 10-60 nanometers) controlled by NP content. At higher loadings much tighter and controlled pores structure could be obtained. Tensile index based on nanofibres alone for all the composites remained between 70-80 Nm/g even at higher loadings, suggesting that NPs do not contribute to the strength. Therefore, the strength is maintained.

Well-developed and highly flexible new nanocellulose composite materials of high NP loading distributed in a unique packing arrangement were produced with a process insuring high NP retention. The composite process is scalable to develop a platform for the preparation of very high surface area, functionalised porous materials with industrial applications as filters, absorbents and catalysts.

2.7 ACKNOWLEDGEMENTS

Thanks to MCEM for scanning electron microscopy and Scot Sharman for technical help. The authors acknowledge the financial support from Australian research council, Australian paper, Carter Holt Harvey, Circa, Norske Skog, and Visy through the Industry Transformation Research Hub grant IH130100016. UG thanks Monash University for MGS and FEIPRS scholarships.

2.8 REFERENCES

1. Schaefer, D.W. and R.S. Justice, *How nano are nanocomposites?* *Macromolecules*, 2007. **40**(24): p. 8501-8517.
2. Winey, K.I. and R.A. Vaia, *Polymer nanocomposites*. *MRS bulletin*, 2007. **32**(04): p. 314-322.
3. Kausch, H. and G. Michler, *Effect of nanoparticle size and size - distribution on mechanical behavior of filled amorphous thermoplastic polymers*. *Journal of applied polymer science*, 2007. **105**(5): p. 2577-2587.
4. Oksman, K., et al., *Manufacturing process of cellulose whiskers/poly(lactic acid) nanocomposites*. *Composites science and technology*, 2006. **66**(15): p. 2776-2784.
5. Kim, J., S. Yun, and Z. Ounaies, *Discovery of cellulose as a smart material*. *Macromolecules*, 2006. **39**(12): p. 4202-4206.
6. Sehaqui, H., et al., *Fast preparation procedure for large, flat cellulose and cellulose/inorganic nanopaper structures*. *Biomacromolecules*, 2010. **11**(9): p. 2195-2198.
7. Klemm, D., et al., *Nanocelluloses as innovative polymers in research and application, in Polysaccharides II*. 2006, Springer. p. 49-96.
8. Farhang, B., *Nanotechnology and lipids*. *Lipid Technology*, 2007. **19**(6): p. 132-135.
9. Sehaqui, H., T. Zimmermann, and P. Tingaut, *Hydrophobic cellulose nanopaper through a mild esterification procedure*. *Cellulose*, 2014. **21**(1): p. 367-382.
10. Korhonen, J.T., et al., *Hydrophobic nanocellulose aerogels as floating, sustainable, reusable, and recyclable oil absorbents*. *ACS applied materials & interfaces*, 2011. **3**(6): p. 1813-1816.
11. Sehaqui, H., et al., *Stretchable and strong cellulose nanopaper structures based on polymer-coated nanofiber networks: an alternative to nonwoven porous membranes from electrospinning*. *Biomacromolecules*, 2012. **13**(11): p. 3661-3667.
12. Tingaut, P., T. Zimmermann, and F. Lopez-Suevos, *Synthesis and characterization of bionanocomposites with tunable properties from poly (lactic acid) and acetylated microfibrillated cellulose*. *Biomacromolecules*, 2009. **11**(2): p. 454-464.

-
13. Varanasi, S., Z.-X. Low, and W. Batchelor, *Cellulose nanofibre composite membranes–Biodegradable and recyclable UF membranes*. Chemical Engineering Journal, 2015. **265**: p. 138-146.
 14. Krol, L.F., et al., *Microfibrillated cellulose-SiO₂ composite nanopapers produced by spray deposition*. Journal of Materials Science, 2015. **50**(11): p. 4095-4103.
 15. Liu, A., et al., *Clay Nanopaper with Tough Cellulose Nanofiber Matrix for Fire Retardancy and Gas Barrier Functions*. Biomacromolecules, 2011. **12**(3): p. 633-641.
 16. Slowing, I.I., et al., *Mesoporous silica nanoparticles for drug delivery and biosensing applications*. Advanced Functional Materials, 2007. **17**(8): p. 1225-1236.
 17. Lu, J., et al., *Mesoporous silica nanoparticles as a delivery system for hydrophobic anticancer drugs*. Small, 2007. **3**(8): p. 1341-1346.
 18. Kim, J.-H., et al., *Colloidal silica nanoparticle-assisted structural control of cellulose nanofiber paper separators for lithium-ion batteries*. Journal of Power Sources, 2013. **242**: p. 533-540.
 19. Garusinghe, U.M., et al., *Assembly of nanoparticles-polyelectrolyte complexes in nanofiber cellulose structures*. Colloids and Surfaces A: Physicochemical and Engineering Aspects, 2016.
 20. Varanasi, S., R. He, and W. Batchelor, *Estimation of cellulose nanofibre aspect ratio from measurements of fibre suspension gel point*. Cellulose, 2013. **20**(4): p. 1885-1896.
 21. Li, Q., et al., *Engineering cellulose nanofibre suspensions to control filtration resistance and sheet permeability*. Cellulose, 2016. **23**(1): p. 391-402.
 22. Ngo, Y.H., et al., *Effect of cationic polyacrylamide dissolution on the adsorption state of gold nanoparticles on paper and their Surface Enhanced Raman Scattering properties*. Colloids and Surfaces A: Physicochemical and Engineering Aspects, 2013. **420**: p. 46-52.
 23. Bringley, J.F., et al., *Controlled, simultaneous assembly of polyethylenimine onto nanoparticle silica colloids*. Langmuir, 2006. **22**(9): p. 4198-4207.
-

24. Li, H., S. Fu, and L. Peng, *Surface modification of cellulose fibers by layer-by-layer self-assembly of lignosulfonates and TiO₂ nanoparticles: Effect on photocatalytic abilities and paper properties*. *Fibers and Polymers*, 2013. **14**(11): p. 1794-1802.
25. Varanasi, S., H.H. Chiam, and W. Batchelor, *Application and interpretation of zero and short-span testing on nanofibre sheet materials*. *Nordic Pulp and Paper Research Journal*, 2012. **27**(2): p. 343.
26. Garusinghe, U.M., et al., *Assembly of nanoparticles-polyelectrolyte complexes in nanofiber cellulose structures*. *Colloids and Surfaces A: Physicochemical and Engineering Aspects*, 2017. **513**: p. 373-379.

CHAPTER 3

INVESTIGATING SILICA NANOPARTICLE – POLYELECTROLYTE STRUCTURES IN MICROFIBRILLATED CELLULOSE FILMS BY SCATTERING TECHNIQUES

THIS PAGE HAS BEEN INTENTIONALLY LEFT BLANK

PREFACE

In the previous chapter, a cationic polyelectrolyte (CPAM), SiO₂ nanoparticles (NPs) with two different sizes and microfibrillated cellulose (MFC) was combined together through simultaneous addition (CSA) method to produce nanocomposites. The effect of NP loading and the NP sizes on the variation in structure and properties were quantified. It was observed that CPAM retains the NPs in the nanocellulose structure. Scanning electron microscopy (SEM) used to characterize the structure was limited in application because the interaction between NPs and CPAM could not be quantified. Understanding how NPs behave in the presence of a polyelectrolyte is crucial to better engineer composites.

This chapter therefore explores the interaction between CPAM and SiO₂ NPs using two complimentary techniques; dynamic light scattering (DLS) and small angle X-ray scattering (SAXS). DLS was used to quantify the conformation and changes in hydrodynamic radius of CPAM adsorbed on the surface of SiO₂ NPs. SAXS was used to obtain the structural assembly of 8 nm SiO₂ NPs under the influence of different CPAM concentrations.

This chapter follows the second objective.

THIS PAGE HAS BEEN INTENTIONALLY LEFT BLANK

CHAPTER 3 INVESTIGATING SILICA NANOPARTICLE – POLYELECTROLYTE STRUCTURES IN MICROFIBRILLATED CELLULOSE FILMS BY SCATTERING TECHNIQUES

3.1 Abstract	115
3.2 Keywords	115
3.3 Introduction	116
3.4 Experimental	117
3.4.1 Material	117
3.4.2 Method	117
3.4.2.1 Preparation of MFC, CPAM and silica NP suspensions	117
3.4.2.2 Preparation of pure MFC sheet	118
3.4.2.3 Preparation of CPAM-silica NP suspension for DLS	118
3.4.2.4 Preparation of MFC-CPAM-SiO ₂ composite for SAXS	118
3.4.3 Characterization	119
3.4.3.1 Dynamic light scattering	119
3.4.3.2 Small angle X-ray scattering	119
3.4.3.3 Scanning electron microscopy	119
3.5 Results and discussion	119
3.5.1 Scanning electron microscopy of MFC-SiO ₂ -CPAM composite sheets	119
3.5.2 Dynamic light scattering on CPAM-NP-suspensions	120
3.5.3 Small angle X-ray scattering on MFC-NP-CPAM composite sheets	122
3.6 Conclusion	126
3.7 Acknowledgement	127
3.8 References	127

THIS PAGE HAS BEEN INTENTIONALLY LEFT BLANK

INVESTIGATING SILICA NANOPARTICLE – POLYELECTROLYTE STRUCTURES IN MICROFIBRILLATED CELLULOSE FILMS BY SCATTERING TECHNIQUES

**Uthpala Garusinghe, Vikram Singh Raghuvanshi, Praveena Raj, Gil Garnier*, Warren
Batchelor***

BioResource Processing Research Institute of Australia (BioPRIA), Department of Chemical
Engineering, Monash University, Clayton 3800, VIC, Australia.

*Corresponding authors: [REDACTED]
[REDACTED]

3.1 ABSTRACT

We report the cationic polyelectrolyte (CPAM)-SiO₂ nanoparticle (NP) interactions in suspension and in a sheet form, when mixed with microfibrillated cellulose (MFC), using dynamic light scattering (DLS) and small angle X-ray scattering (SAXS) techniques. The CPAM-SiO₂ NP suspensions were prepared by adding NPs into CPAM drop wise and composites were prepared by adding CPAM-SiO₂ suspension into MFC and through standard paper making procedure. DLS revealed that increase in CPAM dosage creates larger sized CPAM-NP aggregates because more NPs can be picked up by stretched CPAM chains. SAXS study revealed that CPAM-SiO₂ NP assembly in the formed nanopaper fits well with a spherical core shell model (with SiO₂ partially covered with CPAM) and sphere model (SiO₂ alone) combined together. Understanding the interaction between polyelectrolyte-NP system through such scattering techniques enables us to engineer novel cellulose based composites for specific applications.

3.2 KEYWORDS

Dynamic light scattering (DLS), Small angle X-ray scattering (SAXS), Scanning electron microscopy (SEM), Structure, Solyelectrolyte-nanoparticle system, Cellulose

3.3 INTRODUCTION

Nanotechnology involves the manipulation or self-assembly of individual particles or their aggregates into desired configurations, to create materials and devices with new or vastly different properties and functions [1]. Nanoparticles (NPs) take an important role in nanotechnology because of their unique properties and can be selected for their chemical composition, but also can be tailored for their sizes, shape and surface properties [2]. NPs on their own cannot be used as they self-aggregate or pose the danger of uncontrolled release to the environment when dry. Therefore, ideally NPs need to be embedded into a matrix that is strong, flexible, and durable and also allows the surface area of NPs to be readily available.

Using nanocellulose as a supporting matrix combines the advantage of two constituents to give new composite materials with superior properties. Nanocellulose fibres are a new class of material that has received significant attention over the past decade. This material is of technological interest as it is renewable, biodegradable, exhibits excellent mechanical strength and superior barrier properties, while remaining fully compatible with conventional wood fibres [3]. However, embedding NPs into a nanocellulose matrix at times is difficult, especially when both materials are of same charge. In such cases, polyelectrolytes play an important role for the fixation of NPs onto surfaces in charged systems [4].

Polyelectrolytes play an important role in many industrial applications such as wastewater treatment[5], gene and drug delivery[6, 7], flocculation in paper making[5, 8], sensor development [9, 10], mineral processing[5] and coating processes [11]. This is due to their ability to adsorb at solid-liquid interfaces, thus, modifying surface properties and the interactions between particles and their environment [12]. The understanding of the interaction between polyelectrolytes and surfaces are crucial to optimise surface properties for a specific application. Polyelectrolytes and NPs are used in the papermaking industry as they act as retention aids, adhering fines and mineral fillers on the fibre surface [12-14], while at the laboratory scale polyelectrolytes have been shown to strongly interact with cellulose nanofibres, lowering the gel-point by bridging between fibres and increasing the flow through the fibre network during filtration [15]. Despite the numerous studies concerning the adsorption of polyelectrolytes onto charged NP surfaces which has been studied in the past using both theoretical [16-18] and experimental [4, 11, 12, 19] methods, their modes of action are poorly understood as they depend greatly on the type of polymer and

particles in the system [20]. The conformation of the adsorbed polyelectrolyte on the NP surface is still a largely unexplored subject.

In this paper we quantify the interaction between cationic polyacrylamide –SiO₂ NPs using two complimentary scattering techniques in order to engineer specific structures in the composite. Understanding on the behaviour of cationic dimethylamino-ethyl-methacrylate (CPAM) in SiO₂ nanoparticle (NP) suspension is crucial in production of cellulose-polyelectrolyte-NP based composite films for different applications. Dynamic light scattering (DLS) technique is used to investigate the conformation and changes in hydrodynamic radius of cationic polyacrylamide adsorbed on the surface of SiO₂ NPs. Small angle X-ray scattering (SAXS) technique is used to investigate the effect of CPAM concentration on the SiO₂ NP assemblies formed within the MFC matrix.

3.4 EXPERIMENTAL

3.4.1 Material

Microfibrillated cellulose (MFC) was purchased from DAICEL Chemical Industries Limited, Japan (Grade Celish KY-100G). MFC was supplied at 25 wt% solids content and stored at 5°C. MFC has a mean diameter of 73 nm and the aspect ratio of 142 [21]. Cationic dimethylamino-ethyl-methacrylate (CPAM) polymer with molecular weight 13 MDa and charge density 50% was kindly provided by AQUA+TECH, Switzerland from their SnowFlake Cationics range. 22 nm colloidal silica with surface area 220 m²/g was purchased from Sigma Aldrich at 30 wt% suspension.

3.4.2 Method

3.4.2.1 Preparation of MFC, CPAM and silica NP suspensions

A 3L disintegrator (Mavis Engineering Model No. 8522) was used to disperse 0.2 wt% MFC in deionized water at 15,000 propeller revolutions. 0.01 wt% CPAM suspension was prepared by mixing CPAM with deionized water for minimum of 8 hours prior to the experiments. SiO₂ NPs were diluted to 0.5 wt% from the stock solution using deionized water. The CPAM and SiO₂ NP solutions were sonicated for 2 minutes at 100% amplitude to ensure evenly distribution.

3.4.2.2 Preparation of pure MFC sheet

Sheets were prepared using a British handsheet maker (model T205) which is equipped with a woven filter with an average opening of 74 microns. 0.2 wt% pure MFC suspension was poured into the column and allowed water to drain under gravity. When the film was formed, it was taken out using blotting papers and dried at 105°C using a sheet drier.

3.4.2.3 Preparation of CPAM-silica NP suspension for DLS

0.5 wt% sonicated SiO₂ NP suspension was added through a peristaltic pump at 10 mL/min into the sonicated 0.01 wt% CPAM solution which was stirred at 200 rpm/min with a magnetic stirrer. Amount of SiO₂ NPs in the suspension was fixed at 0.3 g. The mixing process was repeated for three different surface coverages of CPAM to NPs (0.03, 0.05 and 0.09 mg CPAM/m² surface area of SiO₂ NPs). The concentration of the final suspension changes from 0.38-0.26 wt% depending upon CPAM dosage. This method of addition allowed SiO₂ NP suspension to be added drop by drop into the sonicated CPAM solution. Dynamic Light Scattering (DLS) was then used to measure the size of the NPs with adsorbed CPAM on its surface.

3.4.2.4 Preparation of MFC-CPAM-SiO₂ NP composite for SAXS

Preparation of composite sheets involved mixing MFC (1.2 g at 0.2 wt%), SiO₂ NPs (25 wt% of the total composite at 0.1 wt%) and CPAM (different ratios at 0.01 wt%) suspensions together simultaneously. While SiO₂ NPs and MFC used in composite sheets was fixed, four different CPAM dosages were used (0.07, 0.14, 0.2 and 0.5 mg CPAM/m² surface area of SiO₂ NPs). Firstly, CPAM and SiO₂ NP suspensions were mixed together into a beaker through simultaneous addition with two peristaltic pumps. Secondly, CPAM-SiO₂ NP suspension and MFC suspension was mixed again into a beaker through simultaneous addition with two peristaltic pumps to make the final composite suspension. Total mixing time was set to 8 minutes in each step. CPAM was added at different speeds (7.7 - 55 mL/min) depending on the dosage, SiO₂ was added at 50 mL/min and MFC was added at 75 mL/min. The final concentration of the suspension varied between 0.15-0.11 wt% depending on the CPAM dosage. Final suspension was poured into British handsheet maker for composite processing as mentioned above.

3.4.3 Characterization

3.4.3.1 Dynamic light scattering

CPAM- SiO₂ NP suspensions prepared above for dynamic light scattering (DLS) analysis were used as prepared to measure DLS with a Nanobrook Omni (Brookhaven Instruments) using a cuvette cell at 25°C. Diameter distribution of the clusters were calculated using the supplied software.

3.4.3.2 Small angle X-ray scattering

Small angle X-ray scattering (SAXS) measurements were conducted at the SAXS/WAXS beamline at the Australian Synchrotron, Melbourne [22]. Measurements were made in a transmission mode with the X-ray energy of 11 keV. Scattered photons were collected at detector distance of 7.2 m using the Pilatus 1 M detector (Dectris, Baden, Switzerland). The isotropic raw detector images were converted to intensity versus q , $|\vec{q}| = q = \frac{4\pi \sin \theta}{\lambda}$ where θ is the scattering angle and λ is the wavelength (0.113 nm) of incident X-rays. Data reduction with respect to the measurement geometry, masking dead pixels and the beam stop and a subtraction of air scatter were conducted using IDL based ScatterBrain software [23]. The scattered intensity is plotted as a function of the momentum transfer vector q . Data analysis was conducted by fitting the SAXS curves using the SASfit software.

3.4.3.3 Scanning electron microscopy

Scanning electron microscopy (SEM) analysis was performed using FEI Magellan 400 FEGSEM on the composites. Each sample was cut to 3 mm by 3 mm pieces and mounted onto a metal sample holder, coated with a thin layer of Iridium prior to imaging. Accelerating voltage was 3kV and current was 6.3 pA. The images were taken at 30000x and 100000x magnifications.

3.5 RESULTS AND DISCUSSION

3.5.1 Scanning Electron Microscopy of MFC-SiO₂-CPAM composite sheets

Figure 1a shows a scanning electron microscopy (SEM) image of a pure MFC sheet. A wide distribution of pore sizes can be observed. Figure 1b shows SEM images of a MFC with 0.5 mg/m² CPAM dosage on 22 nm SiO₂ NPs respectively. NPs seem to accommodate themselves to the gaps

created by the MFC fibres and fill up without altering the fibre network. While qualitative information can be obtained from SEM, is difficult to fully characterise the samples with SEM alone as 1) SEM images are from a selected area and it does not give enough information about the local distribution of NPs in the matrix, 2) SEM only show the NPs which are on the surface, 3) the interaction or the type of distribution between CPAM-SiO₂ NPs cannot be properly understood or seen. Therefore, SEM alone is not good enough to properly investigate a polyelectrolyte-NP system to optimise performance. Scattering techniques such as DLS and SAXS are useful in obtaining further information on the internal structure of the material in the 1 to 100 nm length scale.

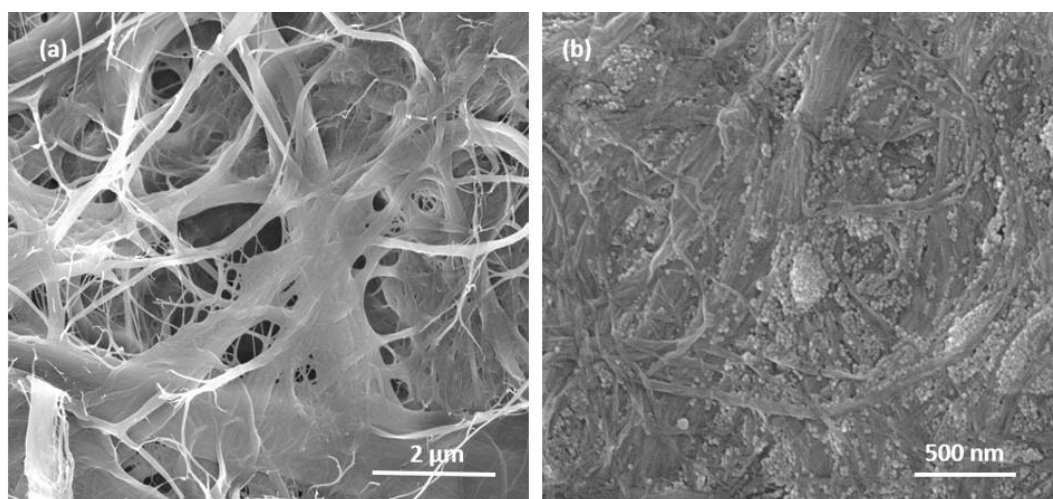


Figure 1: Scanning electron microscopy (SEM) images (a) pure MFC sheet (b) MFC-22nm SiO₂-0.5mg/m² CPAM composite at high magnification.

3.5.2 Dynamic light scattering on CPAM-NP suspensions

Dynamic light scattering (DLS) experiments were conducted to reveal the interaction between SiO₂ NPs and CPAM with respect to different dosages of CPAM. Figure 2a shows the correlation curves for pure SiO₂ NPs and NPs with two different dosages of CPAM (0.03 mg/m² and 0.05 mg/m²). The correlation curve decays at a slower rate with increase in CPAM dosages. For pure NPs the correlation curve decays at around 200 μsec while for the higher CPAM dosage (0.05 mg/m²) the correlation curve decays at 3000 μsec. This corresponds to CPAM adsorption onto the SiO₂ NPs which results in formation of aggregates and reduce the diffusion rate of aggregated particles. Distribution of the NPs and NP aggregates obtained from DLS are shown in the Figure 2b.

The radius of gyration of CPAM with 13 MDa, without accounting for the charged groups is 38 nm when calculated theoretically using the random walk model [24]. Polyelectrolytes with a low charged density have a coiled conformation in solution with smaller diameters which is characterised by a random walk much the same as non-charged polymers in a solvent [25, 26]. Highly charged polymers have stretched out or extended conformations in solution which is due to the closely spaced charged sites resulting in larger diameters [25, 26]. Thus, the actual radius of gyration of CPAM that when stretched out due to repulsion between charged groups on the polymer segment is much larger. In this work, we have used 50% charge density and that is considered fairly high. Therefore, CPAM used in this work is expected to be stretched out and have a more extended conformation on the surface.

Two distinct peaks are seen for each dosage of CPAM in Figure 2b. There is no significant difference in the diameter with increase in CPAM dosage for Peak 1, which has a maximum in the range 19 nm to 23 nm, consistent with measurements of single particles. However, the intensity of Peak 1 reduces when CPAM dosage increased from 0.05 mg/m² onwards, suggesting that number of single SiO₂ NPs that have not formed agglomerates are reducing as the dosage of CPAM increases. With increasing CPAM dosage, the second peak shifted to higher diameters. At 0.003 mg/m² (lower dosage), Peak 2 appeared at 85 nm. This peak shifted to 178 nm and 193 nm with 0.05 mg/m² and 0.09 mg/m² (higher dosages), respectively. This could be due to more stretched out configuration of the polymer causing a high probability of SiO₂ NPs to be picked up and forming larger agglomerates.

However, using DLS as a scattering technique is difficult for higher dosages of CPAM as DLS does not give reliable results when higher amount of polymer is added. At higher doses without a fibre matrix, isolated particles tend to agglomerate into much bigger clusters when compared to being in the sheet form. This is because when CPAM-NP is mixed with MFC to form sheets, fibres has an influence on the size of aggregations and stop bigger agglomerations from forming. Therefore, SAXS is a more suitable scattering technique to measure the particle interactions at higher CPAM dosages.

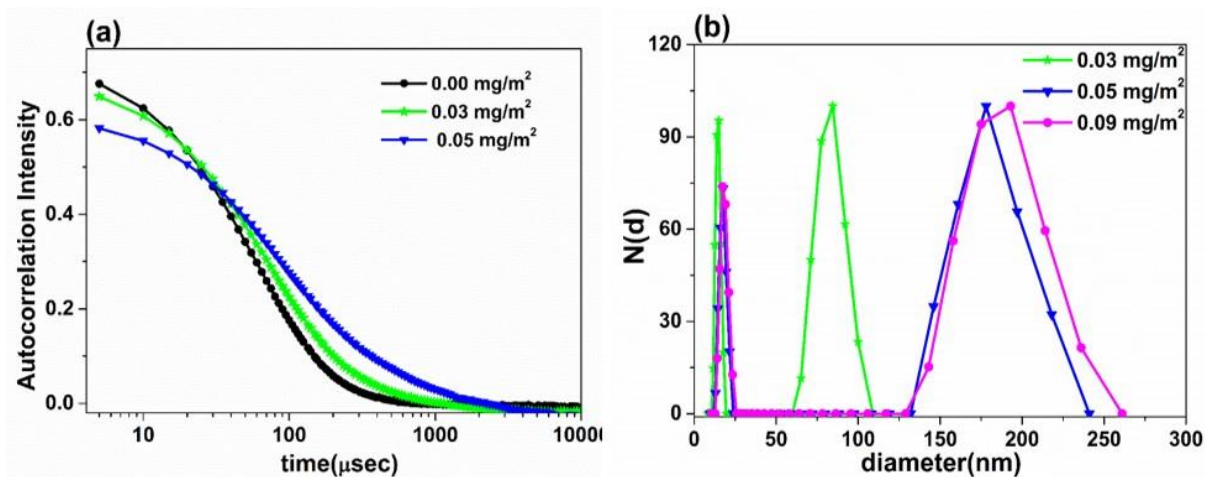


Figure 2: (a) Auto correlation curves of Pure SiO₂ NPs and SiO₂ with CPAM concentration of 0.03 mg/m² and 0.05 mg/m². (b) Diameter distribution obtained from DLS for SiO₂ NPs with CPAM concentration of 0.03 mg/m², 0.05 mg/m² and 0.09 mg/m².

2.5.3 Small angle X-ray scattering on MFC-NP-CPAM composite sheets

Small angle X-ray scattering (SAXS) is a powerful method to give information on the shape, size, distribution of NPs in different kind of matrices [27-31]. SAXS experiments were performed to investigate the effect of CPAM on the dispersion of SiO₂ NPs in the MFC fibre matrix. Figure 3a shows the SAXS curve from the MFC sheet. No features were observed in SAXS curve which is due to the presence of large structure of MFC fibres with large pore sizes as seen in Figure 1a. Figure 3b shows the fitted SAXS curves for the SiO₂ NPs with different dosages of CPAM (0.07-0.50 mg/m²; a higher range than the dosages used in DLS).

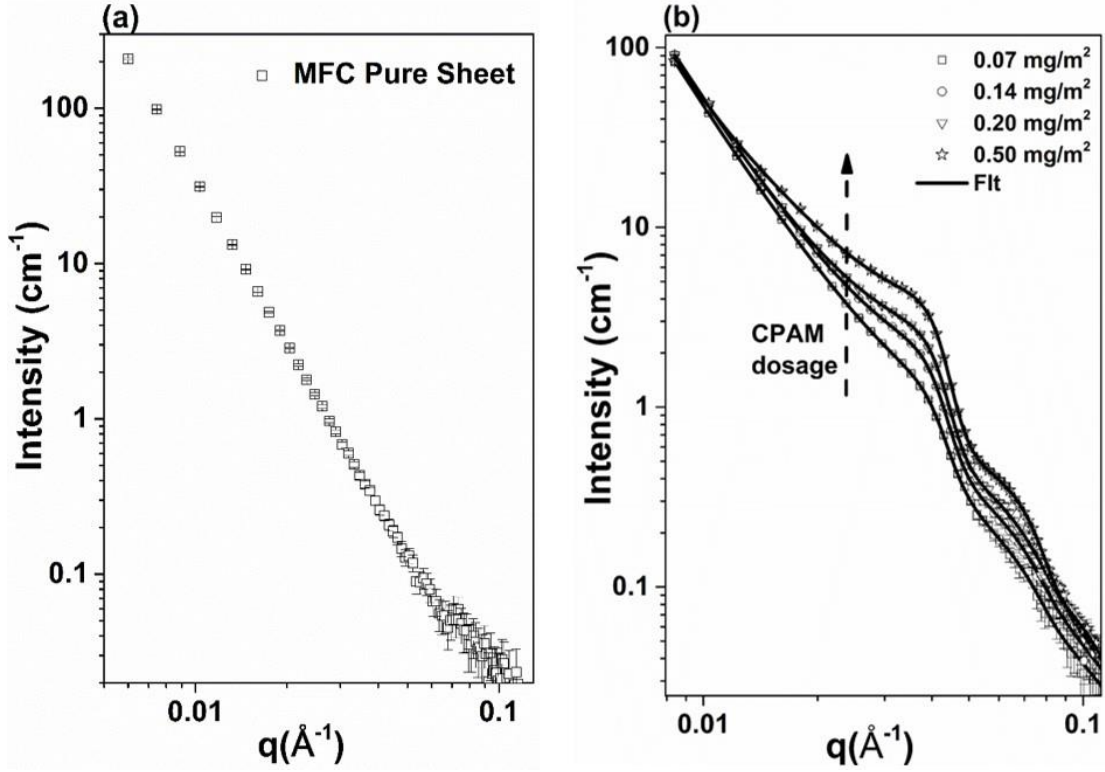


Figure 3: (a) SAXS curve for pure MFC sheet, (b) SAXS curves fitted with the core-shell and spherical models with different CPAM dosages.

Further information from the SAXS curves (Figure 3b) were extracted by nonlinear fitting using combination of different form factor and structure factor using the software SASfit [32]. The total SAXS scattering intensity can be given as:

$$I_{SAXS}(\bar{q}) = \int_0^{\infty} N(r) |F(q, r, \Delta\eta)|^2 S(q, r) dr + Bkg + C^{-\alpha} \quad (1)$$

Where, $N(r)$ is the particle number distribution, $F(q, r, \Delta\eta)$ is the structure model which contains information about shape and size of the particles. In the structure model, $\Delta\eta$ is the effective electron density difference between the particle and the remaining matrix, q is the transferred momentum, $S(q, r)$ is the structure factor contains information on the interaction between the particle and Bkg is the background with the surface scattering term.

The form factor with the combination of the spherical core shell particle and the spherical particle with the lognormal size distribution fits well for all the scattering curves (Figure 3b). The form factor is defined as:

$$F(q, r, \Delta\eta) = F_{sphereshell}(q, r_i, \Delta\eta_s) + F_{sphere}(q, r_i, \Delta\eta_s) \quad (2)$$

Where the F_{sphere} is the form factor of sphere as:

$$F_{\text{sphere}}(q, r, \Delta\eta) = 3\Delta\eta \frac{\sin(qr) - (qr)\cos(qr)}{(qr)^3} \quad (3)$$

And $F_{\text{sphere shell}}$ is the form factor for spherical core shell particles and given as:

$$F_{\text{sphere shell}}(q, r_t, \Delta\eta_s, \nu, \mu) = F_{\text{sphere}}(q, r_t, \Delta\eta_s) - F_{\text{sphere}}(q, \nu r_t, \Delta\eta_s(1 - \mu)) \quad (4)$$

Where, r_t is the radius of the core (SiO_2) + shell (CPAM), which is related to the core radius as $r = \nu r_t$ ($0 < \nu < 1$). $\Delta\eta_s = \eta_{\text{shell}} - \eta_{\text{matrix}}$ is the effective electron density difference between shell and matrix and $\mu\Delta\eta_s$ is the effective electron density difference between the core and the matrix. Additionally, the structure factor was included into the fitting procedure [33, 34]. While fitting a SAXS curve, all the structure determining parameters, size distribution parameters, structure factor parameters and the contrast of the particles were free fitting variables.

The obtained parameters show the average SiO_2 particle diameter of 22 ± 3 nm and thickness of the CPAM layer adsorbed onto the SiO_2 NPs is about 5 ± 0.5 nm. The schematic of the electron density profile for the spherical core shell particle is given in the Figure 4a. It is found that the effective electron density of the core (SiO_2 ; density 2.4 g/cm^3) is larger than the cellulose matrix ($\text{C}_6\text{H}_{10}\text{O}_5$; density 1.5 g/cm^3). Moreover, the effective electron density of shell (CPAM, density: 1.1 g/cm^3) is smaller than the cellulose matrix

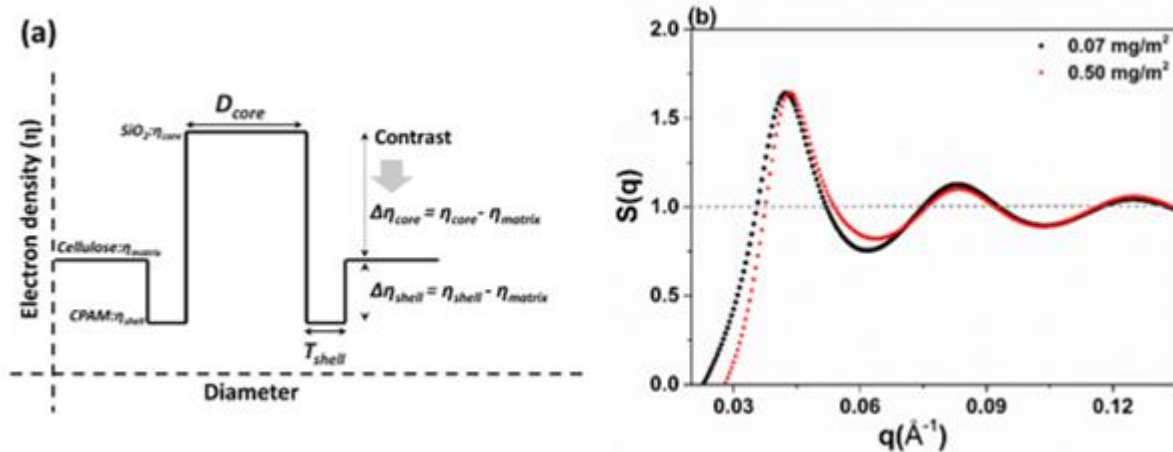


Figure 4: (a) Electron density variation profile for the spherical core shell particle with SiO_2 core, CPAM shell and cellulose matrix, (b) Structure factor obtained after fitting of the SAXS curve for the CPAM dosages of 0.07 mg/m^2 and 0.5 mg/m^2 .

The evaluated resultant structure factor for the two dosages of CPAM (0.07 mg/m² and 0.5 mg/m²) obtained after fitting the SAXS curve is given in Figure 4b. There is a small shift in the structure factor peak of high CPAM dosage (0.5 mg/m²) towards the higher q values with respect to the small CPAM dosage (0.07 mg/m²). The shift towards higher q values indicates a decrease in the inter-particle distance between the particles with the high dosage of CPAM. However, the difference is not significant and peak sharpness is also almost the same. This result reveals that with increase in CPAM dosage, the interaction between 22 nm SiO₂ NPs does not vary strongly.

Both SiO₂ NPs and MFC are negatively charged and therefore is difficult for SiO₂ to directly adsorb onto/within the cellulose matrix. CPAM is a positively charged polymer with the radius of gyration of 38 nm. CPAM acts as a bridge for SiO₂ NPs to be retained within the cellulose matrix. At low CPAM dosage, the CPAM adsorb onto the SiO₂ NPs surface and spread over the NP surface. It is difficult to identify whether CPAM totally covers the surface of NPs or partially cover the surface. In the case when the CPAM covers the surface of NPs completely, then the CPAM forms a positive shell like region over NPs surface. This will not allow NPs to form aggregates due to the electrostatic repulsion between NPs. In the DLS investigation, it was observed that even at the lowest CPAM dosage the NPs form aggregates. Therefore, it is expected that the CPAM partially covers the NPs surface. This results in distribution of both partly CPAM coated NPs and NPs without any CPAM. SAXS curves fits well with the proposed model of distribution of spherical shell (SiO₂ coated in a layer of CPAM) and sphere model (pure SiO₂). Increase in CPAM dosage results in increasing the number of SiO₂ NP aggregates. However, the interaction within the particles does not vary significantly and remain the same as observed by the variation in structure factor peak (Figure 4b).

22 nm SiO₂ NP behaves differently with CPAM compared to 8 nm SiO₂ NPs with CPAM which was published previously [14]. This could probably be due to the size difference between SiO₂ NPs. The structure factor reported for 8 nm SiO₂ NPs with increase in CPAM showed that structure factor sharpness increased and the peak shifted towards lower q value with respect to low CPAM dosage. This suggests that at low CPAM dosages, loosely bounded NP aggregates in the CPAM chain is formed because of the electrostatic repulsion between NPs, therefore the correlation length of the aggregates were about 25-30 nm in size. At high CPAM dosages, more CPAM is available to neutralize the NPs surface and overcome the electrostatic repulsion between NPs, therefore a

strong aggregations between NPs were obtained with a bigger correlation length of about 70 nm [14]. For 22 nm particles used in this study, with increase in CPAM dosages, only the number of structures increases and not the structure size. This proves that different length scales of NPs react differently in a polyelectrolyte system.

We conclude that SAXS technique is a better tool in investigating the polyelectrolyte-NP interactions when the polyelectrolyte concentration is higher. Overall, scattering techniques are essential tools in understanding the behavior of a polyelectrolyte-NP systems to better engineer the properties to develop nanocellulose-NP composites for varies applications.

3.6 CONCLUSION

Interaction between cationic dimethylamino-ethyl-methacrylate (CPAM) and SiO₂ nanoparticles (NPs) in suspension and in a microfibrillated cellulose (MFC) matrix was investigated using scattering methods. This study is beneficial in understanding a polyelectrolyte-NP system with respect to interactions between them, which cannot be obtained from techniques such as scanning electron microscopy (SEM).

Dynamic light scattering (DLS) shows aggregates of NPs at low dosage of CPAM (0.03 mg/m²) and aggregate size increased to larger sizes with increase in CPAM dosage further (0.05-0.09 mg/m²). It was noted that DLS results become unreliable when higher amount of polymer is added as DLS technique is sensitive to charge. Therefore, small angle X-ray (SAXS) techniques as well was used to characterize the system.

SAXS investigation revealed that the distribution of CPAM-NP system fits well with a distribution of spherical shell (from SiO₂ coated in 5 nm layer CPAM around) model and a sphere model (SiO₂ alone) combined, and the number of such systems increase with increase in CPAM dosage. Structure factor obtained from SAXS curves reveals the interaction between NPs does not have a significant effect with respect to the dosage of CPAM.

Overall, this study proves that complimentary scattering techniques are essential in understanding a polyelectrolyte-NP system better to develop nanocellulose based composite material targeted for specific applications.

3.7 ACKNOWLEDGEMENT

Thanks to MCEM for scanning electron microscopy. The financial support from Australian research council, Australian paper, Carter Holt Harvey, Circa, Norske Skog, and Visy through the Industry Transformation Research Hub grant IH130100016 is acknowledged. Thanks Monash University for MGS and FEIPRS scholarships. The authors would like to thank to Dr. Tim Ryan, Dr. Nigel Kirby, Dr. Adrian Hawley and Dr. Chris Garvey for assistance during SAXS measurements at SAXS/WAXS beamline in Australian Synchrotron.

3.8 REFERENCES

1. Farhang, B., *Nanotechnology and lipids*. Lipid Technology, 2007. **19**(6): p. 132-135.
2. Winey, K.I. and R.A. Vaia, *Polymer nanocomposites*. MRS bulletin, 2007. **32**(04): p. 314-322.
3. Kim, J., S. Yun, and Z. Ounaies, *Discovery of cellulose as a smart material*. Macromolecules, 2006. **39**(12): p. 4202-4206.
4. Enarsson, L.-E. and L. Wågberg, *Conformation of preadsorbed polyelectrolyte layers on silica studied by secondary adsorption of colloidal silica*. Journal of colloid and interface science, 2008. **325**(1): p. 84-92.
5. Moody, G.M., *Polymeric Flocculants, in Handbook of Industrial Water Soluble Polymers*. 2007, Blackwell Publishing Ltd. p. 134-173.
6. Dimitrova, M., et al., *Adenoviral Gene Delivery from Multilayered Polyelectrolyte Architectures*. Advanced Functional Materials, 2007. **17**(2): p. 233-245.
7. Benkirane-Jessel, N., et al., *Build-up of Polypeptide Multilayer Coatings with Anti-Inflammatory Properties Based on the Embedding of Piroxicam–Cyclodextrin Complexes*. Advanced Functional Materials, 2004. **14**(2): p. 174-182.
8. Wågberg, L., et al., *On the charge stoichiometry upon adsorption of a cationic polyelectrolyte on cellulosic materials*. Colloids and Surfaces, 1987. **27**(4): p. 163-173.
9. Caruso, F., et al., 1. *Ultrathin Multilayer Polyelectrolyte Films on Gold: Construction and Thickness Determination*. Langmuir, 1997. **13**(13): p. 3422-3426.

-
10. Caruso, F., et al., 2. *Assembly of Alternating Polyelectrolyte and Protein Multilayer Films for Immunosensing*. Langmuir, 1997. **13**(13): p. 3427-3433.
 11. Elbert, D.L., C.B. Herbert, and J.A. Hubbell, *Thin Polymer Layers Formed by Polyelectrolyte Multilayer Techniques on Biological Surfaces*. Langmuir, 1999. **15**(16): p. 5355-5362.
 12. Liufu, S.-C., H.-N. Xiao, and Y.-P. Li, *Adsorption of cationic polyelectrolyte at the solid/liquid interface and dispersion of nanosized silica in water*. Journal of Colloid and Interface Science, 2005. **285**(1): p. 33-40.
 13. Cadotte, M., et al., *Flocculation, retention and drainage in papermaking: a comparative study of polymeric additives*. Canadian Journal of Chemical Engineering, 2007. **85**: p. 240.
 14. Garusinghe, U.M., et al., *Assembly of nanoparticles-polyelectrolyte complexes in nanofiber cellulose structures*. Colloids and Surfaces A: Physicochemical and Engineering Aspects, 2017. **513**: p. 373-379.
 15. Li, Q., et al., *Engineering cellulose nanofibre suspensions to control filtration resistance and sheet permeability*. Cellulose, 2016. **23**(1): p. 391-402.
 16. Wiegel, F.W., *Adsorption of a macromolecule to a charged surface*. Journal of Physics A: Mathematical and General, 1977. **10**(2): p. 299.
 17. Carrillo, J.-M.Y. and A.V. Dobrynin, *Molecular Dynamics Simulations of Polyelectrolyte Adsorption*. Langmuir, 2007. **23**(5): p. 2472-2482.
 18. Turesson, M., C. Labbez, and A. Nonat, *Calcium Mediated Polyelectrolyte Adsorption on Like-Charged Surfaces*. Langmuir, 2011. **27**(22): p. 13572-13581.
 19. Hesselink, F.T., *On the theory of polyelectrolyte adsorption*. Journal of Colloid and Interface Science, 1977. **60**(3): p. 448-466.
 20. Gregory, J. and S. Barany, *Adsorption and flocculation by polymers and polymer mixtures*. Advances in Colloid and Interface Science, 2011. **169**(1): p. 1-12.
 21. Varanasi, S., R. He, and W. Batchelor, *Estimation of cellulose nanofibre aspect ratio from measurements of fibre suspension gel point*. Cellulose, 2013. **20**(4): p. 1885-1896.
-

-
22. Kirby, N.M., et al., *A low-background-intensity focusing small-angle X-ray scattering undulator beamline*. Journal of Applied Crystallography, 2013. **46**(6): p. 1670-1680.
 23. Ansto. SAXS software SCATTERBRAIN. Available from:
<http://www.synchrotron.org.au/aussyncbeamlines/saxswaxs/software-saxswaxs>.
 24. Raj, P., et al., *Effect of cationic polyacrylamide on the processing and properties of nanocellulose films*. Journal of Colloid and Interface Science, 2015. **447**(0): p. 113-119.
 25. Connal, L.A., et al., *pH-Responsive Poly(acrylic acid) Core Cross-Linked Star Polymers: Morphology Transitions in Solution and Multilayer Thin Films*. Macromolecules, 2008. **41**(7): p. 2620-2626.
 26. Zhou, Y., G.J. Jameson, and G.V. Franks, *Influence of polymer charge on the compressive yield stress of silica aggregated with adsorbed cationic polymers*. Colloids and Surfaces A: Physicochemical and Engineering Aspects, 2008. **331**(3): p. 183-194.
 27. Raghuwanshi, V., et al., *Self-assembly of gold nanoparticles on deep eutectic solvent (DES) surfaces*. Chem. Commun., 2014. **50**(63): p. 8693-8696.
 28. Raghuwanshi, V.S., et al., *Structural analysis of Fe–Mn–O nanoparticles in glass ceramics by small angle scattering*. Journal of Solid State Chemistry, 2015. **222**: p. 103-110.
 29. Raghuwanshi, V.S., et al., *Experimental evidence of a diffusion barrier around BaF₂ nanocrystals in a silicate glass system by ASAXS*. CrystEngComm, 2012. **14**(16): p. 5215-5223.
 30. Raghuwanshi, V.S., C. Rüssel, and A. Hoell, *Crystallization of ZrTiO₄ Nanocrystals in Lithium-Alumino-Silicate Glass Ceramics: Anomalous Small-Angle X-ray Scattering Investigation*. Crystal Growth & Design, 2014. **14**(6): p. 2838-2845.
 31. Raghuwanshi, V.S., et al., *Structural analysis of magnetic nanocrystals embedded in silicate glasses by anomalous small-angle X-ray scattering*. Applied Crystallography, 2012. **45**(4): p. 644-651.
-

32. Breßler, I., J. Kohlbrecher, and A.F. Thünemann, *SASfit: a tool for small-angle scattering data analysis using a library of analytical expressions*. Journal of applied crystallography, 2015. **48**(5): p. 1587-1598.
33. Hayter, J.B. and J. Penfold, *An analytic structure factor for macroion solutions*. Molecular Physics, 1981. **42**(1): p. 109-118.
34. Hansen, J.-P. and J.B. Hayter, *A rescaled MSA structure factor for dilute charged colloidal dispersions*. Molecular Physics, 1982. **46**(3): p. 651-656.

CHAPTER 4

ASSEMBLY OF NANOPARTICLES-POLYELECTROLYTE COMPLEXES IN NANOFIBER CELLULOSE STRUCTURES

THIS PAGE HAS BEEN INTENTIONALLY LEFT BLANK

PREFACE

In the previous chapter, dynamic light scattering (DLS) and small angle X-ray scattering (SAXS) was used to quantify the conformation and changes in hydrodynamic radius of CPAM adsorbed on the surface of SiO₂ NPs, and the structural assembly of 8 nm SiO₂ NPs under the influence of different CPAM concentrations, respectively.

This chapter explores the structural assembly of 22 nm SiO₂ NPs under the influence of different CPAM concentration. The effect of different NP sizes on its structural assembly with CPAM is quantified through SAXS.

This chapter follows the second objective.

THIS PAGE HAS BEEN INTENTIONALLY LEFT BLANK

**CHAPTER 4 ASSEMBLY OF NANOPARTICLES - POLYELECTROLYTE
COMPLEXES IN NANOFIBER CELLULOSE STRUCTURES**

4.1 Graphical abstract	139
4.2 Abstract	140
4.3 Keywords	140
4.4 Introduction	140
4.5 Experimental	142
4.5.1 Material	142
4.5.2 Method	142
4.5.2.1 Preparation of MFC, CPAM and NP suspensions	142
4.5.2.2 MFC sheet preparation	143
4.5.2.3 MFC-NP composite preparation	143
4.5.3 Characterization	144
4.5.3.1 Small angle X-ray scattering	144
4.5.3.2 Scanning electron microscopy	145
4.5.3.3 Transmission electron microscopy	145
4.5.3.4 Particle and colloid charge	145
4.6 Results	145
4.7 Discussion	150
4.8 Conclusion	152
4.9 Acknowledgement	153
4.10 References	153

THIS PAGE HAS BEEN INTENTIONALLY LEFT BLANK

Monash University
Declaration for Thesis Chapter 4

In the case of Chapter 4, my contribution to the work involved the following:

Nature of contribution	Extent of contribution (%)
Initiation, key ideas, experimental works, analysis of results, writing up	45

The following co-authors contributed to the work. If co-authors are students at Monash University, the extent of their contributions in percentage must be stated:

Co-author name (s)	Nature of contribution	% of Co-author's contribution*
Vikram Singh Raghuwanshi	Initiation, key ideas, experimental works, analysis of results, writing up	45
Christopher J. Garvey	Paper reviewing and editing	
Swambabu Varanasi	Paper reviewing and editing	
Christopher R. Hutchinson	Paper reviewing and editing	
Warren Batchelor	Key ideas, paper reviewing and editing	Supervisor
Gil Garnier	Key ideas, paper reviewing and editing	Supervisor

The undersigned hereby certify that the above declaration correctly reflects the nature and extent of the candidate's and co-authors' contributions to this work.

Student signature: 

Date: 12/10/2017

The undersigned hereby certify that the above declaration correctly reflects the nature and extent of the student's and co-authors' contributions to this work. In instances where I am not the responsible author I have consulted with the responsible author to agree on the respective contributions of the authors.

Main Supervisor signature: 

Date: 12/10/2017

THIS PAGE HAS BEEN INTENTIONALLY LEFT BLANK

ASSEMBLY OF NANOPARTICLES-POLYELECTROLYTE COMPLEXES IN NANOFIBER CELLULOSE STRUCTURES

Uthpala Garusinghe ^{1,#}, Vikram. S. Raghuwanshi ^{1,#,*}, Christopher J. Garvey ³, Swambabu Varanasi ¹, Christopher. R. Hutchinson ², Warren Batchelor ¹ and Gil Garnier ^{1,*}

BioResource Processing Research Institute of Australia (BioPRIA), Department of Chemical Engineering, Monash University, VIC-3800, Australia

²Department of Materials Science and Engineering, Monash University, VIC-3800, Australia

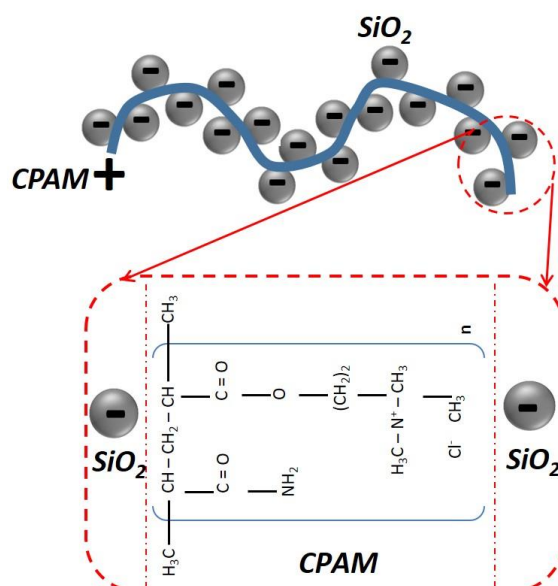
³ANSTO, Locked Bag 2001, Kirrawee DC NSW 2232, Australia

*Corresponding authors: [REDACTED]

[REDACTED]

Equal contributors as first authors

4.1 GRAPHICAL ABSTRACT



4.2 ABSTRACT

We report the effect of cationic polyacrylamide (CPAM) addition on the structural assembly of silica nanoparticles (NPs) within a nanocellulose fibre matrix. Paper like composites are fabricated by first forming complexes of NPs with CPAM, then adding those to a suspension of nanocellulose fibres; followed by filtration, pressing and drying of the final suspension. Complementary small angle X-ray scattering (SAXS) and microscopy (SEM, TEM) investigations of these composites showed a lognormal bimodal distribution of NP sizes. Data analysis allows understanding interparticle interactions within assemblies of SiO₂ NPs at the nanometer scale with respect to different dosage of CPAM. Increasing CPAM dosage increases retention of NPs within the cellulose matrix with stronger interparticle interactions and produces composites with smaller pores. The correlation length of NPs, indicative of the size of the NP clusters increased from 30 to 70 nm as the CPAM dosage increased from 16.5 to 330 mg/g NPs. Retention and assembly of SiO₂ NPs by varying CPAM dosage results from the balance of different interaction forces between NPs, CPAM and nanocellulose fibres. Understanding the effect of CPAM dosage on the various NP and composite structural conformations enables us to engineer novel hierarchically and functional cellulose based structured materials.

4.3 KEYWORDS

Small angle X-ray scattering (SAXS), TEM, silica nanoparticles (NPs), cationic polyacrylamide (CPAM), composites, nanocellulose, fibers

4.4 INTRODUCTION

Cellulose nanofibres are fast becoming widely available low-cost organic nanomaterials with specific properties such as tuneable opacity, low thermal expansion, high stiffness, high strength and flexibility. Cellulose is the most abundant, renewable and biodegradable biopolymer, efficiently produced by well-established manufacturing processes and infrastructures [1-3]. Nanocellulose fibres result from the intense fiberizing of cellulose pulp fibres. Cellulose nanofibres “paper” composites have exciting prospects and emerging applications such as smart clothing [4], transparent conductive films for electronics [5, 6], tissue engineering [7] and barriers [8]. Even though the full commercial scale production of cellulose nanofibres has not yet been fully

achieved, the wide availability of cellulose is promoting the production of new materials with cellulose nanofibres as the main component [9].

Nanocomposites are usually two phase materials consisting of a continuous polymeric phase reinforced by a discontinuous phase consisting of high surface area nanofillers [10]. When the size of fillers shrinks from microscale to nanoscale, the resulting composite develops unusual properties primarily due to the concomitant increase in interfacial area [11]. The properties of nanocomposites depend not only on the properties of their individual components but also on the morphological and interfacial characteristics arising from assembling the individual constituents [12]. In the materials investigated here, nanocellulose is the semi-continuous or connecting phase where silica nanoparticles (NPs) are linked through a retention aid to provide a new structure with voids, in which porosity and pore structure are dependent on NPs. The terms “cellulose nanofibres” and “nanocellulose” are used interchangeably in this paper and nanosilica was selected as model of functional NP.

Since both silica NPs and nanocellulose are negatively charged, an electrostatic repulsion is opposing the retention of NP's in the composite. In such cases, cationic polyelectrolytes are widely used in paper industries as retention aids [13, 14]. Common industrial cationic polyelectrolytes include: cationic dimethylamino-ethyl-methacrylate polyacrylamide (CPAM), polyethylenimine (PEI), Polydiallyldimethylammonium chloride (polyDADMAC) and polyamide-amine-epichlorohydrin (PAE). Among those, CPAM is the most prevalent in industry for its low cost, high performance, and wide range of morphologies available. Also, it has the ability to strongly adsorb onto the negatively charged cellulose fibres[15, 16] and is a stable polymer soluble in water and many organic solvents [17]. Important industrial applications for CPAM include water treatment, oil well stimulation and mineral processing [17]. Previously, we used CPAM to coagulate and retain NPs into nanocellulose and demonstrated that composite pore structure can be controlled [18]. However, the interaction of the CPAM with NPs and the mechanism of structural formation by CPAM induced NPs assembling within the composite at nanoscale have not been explored and there are no good methodology available to quantify NP aggregate at the critical length scale ranging from 1 nm to 1 μ m.

Generally, for characterization, direct methods such as scanning electron microscopy (SEM) and transmission electron microscopy (TEM) are used, but they evaluate a limited area of the

composite and it is difficult to measure interparticle interactions between NPs [19, 20]. Indirect inverse space techniques such as X-ray, neutrons or light scattering provide a complementary statistical perspective on the internal structure of the material. Small angle X-ray scattering (SAXS) is a powerful method to characterize particle or structure size in ranges from ~ 1 to 100 nm [21].

In this study, a novel structural characterization approach is developed to elucidate NP interactions within the respective formed assemblies dispersed in the cellulose matrix. We prepared nanocellulose/SiO₂ nanocomposites using CPAM as a retention aid. SAXS, TEM and SEM were used to quantify and optimize the interaction within silica NP assemblies with respect to different dosage of CPAM and distribution of assemblies within the cellulose matrix. Results from this study will contribute to engineer nanocomposites efficiently with polyelectrolytes. It is the objective of the study to characterize the structure of novel inorganic NP –organic fibre composites at the critical length scale affecting catalysis, permeability and biocompatibility.

4.5 EXPERIMENTAL

4.5.1 Material

Microfibrillated cellulose (MFC) was purchased from DAICEL Chemical Industries Limited, Japan (grade Celish KY-100G). The MFC was supplied at 25 % solids content and stored at 5 °C as received. The surface area of MFC is 31.1 m²/g [22, 23]. Cationic dimethylamino-ethyl-methacrylate polyacrylamide (CPAM) polymer of high molecular weight (13 MDa) and with a charge density of 40 wt% (F1, SnowFlake Cationics) was graciously supplied by AQUA+TECH, Switzerland. NexSil 8 Aqueous Colloidal Silica was provided by IMCD Australia Ltd as 30 wt% suspensions. The manufacturer reported a colloidal silica average diameter of 8 nm and a specific surface area of 330 m²/g.

4.5.2 Method

4.5.2.1 Preparation of MFC, CPAM and NP suspensions

MFC suspensions (0.2 wt%) were prepared by dispersing fibres in deionized water uniformly using a disintegrator equipped with a 3 L vessel at 15000 propeller revolutions. CPAM solutions (0.01 wt%) were prepared by dissolving CPAM powder in deionized water for 8 hours using a magnetic stirrer prior to nanocomposite fabrication. SiO₂ NP (0.1 wt%) suspensions were prepared by

diluting 30 wt% original silica NP suspension using deionized water, and the suspension was stirred using a magnetic stirrer for 10 minutes before use. Mixing time is important in both cases to obtain homogenous suspensions. All suspensions were prepared at room temperature. The pH of final solutions is about 8 and does not vary significantly with different dosage of CPAM.

4.5.2.2 MFC sheet preparation

MFC sheets were prepared [24] using a standard British hand sheet maker (model T 205). Concentrated MFC suspension (0.2 wt%) was poured into the hand sheet maker column and allowed to drain under gravity. After the water drained, the formed film was removed from the mesh using blotting papers, then pressed and dried using a sheet drier at 100 °C.

4.5.2.3 MFC-NP composite preparation

Composite preparation involves a two-step method (Figure 1). Firstly, CPAM (0.01 wt%) and SiO₂ (0.1 wt%) suspensions were mixed simultaneously together using a hand stirrer (model: HB968NSSJH, 600 watt). Secondly, prepared CPAM-SiO₂ suspension was mixed with MFC (0.2 wt%) suspension to obtain the final suspension of the mixture close to 0.15 wt%. This method was adopted from the controlled simultaneous assembly (CSA) of Bringley et al [25] where he mixed silica colloids and polyethylenimine together.

MFC and SiO₂ masses were kept constant at 1.2 g and 0.12 g, respectively for all composites. Three different CPAM dosages (1.98 mg, 3.96 mg and 39.6 mg) were used. The mixing time in each step was set to a total of 8 minutes. The flowrate at which CPAM was mixed varied from 2.5 mL/min to 49.5 mL/min. MFC and SiO₂ suspensions were mixed at 75 mL/min and 84 mL/min respectively. The final suspension was poured into the British hand sheet maker and the composite film was prepared as described above (MFC sheet preparation). Table 1 summarizes the type of composites prepared.

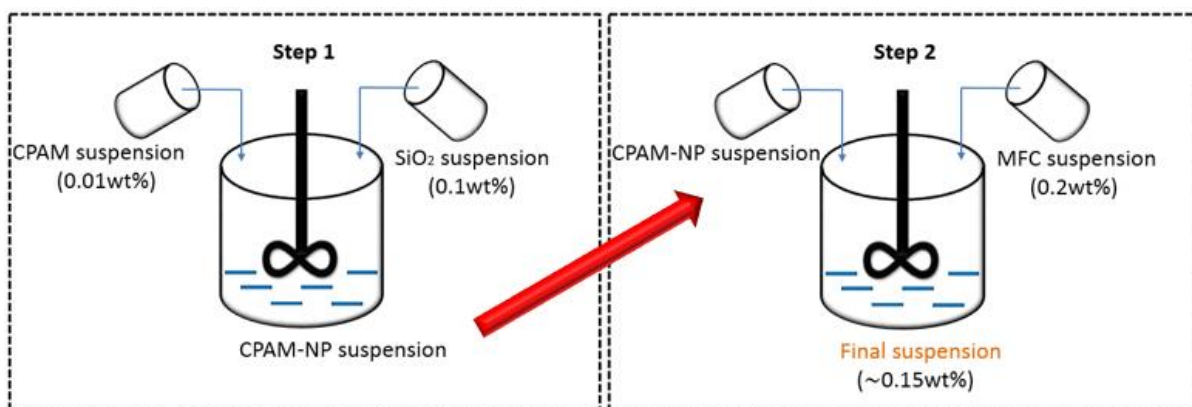


Figure 1: NP-CPAM complexes are first formed (step 1) and then mixed with a cellulose nanofiber suspension (step 2).

Table I: Composition of SiO₂-nanocellulose composites, High (H), Medium (M) and Low (L) denote the CPAM concentration.

Samples	MFC (g)	SiO ₂ (mg)	CPAM (mg)
Pure MFC	1.2	--	--
High (H)	1.2	120 (10 wt%)	39.6
Medium (M)	1.2	120 (10 wt%)	3.96
Low (L)	1.2	120 (10 wt%)	1.98

4.5.3 Characterization

4.5.3.1 Small angle X-ray scattering

Two instruments were used for small angle X-ray scattering (SAXS) measurements. SAXS analyses were first made on a Laboratory Bruker N8 Horizon using a CuK α ($\lambda = 0.154$ nm) micro-source. The scattered photons were collected using a 2D Vantec-500 detector with a pixel size of ~ 70 $\mu\text{m} \times 70$ μm . The scattered photons were collected at the sample to detector distance of 0.6 m which covers the q range from ~ 0.15 to 3.7 nm^{-1} . Radial averaging was used to obtain the final scattering curves. For data reduction, Bruker EVA software was used. Data analysis was performed using SASFit software [26-28].

SAXS measurements were also made in a transmission mode on a Pilatus 1M detector (Dectris, Baden, Switzerland) at the Australian Synchrotron's SAXS/WAXS beamline [29] with a sample to

detector distance of 7.2 m. The isotropic raw detector images were converted to intensity versus q , where $q = 4\pi\sin(\theta)/\lambda$ defined by $\theta/2$ the scattering angle and λ the wavelength (0.113 nm) of the incident x-rays and q range between 0.01-1 nm⁻¹. The scattered intensity is plotted as a function of the momentum transfer vector q . Specific macro's written [30] for the program IgorPro [31] accounted for the measurement geometry, masking dead pixels and the beam stop and a subtraction of air scatter.

4.5.3.2 Scanning electron microscopy

Scanning electron microscopy (SEM) was performed using a FEI Nova NanoSEM 450 FEG. Secondary electron images were captured. This mode produces high-resolution images and avoids any problems associated with sample charging. A small square (3 x 3 mm) of composite was mounted onto a metal substrate with a carbon tape. The sample was then coated with a thin layer of Iridium. The accelerating voltage was 5 kV and images were captured at 30,000 to 100,000 magnifications.

4.5.3.3 Transmission electron microscopy

Transmission electron microscopy (TEM) was performed using FEI Tecnai G2 T20 TWIN. For sample preparation, copper grid of 3 mm with a thin carbon layer was dipped into a NP-CPAM suspension and dried. The accelerating voltage was 200 kV and images were captured at 250,000 magnifications at 100 nm scale.

4.5.3.4 Particle and colloid charge

The zeta potentials were determined by performing measurement using a Nanobrook Omni (Brookhaven Instruments) in a cuvette cell at 25 °C. The software determines the electrophoretic mobility from an electrophoresis experiment by laser Doppler velocimetry and applying Smoluchowski equation to calculate zeta potential. CPAM and SiO₂ NP concentrations were used at 0.5 mg/mL and 0.01 wt% respectively.

4.6 RESULTS

SAXS measurements were performed to determine the statistical description of the internal composite structure of SiO₂ NPs dispersed in a cellulose matrix [32-38]. Figure 2a shows the SAXS measurements of a MFC sheet. The SAXS curve for the pure MFC sample shows a weak correlation

peak at $q = 1.3 \text{ nm}^{-1}$ indicating the presence of weakly correlated small heterogeneities at length-scales of about 3-5 nm. This weak correlation peak is superimposed upon a broader signal, which is indicative of a broad distribution of length-scales, for example a fibre network. The characteristic size of the elementary fibres is between 3-5 nm, and the major contribution to the scattering is from the fibre/nanofiber surface [39, 40].

Figure 2b displays the SEM micrograph of the pure MFC sheet. The micrograph shows that the fibres are isotropically oriented to form a highly entangled network with a wide distribution of pore sizes. This is consistent with the view obtained from SAXS measurements. The average diameter of the fibres was found to be 73 nm [41]. These microfibrils are bundles of elementary nanofibers which are responsible for the weak SAXS correlation peak.

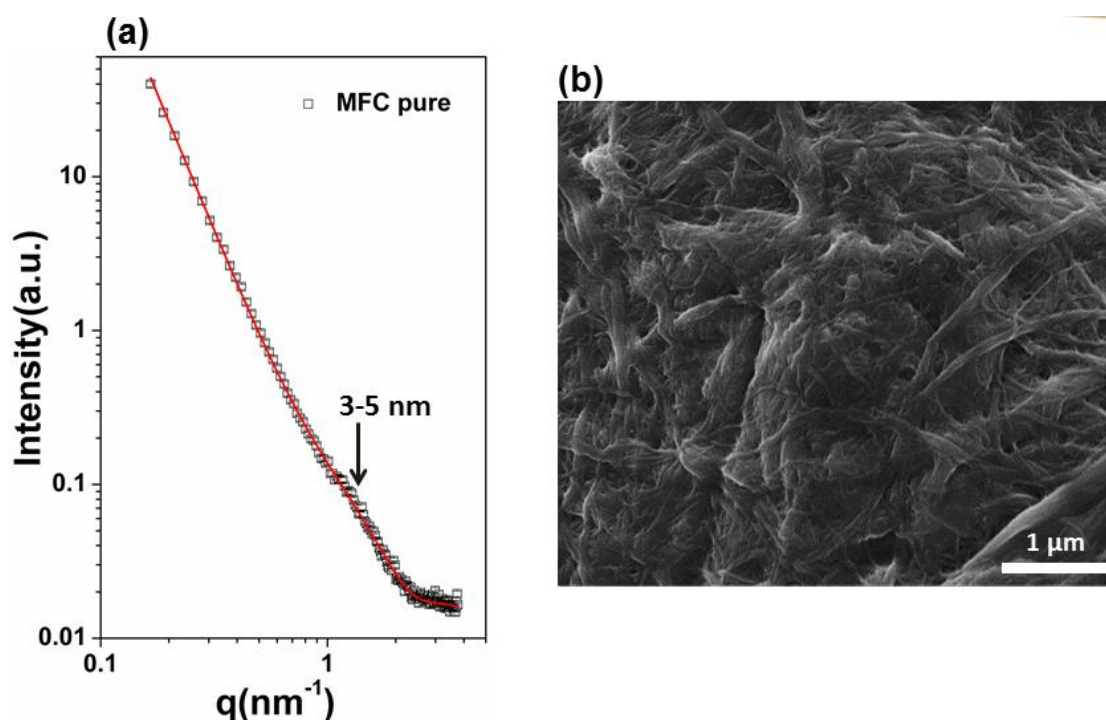


Figure 2: (a) SAXS curve of the pure MFC sheet. The solid line shows the modelled fit. Arrow shows the diameter of the sample for a peak obtained at a particular q value. (b) SEM image of the MFC sheet at 50,000 magnification.

SAXS measurements with a synchrotron can probe a wide structure size range at a high resolution and statistics, which is unachievable with a laboratory SAXS instrument. Figure 3a shows the synchrotron SAXS curves of the MFC-SiO₂ NP composites at different CPAM dosages. All the SAXS curves show two maxima at fixed q positions of $q=0.4 \text{ nm}^{-1}$ and 0.2 nm^{-1} which indicates the existence of two kinds of size distributions and volume fractions in the composite. As the CPAM

dosage increases, the SAXS peak at $q=0.4 \text{ nm}^{-1}$ becomes more pronounced and broader for the q ranging between $0.0 - 0.7 \text{ nm}^{-1}$. The peaks at $q=0.8 \text{ nm}^{-1}$ indicate the formation of structures of about 8 nm and the peaks at $q=0.4 \text{ nm}^{-1}$ reveal the formation of larger structures of about 15-20 nm; these are shown by the arrows in Figure 3a.

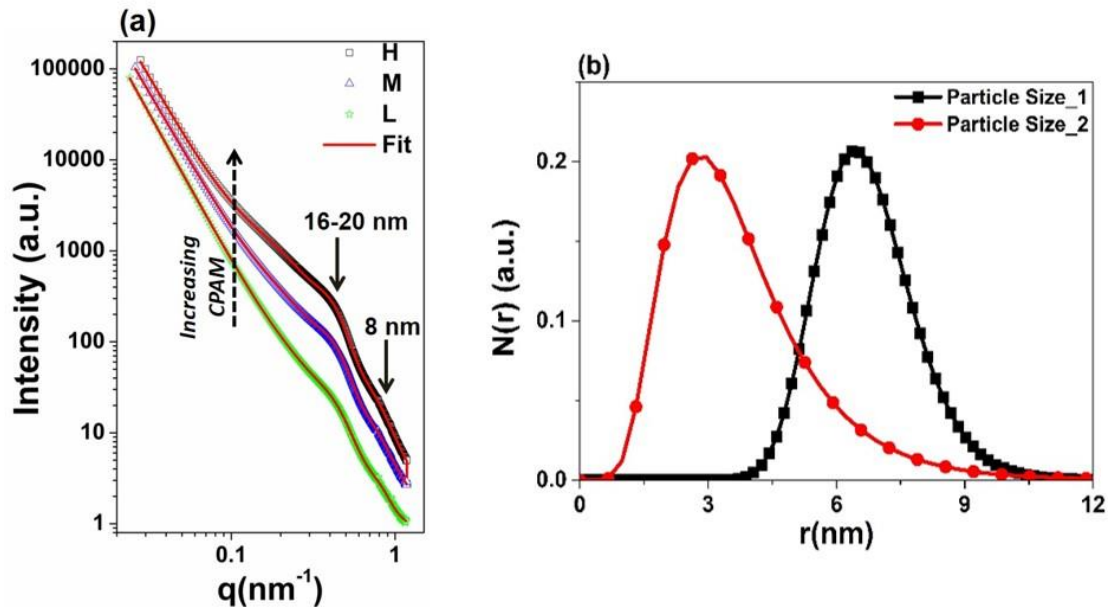


Figure 3: (a) SAXS curves fitted with the bimodal distribution of the particles with different CPAM dosages; Sample H (High CPAM dosage), Sample M (Medium CPAM dosage), and Sample L (low CPAM dosage). The solid red line shows the fit and the arrows show the diameter obtained from the particular peak position. (b) Lognormal size distribution curves for the sample with the high dosage of CPAM (H).

The quantitative analysis of size, size distribution and number density of the particles was evaluated by non-linear fitting of the curves by using the software SASFit [32-35]. Here, a model for bimodal distribution of spheres and a structure factor for hard spheres with a local monodisperse approximation was fitted to the SAXS curves [42-44]. Details on the modelling of the SAXS curves are given in Appendix I B1 and B2. Figure 3b shows the lognormal bimodal distribution of spherical shape particles obtained after model fitting of the scattering curves. The size parameters reveal that the smaller particle diameter is about 8 nm and the larger particle diameter is between 15-20 nm. The average diameter of 8 nm for smaller structure and 15-20 nm for the bigger structure were determined after fitting the respective SAXS curves. Dynamic light

scattering (DLS) measurements on the initial nanoparticle suspension also shows the corresponding bimodal size distribution, which is in agreement with the SAXS results (Appendix I B3).

Evidence on the assemblies of SiO₂-CPAM complexes before addition to the MFC suspension were obtained by the TEM measurements. Figure 4 shows the TEM micrograph on solution of SiO₂/CPAM at high CPAM dosage and prior to the addition of the MFC. In the TEM micrograph, two different kinds of particle sizes and assemblies of NPs are clearly observed (Appendix I B4). The results obtained from TEM analysis are in good agreement with the SAXS results.

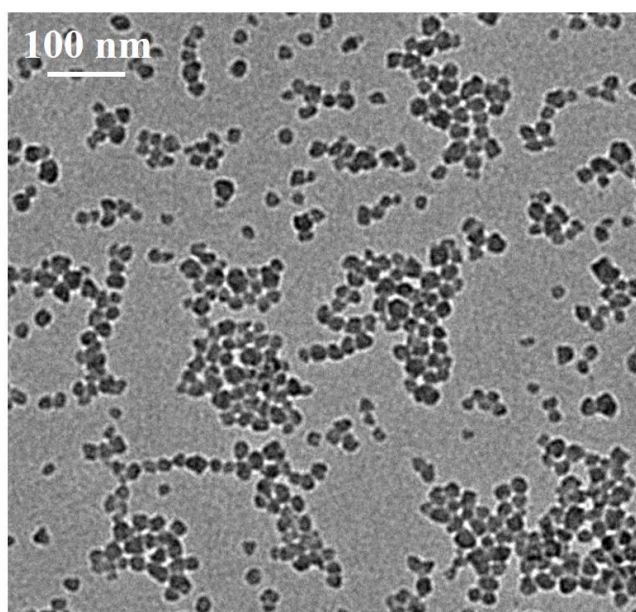


Figure 4: TEM micrograph for the SiO₂/CPAM complexes at high CPAM dosage prior to the addition of MFC suspension.

The structure factor calculated from the SAXS curves accounts for the correlation between the NPs and interparticle interactions [19]. Figure 5a shows the hard sphere structure factor for SiO₂ NPs with local monodisperse approximation used to fit the respective SAXS curves [32, 35]. Figure 5a indicates that the clusters of SiO₂ NPs formed in the cellulose fibre matrix are a direct function of the CPAM dosage. As CPAM amount increases, the sharpness of the structure factor peak increases and the peak shifts towards higher q values with respect to the sample with low CPAM dosage. This indicates increase in the volume fraction of NPs and decrease in interparticle separation with increase in CPAM dosage. Figure 5b shows the correlation length obtained from

the structure factor, which reveals an increase in interaction between SiO₂ NPs at the high dosage of CPAM.

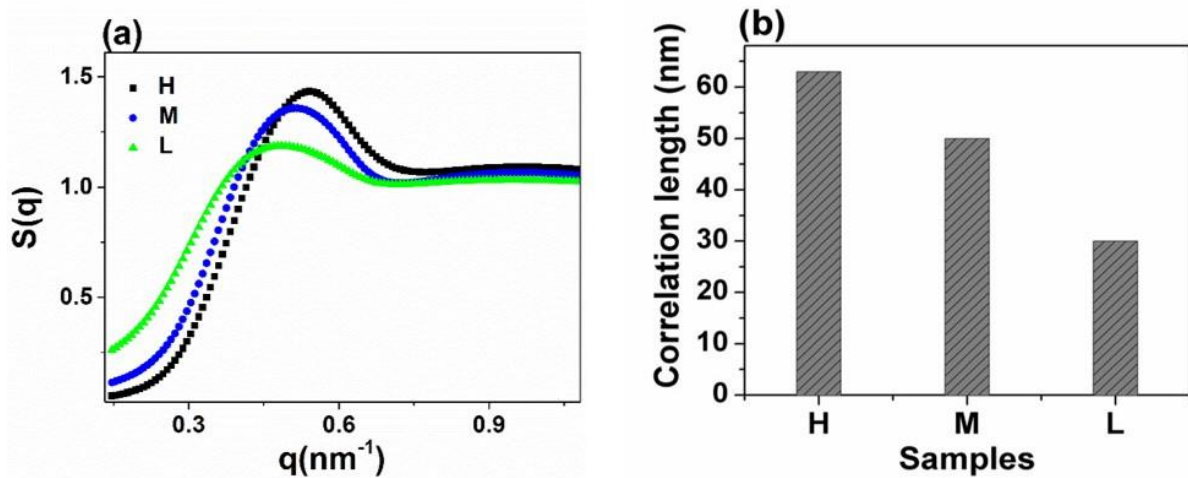


Figure 5: (a) Evaluated structure factor $S(q)$ for the samples with different CPAM dosages; sample H has high CPAM, M medium and sample L has low CPAM. (b) Correlation length obtained from the SAXS data analysis.

SEM images of the SiO₂ composites are shown in Figure 6a-b for low and high CPAM loadings, respectively. For the composite with low CPAM dosage, the SiO₂ NPs cluster size is smaller and less particles are retained in the cellulose fibre matrix. NPs and small NP clusters accommodate themselves randomly within the fibre matrix without changing any fibre position. Figure 6a is similar to Figure 2b but with bigger pores within the fibre network filled up by NPs. At high CPAM dosage, more and more NPs come into contact and bound with each other, resulting in larger clusters or assemblies with high retention. When the fibre gaps within the structure are not sufficiently large to accommodate the big NPs clusters, the fibres expand to make space. This changes the structure of the composite: volume increases and density decreases, as clearly seen in Figure 6b.

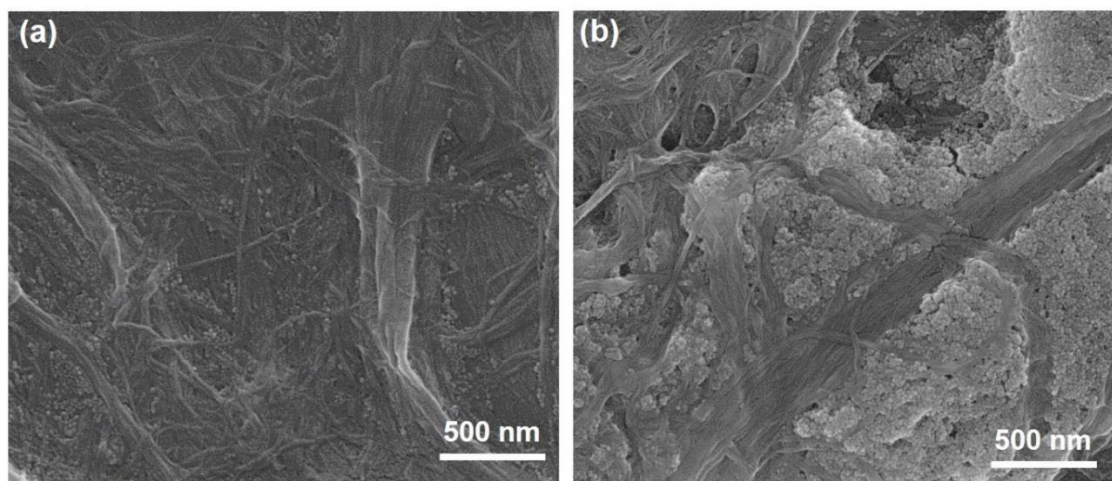


Figure 6: SEM micrograph of the MFC sheet containing SiO₂ nanoparticles with (a) low (L) CPAM dosage and (b) high (H) CPAM dosage.

4.7 DISCUSSION

We combined SAXS and microscopic (TEM, SEM) methods to characterize at the nanoscale the structural assemblies/aggregates formed by SiO₂ NPs within a cellulose fibre matrix; CPAM concentration was used to vary the fraction and size of NP aggregation. From our measurement, SiO₂ NPs are negatively charged and form stable aqueous suspensions due to a high zeta potential of -30 mV. On the other hand, CPAM in suspension is positively and strongly charged with a zeta potential for the polymer coil of +76 mV and a charge density of 10⁻³ eq/g. Both SiO₂ and cellulose are negatively charged and therefore SiO₂ NPs do not readily adsorb onto the surface of cellulose. This is consistent with the interpretation of SAXS measurements conducted on the composite without any CPAM (Appendix I B5). There is a little difference between this material and the structure characterized with the pure MFC sheet with SAXS. A small amount of CPAM has a significant effect on the interactions between SiO₂ NPs and cellulose fibres. CPAM acts as a retention aid for NPs.

SAXS and TEM data analysis corroborate the formation of different size of aggregates of SiO₂ NPs in cellulose matrix at the different CPAM dosages. TEM micrographs (Figure 4) of the SiO₂/CPAM complexes prior to the addition of MFC suspension reveals that in the presence of CPAM, the SiO₂ NPs aggregate and form assemblies. These assemblies are consisting of two size of NPs (8 and 20 nm) as shown in the Appendix I B4. After addition of SiO₂/CPAM suspension into MFC suspension (step 2), it is hard to obtain TEM micrograph due to difficulty in sample preparation and to get

reliable results. Therefore, SAXS measurements were made to obtain much better average information on interparticle spacing within the assemblies of SiO₂ NPs at the nanometer scale.

SAXS data analysis show that these assemblies of SiO₂ NPs consist of NPs structures of diameter ranging between 8 and 20 nm (Figure 3b). The diameter of NPs is about two to four times smaller than the expected radius of gyration of a CPAM molecule ($R_g = 30\text{-}35$ nm) assuming random coil at theta conditions (more if electrostatic forces are involved). Therefore, the SiO₂ NPs can easily adsorb onto the CPAM surface or even diffuse within the coil structure to interact directly with the CPAM cations. It is expected that the large CPAM coils are decorated with the SiO₂ NPs and form assemblies by electrostatic interactions and CPAM conformations [45].

Structure factor analysis reveal the information on the correlation between the aggregated SiO₂ NPs assemblies. In Figure 5a, it is seen that for the high dosage of CPAM the structure factor peak is sharper and shifts towards high q values as compared to the structure factor peak for low CPAM dosage, which indicates narrow distribution of inter-particle separations with high volume fractions. Moreover, increase in the amplitude of structure factor peak reveals the strong interparticle interactions within the assemblies of SiO₂ NPs. This is because at the high CPAM dosage more polyelectrolyte is available to neutralize the NPs surface and overcome the electrostatic repulsion between the particles, resulting in an increase in contact aggregation between the SiO₂ NPs. This results in the formation of large size assemblies having a higher correlation length of about 70 nm and with high volume fraction of NPs within the assemblies. This is in agreement with the TEM measurements shown in Figure 4. Recently, Ganesan et al also reported the aggregation of charged NPs in the surrounding of oppositely charged polymers by using mean field self-consistent theory model [46, 47]. They described that at low polymer concentration, the charged NPs form polymer-bridged clusters and by increasing the polymer concentration, clusters are formed by inter-particle bridging.

However, at the low CPAM dosage, the structure factor peak is broad, lower in amplitude and shifts towards lower q values which resembles the loosen SiO₂ NPs aggregates structure with smaller volume fraction and wider distributions. At low CPAM dosage and for a fixed SiO₂ NPs concentration, the tendency to form aggregates/assemblies decreases. This is due to the low density of CPAM available to neutralize the SiO₂ NPs; hence, an electrostatic repulsion between

the SiO₂ NPs dominates and leads to the formation of polymer-bridged aggregates of loosely bounded SiO₂ NPs.

Surface coverage of NPs by CPAM directly depends upon the conformation CPAM adopts on the surface of the spherical NPs upon adsorption. The total specific surface area of SiO₂ NPs ($r = 4\text{ nm}$) is $330\text{ m}^2/\text{g}$. There are two extreme cases of CPAM adsorption conformation of interest. Should the CPAM remains coiled to adsorb in the form of a blob/sphere of radius 30 nm , it can then cover about 15% of the surface area of SiO₂ NPs. However, should CPAM stretch and adsorb as an extended chain wire of length $22,744\text{ nm}$ (end to end distance; contour length), then it will fully saturate the available surface area of the NPs. Precise estimate of CPAM surface coverage requires measurement as the exact CPAM adsorption conformation which remains undetermined.

4.8 CONCLUSION

A series of novel SiO₂-nanocellulose composites of different structures was developed and characterized. SiO₂ nanoparticle (NP) assemblies of different sizes were formed by varying the dosage of CPAM in a nanocellulose matrix. Small angle X-ray scattering (SAXS) and transmission electron microscopy (TEM) measurements reveal the formation of NPs assemblies consisting of bimodal distribution of NPs with smaller particle diameter of 8 nm and large particle diameter of $15\text{-}20\text{ nm}$, respectively. Structure factor obtained from SAXS data analysis shows that at high dosage of CPAM, the assemblies of NPs formed within the cellulose matrix have high volume fraction. Moreover, the NPs in the assemblies have a lower interparticle distance, are strongly bounded, and have larger correlation length. An increase in CPAM dosage increases the retention of NPs assemblies within the cellulose matrix. However, at low dosage of CPAM, the retention of NPs within the cellulose matrix is low (smaller volume fraction) and the assemblies have a loosen structure with weak interparticle interaction. Characterizing and controlling NPs assemblies dispersed in a nanocellulose matrix allows tailoring a novel generation of sustainable composites for applications requiring selected catalytical, permeability or biocompatibility properties.

4.9 ACKNOWLEDGEMENT

Financial support is from Australian Research Council (ARC), Australian paper, Carter Holt Harvey, Circa, Norske Skog, Circa and Visy through the Industry Transformation Research Hub grant IH130100016. Thanks to MCEM for scanning electron microscopy, Australian Synchrotron for SAXS measurements and Praveena Raj for discussions. The authors gratefully acknowledge using the Bruker N8 Horizon SAXS funded from ARC LIEF LE130100072.

4.10 REFERENCES

1. Siró, I. and D. Plackett, *Microfibrillated cellulose and new nanocomposite materials: a review*. Cellulose, 2010. **17**(3): p. 459-494.
2. Klemm, D., et al., *Cellulose: fascinating biopolymer and sustainable raw material*. Angewandte Chemie International Edition, 2005. **44**(22): p. 3358-3393.
3. Klemm, D., H.P. Schmauder, and T. Heinze, *Cellulose*. Biopolymers online, 2005.
4. Gao, K., et al., *Cellulose nanofibers/reduced graphene oxide flexible transparent conductive paper*. Carbohydrate Polymers, 2013. **97**(1): p. 243-251.
5. Zhu, H., et al., *Transparent paper: fabrications, properties, and device applications*. Energy & Environmental Science, 2014. **7**(1): p. 269-287.
6. Nogi, M., et al., *Optically transparent nanofiber paper*. Advanced materials, 2009. **21**(16): p. 1595-1598.
7. Pham, Q.P., U. Sharma, and A.G. Mikos, *Electrospinning of polymeric nanofibers for tissue engineering applications: a review*. Tissue engineering, 2006. **12**(5): p. 1197-1211.
8. Aulin, C., M. Gällstedt, and T. Lindström, *Oxygen and oil barrier properties of microfibrillated cellulose films and coatings*. Cellulose, 2010. **17**(3): p. 559-574.
9. Krol, L.F., et al., *Microfibrillated cellulose-SiO₂ composite nanopapers produced by spray deposition*. Journal of Materials Science, 2015. **50**(11): p. 4095-4103.
10. Vaia, R.A. and E.P. Giannelis, *Polymer nanocomposites: status and opportunities*. MRS bulletin, 2001. **26**(05): p. 394-401.

-
11. Winey, K.I. and R.A. Vaia, *Polymer nanocomposites*. MRS bulletin, 2007. **32**(04): p. 314-322.
 12. Sanchez, C., et al., "Chimie douce": *A land of opportunities for the designed construction of functional inorganic and hybrid organic-inorganic nanomaterials*. Comptes Rendus Chimie, 2010. **13**(1): p. 3-39.
 13. Asselman, T. and G. Garnier, *The role of anionic microparticles in a poly(acrylamide)-montmorillonite flocculation aid system*. Colloids and Surfaces A: Physicochemical and Engineering Aspects, 2000. **170**(1): p. 79-90.
 14. Asselman, T. and G. Garnier, *Mechanism of Polyelectrolyte Transfer during Heteroflocculation*. Langmuir, 2000. **16**(11): p. 4871-4876.
 15. Lindström, T. and C. Söremark, *Adsorption of cationic polyacrylamides on cellulose*. Journal of colloid and interface science, 1976. **55**(2): p. 305-312.
 16. Tanaka, H., et al., *Competitive adsorption of cationic polyacrylamides with different charge densities onto polystyrene latex, cellulose beads and cellulose fibres*. Journal of pulp and paper science, 1999. **25**(8): p. 283-288.
 17. Bikales, N.M., *Preparation of acrylamide polymers, in Water-Soluble Polymers*. 1973, Springer. p. 213-225.
 18. Varanasi, S., Z.-X. Low, and W. Batchelor, *Cellulose nanofibre composite membranes—Biodegradable and recyclable UF membranes*. Chemical Engineering Journal, 2015. **265**: p. 138-146.
 19. Qiu, D., et al., *A small-angle X-ray scattering study of the interactions in concentrated silica colloidal dispersions*. Langmuir, 2006. **22**(2): p. 546-552.
 20. Ottewill, R.H., *Stability and Instability in Disperse Systems*. Journal of Colloid and Interface Science, 1977. **58**(2): p. 357-373.
 21. Schnablegger, H. and Y. Singh, *A practical guide to SAXS*. Anton Paar, Graz, Austria, 2006.
 22. Raj, P., et al., *Effect of cationic polyacrylamide on the processing and properties of nanocellulose films*. Journal of colloid and interface science, 2015. **447**: p. 113-119.
-

-
23. Sehaqui, H., et al. *Biomimetic aerogels from microfibrillated cellulose and xyloglucan*. in *ICCM-17 17th International Conference on Composite Materials, Edinburgh, United Kingdom*. 2009.
 24. Varanasi, S. and W.J. Batchelor, *Rapid preparation of cellulose nanofibre sheet*. *Cellulose*, 2013. **20**(1): p. 211-215.
 25. Bringley, J.F., et al., *Controlled, simultaneous assembly of polyethylenimine onto nanoparticle silica colloids*. *Langmuir*, 2006. **22**(9): p. 4198-4207.
 26. Kohlbrecher, J. and I. Bressler, *Software package SASfit for fitting small-angle scattering curves*; 2010. URL: <http://kur.web.psi.ch/sans1/SANSSoft/sasfit.html>.
 27. Breßler, I., J. Kohlbrecher, and A.F. Thünemann, *SASfit: a tool for small-angle scattering data analysis using a library of analytical expressions*. *Journal of applied crystallography*, 2015. **48**(5): p. 1587-1598.
 28. Pedersen, J.S., *Analysis of small-angle scattering data from colloids and polymer solutions: modeling and least-squares fitting*. *Advances in colloid and interface science*, 1997. **70**: p. 171-210.
 29. Kirby, N.M., et al., *A low-background-intensity focusing small-angle X-ray scattering undulator beamline*. *Journal of Applied Crystallography*, 2013. **46**(6): p. 1670-1680.
 30. Ilavsky, J., *Nika: software for two-dimensional data reduction*. *Journal of Applied Crystallography*, 2012. **45**(2): p. 324-328.
 31. WaveMetrics, I., *Igor Pro*. WaveMetrics, Inc. PO Box 2088, Lake Oswego, OR 97035 USA, 2011. **6**.
 32. Raghuwanshi, V., et al., *Self-assembly of gold nanoparticles on deep eutectic solvent (DES) surfaces*. *Chem. Commun.*, 2014. **50**(63): p. 8693-8696.
 33. Raghuwanshi, V.S., et al., *Structural analysis of Fe–Mn–O nanoparticles in glass ceramics by small angle scattering*. *Journal of Solid State Chemistry*, 2015. **222**: p. 103-110.
-

-
34. Raghuwanshi, V.S., et al., *Experimental evidence of a diffusion barrier around BaF 2 nanocrystals in a silicate glass system by SAXS*. CrystEngComm, 2012. **14**(16): p. 5215-5223.
 35. Raghuwanshi, V.S., et al., *Deep Eutectic Solvents for the Self-Assembly of Gold Nanoparticles: A SAXS, UV-Vis, and TEM Investigation*. Langmuir, 2014. **30**(21): p. 6038-6046.
 36. Raghuwanshi, V.S., C. Rüssel, and A. Hoell, *Crystallization of ZrTiO₄ Nanocrystals in Lithium-Alumino-Silicate Glass Ceramics: Anomalous Small-Angle X-ray Scattering Investigation*. Crystal Growth & Design, 2014. **14**(6): p. 2838-2845.
 37. Raghuwanshi, V.S., et al., *Structural analysis of magnetic nanocrystals embedded in silicate glasses by anomalous small-angle X-ray scattering*. Applied Crystallography, 2012. **45**(4): p. 644-651.
 38. Hoell, A., et al., *SAXS study of CaF₂ nanoparticles embedded in a silicate glass matrix*. Journal of Applied Crystallography, 2014. **47**(1): p. 60-66.
 39. Jakob, H.F., P. Fratzl, and S.E. Tschegg, *Size and arrangement of elementary cellulose fibrils in wood cells - A small-angle x-ray-scattering study of Picea Abies*. Journal of Structural Biology, 1994. **113**(1): p. 13-22.
 40. Jakob, H.F., S.E. Tschegg, and P. Fratzl, *Hydration dependence of the wood-cell wall structure in Picea abies. A small-angle X-ray scattering study*. Macromolecules, 1996. **29**(26): p. 8435-8440.
 41. Varanasi, S., R. He, and W. Batchelor, *Estimation of cellulose nanofibre aspect ratio from measurements of fibre suspension gel point*. Cellulose, 2013. **20**(4): p. 1885-1896.
 42. Vrij, A., *Mixtures of hard spheres in the Percus-Yevick approximation. Light scattering at finite angles*. The Journal of Chemical Physics, 1979. **71**(8): p. 3267-3270.
 43. Pedersen, J.S., *Determination of size distribution from small-angle scattering data for systems with effective hard-sphere interactions*. Journal of applied crystallography, 1994. **27**(4): p. 595-608.
-

44. Percus, J.K. and G.J. Yevick, *Analysis of classical statistical mechanics by means of collective coordinates*. Physical Review, 1958. **110**(1): p. 1.
45. Solberg, D. and L. Wågberg, *Adsorption and flocculation behavior of cationic polyacrylamide and colloidal silica*. Colloids and Surfaces A: Physicochemical and Engineering Aspects, 2003. **219**(1): p. 161-172.
46. Pryamitsyn, V. and V. Ganesan, *Interplay between Depletion and Electrostatic Interactions in Polyelectrolyte–Nanoparticle Systems*. Macromolecules, 2014. **47**(17): p. 6095-6112.
47. Pandav, G., et al., *Multibody Interactions, Phase Behavior, and Clustering in Nanoparticle–Polyelectrolyte Mixtures*. The Journal of Physical Chemistry B, 2015. **119**(45): p. 14536-14550.

THIS PAGE HAS BEEN INTENTIONALLY LEFT BLANK

CHAPTER 5

NANOCELLULOSE – MONTMORILLONITE COMPOSITES OF LOW WATER VAPOUR PERMEABILITY

THIS PAGE HAS BEEN INTENTIONALLY LEFT BLANK

PREFACE

In previous chapters (Chapter 2-4), SiO₂ NPs were used as a model inorganic NP to produce nanocomposites with nanocellulose. Cationic polyacrylamide (CPAM) was used to retain and bridge NPs to nanocellulose. The structure-property relationship with varying NP content and NP sizes were quantified. The interaction between NPs and CPAM was quantified as well.

This chapter uses the expertise obtained from the previous experimental 3 chapters in production and characterization of nanocomposites, to produce montmorillonite (MMT) - nanocellulose composites for water vapour barrier applications. Particularly, the focus is to engineer the material to be strong, flexible, biodegradable, recyclable, easy to scale up and with very low water vapour permeability.

This chapter follows the third objective.

THIS PAGE HAS BEEN INTENTIONALLY LEFT BLANK

**CHAPTER 5 NANOCELLULOSE – MONTMORILLONITE COMPOSITES
OF LOW WATER VAPOUR PERMEABILITY**

5.1 Graphical abstract	165
5.2 Abstract	165
5.3 Keywords	166
5.4 Introduction	166
5.5 Experimental	168
5.5.1 Material	168
5.5.2 Method	168
5.5.2.1 Production of nanocellulose	168
5.5.2.2 Nanocellulose film preparation	168
5.5.2.3 Production of nanocellulose/MMT composites	169
5.5.3 Characterization	169
5.5.3.1 Structure and morphology study	169
5.5.3.2 Thickness measurements	170
5.5.3.3 Strength measurements	170
5.5.3.4 Particle and colloid charge	170
5.5.3.5 X-ray diffraction	170
5.5.3.6 Barrier properties	171
5.6 Results	171
5.6.1 Nanocellulose and MMT morphology	171
5.6.2 Structure of nanocellulose/MMT sheet	172
5.6.3 Mechanical properties	176
5.6.4 Barrier properties	177
5.7 Discussion	178
5.7.1 Barrier properties of nanocellulose/MMT sheets	178
5.7.2 Mechanical properties of nanocellulose/MMT paper	181
5.7.3 Literature comparison	181
5.8 Conclusion	185

CHAPTER 5

5.9 Acknowledgement	186
5.10 References	186

NANOCELLULOSE – MONTMORILLONITE COMPOSITES OF LOW WATER VAPOUR PERMEABILITY

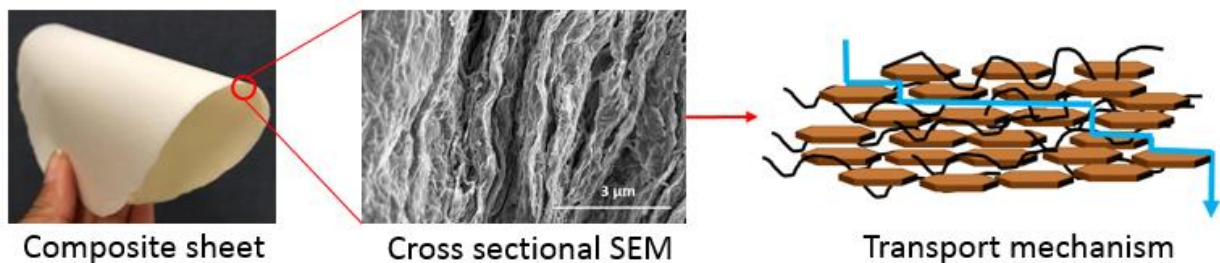
Uthpala M. Garusinghe, Swambabu Varanasi, Vikram. S. Raghuwanshi, Gil Garnier* and Warren Batchelor*

BioResource Processing Research Institute of Australia (BioPRIA), Department of Chemical Engineering, Monash University, VIC-3800, Australia

*Corresponding authors: [REDACTED]

[REDACTED]

5.1 GRAPHICAL ABSTRACT



5.2 ABSTRACT

A simple technique was developed to well disperse montmorillonite (MMT) into novel nanocellulose composites of varying MMT content (9.1-37.5 wt%). The objective was to develop nanocellulose-MMT composites of very low water vapour permeability (WVP) by increasing the composite tortuosity. The new composites are strong (strength-110 MPa), stiff (modulus-11 GPa) yet flexible. Scanning electron micrographs revealed MMT platelets to be uniformly distributed across and within the composite, creating a tortuous path restricting water molecules diffusion. WVP decreased by half, from $24.2 \pm 2.7 \text{ g} \cdot \mu\text{m} / \text{m}^2 \cdot \text{day} \cdot \text{kPa}$ without MMT to $13.3 \pm 2.0 \text{ g} \cdot \mu\text{m} / \text{m}^2 \cdot \text{day} \cdot \text{kPa}$ with only 16.7 wt% MMT. Further increasing the MMT content increased composite WVP, due to MMT aggregation. Two separate MMT dispersion methods were tested

to break down MMT stacks and improve WVP by increasing MMT available surface area: (a) sonication, which worsened WVP, and (b) high pressure homogenization, which reduced WVP further to $6.33 \pm 1.5 \text{ g} \cdot \mu\text{m} / \text{m}^2 \cdot \text{day} \cdot \text{kPa}$ with 23.1 wt% MMT. This is the lowest WVP reported in literature for nanocellulose-MMT composites. This study developed a recyclable composite of very low WVP. These thin, inexpensive, strong and flexible nanocellulose-MMT composites present a new and attractive option as recyclable/compostable packaging materials for large volume packing applications where water vapour protection is critical.

5.3 KEYWORDS

Montmorillonite (MTM), nanocellulose, composites, water vapour permeability (WVP), packaging.

5.4 INTRODUCTION

There is a need for new cellulosic packaging materials and membranes having strong moisture barrier performance for application in food, electronics and pharmaceutical industry which are sustainable and prevent global warming [1, 2]. For packaging, this material should be flexible, strong, recyclable inexpensive and fully biodegradable when finally disposed at the end of its product life.

Most current packagings rely on petrochemical-based materials such as polyethylene (PE) and polypropylene (PP) polyolefins, polystyrene (PS), polyethylene terephthalate (PET), polyvinylidene chloride (PVDC) and poly(vinyl chloride) (PVC) [3] as barriers to moisture. These materials are difficult to recycle and non-biodegradable. There is a need for performant composites made from renewable bio-based materials. Here, cellulose derived from wood fibres stands out as material of high potential.

Cellulose is more than an environmentally friendly material; it is a polymer with good mechanical properties and low thermal expansion; it is also easy to chemically functionalize, cheap and widely abundant. Cellulose can be homogenized to produce nanocellulose by reducing the diameter of individual cellulose fibres [4]. Nanocellulose fibres have a high aspect ratio with a diameter of 5-100 nm and length of a few microns, providing high network ability by entanglement [5]. Nanocellulose can be processed into strong films [6], membranes [7], aerogels [8] and biocomposites [9].

Nanocellulose can be processed into films by vacuum filtration [10], solvent casting method [11] and also hot pressing [12]; of those, vacuum filtration is the fastest process. Strong films are formed by the interacting nanocellulose fibres arranged randomly into a 2D isotropic structure [13]. The low porous structure which results from the entangled packing of nanofibers enables to engineer nanocellulose sheets into barrier materials, particularly gas barriers. The oxygen permeability (OP) of nanocellulose sheets ($0.004 \text{ cm}^3 \cdot \mu\text{m} \cdot \text{m}^{-2} \cdot \text{day}^{-1} \cdot \text{kPa}^{-1}$) [14] are orders of magnitude lower than those achieved with petroleum based barrier materials such as ethylene-vinyl alcohol copolymers (EVOH) ($0.77 \text{ cm}^3 \cdot \mu\text{m} \cdot \text{m}^{-2} \cdot \text{day}^{-1} \cdot \text{kPa}^{-1}$) [15], low density polyethylene (LDPE) ($1900 \text{ cm}^3 \cdot \mu\text{m} \cdot \text{m}^{-2} \cdot \text{day}^{-1} \cdot \text{kPa}^{-1}$) [16], PVDC ($0.1\text{-}3 \text{ cm}^3 \cdot \mu\text{m} \cdot \text{m}^{-2} \cdot \text{day}^{-1} \cdot \text{kPa}^{-1}$) [17] and PVC ($20\text{-}80 \text{ cm}^3 \cdot \mu\text{m} \cdot \text{m}^{-2} \cdot \text{day}^{-1} \cdot \text{kPa}^{-1}$) [17]. Due to the high polarity of nanocellulose, water vapour affects the fibre-fibre bonds. This material characteristic weakens the original strong bonds holding the dry 2D structure, decreasing water permeability and deteriorating material stability [18, 19]. Controlling the water vapour transmission rates is critical to engineer good packaging materials and membranes with the required ability to extend the shelf life of moisture sensitive goods [20].

To enhance both oxygen and water barrier properties of nanocellulose sheets, inorganic nanomaterials have been introduced to the matrix, creating organic/inorganic composites. Among those nanoparticles, montmorillonite (MMT) stands out as reinforcement for polymeric matrices because of its high in-plane strength and stiffness, improving both barrier and mechanical properties [21, 22]. Disk shaped MMTs creates a tortuous path when arranged orthogonally to the diffusion pathway of permeating molecules. Composites made with nanocellulose- MMT therefore reduce the mass flux through the membrane, contributing to low OP and WVP values [23]. Further, the extent and the homogeneity of MMT dispersion is critical to enhance composite permeability properties [24, 25]. A performant MMT dispersion technique is required to achieve the targeted material properties.

MMT agglomeration plays an important role in the performance of diffusion barrier composite films [26]. Clay content exceeding 5 wt% decreases composite strength (brittleness) with the formation of large MMT agglomerates that functions as defects [27]. There are only a few studies on MMT/nanocellulose composites that have focused on WVP. This study analyses the effect of MMT agglomeration and systematically investigates the effect MMT content and structure on composite properties. We raise the hypothesis that by maximizing the surface area of MMT and

controlling the composite process, strong MMT-nanocellulose composites of very low WVP can be engineered. In this work, nanocellulose was used in combination with MMT to produce strong and flexible functional composite material by using a facile and scalable method. These nanocomposite-MMT clay composites are cheap, environmentally friendly and of very low WVP; they are ideal for packaging and membrane applications.

5.5 EXPERIMENTAL

5.5.1 Material

Microfibrillated cellulose (MFC) was purchased from DAICEL Chemical Industries Limited, Japan (grade Celish KY-100G). The MFC was supplied at 25% solids content and stored at 5°C as received. Rockwood Cloisite NA+ is a montmorillonite (MMT) powder kindly provided by Rockwood holdings, United States. The MMT powder was dispersed into deionized water (0.2 wt%) and agitated using a magnetic stirrer bar for 1 hour. Anhydrous calcium chloride (1-2 mm) was purchased from Science Supply Australia.

5.5.2 Method

5.5.2.1 Production of nanocellulose

A disintegrator equipped with 3 L vessel was used to disintegrate and dilute MFC to 0.5 wt% in deionized water at 15000 propeller revolutions. Homogenization was carried out to the diluted suspension using GEA Niro Soavi (Type: PANDAPLUS 2000) homogenizer at 1000 bar and 5 passes. Homogenized MFC (nanocellulose) have the average diameter of 20 nm and an aspect ratio of 286 which was measured by sedimentation technique [28] (Appendix I Figure C1-Figure C3). Solid content of nanocellulose after homogenization was measured again by pouring a known amount of suspension to a crucible followed by measuring the mass of the crucible after it was oven dried at 105°C for 4 hours. Suspension was diluted to 0.2 wt% for composite sheet preparation.

5.5.2.2 Nanocellulose film preparation

Nanocellulose films were prepared using a standard British hand sheet maker (model T205). Rapid sheet preparation method developed from our previous work was adapted [10]. The hand sheet maker was equipped with a woven filter with an average opening of 74 microns. A Whatman wet

strengthened filter paper (WHAT1114-185) with a pore size of 25 microns was placed on top of woven filter mesh and 0.2 wt% nanocellulose suspension (with 1.2 dry grams of nanocellulose) was poured into the chamber. Vacuum was applied until the film was formed. After the water drained, film was removed from the filter paper using blotting papers, pressed at 385 kPa for 5 minutes and then dried for 10 minutes at 105°C using a sheet drier.

5.5.2.3 Production of nanocellulose/MMT composites

Composite films with 9.1, 16.7, 23.1, 28.6, 33.3, 37.5 wt% MMTs were prepared as follows. A 0.2 wt% MMT dispersion containing one of 0.12, 0.24, 0.36, 0.48, 0.6, and 0.72 g of MMT was added at a flow rate of 20 mL/min to a beaker containing 0.2 wt% nanocellulose suspension (1.2 g of nanocellulose) to obtain composite suspensions with weight ratios of MMT to nanocellulose of 1:10, 1:5, 1:3.33, 1:2.5, 1:2, and 1:1.67, respectively. The nanocellulose suspensions were continually mixed during addition. The mixing time varied from 3 minutes to 18 minutes with MMT loading. Final suspension was poured into the British hand sheet maker and the composites were prepared as mentioned above.

Composite processing methodologies were tested by preparing two additional sets of composites; 1) by sonicating (sonicator model: VCX750 purchased from John Morris Scientific Pty Ltd for, used for 10 minutes at 80% amplitude) and 2) by high pressure homogenizing (1000 bar and 2 passes) above prepared original suspensions before sheet formation as mentioned above.

5.5.3 Characterization

5.5.3.1 Structure and morphology study

SEM analysis was performed using FEI Magellan 400 FEGSEM on front and cross sections of the composites. Samples were soaked in liquid N₂ and a fracture was done using a tweezer. Sample was mounted onto a metal sample holder and coated with a thin layer of Iridium prior to imaging.

TEM analysis was performed using FEI Tecnai G2 T20 TWIN on MMT suspensions. A copper grid of 3 mm with thin carbon layer on it was used to dip inside the MMT suspension and dried prior to imaging.

5.5.3.2 Thickness measurements

Thickness of the composites was measured using L&W thickness tester (model no 222) at ten points and then averaged.

5.5.3.3 Strength measurements

Composites were cut into small strips of 120 mm long and 15 mm wide and equilibrated at 23°C and 50% relative humidity for a minimum of 24 hours prior to dry tensile testing based on Australian/New Zealand Standard Methods 448 s and 437 s. The test span was 100 mm long. An Instron tensile tester (model 5566) was used to record the force against displacement with constant rate of elongation of 10 mm/min. For each sample, a mean value was obtained from 20 valid tests.

5.5.3.4 Particle and colloidal charge

The zeta potential measurements of nanocellulose and MMTs were performed with a Nanobrook Omni (Brookhaven Instruments) in a cuvette cell at 25 °C. Using the supplied software, zeta potential was calculated by determining electrophoretic mobility from an electrophoresis experiment using laser Doppler velocimetry and applying the Smoluchowski equation. Prior to the measurement, the 0.2 wt% nanocellulose suspension was centrifuged at 4400 rpm for 20 minutes to remove big aggregates and the supernatant containing colloidal nanocellulose was then used to measure the zeta potential. 0.2 wt% MMT suspension was used as it is for the measurements.

5.5.3.5 X-ray diffraction (XRD)

X-ray diffraction was conducted on MMT powder, pure nanocellulose sheets and composites using Rigaku Miniflex 600 equipped with an energy dispersive solid state detector which collects x-rays from a Cu tube operating at 40 kV and 15 mA. Scattered radiation was collected using a step size of 0.02° and at a scan speed of 2 degrees per minute for a range between 2° to 34°. From the XRD data, the interlayer spacing of MMTs was calculated using Bragg's law as follows:

$$d = \frac{\lambda}{2\sin\theta} \quad (\text{Equation 1})$$

Where d is the d-spacing (nm) is, λ is the wavelength of X-ray beam (nm), and θ is the angle of incidence.

5.5.3.6 Barrier properties

Water vapour transmission rate (WVTR) was conducted according to ASTM E96/E96M standard method [29]. Permeability cups complying with ASTM E96 standard were purchased from Thwing-Albert Instrument, USA. WVTR was carried out at 23°C and 50% relative humidity. Composites were kept in oven at 105°C for 4 hours before the testing. The variation in mass with time was recorded and the slope of the straight line was used to calculate WVTR.

5.6 RESULTS

Three types of nanocellulose-montmorillonite (MMT) composites were engineered through different preparation methods and by varying the MMT loadings (9.1-37.5 wt%). The water vapour permeability (WVP) properties were evaluated for each type of composite. All composites were flexible and foldable. The composites colour yellowished as the MMT content increased. This is due to the absorption spectra of MMT and similar observations were mentioned in literature [30].

5.6.1 Nanocellulose and MMT morphology

Nanocellulose of diameter and length of 20 nm and 5.7 μm , respectively, were prepared by homogenizing microfibrillated cellulose (MFC). Diameter and aspect ratio (used to calculate length) calculations are presented in supporting information S1-S3. The zeta potential measured for 0.2 wt% nanocellulose and 0.2 wt% MMT was -26 mV and -30.5 mV respectively, confirming electrostatically stable suspensions [31].

MMT particle size and shape varies upon MMT origin and composition. Silicon and aluminium are the main constituents. The chemical composition of the American MMT used is 49.4% SiO_2 , 19.7% Al_2O_3 , 0.8% Fe_2O_3 , 0.3% MgO , 1.5% CaO , 1.5% Na_2O and K_2O , and 25.7% H_2O [32]; giving a silica to alumina ratio of 2.5. Because of the silanol groups, the plates in the MMT layers have a negative charge while edges are positively charged; this provides self-ordering capability for MMTs during the filtration process. However, when in suspension, these charges are attractive causing detrimental MMT flocs/stacks [33].

Transmission electron microscopy (TEM) images of the MMT platelets reveal a distribution of shapes and sizes (Figure 1). Chemically exfoliated structures were not seen; the actual thickness

of the clay was difficult to obtain. However, the lateral dimensions of MMTs varies between 300-1000 nm in length.

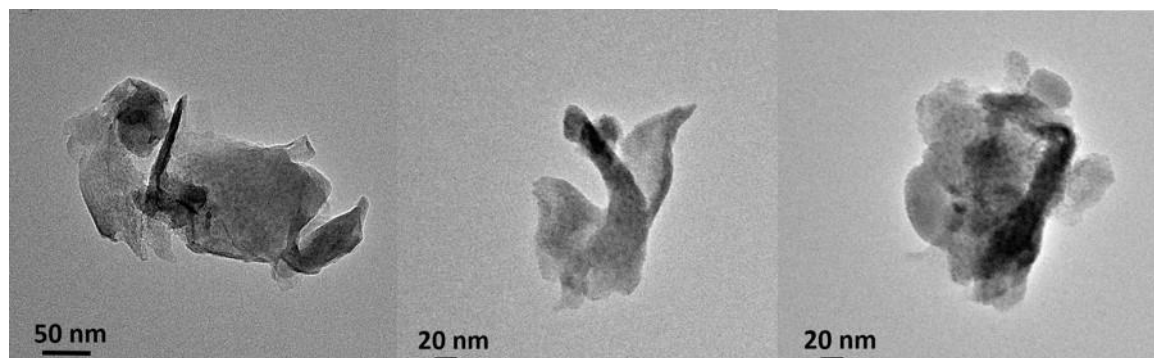


Figure 1: TEM images of montmorillonite (MMT) platelets

5.6.2 Structure of nanocellulose/MMT sheet

Energy-dispersive X-ray (EDX) and scanning electron microscopy (SEM) analysis was conducted on the composite sheets to quantify their morphology: structural differences, uniformity and dispersion of MMT within the cellulose matrix (Figure 2). Elemental mapping through EDX (along the cross section of the sheet) shows a homogeneous component distribution. For pure nanocellulose sheet (no MMT), only carbon and oxygen elements were measured (Figure 2a). Carbon is in excess compared to oxygen because of the chemical structure of cellulose ($C_6H_{10}O_5$) [34], the carbon to oxygen ratio was constant (estimate of 4.7 from Figure 2a intensities). The intensity variation observed was due to the uneven surface of the cross section during sample preparation for EDX analysis.

The elemental mapping conducted on the 33.3 wt% MMT composite sheet showed the presence of MMT throughout the cross section (Figure 2b). The silicon and aluminium contents were higher than the other MMT elements. The ratio of silicon to aluminium was estimated to 1.8 (from Figure 2b), close to the expected MMT ratio. Additional mapping of the SEM images is available in Appendix I Figure C4. Wavy lines appear in the cross section of the 28.6 wt% MMT composite (Figure 2c) which indicates a layered structure [35]. These characteristics were reported for different organic-inorganic composites [36, 37]. The primary driving force for layered structures are the hydrogen bonding and electrostatic interactions [35].

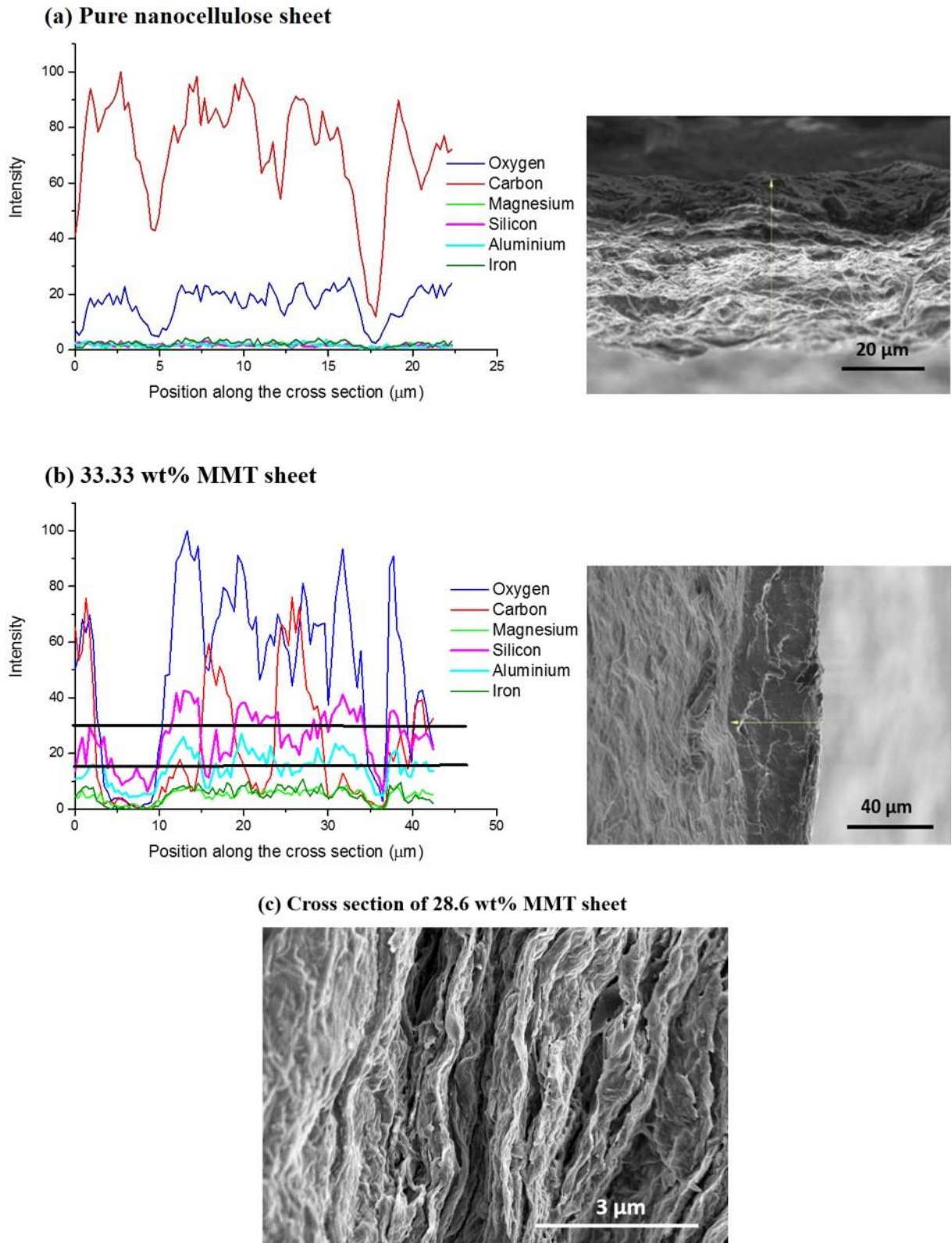
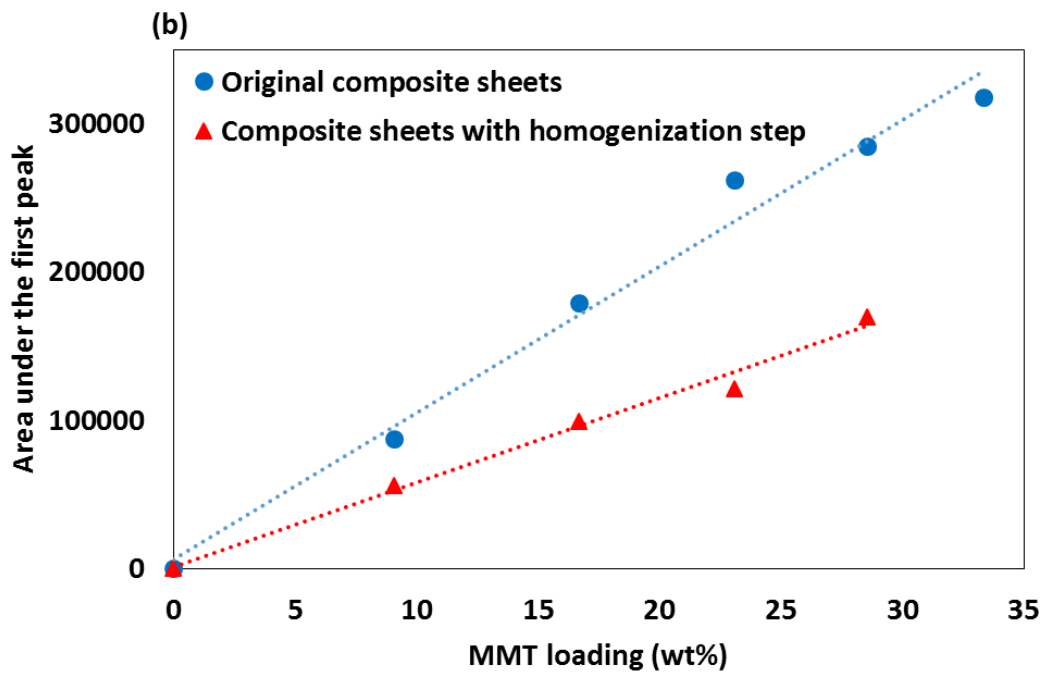
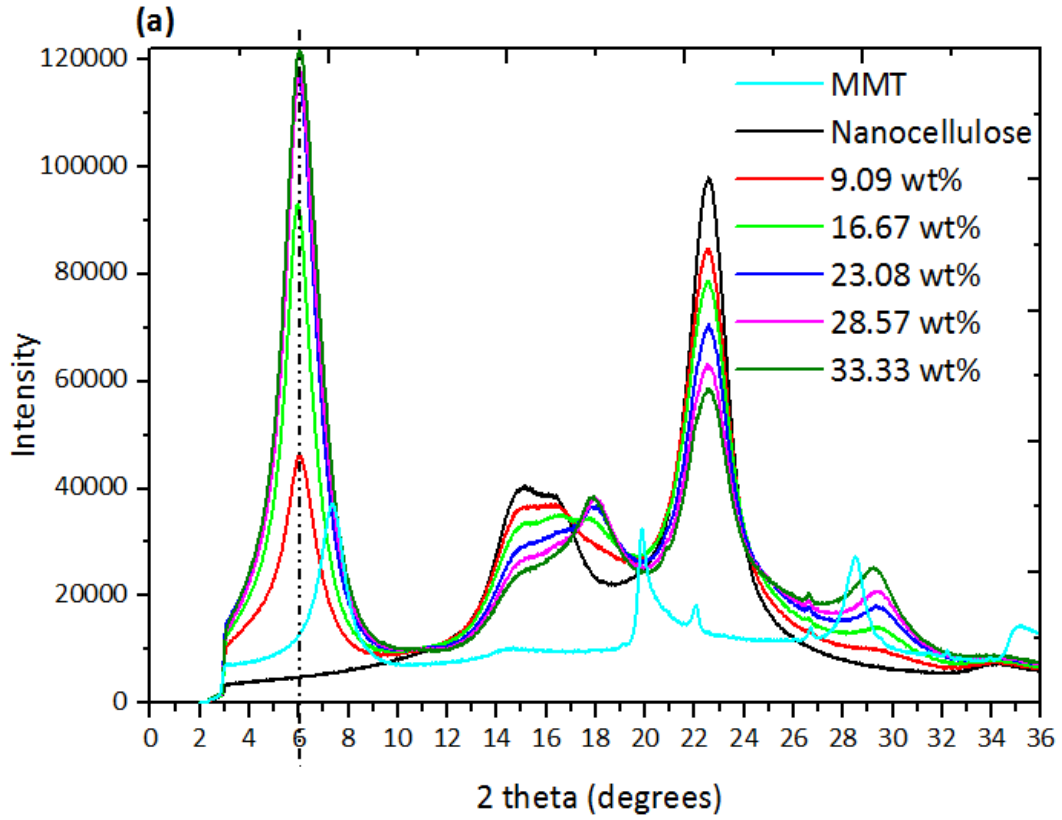


Figure 2. EDX and SEM images of composite sheets with various MMT compositions. Line scan across 0 wt% and 33.3 wt% sheet cross sections are shown in (a and b). The

cross-sectional image of the sheet with 28.6 wt% MMT shown in c) reveals a strong orientation of MMT platelets parallel to the substrate.

XRD was selected to quantify the orientation and phase present in MMT or nanocellulose network. Figure 3(a) shows XRD patterns for MMT, pure nanocellulose sheet and composite sheets with different MMT loading. Nanocellulose sheet has no characteristic peak in the 2° - 10° range. Any peaks in that range are due to MMT and represent the interlayer spacing between MMT's platelets which define the state of MMT within the nanocomposite structure [38]. The diffraction peak of MMT at angle 7.36° (corresponding to interlayer spacing of 1.2 nm) shifted to 6° (interlayer spacing 1.5 nm) with 9.1 wt % MMT in the sheet. Thereafter, peak positions remained constant and only intensity increased with MMT loading. Figure 3(b) shows the area under the first XRD peak versus MMT loading for the original composite sheets and composites produced with an additional high pressure homogenization step. The area under the peak directly correlates with the intensity, which corresponds to the amount of MMTs arranged in a given orientation. Peak area for the original composite was lower than for composite with homogenization. Figure 3(c) shows the diffraction angle (2 theta) of the first peak for the same sets of composites as a function of MMT loading. The peak position does not change significantly and only the intensity varies (XRD patterns for composite with high pressure homogenization step are in Appendix I Figure C5).



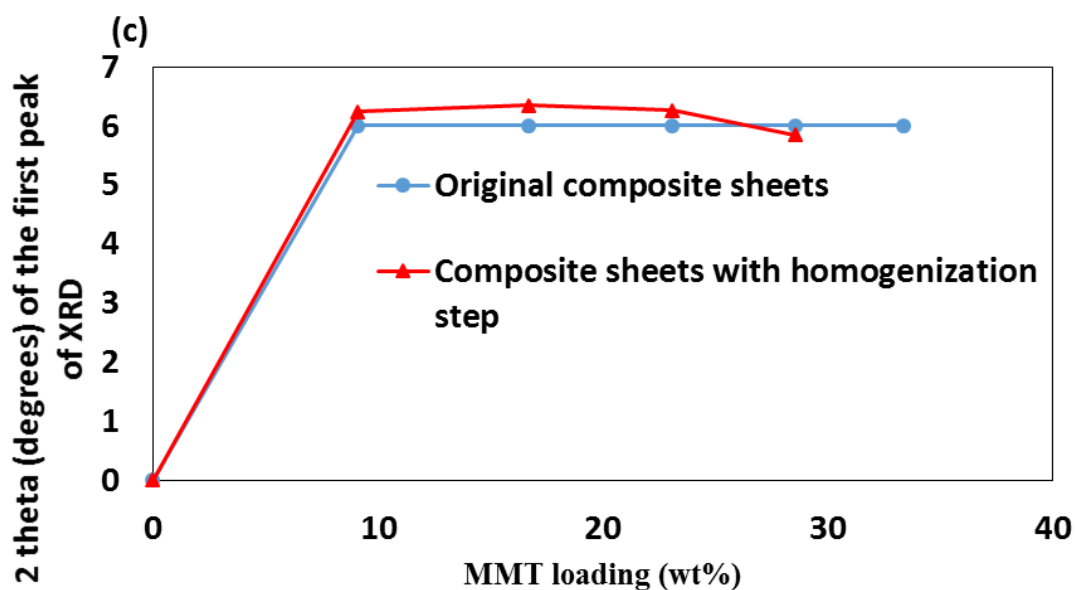


Figure 3: (a) XRD patterns of MMT, nanocellulose sheet and original composite sheets with different MMT loadings, (b) Area under the first XRD peak for original composite sheets and composite sheets with additional homogenization step, (c) 2 theta value of the first peak of the XRD graph with the loading of MMT for both sets of composites.

5.5.3 Mechanical properties

Mechanical properties were measured for composite of varying MMT content (Figure 4). All films are strong (average ~ 104 MPa). Microfibrillated cellulose (MFC) with an average diameter and length of 73 nm and 10.4 μm , respectively, were homogenized into nanocellulose. Maximum stress of 54.6 MPa and modulus of 4.6 GPa were measured for the MFC sheet (60 gsm). Nanocellulose sheets (20 nm diameter and 5.7 μm length) had a breaking stress of 105.7 MPa and modulus of 6.9 GPa.

Elastic modulus increased with MMT content compared to nanocellulose sheet (6.9 GPa), while strain at break did not change much and remained between 3.3 and 4.8%. The highest modulus was obtained at 10.6 GPa for 37.5 wt% MMT. Although the stress increased initially for low MMT content and decreased thereafter, overall, there is no significant variation in the stress at break. Low content of MMT addition (9.1-23.1 wt%) resulted in an increase in stress up to 108.8 ± 2.4

MPa. High content of MMT addition (28.6-37.5 wt%) decreased the stress slightly where the lowest stress being 97.5 ± 2.7 MPa for 37.5 wt%. All composites remained flexible and foldable.

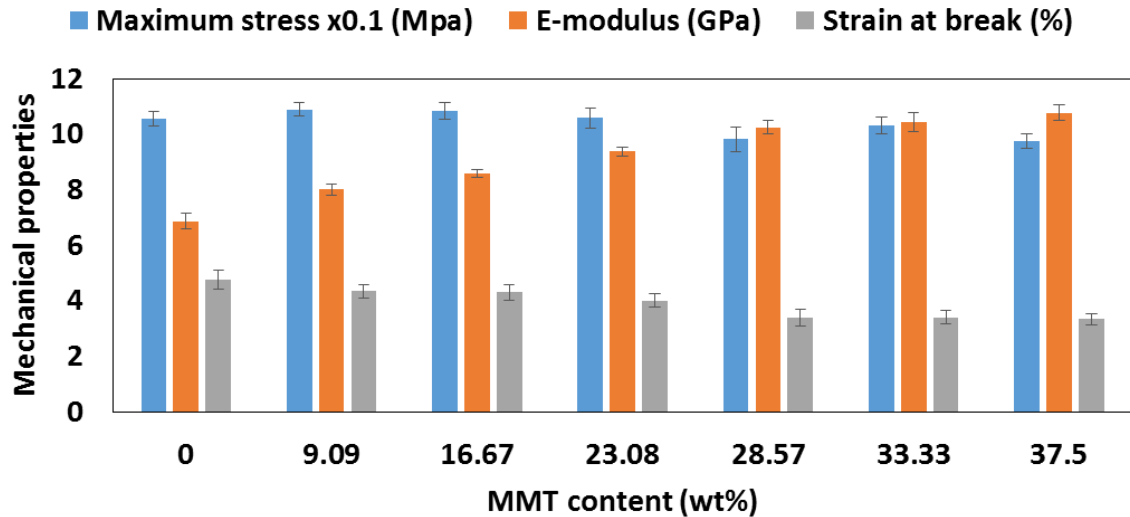


Figure 4: Mechanical properties obtained from tensile testing for original composite sheets with MMT loading. (a) maximum stress (blue), (b) elastic modulus (orange) and (c) strain to failure (grey). Deviations are based on 95% confidence level.

5.6.4 Barrier properties

Water vapour permeability (WVP) for composites prepared with different processing conditions is shown in Figure 5. Testing was conducted at 23°C and 50% relative humidity. For the original composite series, WVP decreased as MMT increased, reached a minimum at 16.7 wt% (13.3 ± 2.0 g.μm/m².day.kPa) and then increased again. For composites with a high pressure homogenizing step, the WVP decreased with MMT addition, reaching a minimum at 23.1 wt% (6.3 ± 1.5 g.μm/m².day.kPa) and then increasing again. We also tested the WVP for composites with a sonication step, where WVP increased significantly with MMT loading.

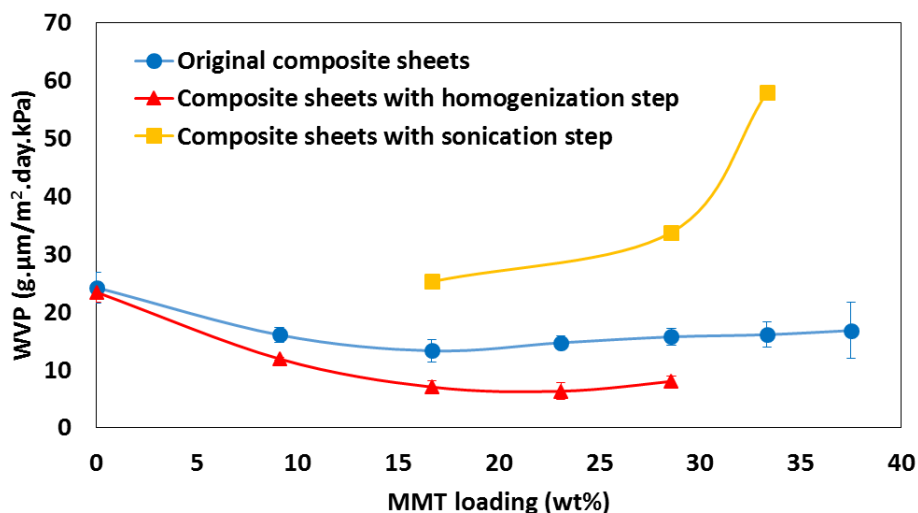


Figure 5: WVP of nanocellulose/MMT composites. Original composite sheets (blue dots), composite sheets with high pressure homogenization step (red triangles) and sonication step (yellow squares).

5.7 DISCUSSION

Our primary objective was to produce nanocellulose/montmorillonite (MMT) composites with well dispersed MMTs and nanocellulose to improve water barrier properties. The hypothesis tested was that MMT decreases cellulose composite permeability by increasing composite tortuosity. Here, we tested how the suspension state and the MMT aggregation depend on composite processing methodology. Solvent casting and evaporation are the most cited methods to prepare such composites, mostly for the larger area and well defined coating thickness they provide [3, 12]. However, the film formation using these techniques requires hours to days to process. Therefore, filtration process is easier [12, 35, 39]. Here, film formation involves the continuous addition of the MMT suspension to the agitated nanocellulose suspension, followed by filtration. The major advantages of this method are its simplicity, rapidity and the improved composite properties achieved. The technique can also easily be scaled up to industrial scale.

5.7.1 Barrier properties of nanocellulose/MMT sheets

The water vapour permeability (WVP) is affected by many parameters such as the type and structure of MMT, its dispersion and content in the nanocellulose matrix; all of which were tested in this study. SEM and EDX (Figure 2) confirmed that MMT particles are well distributed within and

across the sheet, creating a tortuous path for the permeating water molecules. No large MMT aggregations were observed by SEM. Some small scale aggregation was expected at high MMT loading.

In the nanocellulose matrix, MMTs can form one of three structure: 1) an exfoliated structure where MMT layers are completely separated, 2) an intercalated structure where nanocellulose can penetrate into MMT layers and alter the layer distances leaving the overall structure intact, and 3) a tactoid structure where MMT layers are not separated [40]. XRD conducted (Figure 3a) on the original composite sheets revealed the peak shift between 7.36° to 6° corresponds to an increase in layer distance of 0.3 nm. This increase is too small to enable nanocellulose to diffuse between MMT layers as the smallest diameter achieve by a nanocellulose fibril is 3 nm [41]. The structure of MMT in nanocellulose matrix is therefore tactoid. TEM images (Figure 1) also support the tactoid bulky structure as no delaminated individual layers was detected. The slight increase in interlayer spacing observed could be due to water molecules wedging into the interlayer and hydrating the cations, resulting in repulsive forces expanding the MMT layer [38].

WVP decreased for the original composite sheets (Figure 5, dots) with increase in MMT content up to 16.7 wt%. This is because the arrangement of MMT platelet's largest dimension perpendicular to the diffusion pathway creates a tortuous path which reduces WVP. Beyond 16.7 wt% MMT loading, WVP increased again as the hydrophilic MMT absorbs more water into the composite and MMT aggregates at high loading which opens new pores into the structure. The latter mechanism is believed to be predominant for permeability. Increase in intensity of the area under the first peak in Figure 3a proves the MMTs stacks formation in the original composite sheets, especially at high loadings.

The dispersion methodology of MMT in suspension is critical in engineering the WVP properties of composites. Clay stacking at high MMT loading is a common problem. Two MMT dispersion methods were investigated by using the same production process but with suspensions mixed to higher intensity: high pressure homogenization and sonication of the composite suspensions before sheet formation. WVP of composites processed with high pressure homogenization shows a similar pattern to that of the original, but with lower WVP values. XRD on the high pressure homogenized composites proved two phenomena: 1) the MMT stacks formed in the original composite sheets are broken down and 2) the preparation method does not change the structure

of MMT. The first point is proven by Figure 3(b) indicating that the area under the first peak for the high pressure homogenized composite sheets is lower than that of the original composite sheets with the same MMT loading (less stacks). The second point is demonstrated by Figure 3(c) which shows that the position of the first XRD peak does not change with MMT loading for both composites, indicating that the MMT tactoid structure in the composite does not change. Therefore, introducing high intensity clay delamination with homogenization improved WVP results by breaking down the MMT stacks, improving the effective surface area available, thus creating a more tortuous path (Figure 6, mechanism). Another approach to overcome the MMT stacking problem was to sonicate the suspension at high intensity before sheet making. However, this worsened the WVP results which may result from fracturing individual MMT platelets into fragments, decreasing the tortuous path. Processing greatly influences MMT aggregation and composites properties and performances.

There is a relationship between processing methodology and final composite properties. Evidences suggest that once MMT is mixed with nanocellulose, shear profile and mixing time are critical. If not processed quickly into composites, MMTs restack into large aggregates [42] driven by electrostatic and Van der Waals forces [43].

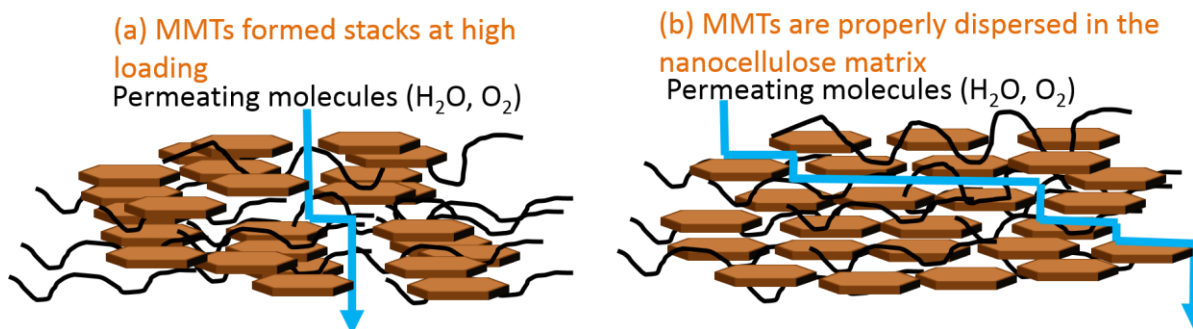


Figure 6: Mechanisms of MMT-stacking and arrangement of stacks in nanocellulose network (not to scale). (a) MMTs stack formation at high MMT loading; decrease the tortuous path; (b) MMT stacks are broken down using high pressure homogenization of nanocellulose/MMT suspension; increase the tortuous path for same amount of MMT.

5.7.2 Mechanical properties of nanocellulose/MMT sheets

Well dispersed MMT into nanocellulose suspension improves composite strength. The strength is important as we need strong composites for application perspective. The elastic moduli increased as well dispersed MMT restrict initial nanofiber movement upon force loading; this is further increased by strong interactions and hydrogen bonds between MMT and nanocellulose. The stress slightly decreased at high MMT content due to weak aggregation acting as stress initiator in composites [44]. The amount of MMT does not significantly reduce the composite strength, providing promising mechanical properties. Table 1 presents the mechanical properties reported in the literature for other nanocellulose-clay materials targeting water vapour barrier applications. The values reported for these nanocellulose composites vary significantly depending on sources, sizes, treatments of clay and production methods. For example, nanofibrillated cellulose (NFC)-vermiculite (VER) composites reported gave high stress values of 244 ± 24 MPa because of the significant reduction in NFC diameter (5-20 nm) due to carboxymethylation treatment [3]. Cellulose nanofibrils (CNFs) prepared through enzymatic pretreatment and homogenization (14 nm diameter) gave a stress of 91 MPa and reduced to 80 MPa when combined with mineral MMT [45]. This reduction could be due to improper dispersion of MMT in the composite.

5.6.3 Literature comparison

Table I compares the WVP values collected from nanocellulose-clay composites previously published. Although significant studies on cellulose-clay composites exist, only nine investigations aimed at reducing WVP. Various nanocellulose-nanoclay composites were made with surfactant [46], nanofibrillated cellulose surface modification [39, 47, 48], and poly(vinyl alcohol) and poly(acrylic acid) polymer addition [18]. Similar cellulose nanofibre-clay composites, but made from a different methodology, reported WVP of $1,800,000 \text{ g}\cdot\mu\text{m}/\text{m}^2\cdot\text{day}\cdot\text{kPa}$ [49]; WVP for nanofibrillated cellulose-vermiculite composite is $60.5 \text{ g}\cdot\mu\text{m}/\text{m}^2\cdot\text{day}\cdot\text{kPa}$ [3], bacterial cellulose with unmodified MMT composite, $53.3 \text{ g}\cdot\mu\text{m}/\text{m}^2\cdot\text{day}\cdot\text{kPa}$ [50] and the lowest WVP value reported for cellulose nanofibrils-mineral MMT composite made by solvent casting is $16.4 \text{ g}\cdot\mu\text{m}/\text{m}^2\cdot\text{day}\cdot\text{kPa}$ [45]. Some WVP values reported in Table 1 are very high because testing was conducted at higher relative humidity; these values cannot be compared to ours. The composites prepared here have the lowest WVP value reported of $6.3 \pm 1.5 \text{ g}\cdot\mu\text{m}/\text{m}^2\cdot\text{day}\cdot\text{kPa}$ at 23.1 wt% MMT while maintaining flexibility, recyclability and biodegradability. This review highlights that processing methodology

affects film properties. The simple method developed produced strong and flexible nanocellulose/MMT composites of the lowest WVP values .

Table I: Literature comparison of WVP for nanocellulose-clay based materials.

Composite type	Clay composition in the total composite	Production process	Temperature & Relative humidity	WVP ($\text{g um m}^{-2} \text{ day}^{-1} \text{ kPa}^{-1}$)	Tensile strength (MPa)	Modulus (GPa)	Strain (%)	Reference
Cellulose nanofibre (CNF)-clay	25 wt%	Vacuum filtration followed by vacuum oven dry	23°C, 50%	1800000 ^a	-	-	-	[49]
Cellulose foam with Tween 80 surfactant-surface modified montmorillonite	2.5 wt%	High shear homogenization and casting	20°C, 50%	216000	13.1±1.7	0.455	3.7±0.3	[46]
Trimethylammonium-modified nanofibrillated cellulose and layered silicate (TMA-NFC/Mica R120)	50 wt%	High shear homogenization followed by pressure filtration and vacuum hot-pressing	23°C, 85%	2200	104±5	9.5±0.2	1.9±0.3	[39]
Trimethylammonium-modified nanofibrillated cellulose and vermiculite (TMA-NFC/Vermiculite)	50 wt%	High shear homogenization followed by pressure filtration and vacuum hot-pressing	23°C, 85%	1400	135±4	10.3±1.1	3.3±0.7	[48]
Poly(vinyl alcohol) (PVA)-Poly(acrylic acid) (PAA)-NFC-sodium montmorillonite (MMT)	50 wt%	Solvent casting	23°C, 50%	105	approx1 90±11	approx. 15.9±0.3	approx. 3±0.5	[18]
Nanofibrillated cellulose (NFC)-vermiculite (VER)	20 wt%	24 h mixing followed by two high pressure	23°C, 50%	60	244±24	17.3±0.4	4.8±0.7	[3]

CHAPTER 5

		homogenization; and then solvent evaporation						
Bacterial cellulose (BC)- unmodified MMT	9 wt%	<i>In-situ</i> assembling or one-step biosynthesis process	25°C, 50%	53 ^a	-	-	-	[50]
Low methoxyl pectin (LMP)- carboxymethyl cellulose (CMC)-MMT	4 wt% (LMP-CMC ratio was 10:0)	Solvent casting	25°C, 50%	29	15.83	-	11±3	[47]
Cellulose nanofibrils (CNFs)- mineral montmorillonite (MMT)	32.5 wt%	Solvent casting	23°C, 50%	16	80	7.8	2.8	[45]

Note: the best film based on WVP from each article was chosen. Some of the tensile values are read off from graphs

^a pressure at which water vapour transmission conducted was assumed to be at atmospheric pressure since pressure was not specified.

5.8 CONCLUSION

A simple method was developed to produce strong nanocellulose/montmorillonite (MMT) composites having the lowest water vapour permeability (WVP) reported. The technique well disperses MMT into the nanocellulose matrix which significantly increases the network tortuosity; the method is also easily scalable into a manufacture process.

Nanocellulose composites of MMT content varying from 0 to 37.5 wt% were constructed. Transmission electron microscopy and X-ray diffraction analysis revealed MMT not to exfoliate in the cellulose composites but to remain as a tactoid structure. Scanning electron microscopy showed MMTs to be well distributed across and within the composite sheet, which contributes to a path of significantly increased tortuosity restricting diffusion of water molecules. The nanocellulose-MMT composites retained strength. With MMT loading as high as 37.5 wt%, the maximum stress and strain at break were maintained at 97.5 ± 2.7 MPa and 3.3%, respectively. The composites also remained strong and flexible when wet, characteristics required for application as packaging and membrane material. WVP is a parabolic function of the MMT concentration in the composite. WVP first decreased with addition of MMT due to the formation of path of increased tortuosity to reach a minimum, and then increased, as MMT aggregates which increased composite porosity. Sonication and high pressure homogenization of the MFC-MMT suspensions (before the filtration step) were investigated. Sonication worsened composite permeability while homogenization improved it significantly, where the lowest being 6.3 ± 1.5 g. μ m/m².day.kPa at 23.1 wt% loading. This value is the lowest reported for nanocellulose-clay based composites. These results support the hypothesis that MMTs form stacks at high loadings and the controlled breakdown of such stacks in a nanocellulose composites improves WVP properties.

This study presented an industrially scalable process to manufacture a novel thin, flexible and strong nanocellulose-MMT composite separation of very low WVP. These low cost and sustainable composites are ideal for packaging and membrane applications.

5.9 ACKNOWLEDGEMENT

The financial support of the Australian research council, Australian paper, Carter Holt Harvey, Circa, Orora, Norske Skog and Visy through the Industry Transformation Research Hub grant IH130100016 is acknowledged. Thanks to Monash University for MGS and FEIPRS scholarships and the MCEM centre for electron microscopy.

5.10 REFERENCES

1. Tharanathan, R., *Biodegradable films and composite coatings: past, present and future*. Trends in Food Science & Technology, 2003. **14**(3): p. 71-78.
2. Jung, K., et al., *High performance organic-inorganic hybrid barrier coating for encapsulation of OLEDs*. Journal of Materials Chemistry, 2011. **21**(6): p. 1977-1983.
3. Aulin, C., G. Salazar-Alvarez, and T. Lindström, *High strength, flexible and transparent nanofibrillated cellulose–nanoclay biohybrid films with tunable oxygen and water vapor permeability*. Nanoscale, 2012. **4**(20): p. 6622-6628.
4. Nakagaito, A.N. and H. Yano, *Novel high-strength biocomposites based on microfibrillated cellulose having nano-order-unit web-like network structure*. Applied Physics A: Materials Science & Processing, 2005. **80**(1): p. 155-159.
5. Sehaqui, H., T. Zimmermann, and P. Tingaut, *Hydrophobic cellulose nanopaper through a mild esterification procedure*. Cellulose, 2014. **21**(1): p. 367-382.
6. Sehaqui, H., et al., *Fast preparation procedure for large, flat cellulose and cellulose/inorganic nanopaper structures*. Biomacromolecules, 2010. **11**(9): p. 2195-2198.
7. Sehaqui, H., et al., *Stretchable and strong cellulose nanopaper structures based on polymer-coated nanofiber networks: an alternative to nonwoven porous membranes from electrospinning*. Biomacromolecules, 2012. **13**(11): p. 3661-3667.
8. Korhonen, J.T., et al., *Hydrophobic nanocellulose aerogels as floating, sustainable, reusable, and recyclable oil absorbents*. ACS applied materials & interfaces, 2011. **3**(6): p. 1813-1816.

-
9. Tingaut, P., T. Zimmermann, and F. Lopez-Suevos, *Synthesis and characterization of bionanocomposites with tunable properties from poly (lactic acid) and acetylated microfibrillated cellulose*. *Biomacromolecules*, 2009. **11**(2): p. 454-464.
 10. Varanasi, S. and W.J. Batchelor, *Rapid preparation of cellulose nanofibre sheet*. *Cellulose*, 2013. **20**(1): p. 211-215.
 11. Taniguchi, T. and K. Okamura, *New films produced from microfibrillated natural fibres*. *Polymer International*, 1998. **47**(3): p. 291-294.
 12. Österberg, M., et al., *A fast method to produce strong NFC films as a platform for barrier and functional materials*. *ACS applied materials & interfaces*, 2013. **5**(11): p. 4640-4647.
 13. Henriksson, M., et al., *Cellulose nanopaper structures of high toughness*. *Biomacromolecules*, 2008. **9**(6): p. 1579-1585.
 14. Fukuzumi, H., et al., *Transparent and high gas barrier films of cellulose nanofibers prepared by TEMPO-mediated oxidation*. *Biomacromolecules*, 2008. **10**(1): p. 162-165.
 15. Lagaron, J.M., et al., *Improving packaged food quality and safety. Part 2: Nanocomposites*. *Food Additives & Contaminants*, 2005. **22**(10): p. 994-998.
 16. Krochta, J.M., E. Baldwin, and M. Nisperos-Carriedo, *Permeability properties of edible films*. *Edible Coatings and Films to Improve Food Quality*, 1994: p. 139.
 17. Lange, J. and Y. Wyser, *Recent innovations in barrier technologies for plastic packaging—a review*. *Packaging Technology and Science*, 2003. **16**(4): p. 149-158.
 18. Spoljaric, S., et al., *Nanofibrillated cellulose, poly (vinyl alcohol), montmorillonite clay hybrid nanocomposites with superior barrier and thermomechanical properties*. *Polymer Composites*, 2014. **35**(6): p. 1117-1131.
 19. Twede, D., et al., *Cartons, crates and corrugated board: handbook of paper and wood packaging technology*. 2014: DEStech Publications, Inc.
 20. Ashely, R., *Permeability and plastic packaging. Polymer Permeability*, Elsevier Applied Science, London, UK, 1985: p. 269-308.
-

-
21. Yilmaz, O., et al., *On the stability and properties of the polyacrylate/Na-MMT nanocomposite obtained by seeded emulsion polymerization*. European Polymer Journal, 2012. **48**(10): p. 1683-1695.
 22. Priolo, M.A., et al., *Super gas barrier of transparent polymer– clay multilayer ultrathin films*. Nano letters, 2010. **10**(12): p. 4970-4974.
 23. Gusev, A.A. and H.R. Lusti, *Rational design of nanocomposites for barrier applications*. Advanced Materials, 2001. **13**(21): p. 1641-1643.
 24. Ray, S.S. and M. Okamoto, *Polymer/layered silicate nanocomposites: a review from preparation to processing*. Progress in polymer science, 2003. **28**(11): p. 1539-1641.
 25. Alexandre, M. and P. Dubois, *Polymer-layered silicate nanocomposites: preparation, properties and uses of a new class of materials*. Materials Science and Engineering: R: Reports, 2000. **28**(1): p. 1-63.
 26. Möller, M.W., et al., *UV - Cured, Flexible, and Transparent Nanocomposite Coating with Remarkable Oxygen Barrier*. Advanced Materials, 2012. **24**(16): p. 2142-2147.
 27. Okada, A. and A. Usuki, *Twenty years of polymer - clay nanocomposites*. Macromolecular Materials and Engineering, 2006. **291**(12): p. 1449-1476.
 28. Varanasi, S., R. He, and W. Batchelor, *Estimation of cellulose nanofibre aspect ratio from measurements of fibre suspension gel point*. Cellulose, 2013. **20**(4): p. 1885-1896.
 29. ASTM E96 / E96M-16, *Standard Test Methods for Water Vapor Transmission of Materials*, ASTM International, 2016.
 30. Ward, W., et al., *Gas barrier improvement using vermiculite and mica in polymer films*. Journal of membrane science, 1991. **55**(1): p. 173-180.
 32. nanoComposix, *ZETA POTENTIAL ANALYSIS OF NANOPARTICLES*. 2012: San Diego, CA p. 1-6.
 32. Ross, C.S. and S.B. Hendricks, *Minerals of the montmorillonite group, their origin and relation to soils and clays*. 1945. p. 2330-7102.
 331. Neimo, L., et al., *Papermaking chemistry*. 1999: Fapet Oy.
-

-
34. Klemm, D., et al., *Cellulose: fascinating biopolymer and sustainable raw material*. Angewandte Chemie International Edition, 2005. **44**(22): p. 3358-3393.
 35. Liu, A., et al., *Clay nanopaper with tough cellulose nanofiber matrix for fire retardancy and gas barrier functions*. Biomacromolecules, 2011. **12**(3): p. 633-641.
 36. Walther, A., et al., *Large-area, lightweight and thick biomimetic composites with superior material properties via fast, economic, and green pathways*. Nano letters, 2010. **10**(8): p. 2742-2748.
 37. Wang, R., et al., *Deformation mechanisms in nacre*. Journal of Materials Research, 2001. **16**(09): p. 2485-2493.
 38. Stiller, B., *The effect of montmorillonite nanoclay on mechanical and barrier properties of mung bean starch films*. 2008, Clemson University.
 39. Ho, T.T., et al., *Composites of cationic nanofibrillated cellulose and layered silicates: water vapor barrier and mechanical properties*. ACS applied materials & interfaces, 2012. **4**(9): p. 4832-4840.
 40. Carrado, K.A., *Synthetic organo-and polymer-clays: preparation, characterization, and materials applications*. Applied Clay Science, 2000. **17**(1): p. 1-23.
 41. Isogai, A., T. Saito, and H. Fukuzumi, *TEMPO-oxidized cellulose nanofibers*. Nanoscale, 2011. **3**(1): p. 71-85.
 42. Shori, S., et al., *Effect of interfacial pretreatment on the properties of montmorillonite/poly (vinyl alcohol) nanocomposites*. Journal of Applied Polymer Science, 2015. **132**(18).
 43. Furukawa, Y., et al., *Aggregation of montmorillonite and organic matter in aqueous media containing artificial seawater*. Geochemical transactions, 2009. **10**(1): p. 2.
 44. Wang, K., et al., *Epoxy nanocomposites with highly exfoliated clay: mechanical properties and fracture mechanisms*. Macromolecules, 2005. **38**(3): p. 788-800.
 45. Bardet, R., et al., *Substitution of nanoclay in high gas barrier films of cellulose nanofibrils with cellulose nanocrystals and thermal treatment*. Cellulose, 2015. **22**(2): p. 1227-1241.
-

46. Ahmadzadeh, S., et al., *Nanoporous cellulose nanocomposite foams as high insulated food packaging materials*. Colloids and Surfaces A: Physicochemical and Engineering Aspects, 2015. **468**: p. 201-210.
47. Yu, W.X., et al., *Properties of low methoxyl pectin - carboxymethyl cellulose based on montmorillonite nanocomposite films*. International Journal of Food Science & Technology, 2014. **49**(12): p. 2592-2601.
48. Ho, T., et al., *Liquid ammonia treatment of (cationic) nanofibrillated cellulose/vermiculite composites*. Journal of Polymer Science Part B: Polymer Physics, 2013. **51**(8): p. 638-648.
49. Honorato, C., et al., *Transparent nanocellulose-pigment composite films*. Journal of Materials Science, 2015. **50**(22): p. 7343-7352.
50. Algar, I., et al., *Improved Permeability Properties for Bacterial Cellulose/Montmorillonite Hybrid Bionanocomposite Membranes by In-Situ Assembling*. Journal of Renewable Materials, 2016. **4**(1): p. 57-65.

CHAPTER 6

WATER RESISTANT CELLULOSE – TITANIUM DIOXIDE COMPOSITES FOR PHOTOCATALYSIS

THIS PAGE HAS BEEN INTENTIONALLY LEFT BLANK

PREFACE

This chapter also uses the expertise obtained from experimental Chapter 2-4 in production and characterization of nanocomposites, to produce titanium dioxide (TiO₂) - nanocellulose composites for photocatalytic applications.

Here, polyamide-amine-epichlorohydrin (PAE) is used as a retention aid and also most importantly as a wet strengthening agent. The effect of PAE on photocatalytic activity of the TiO₂-nanocellulose composite is quantified. Small angle X-ray scattering (SAXS) and scanning electron microscopy (SEM) was also used to quantify the internal structure. The focus was to produce a portable, green highly effective photocatalytic material that is reproducible, cheap, easy to produce and easily scalable.

This chapter follows the third objective.

THIS PAGE HAS BEEN INTENTIONALLY LEFT BLANK

CHAPTER 6 WATER RESISTANT CELLULOSE – TITANIUM DIOXIDE COMPOSITES FOR PHOTOCATALYSIS

6.1 Graphical abstract	197
6.2 Abstract	197
6.3 Keywords	198
6.4 Introduction	198
6.5 Experimental	200
6.5.1 Material	200
6.5.2 Method	200
6.5.2.1 MFC sheet preparation	200
6.5.2.2 MFC-PAE-TiO ₂ composite sheet preparation	200
6.5.2.3 Photodegradation of methyl orange	201
6.5.3 Characterization	202
6.5.3.1 Structure and morphology study	202
6.5.3.2 Particle and colloid charge	202
6.5.3.3 PAE adsorption on MFC	202
6.5.3.4 Small angle X-ray scattering	202
6.6 Results	203
6.6.1 Photocatalytic activity performance.....	204
6.6.2 Photocatalysis repeatability	206
6.6.3 PAE effect on MFC flocculation	208
6.6.4 Retention efficiency of TiO ₂ in the composites	209
6.6.5 TiO ₂ and MFC morphology in composites.....	210
6.6.6 Small angle X-ray scattering	212
6.7 Discussion	213
6.6.1 Quality and durability of MFC-PAE-TiO ₂ composite.....	213
6.6.2 Effect of PAE on TiO ₂ nanoparticle retention	215
6.6.3 Composites photocatalysis activity	216
6.8 Conclusion	218

CHAPTER 6

6.9 Acknowledgement	219
6.10 References	220

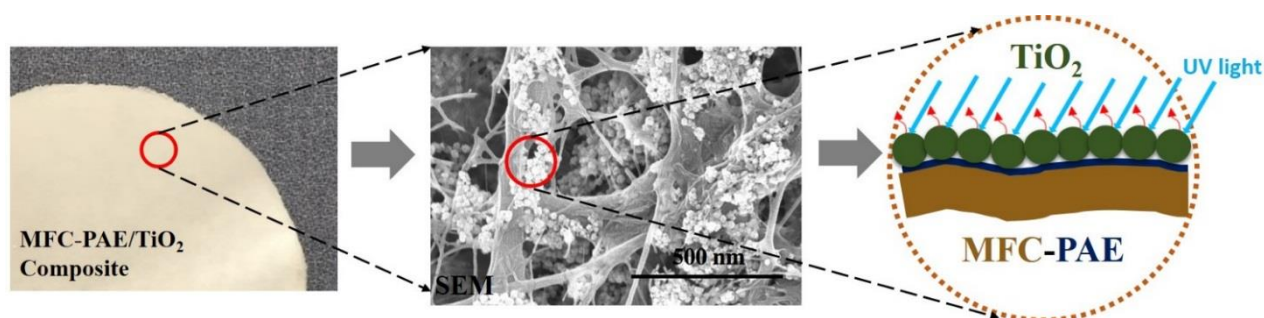
WATER RESISTANT CELLULOSE – TITANIUM DIOXIDE COMPOSITES FOR PHOTOCATALYSIS

Uthpala M. Garusinghe, Vikram. S. Raghuwanshi, Warren Batchelor* and Gil Garnier*

BioResource Processing Research Institute of Australia (BioPRIA), Department of Chemical Engineering, Monash University, VIC-3800, Australia

*Corresponding authors: [REDACTED]

6.1 GRAPHICAL ABSTRACT



6.2 ABSTRACT

Novel water resistant photocatalytic composites of microfibrillated cellulose (MFC) – polyamide-amine-epichlorohydrin (PAE) – titanium dioxide (TiO₂) nanoparticles (NPs) were prepared by a simple two step mixing process. The composites produced are flexible, uniform, reproducible and reusable; they can readily be removed from the pollutant once used. Only a small amount of TiO₂ NPs are required for the loaded composites to exhibit a remarkable photocatalytic activity which is quantified here as achieving at least 95% of methyl orange (MO) degradation under 150 min of UV light irradiation for the composite with best combination. The cellulose network combined with PAE strongly retains NPs and hinders their release in the environment. PAE dosage (10 and 50 mg/g MFC) controls the NP retention in the cellulose fibrous matrix. As TiO₂ content increases, the photocatalytic activity of the composites levels off to a constant; this is reached at 2 wt% TiO₂ NPs for 10 mg/g PAE and 20 wt% for 50 mg/g PAE. SEM and SAXS analysis confirms the uniform

distribution of NPs and their formation of aggregates in the cellulose fibre network. These economical and water resistant photocatalytic paper composites made by a simple, robust and easily scalable process are ideal for applications such as waste water treatment where efficiency, reusability and recyclability are important.

6.3 KEYWORDS

Photocatalysis, Titanium dioxide, Microfibrillated cellulose, polyamide-amine-epichlorohydrin, composites, aggregation, water resistant.

6.4 INTRODUCTION

Inorganic nanoparticles-polymer composites have recently gained much attention for engineering functional materials and interfaces. Metals and metal oxides nanoparticles (NPs) such as TiO_2 [1], Au [2] and Fe_2O_3 [3] are distinct materials with size dependent properties in photocatalysis and photoelectronics applications [4]. Among those, TiO_2 NPs are low cost material for industrial applications in photo-catalysis, photochemical hydrogen production [5], water purification and solar energy conversion [6, 7].

In 1972, Fujishima and Honda discovered photocatalysis with TiO_2 NPs [8]. Anatase TiO_2 gives high oxidizing power when irradiated by UV light, which has generated tremendous interest thanks to its low cost, high chemical stability and low toxicity [9-11]. Optical excitation with energy exceeding TiO_2 band gap energy results in the formation of conduction band electrons and valence band holes. Both are powerful reductants and oxidants [12]. Hydroxyl radicals produced in TiO_2 can be used to convert many organic compounds to CO_2 and H_2O . Therefore, TiO_2 has been used to decompose various environmental pollutants [13, 14]. The size and the length scale of these NPs play a major role in its properties and applications [15].

Nano scale TiO_2 (1-100 nm) possesses high surface area and shows enhanced photocatalytic activity [15]. However, TiO_2 tendency to form agglomerates can significantly decrease its activity [16-18]. Using bare TiO_2 NPs in water treatment has issues in their collection and poses uncontrolled NPs release as an environmental danger [19-22]. Incorporating TiO_2 NPs directly into a matrix combines the advantages of NPs stability and retention; this enables water treatment without risk of NPs leaching or contamination [23].

Previously, researchers have engineered composites with TiO₂ NPs embedded in different networks such as silicon, carbon fibre, cellulose fibre and polypropylene/clay [24-27]. However, these composites have issues either in retention of NPs, are expensive to produce, difficult to recycle, non-biocompatible, lack of reusability or are not showing effective or controlled photocatalytic activity. There is a lack of fundamental understanding of the retention, dispersion and aggregation of NPs for the controlled photocatalysis activity of composites.

Many strategies have been explored for retaining inorganic NPs in sustainable material networks [28-30]. In this category, microfibrillated cellulose (MFC) is a low cost, biodegradable and recyclable natural fibrous matrix having high specific strength and surface area promising good NPs integration [22, 31, 32]. MFC is more stable in aqueous environments than conventional wood fibres [33, 34]. Previously, many methods to produce and characterize MFC-NPs composites with high NP loadings (80 wt%) and controlled nanostructures were reported [29, 35, 36].

We raise the hypothesis that the content and the aggregation state of TiO₂ in MFC composites control their photocatalytic activity when exposed to UV light. Our proposed methodology is to disperse TiO₂ NPs in a MFC network with controlled retention, distribution and agglomeration, while keeping the wet strength of the produced composites. These parameters are believed to be important variables for optimizing the photocatalytic activity of composites. Therefore, a material which serves as both wet strength and NP's retention aid is required. Polyamide-amine epichlorohydrin (PAE) is a widely used wet-strength agent in the tissue and packaging industries. Its wet strength develops primarily by ester bond formation between the azetidinium groups of PAE with the carboxyl groups of the bleached cellulose fibres and is achieved during the drying process [37].

In this study, MFC is investigated as TiO₂ NPs carrier to produce water resistant fibrous composites of varying NPs loading. Here, PAE is used both as wet strength agent to consolidate the MFC structure and as a retention aid for the TiO₂ NPs. Photocatalytic activity of composites with different NPs and PAE dosages is monitored by measuring the degradation kinetics of Methyl Orange (MO) solutions by UV irradiation. By changing the PAE concentration, we aim to vary the TiO₂ aggregation state. Scanning electron microscopy (SEM) and Small angle X-ray Scattering (SAXS) measurements are used to quantify TiO₂ NP distribution in the composites and are analysed in terms of PAE content. Our objective is to produce bio-compatible and reusable TiO₂ NPs/MFC

composites of controlled photocatalysis. Further, we aim at exploring TiO₂ catalytic activity in terms of NPs distribution and aggregation state controlled with PAE dosage.

6.5 EXPERIMENTAL

6.5.1 Material

Microfibrillated cellulose (MFC) was purchased from DAICEL Chemical Industries Limited, Japan (grade Celish KY-100G). MFC was supplied at 25 wt% solids and stored at 5°C as received. The mean diameter and the aspect ratio of MFC was 73 nm and 100-150, respectively [38]. Anatase titanium dioxide (TiO₂) was purchased from US Research Nanomaterials, USA. The nanoparticle (NP) size ranged within 30-50 nm and was received at 40 wt% solids. The commercial polyamide-amine-epichlorohydrin (PAE) was provided by Nopco Paper Technology Pty Ltd, Australia (33 wt% solids). Methyl Orange (MO) was purchased as a powder from Sigma Aldrich.

6.5.2 Method

6.5.2.1 MFC sheet preparation

MFC sheets were prepared using a standard British hand sheet maker (model T205). The hand sheet maker was equipped with a woven filter with an average opening of 74 microns. A Whatman wet strengthened filter paper (WHAT1114-185) with a pore size of 25 microns was placed on top of the woven filter and a 0.3 wt% MFC suspension (with 1.2 g dry mass of MFC) was poured into the column. Once the water drained under gravity, the wet film was taken out using blotter papers, the filter paper was removed, and the sheet was pressed at 385 kPa for 5 minutes and then dried at 105 °C using a sheet drier.

6.5.2.2 MFC-PAE-TiO₂ composite sheet preparation

Two sets of MFC-PAE-TiO₂ composites were produced:

1. **Composites with low PAE dosage:** 0.3 wt% MFC (1.2 g fixed), 0.01 wt% PAE (10 mg PAE/g MFC fixed) and with varying TiO₂ loading at 0.5, 1, 2, 5, 10, 40 and 80 wt%.
2. **Composites with high PAE dosage:** 0.3 wt% MFC (1.2 g fixed), 0.03 wt% PAE (50 mg PAE/g MFC fixed) and with varying TiO₂ loading at 2, 5, 20, 40 and 80 wt%.

The composites were prepared in a two-step process. Firstly, the PAE suspension was added at a constant flowrate of 30 mL/min into a beaker containing 0.3 wt% (1.2 g fixed) MFC, while stirring the suspension using a hand stirrer (high shear mixing). Secondly, 0.1 wt% TiO₂ suspensions were strongly sonicated (sonicator model: VCX750 purchased from John Morris Scientific Pty Ltd for, used for 10 minutes at 80 % amplitude) and added to the MFC-PAE suspension at a constant flowrate of 20 mL/min, while stirring the entire suspension.

Suspensions were poured into the British hand sheet maker and the composite sheets were made as described above.

6.5.2.3 Photodegradation of methyl orange

The photocatalytic degradation tests were carried out at room temperature using MO as a model dye. A 100 W lamp (365 nm wavelength) was used as the light source. The samples were cut into 2.5 x 2.5 cm² pieces and dispersed in a 50 mL beaker filled with 15 mL of 5 ppm pH 3 MO aqueous solution. The sample immersed in the beaker was kept in the dark for 2 hours until the maximum adsorption of MO by MFC prior to photocatalytic experiment was reached. The beaker was then subjected to UV radiation for MO photocatalytic degradation. The distance between the liquid surface and the light source was 19 cm. At given irradiation time intervals, the solution was collected for analysis using UV-vis spectroscopy (Model: Cary 60 UV-Vis, Agilent Technologies). Experimental set up is shown in Figure 1.

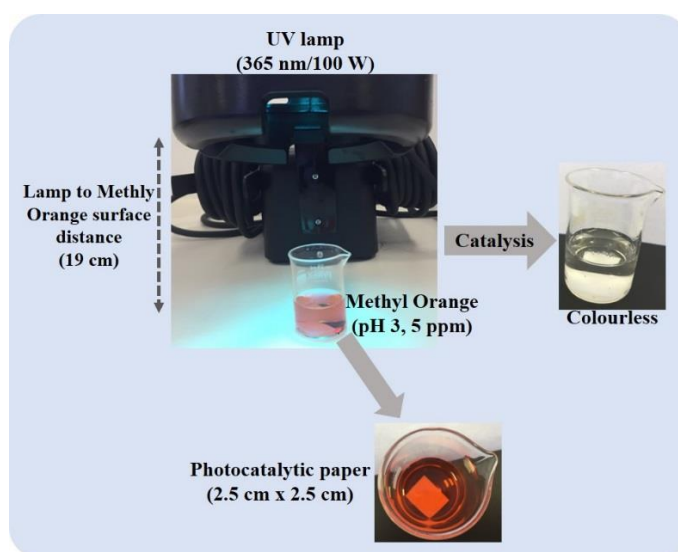


Figure 1: Experimental setup for photocatalytic degradation of methyl orange. The paper samples were cut to squares (2.5 cm x 2.5 cm).

6.5.3 Characterization

6.5.3.1 Structure and morphology study

Scanning electron microscopy (SEM) analysis of the composite sheets was performed using a FEI Magellan 400 FEGSEM. Samples were cut into 3 x 3 mm² mounted onto a metal sample holder and coated with a thin layer of Iridium prior to imaging.

6.5.3.2 Particle and colloid charge

The zeta potential measurements of MFC, TiO₂ and PAE were performed with a Nanobrook Omni (Brookhaven Instruments) in a cuvette cell at 25 °C. The zeta potential was calculated, using the supplied software, by determining electrophoretic mobility from an electrophoresis experiment using laser Doppler velocimetry and applying the Smoluchowski equation. PAE at 0.01 wt% concentration was added at different dosages to a 0.3 wt% MFC suspension and mixed using a hand stirrer for 3 minutes. MFC-PAE suspension was centrifuged at 4400 rpm for 20 minutes to remove big agglomerates and the supernatant was used to measure zeta potential.

6.5.3.3 PAE adsorption on MFC

This method described by Peng and Garnier [39] was adopted. Particle charge detector (Mutek PCD-03, BGT Instruments) was used to titrate the amount of PAE in the supernatant after centrifugation using an opposite charged polyelectrolyte until point of zero charge is met. The polyelectrolyte used was PES-Na of known concentration (0.000125 N), and was added at 10 mL dosages to the PAE-MFC supernatant. Titrant consumption was measured in mL and converted into PAE concentration through a standard curve method.

6.5.3.4 PAE Small angle X-ray scattering

Small angle X-ray scattering (SAXS) measurements were made on a Laboratory Bruker N8 Horizon using a CuK α ($\lambda = 0.154$ nm) micro-source. The sample to detector distance was 0.6 m covering the q range between ~ 0.15 to 3.7 nm⁻¹. The scattered photons after interacting with the sample were collected using a 2D Vantec-500 detector (pixel size ~ 70 μ m \times 70 μ m). Final scattering curves were obtained after data reduction and radial averaging using Bruker EVA software.

6.6 RESULTS

The photocatalytic activity of water resistant, thin and flexible cellulose/PAE/titanium dioxide (TiO_2) nanoparticles (NPs) composites was investigated by following the UV induced degradation kinetics of Methyl Orange (MO) dye aqueous solutions. Composites varying in TiO_2 NPs and PAE contents were prepared. The UV-vis spectroscopy for MO aqueous solutions denotes two distinct absorption peaks appearing at 275 nm and 500 nm (Figure 2). The band at 500 nm was selected to measure the effect of photocatalysis on the degradation of MO as this peak decreases rapidly as increases UV light exposure time of the photocatalytic material (Appendix I -Figure D1). In 3 hours the colour of the MO solution changes from an intense red/orange to colourless, which indicates degradation of MO (Figure 2 inset).

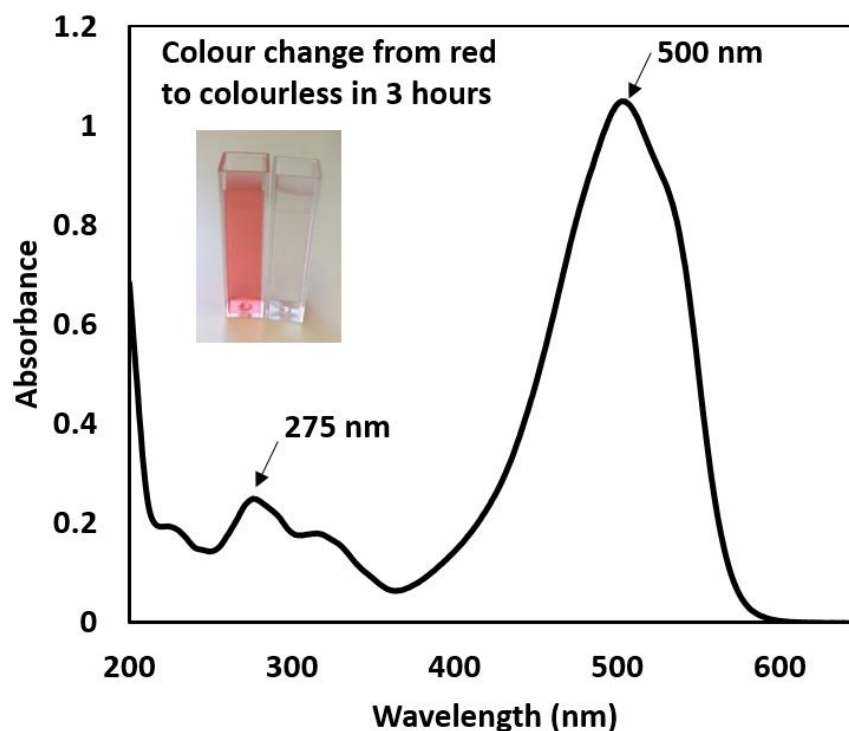


Figure 2: UV-visible spectrum of a methyl orange aqueous solution indicating two absorption maxima. The inset illustrates the methyl orange solution colour change by photocatalysis before and after 3 hours UV exposure over TiO_2 -MFC composite.

6.6.1 Photocatalytic activity performance

The photocatalytic degradation kinetics of MO is shown as a function of TiO₂ loading for 10 mg/g (10 mg PAE/g MFC) and 50 mg/g (50 mg PAE/g MFC) in Figures 3a and 3b, respectively. The intensity of the MO peak decreases with exposure time for all composites. Although the rate at which MO decomposes changes for different composites, it takes roughly 3 hours for MO colour to change from the original red/orange colour to transparent and colourless (Figure 2 inset).

There is virtually no photocatalytic activity shown by composites without TiO₂ (MFC-PAE only) as indicated in Figure 3 (filled squares). Due to the initial adsorption of the MO dye onto MFC, its concentration initially decreased by ~20 % in about 2 hours as MFC-PAE paper is kept under visible light. The adsorption equilibrium is gradually reached after 4 hours. Therefore, all test samples were kept in MO solutions and in the dark for 2 hours prior to UV light irradiation.

The performance of the TiO₂-MFC composites made with lower PAE dosage (10 mg/g) is shown in Figure 3a. As TiO₂ loading increased to 1 and 2 wt%, the photocatalytic activity systematically increased. At 2 wt% a noticeable increase in photocatalytic activity was observed compared to 1 wt%. Composites with addition levels of 5 to 80 wt% TiO₂ behaved similarly to 2 wt% and showed the highest photocatalytic activity for this group. Photocatalytic activity decreased in a weak exponential fashion to 20 % of the original dye concentration after ~120 minutes for the 2-80 wt% TiO₂ composites group and ~150 minutes for the 1 wt% TiO₂ composite.

The degradation curve for 40 wt% TiO₂-MFC composite with no PAE is also shown in Figure 3a (filled diamonds). There is still photocatalytic activity; this suggests that some TiO₂ NPs are retained- even with no PAE present.

The performance of TiO₂-MFC composites with the high PAE dosage (50 mg/g) is shown in Figure 3b. The degradation pattern is similar to that of composites with 10 mg/g; however, the photocatalytic activity saturation is reached at 20 wt% TiO₂ loading and remains constant thereafter. The overall degradation rate with 20-80 wt% TiO₂ was faster than for composites made with 10 mg/g (indicated by plotting the degradation graph for 40 wt% TiO₂ sheet with 50 mg/g in Figure 3a-dotted line). Here, the photocatalytic activity decreased to 20% of the original dye concentration after ~90 minutes for the 20-80 wt% TiO₂ composites group and ~120 minutes for the 2-5 wt% TiO₂ composite group.

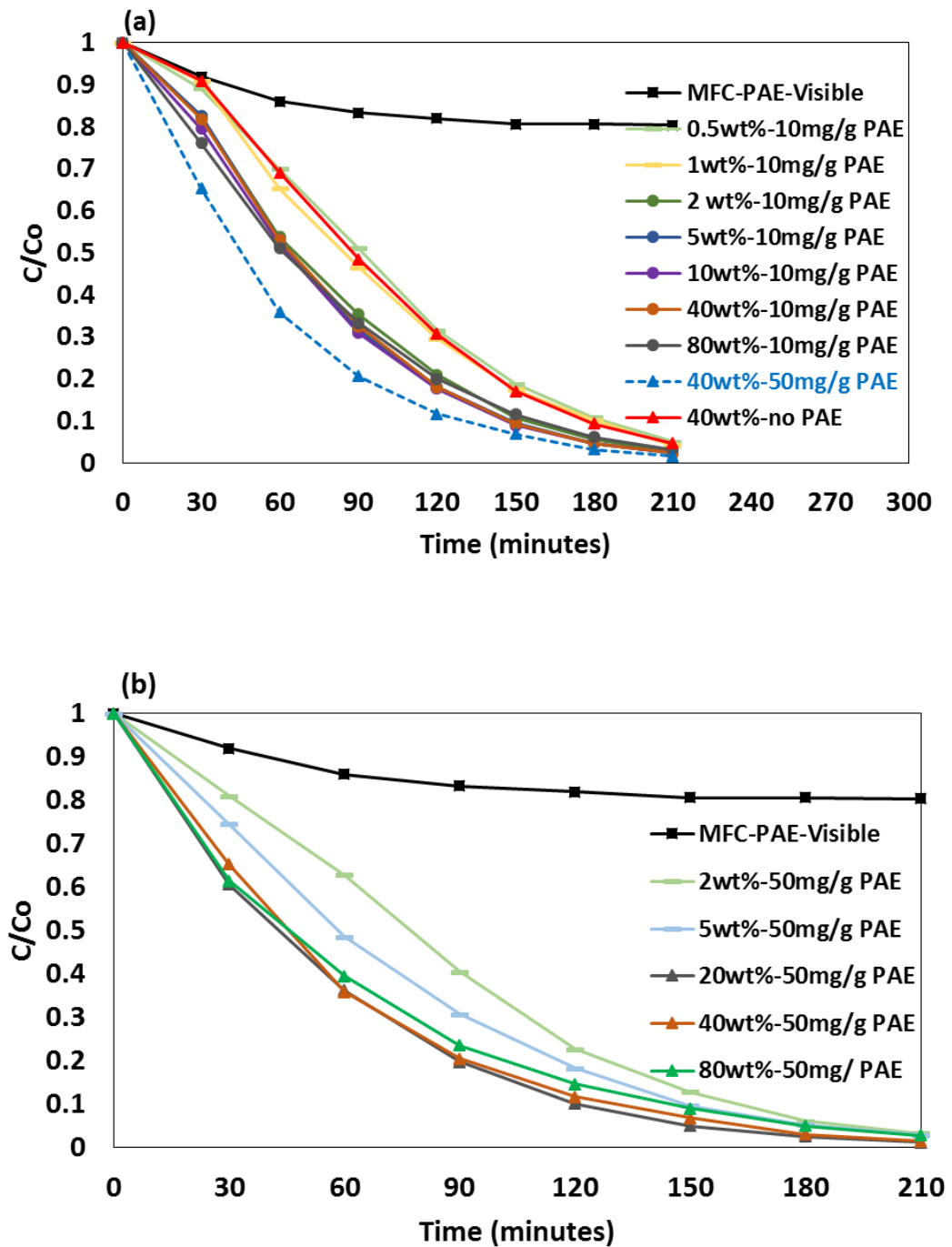
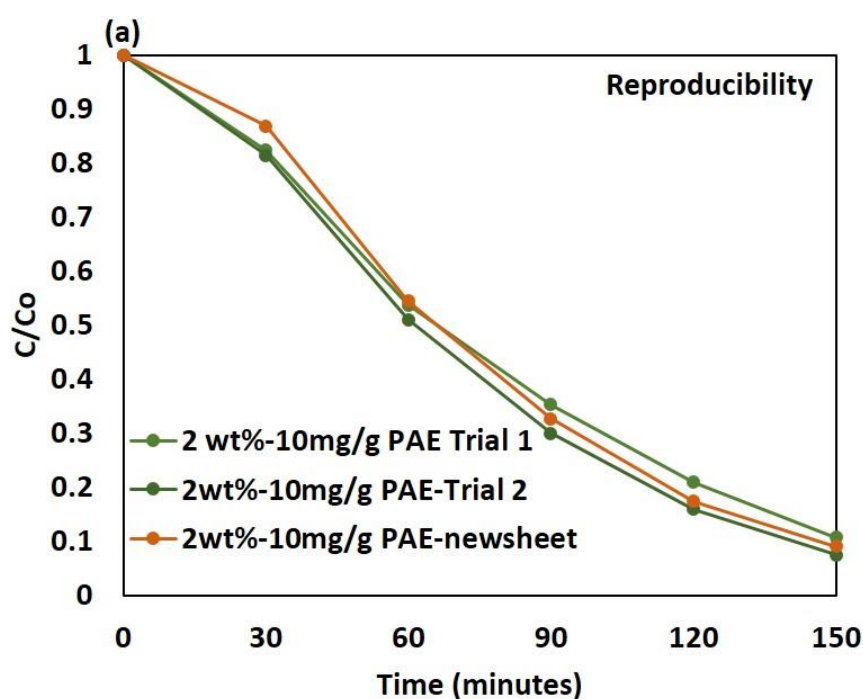


Figure 3: Photocatalytic activity of TiO₂-MFC composites with different TiO₂ loadings retained with (a) 10mg PAE/g MFC and (b) 50mg PAE/g MFC.

6.6.2 Photocatalysis repeatability

Uniformity of the sheet and photocatalytic activity repeatability was measured by cutting two test strips (2.5 cm x 2.5 cm) from two different locations from the same original composite. Reproducibility of sheet was tested by preparing two different composite sheets with the same TiO₂, MFC and PAE content and testing their photocatalytic activity. Figure 4a & b shows an excellent repeatability and reproducibility in the MO photocatalytic degradation from composite sheets made with 2 wt% and 5 wt% TiO₂ retained with 10 mg PAE /g.

Sheet reusability was measured by testing the photocatalytic activity of the same sample 3 times. After each run, the test piece was washed with deionized water to remove any MO residue and dried. Photocatalytic activity of the composite sheets with 1 wt% TiO₂ and PAE 10 mg/g shows identical activity even after 3 cycles (Figure 4c).



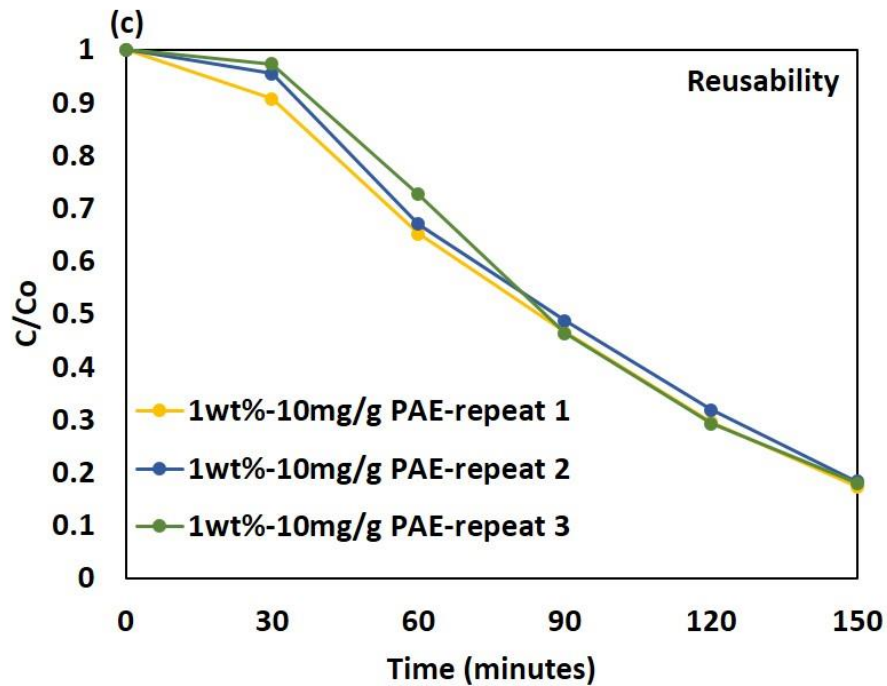
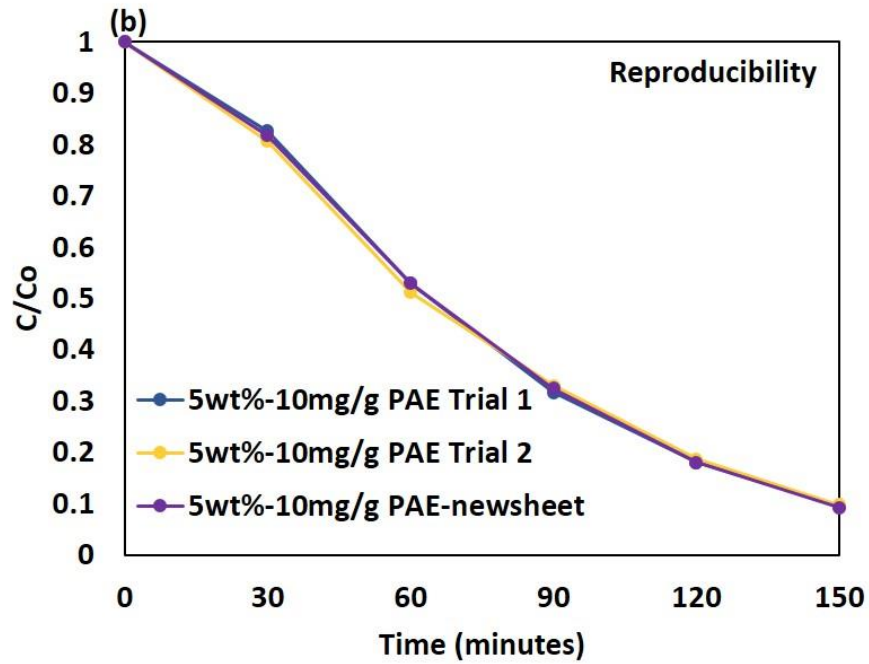


Figure 4: Photocatalytic repeatability and reproducibility for MO solution degradation over UV irradiated MFC-TiO₂ composites made with 10 mg PAE/g MFC and: (a) 2 wt% and (b) 5 wt% TiO₂; (c) Composite reusability for 3 full testing cycles (1wt% TiO₂ and 10 mg PAE/g).

6.6.3 PAE effect on MFC flocculation

The adsorption isotherm of PAE onto MFC is presented in Figure 5. PAE has a high affinity for MFC as shown by the initial linear portion of the curve having a slope of 1 (Figure 5 inset). The linear part of the curve states that all PAE in solution adsorbs onto MFC until a concentration of 10 mg/g. The PAE adsorption then slows down, to eventually reach a plateau at around 15 mg PAE/g MFC.

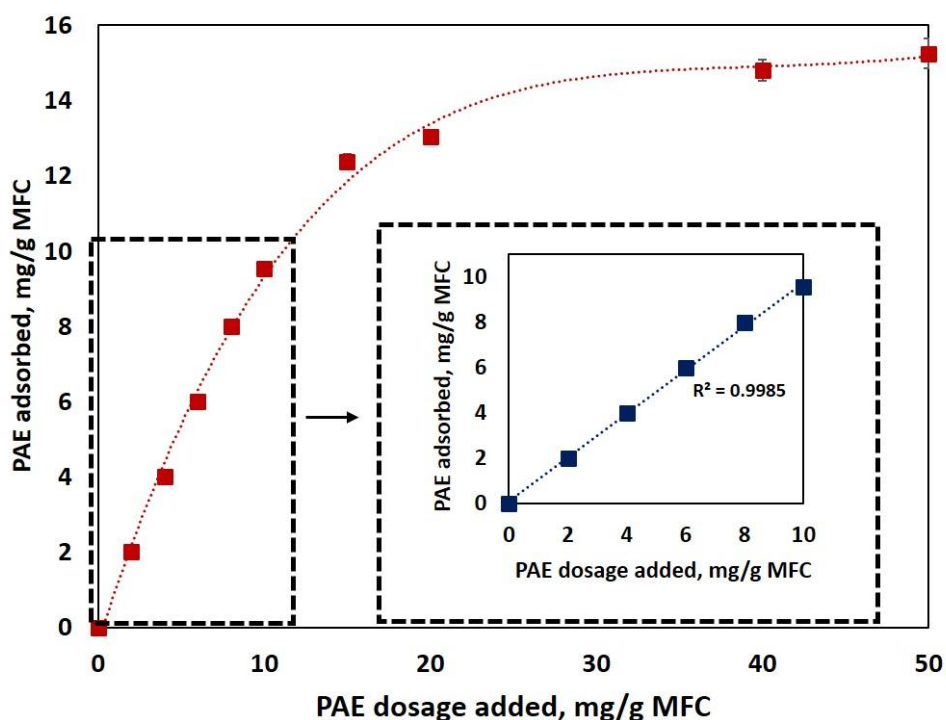


Figure 5: Adsorption isotherm of PAE adsorbed on MFC as a function of PAE concentration in solution. The inset highlights the linear adsorption portion at low PAE concentrations. Error bars indicate the standard deviation.

Figure 6 shows the MFC zeta potential as a function of PAE concentration. MFC has a zeta potential of -26 mV, while that of TiO_2 is -11 mV (shown by filled square). MFC charge increases linearly with PAE concentration up to 10 mg/g, corresponding to a charge of +25 mV, to level off thereafter and reach a plateau at +40 mV for a PAE dosage of 50 mg/g. Colloids having an absolute charge higher than 25 mV are considered to be stable. This means that MFC is expected to be stable in solution, while there is a possibility for TiO_2 to form some small or weak aggregates in solution, and even to weakly deposit onto MFC. However, MFC and TiO_2 NPs fully covered by PAE are expected to be

strongly electrostatically stabilized; no TiO_2 aggregates nor TiO_2 adsorption onto MFC are expected.

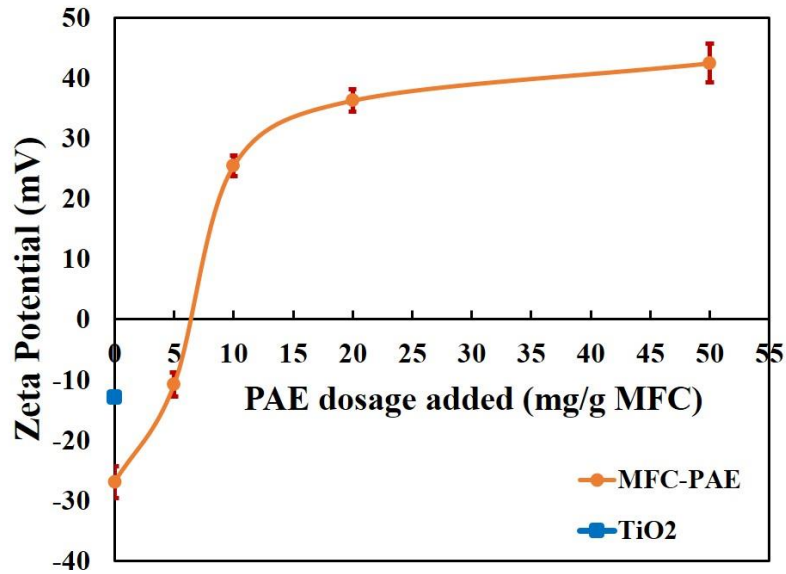


Figure 6: Zeta potential of PAE-MFC suspensions as a function of PAE dosage (mg PAE/g MFC). The supernatant of PAE in a MFC suspension was analyzed after centrifugation according to [40].

6.6.4 Retention efficiency of TiO_2 in the composites

Retention efficiency is defined as the actual TiO_2 NPs present in the composite sheet over the total amount used. Retention was measured from mass balance during composite preparation. Figure 7 shows the actual TiO_2 NPs retention in the composite plotted with respect to NP loading. The retention of NPs increases linearly up to 30 wt% NPs for both PAE dosages. A drop in the retention efficiency for both PAE dosage is observed as increases NPs loading. Afterwards the retention of NPs for 10 mg/g PAE drops faster than for 50 mg/g PAE. For 80 wt% NP loading, the composite with 10 mg PAE /g retains 50 % of the NPs, while that with 50mg PAE /g retain 60% NPs.

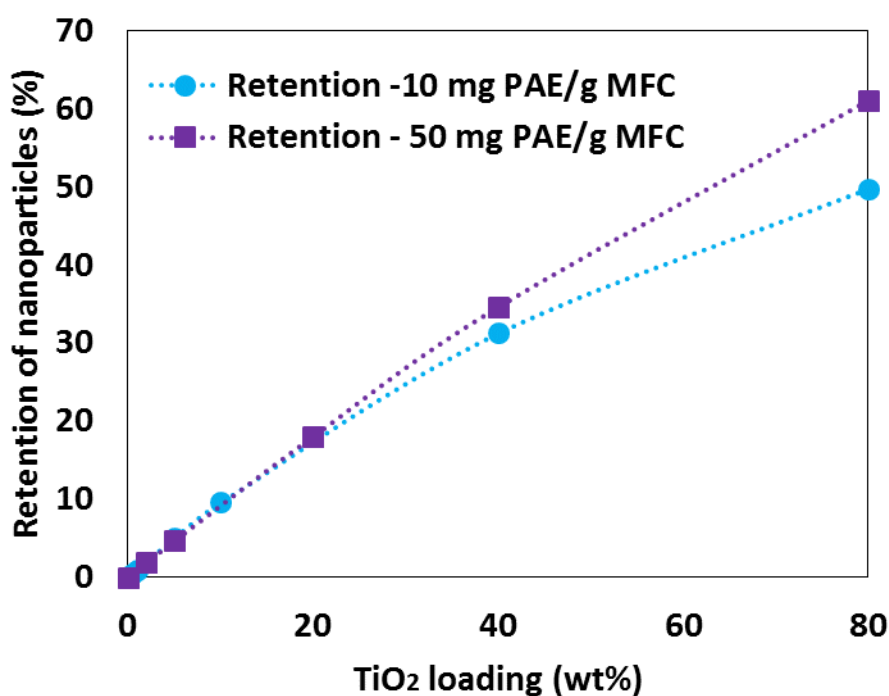


Figure 7: Retention of TiO₂ nanoparticles as a function of initial TiO₂ loading for different dosages of PAE (10 mg/g and 50 mg/g).

6.6.5 TiO₂ and MFC morphology in composites

Scanning electron microscopy (SEM) was performed on all MFC/TiO₂ composites with PAE dosage of 10 mg/g and 50 mg/g and different TiO₂ NP's content (Figures 8 and 9). For 10 mg PAE/g, individual NPs or very small TiO₂ aggregate are present on the composite surface for 1-2 wt% TiO₂ loadings (Figure 8a-b). Relatively large TiO₂ aggregates are observed for 5-80 wt% TiO₂ loadings (Figure 8c-f); the NP surface coverage seems to be similar for 40 wt% TiO₂ loadings and higher.

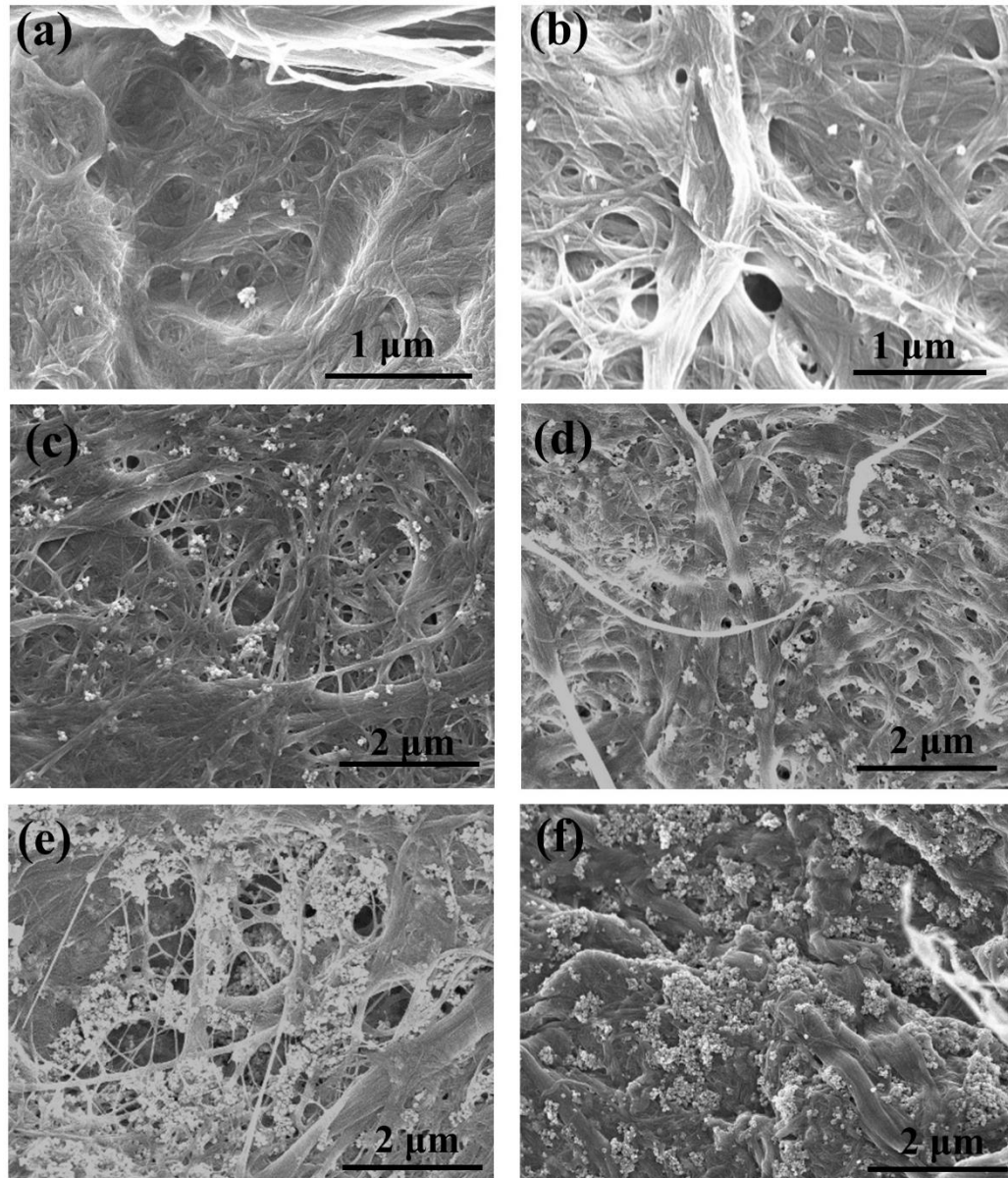


Figure 8: SEM images of TiO_2 composites with 10 mg PAE/g MFC: (a) 1 wt%, (b) 2 wt%, (c) 5 wt%, (d) 10 wt%, (e) 40 wt% and (f) 80 wt% TiO_2 .

For composites with 50 mg PAE/g, individual TiO_2 NPs are seen up to 5 wt% loading (Figure 9a-b), beyond which NPs aggregates into big clusters (Figure 9c-d). Again, the surface coverage of TiO_2 present at higher loadings (20-80 wt%) all looks identical but higher than those made with the lower PAE dosage (10 mg/g).

Interestingly, TiO_2 NPs aggregates are present on the surface of MFC fibres rather than in the pores formed between fibres (Figures 8 and 9). This is due to the preparation method, where PAE is added first to MFC to create a PAE monolayer on MFC, followed by TiO_2 addition onto the MFC-

PAE suspensions. The aggregates are irregular in shape and size. The MFC fibre structure does not change even at high TiO₂ loading; TiO₂ NPs do not accommodate themselves in the pores between fibres.

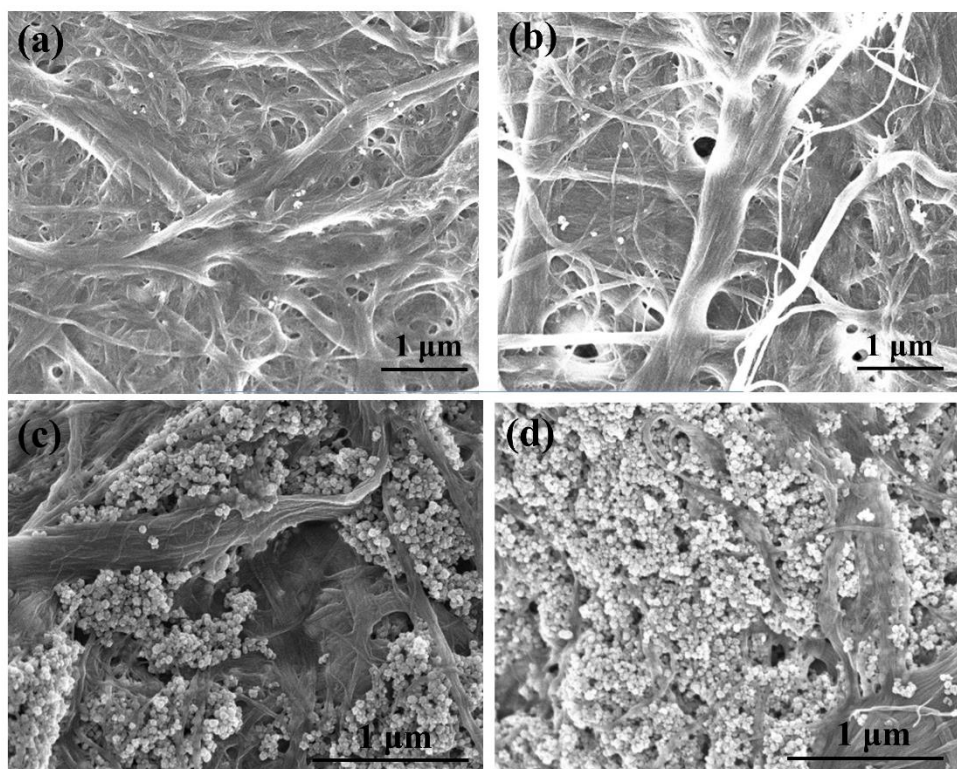


Figure 9: SEM images of TiO₂ composites with 50 mg PAE/g MFC: (a) 2 wt%, (b) 5 wt%, (c) 20 wt%, and (d) 80 wt% TiO₂.

6.6.6 Small angle X-ray scattering

Small angle X-ray scattering (SAXS) was performed on all composites to measure the average NPs distribution per unit volume. Figure 10 shows SAXS curves for samples prepared with 10 mg PAE/g and different TiO₂ loading (0.5-80 wt%). The SAXS curves intensity increases with the concentration of TiO₂ NPs in the composites. All SAXS curves show a kink at $q^*=0.035 \text{ \AA}^{-1}$ which divides SAXS curves into two different slope regions referred to as low and high q region (shown by dashed line).

The slopes in SAXS curves represent the fractal dimensions at different length scale. At high q region slope represent the surface scattering/fractals (smoothness of surface) and at lower q values slope shows the scattering from aggregates/mass fractals. Slope varies as the power-law

exponent ($q^{-\alpha}$) of scattering intensity. For the mass fractals, value of α lies within $0 < \alpha < 3$, and $3 < \alpha < 4$ for surface fractals [41, 42].

In Figure 10, slope at the high q region is q^{-4} ($q^* > q$) shows the surface fractal region and $\alpha=4$ reveals that the NPs surface is smooth. The slope at the low q region is $q^{-2.6}$ ($q^* < q$) represents the mass fractal region ($\alpha=2.6$) and is interpreted as evidence of the formation of NPs aggregates [43].

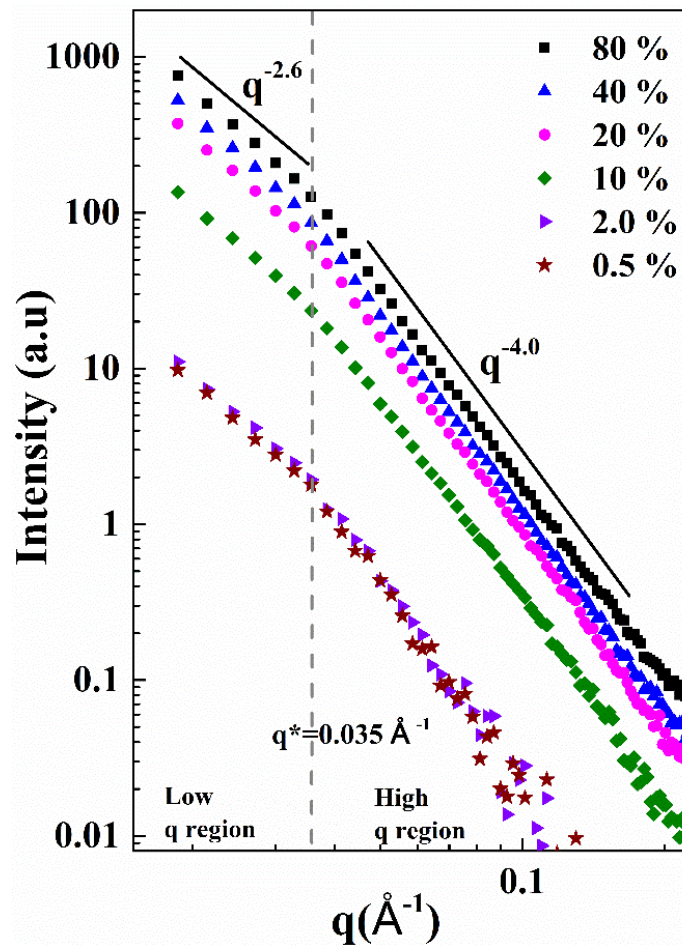


Figure 10: SAXS curves for the MFC/TiO₂ composites with 10 mg/g of PAE and different loading of NPs from 0.5 to 80 wt%.

6.7 DISCUSSION

6.7.1 Quality and durability of MFC-PAE-TiO₂ composites

TiO₂ paper composites of different TiO₂ nanoparticles (NPs) content were prepared with two PAE dosages (10 mg and 50 mg PAE/g MFC). The photocatalytic activity was tested under standard

conditions using aqueous solutions of methyl orange (MO) dye. MO is an azo dye of relatively high toxicity and poor biodegradability which provides a good reference for waste water residues from the printing and dyeing industries [17]. The effect of TiO₂ NPs (30-50 nm) and their aggregates distribution as influenced by PAE was analysed by combining scanning electron microscopy (SEM), small angle X-ray scattering (SAXS) and photocatalytic kinetics. NPs aggregation is crucial as it influences the ability of the material to absorb and scatter incoming radiation, which greatly affects the photocatalytic activity [44].

Here, the addition of PAE was part of the strategy to engineer paper wet strength to develop durable MFC-TiO₂ composites able to sustain harsh applications in aqueous environments. PAE serves two functions. First, it cross-links cellulosic fibres, producing non-woven materials that remain durable when used wet and under long UV light exposure; second, it retains TiO₂ NPs onto the MFC fibres and within the fibrous composite structure. Previous work done with PAE in cellulose paper systems have proven that an addition of 10 mg PAE/g fibre retain the wet-strength of the paper, making it water resistant [33]. MFC-PAE-TiO₂ composites are very efficient at degrading organic dye in solution and have the sufficient wet strength to be robustly manipulated. The photocatalysis results in Figure 3 also indicates that neither PAE nor MFC contributes to the photocatalytic activity which is solely based on the presence and distribution of TiO₂.

The flexible TiO₂ composite sheets investigated are simpler to produce than most methods described in literature that use dopants, carbon and other materials and tedious preparation methods [17, 18, 24, 45]. The composites show excellent photocatalytic activity in degrading MO and are uniform, reproducible and re-usable (Figure 4). In the reusability test cycles, no noticeable mass loss of TiO₂ NPs or broken MFC structure was observed. The composites can easily be removed from the polluted water after the reaction is completed and are expected to be fully recyclable using current equipment and processes [33]. Figure 4c shows that the composites produced are reusable even after the third cycle.

TiO₂ has a characteristic UV-Vis absorbance peak which depends on particle size and concentration. Anatase TiO₂ absorbance occurs at wavelength range of 350-390 nm [46]. MO solutions were monitored through UV-Vis every 30 minutes. In this time interval, no characteristic peak between 350-390 nm was observed (Appendix I-Figure D1). This indicates that no TiO₂ NPs have been desorbed and diffused from the composite into the MO solution which confirms the stability of

TiO₂ in the MFC matrix. Using PAE to embed TiO₂ into the MFC matrix and consolidate the composite resolves the instability problems that typically arise from NPs alone.

6.7.2 Effect of PAE on TiO₂ nanoparticle retention

We raised two hypotheses in this study. The first is that the distribution and aggregation of TiO₂ NPs both affect the TiO₂-MFC composite photocatalytic activity; the second is that PAE dosage governs the retention of TiO₂ NPs. PAE adsorption onto MFC reaches the maximum capacity of adsorption at 15 mg/g (Figure 5). This is about twice the value reported for PAE adsorption onto eucalyptus fibres (8.6 mg/g) [47]. Assuming MFC to be uniform cylinders of 10.37 μm long and of average diameter 73 nm [38], the specific surface area of MFC is 36.5 m²/g. The surface area reported for MFC characterized through mercury porosimetry and BET are 31.1 m²/g [40] and 35 m²/g [48], respectively. A specific PAE adsorption of 0.41 mg/m² results for MFC which is consistent with the range of polyelectrolyte adsorption (0.4-1 mg/m²) [49].

Because of its low molecular weight (200 kDa) and chemical composition with 2 interacting functionalities (primary and secondary amines and azetidinium), PAE is expected to transfer to some extent from MFC to TiO₂ upon collision [50]. This would result in TiO₂ aggregate formation. Such TiO₂ aggregates can be seen by SEM, especially at the high TiO₂ loadings (Figure 8 and 9).

Adding 10 mg PAE/g saturates all MFC fibres which induces a charge reversal to +25 mV – charge of opposite sign but equivalent magnitude to the original (Figure 6). At this dosage, all PAE is adsorbed onto MFC (Figure 5). No excess free PAE is expected in solution. Under those conditions, all TiO₂ NPs are anticipated to adsorb onto MFC with a high retention efficiency. This means that the TiO₂ content on MFC fibres should increase pseudo linearly with TiO₂ add-on.

At 50 mg PAE/g, all the MFC fibres are saturated with PAE and there is an important excess free PAE remaining in solution. PAE adsorbs at 15 mg/g MFC; this means 18 mg is consumed by MFC fibres, leaving 42 mg PAE in solution. Assuming PAE adsorbs onto TiO₂ in the same morphology/conformation as on MFC, at 0.41 mg/m² (specific PAE adsorption on MFC), then the free PAE in solution can cover 102 m² of TiO₂, or nearly 2.88 g of TiO₂ which corresponds to 67 wt% loading in the composites. This means for TiO₂ content lower than 67 wt%, all TiO₂ NPs are expected to be fully covered by PAE, as are the MFC fibres to which PAE was previously adsorbed; no TiO₂ retention due to electrostatic interactions is expected.

Figure 6 shows the zeta potential of +40 mV at 50 mg PAE/g of suspension. This reveals a strongly electrostatically stabilised system, and no adsorption of TiO₂ onto MFC, or homocoagulation of TiO₂ or MFC fibres are expected. That was not the case. SEM (Figure 9) and photocatalysis activity (Figure 3b) contradict this expectation. For one, TiO₂ NPs and aggregates are seen by SEM to be present on MFC surfaces. Also, photocatalysis is at the highest for composites containing 20 to 80 wt% TiO₂. Further, there is photocatalysis and TiO₂ retention even for the very low loadings (2 to 5 wt% TiO₂) for which not only are both components of the system saturated with PAE, but there is also a large excess of PAE in solution. These results state that PAE does not follow trivial polyelectrolyte adsorption behaviour. PAE very likely adsorbs as partial multilayer at very high concentrations. Adsorption isotherm was thus further quantified under the exceptional conditions of 120 mg PAE/g MFC. A slight increase in adsorption capacity was indeed recorded (Appendix I Figure D2). PAE is known for its ability to cross link during drying, which suggests some ability to assemble at very high concentrations.

The PAE adsorption, TiO₂ retention and TiO₂ coagulation expectations from fundamental principles clearly contradict the photocatalytic, retention efficiency measurements as well as the SEM results. This means that PAE behaves differently from the trivial polyelectrolyte adsorption behaviour previously discussed.

6.7.3 Composites photocatalysis activity

Photocatalysis is a surface phenomenon. Only the TiO₂ NPs retained on the composite external surface, which is irradiated by UV light, can take part in the photocatalysis process. At 10 mg PAE/g, all PAE is adsorbed onto MFC (Figure 5) creating a monolayer of PAE on MFC. Since maximum adsorption results at 15 mg/g, this means that at 10 mg PAE/g some of the MFC surface is still not coated by PAE. As TiO₂ NPs are added, the amount of TiO₂ that can be retained on the surface for 10 mg of PAE is less than at 50 mg PAE. This can be seen by the higher retention found for the 50 mg PAE/g as compared to those made with 10 mg PAE/g (Figure 7).

However, at 50 mg PAE/g, the entire MFC surface is completely covered by PAE and there is excess in solution. This excess PAE interacts firstly with the incoming TiO₂ NPs and hinders their agglomeration into large agglomerates by electro-steric stabilisation. This increases the TiO₂

surface area available for photocatalysis; this also accounts for the higher photocatalysis for composites made with 50 mg PAE/g.

Saturation of the photocatalytic activity after reaching a critical TiO₂ loading (at a particular PAE dosage) might be due to the formation of large agglomerates which constrain the effective surface area available for photocatalysis. SEM showed (Figure 8) that at 2 wt% TiO₂ (10 PAE mg/g), there are less individual NPs compared to composites with 40-80 wt% TiO₂.

The influence of wet strength resins on photocatalytic activity was first studied by Zhang et al. (2013) who claimed that PAE addition slightly decreased photocatalytic activity due to a reduction in TiO₂ retention in paper [24]. This statement contradicts our results. We found that PAE helps retain more TiO₂ NPs in paper (Figure 7) which is in agreement with the SAXS results (Figure 9). However, comparison of photocatalytic activity results is not direct nor straightforward. This is because of the many variables influencing catalytic activity. This is illustrated in Table I which compares the photocatalytic dye degradation in aqueous solution from selected studies with TiO₂/cellulose composites.

Table I: Literature comparison of the material performances

Composite type	Degrading medium	UV lamp conditions	Time taken to degrade by 90%	Reference
40wt% TiO ₂ nanobelt paper TiO ₂ particle size: 21 nm Test piece: 1 x 1cm ²	Methyl Orange 20 mL 0.02 g/L	30 W, 294 nm	~2.5 hours	[28]
TiO ₂ /cellulose fibre composite TiO ₂ particle size: 25-30 nm Test piece: 3 x 3 cm ²	Methyl Orange 20 mL 20 mg/L	30W	~7 hours	[24]
TiO ₂ /regenerated cellulose paper Test piece: 1 x 8 cm ²	Phenol 320 mL 67.2 mg/L	6 W, 253 nm,	~102 hours	[51]
10 wt% TiO ₂ /bleached softwood cellulose fibre composite Test piece: 2.5 x 0.7 cm ²	Methyl Orange 0.25 mM in 4 ml water	72W 320-400 nm	~13 hours	[52]
TiO ₂ nanorods /regenerated cellulose films	Methylene blue 150 mL 40 mg/L	30W, 312 nm	~4 hours	[22]

Note: the independent variable is radiation intensity: photon per unit area per time. Geometry of the system, particularly the distance from surface and the diffusion angle, affects this a lot.

Figure 11 shows the rate constant normalized per grams of TiO₂ NPs present in the composite samples tested in this study. The graph indicates that low TiO₂ loadings provide the best photocatalytic activity per unit TiO₂. This material performed best at 0.5-2 wt% TiO₂ loading. The photocatalytic activity of the TiO₂-MFC composites prepared at this work is very effective under UV irradiation; only a small amount of TiO₂ is needed to effectively degrade MO.

TiO₂-cellulose composites were engineered to be easy to manufacture by process easily scalable; the composites produced are water resistant, flexible, cost effective, and most importantly, reproducible. These composites are green and can be used in applications such as waste water treatment, antibacterial, drug delivery and medical [53, 54].

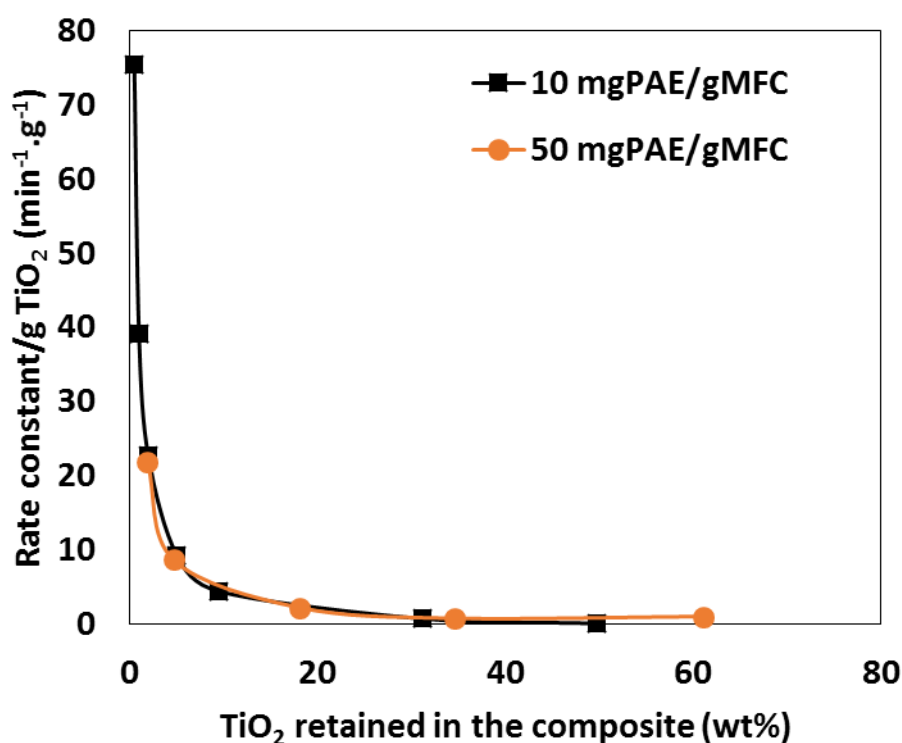


Figure 11: Photocatalytic performance of the material represented by plotting the variation in rate constant as function of the TiO₂ amount retained in the composite.

6.8 CONCLUSION

Water resistant microfibrillated cellulose (MFC) – polyamide-amine-epichlorohydrin (PAE) – titanium dioxide (TiO₂) composites were prepared by a simple two-step process, where PAE was first added to a MFC suspension, followed by TiO₂ addition. These composites are simple to

prepare, economical and the process is easily scalable. Photocatalytic activity of the composites produced was tested by following the degradation of methyl orange (MO) aqueous solutions under UV irradiation. Results show that neither MFC nor PAE or their combination contributed to photocatalytic activity; only the TiO₂ NPs embedded in the sheets do. TiO₂ NPs are uniformly distributed within the composite sheets as shown by the excellent special repeatability in photocatalysis measured. Further, these composites are reusable; the same reproducible photocatalytic efficiency was achieved by testing a same test strip 3 times with no loss of TiO₂ NPs leaching into solution.

Comparing photocatalytic activity of composites with two different dosage of PAE (10 and 50 mg PAE/g of MFC) revealed a higher activity and TiO₂ NPs retention for the high PAE dosage. MO degraded to 5% of its original concentration in 180 min for composites with low PAE and 150 min for composites with high PAE. Photocatalytic is a non- monotonous function of TiO₂ content. For composites made with 10 and 50 mg PAE/g and various amounts of NP, the photocatalytic activity increased up to 2 and 20 wt% TiO₂ NP and remained constant thereafter. SEM indicated that at low TiO₂ loading, NPs retain as individual particles on MFC, whereas TiO₂ aggregates at higher loadings. SAXS showed the formation of mass fractals aggregates at different NPs loading. PAE adsorption isotherms revealed a maximum PAE adsorption on MFC (Γ_{\max}) at 15 mg/g. Expectation resulting from PAE steric and bridging mechanism with maximum coagulation at half surface coverage contradicted the TiO₂ retention efficiency measurements. This suggests that PAE does not follow trivial polyelectrolyte adsorption behaviour. The current study provides a novel insight in engineering NPs embedded cellulose based biodegradable, flexible and recyclable composites with high potential for applications requiring photocatalysis without any residual contamination.

6.9 ACKNOWLEDGEMENT

The financial support of the Australian research council, Australian paper, Carter Holt Harvey, Circa, Orora, Norske Skog and Visy through the ARC Industry Transformation Research Hub - Biomanufacturing Advanced Materials Initiative (BAMI) grant IH130100016 is acknowledged. Thanks to Monash University for MGS and FEIPRS scholarships and the MCEM centre for electron microscopy. The authors gratefully acknowledge Dr. Jisheng Ma for helping in SAXS measurements at the Bruker N8 Horizon SAXS funded from ARC LIEF LE130100072.

6.10 REFERENCES

- [1] M. Kemell, V. Pore, M. Ritala, M. Leskelä, M. Lindén, *Atomic layer deposition in nanometer-level replication of cellulosic substances and preparation of photocatalytic TiO₂/cellulose composites*, *Journal of the American Chemical Society*, **127** (2005) 14178-14179.
- [2] Y. Shin, I.-T. Bae, B.W. Arey, G.J. Exarhos, *Facile stabilization of gold-silver alloy nanoparticles on cellulose nanocrystal*, *The Journal of Physical Chemistry C*, **112** (2008) 4844-4848.
- [3] S. Liu, L. Zhang, J. Zhou, J. Xiang, J. Sun, J. Guan, *Fiberlike Fe₂O₃ macroporous nanomaterials fabricated by calcinating regenerate cellulose composite fibers*, *Chemistry of Materials*, **20** (2008) 3623-3628.
- [4] H. Tada, T. Ishida, A. Takao, S. Ito, *Drastic enhancement of TiO₂-photocatalyzed reduction of nitrobenzene by loading Ag clusters*, *Langmuir*, **20** (2004) 7898-7900.
- [5] K. Maeda, K. Domen, *Photocatalytic water splitting: recent progress and future challenges*, *The Journal of Physical Chemistry Letters*, **1** (2010) 2655-2661.
- [6] N. Savage, M.S. Diallo, *Nanomaterials and water purification: opportunities and challenges*, *Journal of Nanoparticle research*, **7** (2005) 331-342.
- [7] D. Kuang, J. Brillet, P. Chen, M. Takata, S. Uchida, H. Miura, K. Sumioka, S.M. Zakeeruddin, M. Grätzel, *Application of highly ordered TiO₂ nanotube arrays in flexible dye-sensitized solar cells*, *ACS nano*, **2** (2008) 1113-1116.
- [8] A. Fujishima, K. Honda, *Electrochemical photolysis of water at a semiconductor electrode*, *nature*, **238** (1972) 37-38.
- [9] K. Hashimoto, K. Wasada, M. Osaki, E. Shono, K. Adachi, N. Toukai, H. Kominami, Y. Kera, *Photocatalytic oxidation of nitrogen oxide over titania-zeolite composite catalyst to remove nitrogen oxides in the atmosphere*, *Applied Catalysis B: Environmental*, **30** (2001) 429-436.

-
- [10] J. Manassah, *Treatment of highly polluted paper mill waste water by solar photocatalytic oxidation with synthesized nano TiO₂*, in: Green Technology and Environmental Conservation (GTEC 2011), 2011 International Conference on, IEEE, 2011, pp. 356-361.
- [11] F. Wei, H. Zeng, P. Cui, S. Peng, T. Cheng, *Various TiO₂ microcrystals: controlled synthesis and enhanced photocatalytic activities*, Chemical Engineering Journal, **144** (2008) 119-123.
- [12] N. Serpone, A. Emeline, *Suggested terms and definitions in photocatalysis and radiocatalysis*, International Journal of Photoenergy, **4** (2002) 91-131.
- [13] M.R. Nimlos, W.A. Jacoby, D.M. Blake, T.A. Milne, *Direct mass spectrometric studies of the destruction of hazardous wastes. 2. Gas-phase photocatalytic oxidation of trichloroethylene over titanium oxide: products and mechanisms*, Environmental science & technology, **27** (1993) 732-740.
- [14] A. Fujishima, T.N. Rao, D.A. Tryk, *Titanium dioxide photocatalysis*, Journal of Photochemistry and Photobiology C: Photochemistry Reviews, **1** (2000) 1-21.
- [15] H. Zhang, P. Xu, G. Du, Z. Chen, K. Oh, D. Pan, Z. Jiao, *A facile one-step synthesis of TiO₂/graphene composites for photodegradation of methyl orange*, Nano Research, **4** (2011) 274-283.
- [16] N. Mandzy, E. Grulke, T. Druffel, *Breakage of TiO₂ agglomerates in electrostatically stabilized aqueous dispersions*, Powder technology, **160** (2005) 121-126.
- [17] X. Zhang, W. Chen, Z. Lin, J. Yao, S. Tan, *Preparation and photocatalysis properties of bacterial cellulose/TiO₂ composite membrane doped with rare earth elements*, Synthesis and Reactivity in Inorganic, Metal-Organic, and Nano-Metal Chemistry, **41** (2011) 997-1004.
- [18] G. Li, A.G. Nandgaonkar, Q. Wang, J. Zhang, W.E. Krause, Q. Wei, L.A. Lucia, *Laccase-immobilized bacterial cellulose/TiO₂ functionalized composite membranes: Evaluation for photo-and bio-catalytic dye degradation*, Journal of Membrane Science, **525** (2017) 89-98.
- [19] D.M. Alrousan, P.S. Dunlop, T.A. McMurray, J.A. Byrne, *Photocatalytic inactivation of E. coli in surface water using immobilised nanoparticle TiO₂ films*, Water research, **43** (2009) 47-54.
-

-
- [20] T.C. Long, N. Saleh, R.D. Tilton, G.V. Lowry, B. Veronesi, *Titanium dioxide (P25) produces reactive oxygen species in immortalized brain microglia (BV2): implications for nanoparticle neurotoxicity*, *Environmental Science & Technology*, **40** (2006) 4346-4352.
- [21] S.B. Lovern, J.R. Strickler, R. Klaper, *Behavioral and physiological changes in Daphnia magna when exposed to nanoparticle suspensions (titanium dioxide, nano-C60, and C60HxC70Hx)*, *Environmental science & technology*, **41** (2007) 4465-4470.
- [22] M.A. Mohamed, W. Salleh, J. Jaafar, A. Ismail, M.A. Mutalib, S.M. Jamil, *Incorporation of N-doped TiO₂ nanorods in regenerated cellulose thin films fabricated from recycled newspaper as a green portable photocatalyst*, *Carbohydrate polymers*, **133** (2015) 429-437.
- [23] A. Snyder, Z. Bo, R. Moon, J.-C. Rochet, L. Stanciu, *Reusable photocatalytic titanium dioxide–cellulose nanofiber films*, *Journal of colloid and interface science*, **399** (2013) 92-98.
- [24] J. Zhang, W. Liu, P. Wang, K. Qian, *Photocatalytic behavior of cellulose-based paper with TiO₂ loaded on carbon fibers*, *Journal of Environmental Chemical Engineering*, **1** (2013) 175-182.
- [25] J. Shi, J. Zheng, P. Wu, X. Ji, *Immobilization of TiO₂ films on activated carbon fiber and their photocatalytic degradation properties for dye compounds with different molecular size*, *Catalysis Communications*, **9** (2008) 1846-1850.
- [26] T. Ochiai, T. Hoshi, H. Slimen, K. Nakata, T. Murakami, H. Tatejima, Y. Koide, A. Houas, T. Horie, Y. Morito, *Fabrication of a TiO₂ nanoparticles impregnated titanium mesh filter and its application for environmental purification*, *Catalysis Science & Technology*, **1** (2011) 1324-1327.
- [27] J. Li, C. Chen, J. Zhao, H. Zhu, J. Orthman, *Photodegradation of dye pollutants on TiO₂ nanoparticles dispersed in silicate under UV–VIS irradiation*, *Applied Catalysis B: Environmental*, **37** (2002) 331-338.
- [28] J. Wang, W. Liu, H. Li, H. Wang, Z. Wang, W. Zhou, H. Liu, *Preparation of cellulose fiber–TiO₂ nanobelt–silver nanoparticle hierarchically structured hybrid paper and its*
-

-
- photocatalytic and antibacterial properties*, Chemical engineering journal, **228** (2013) 272-280.
- [29] U.M. Garusinghe, V.S. Raghuwanshi, C.J. Garvey, S. Varanasi, C.R. Hutchinson, W. Batchelor, G. Garnier, *Assembly of nanoparticles-polyelectrolyte complexes in nanofiber cellulose structures*, Colloids and Surfaces A: Physicochemical and Engineering Aspects, **513** (2017) 373-379.
- [30] S. Li, J. Huang, *Cellulose - Rich Nanofiber - Based Functional Nanoarchitectures*, Advanced Materials, **28** (2016) 1143-1158.
- [31] F. Hoeng, A. Denneulin, J. Bras, *Use of nanocellulose in printed electronics: a review*, Nanoscale, **8** (2016) 13131-13154.
- [32] Y.H. Ngo, D. Li, G.P. Simon, G. Garnier, *Paper surfaces functionalized by nanoparticles*, Advances in colloid and interface science, **163** (2011) 23-38.
- [33] J. Su, W.K. Mosse, S. Sharman, W. Batchelor, G. Garnier, *Paper strength development and recyclability with polyamideamine-epichlorohydrin (PAE)*, BioResources, **7** (2012) 0913-0924.
- [34] S. Varanasi, W. Batchelor, *Superior non-woven sheet forming characteristics of low-density cationic polymer-cellulose nanofibre colloids*, Cellulose, **21** (2014) 3541-3550.
- [35] U.M. Garusinghe, S. Varanasi, G. Garnier, W. Batchelor, *Strong cellulose nanofibre-nanosilica composites with controllable pore structure*, Cellulose, 1-11.
- [36] V.S. Raghuwanshi, U.M. Garusinghe, J. Ilavsky, W.J. Batchelor, G. Garnier, *Effect of nanoparticles size and polyelectrolyte on nanoparticles aggregation in a cellulose fibrous matrix*, Journal of Colloid and Interface Science, **510** (2018) 190-198.
- [37] T. Obokata, A. Isogai, *The mechanism of wet-strength development of cellulose sheets prepared with polyamideamine-epichlorohydrin (PAE) resin*, Colloids and Surfaces A: Physicochemical and Engineering Aspects, **302** (2007) 525-531.
- [38] S. Varanasi, R. He, W. Batchelor, *Estimation of cellulose nanofibre aspect ratio from measurements of fibre suspension gel point*, Cellulose, **20** (2013) 1885-1896.
-

-
- [39] P. Peng, G. Garnier, *Effect of cationic polyacrylamide adsorption kinetics and ionic strength on precipitated calcium carbonate flocculation*, *Langmuir*, **26** (2010) 16949-16957.
- [40] P. Raj, S. Varanasi, W. Batchelor, G. Garnier, *Effect of cationic polyacrylamide on the processing and properties of nanocellulose films*, *Journal of colloid and interface science*, **447** (2015) 113-119.
- [41] A.Y. Cherny, E. Anitas, V. Osipov, A. Kuklin, *Small-angle scattering from multiphase fractals*, *Journal of Applied Crystallography*, **47** (2014) 198-206.
- [42] T.P. Rieker, M. Hindermann-Bischoff, F. Ehrburger-Dolle, *Small-angle X-ray scattering study of the morphology of carbon black mass fractal aggregates in polymeric composites*, *Langmuir*, **16** (2000) 5588-5592.
- [43] G. Beaucage, *Small-angle scattering from polymeric mass fractals of arbitrary mass-fractal dimension*, *Journal of Applied Crystallography*, **29** (1996) 134-146.
- [44] F. Pellegrino, L. Pellutiè, F. Sordello, C. Minero, E. Ortel, V.-D. Hodoroaba, V. Maurino, *Influence of Agglomeration and Aggregation on the Photocatalytic Activity of TiO₂ Nanoparticles*, *Applied Catalysis B: Environmental*, (2017).
- [45] X. An, D. Cheng, L. Dai, B. Wang, H.J. Ocampo, J. Nasrallah, X. Jia, J. Zou, Y. Long, Y. Ni, *Synthesis of nano-fibrillated cellulose/magnetite/titanium dioxide (NFC@ Fe₃O₄@ TNP) nanocomposites and their application in the photocatalytic hydrogen generation*, *Applied Catalysis B: Environmental*, **206** (2017) 53-64.
- [46] C.-C. Weng, K.-H. Wei, *Selective distribution of surface-modified TiO₂ nanoparticles in polystyrene-*b*-poly (methyl methacrylate) diblock copolymer*, *Chemistry of materials*, **15** (2003) 2936-2941.
- [47] Z. Huang, T. Gengenbach, J. Tian, W. Shen, G. Garnier, *The role of polyaminoamide-epichlorohydrin (PAE) on antibody longevity in bioactive paper*, *Colloids and Surfaces B: Biointerfaces*, (2017).
- [48] H. Sehaqui, M. Salajkova, Q. Zhou, L.A. Berglund, *Biomimetic aerogels from microfibrillated cellulose and xyloglucan*, in: *ICCM-17 17th International Conference on Composite Materials*, Edinburgh, United Kingdom, 2009.
-

-
- [49] G. Fleer, M.C. Stuart, J. Scheutjens, T. Cosgrove, B. Vincent, *Polymers at interfaces*, in, Chapman & Hall, 1993.
- [50] T. Asselman, G. Garnier, *Mechanism of polyelectrolyte transfer during heteroflocculation*, *Langmuir*, **16** (2000) 4871-4876.
- [51] J. Zeng, S. Liu, J. Cai, L. Zhang, *TiO₂ immobilized in cellulose matrix for photocatalytic degradation of phenol under weak UV light irradiation*, *The Journal of Physical Chemistry C*, **114** (2010) 7806-7811.
- [52] I. Chauhan, P. Mohanty, *In situ decoration of TiO₂ nanoparticles on the surface of cellulose fibers and study of their photocatalytic and antibacterial activities*, *Cellulose*, **22** (2015) 507-519.
- [53] O. Galkina, V. Ivanov, A. Agafonov, G. Seisenbaeva, V. Kessler, *Cellulose nanofiber–titania nanocomposites as potential drug delivery systems for dermal applications*, *Journal of Materials Chemistry B*, **3** (2015) 1688-1698.
- [54] O. Galkina, K. Önnby, P. Huang, V. Ivanov, A. Agafonov, G. Seisenbaeva, V. Kessler, *Antibacterial and photochemical properties of cellulose nanofiber–titania nanocomposites loaded with two different types of antibiotic medicines*, *Journal of Materials Chemistry B*, **3** (2015) 7125-7134.

THIS PAGE HAS BEEN INTENTIONALLY LEFT BLANK

CHAPTER 7

CONCLUSION AND PERSPECTIVES

THIS PAGE HAS BEEN INTENTIONALLY LEFT BLANK

CHAPTER 7 CONCLUSION AND PERSPECTIVES

7.1	CONCLUSION	231
7.1.1	Characterization of the structure-property relationship of nanocellulose-polyelectrolyte-NP composites	231
7.1.2	Characterization of the internal structure of NP-polyelectrolyte complexes in nanocellulose matrix	232
7.1.3	Produce functional NP-nanocellulose composites targeted towards specific applications	233
	7.1.3.1 Nanocellulose-MMT composites for water barrier applications	234
	7.1.3.2 Nanocellulose-TiO ₂ composites for photocatalytic applications	234
7.2	PERSPECTIVES	235

THIS PAGE HAS BEEN INTENTIONALLY LEFT BLANK

7.1 CONCLUSION

While there are nanocellulose-inorganic nanoparticle (NP) composites that have been previously reported in the literature, there has been no detailed investigations on the effect of addition on NPs with combination of nanocellulose and polyelectrolytes on the structure of the composite and the effect of the structure on final composite properties. As the diameter of polyelectrolytes is in the same range as nanocellulose, the effect of the combination of three nanoscale materials on the final composite properties has not been well understood. Also, due to reduction in size, the characterization techniques available to characterize the NP-polyelectrolyte structure in nanocellulose matrix have generally been restricted to the surface. To characterize the structure properly, to understand the structural assembly of NPs under the influence of different polyelectrolyte dosages, a complementary scattering technique is promising.

This thesis has reported three main interrelated avenues of research. Firstly, quantification of the structure-property relationship of nanocellulose – polyelectrolyte - NP composites. Secondly, characterization of the internal structure of NP-polyelectrolyte complexes in nanocellulose matrix. Lastly, functional NP-nanocellulose composites targeted towards specific applications have been produced, using the expertise developed through first two avenue of research.

7.1.1 Characterization of the structure-property relationship of nanocellulose – polyelectrolyte – NP composites.

Two different silicon dioxide (SiO_2) NP sizes were used to produce nanocellulose – cationic polyacrylamide (CPAM) – NP composites with varying NP loading. CPAM and SiO_2 NPs were mixed together first, and then the CPAM-NP suspension and nanocellulose suspension were mixed to obtain the final composite suspension. Composite sheets were then made using standard laboratory paper making techniques. Effect of NP size and loading on the structure and properties of the composite was characterized using scanning electron microscopy (SEM), mercury porosimetry, thickness measurements and by measuring strength of the composites.

Retention measurements showed that with CPAM and the preparation method used, over 90% of the NPs are retained in the range of 5-80 wt% NP loading. Without CPAM, the retention significantly dropped; reaching 20% at 80 wt% loading. Therefore, addition of CPAM is extremely crucial in production of nanocellulose-NP composites especially when both materials have the

same charge. SEM images of nanocellulose alone indicates that nanocellulose create a porous network due to fibre entanglement as the film is formed. At lower levels of NP loading, the NPs and their aggregates accommodate themselves in the pores created by nanofibres and fill them. This reduces the volume of larger pores in the fibrous matrix. At high NP loading, NP aggregates become larger than the available pore size, therefore embedding these into the matrix pushes the nanofibres apart. At this point, the thickness of composites begins to increase and a narrow pore size distribution is obtained. The structure changes from on dominated by the nonwoven film structure to a packed bed structure. Larger NP sizes change the composite structure to a packed bed structure at low loading compared to smaller NP sizes. The tensile index remained at 70-80 Nm/g even at high loadings, indicating that NPs do not affect the strength.

This work concludes that based on NP size, loading and preparation method, the structure of the final composite can be tailored to obtain specific properties. Here, a structure-property relationship model was developed.

7.1.2 Characterization of the internal structure of NP-polyelectrolyte complexes in nanocellulose matrix.

As nanocellulose – CPAM – SiO₂ NP composite were produced, it was realised that SEM is a poor tool to characterize the composites. Although, the structural arrangement of the NPs and nanocellulose can be seen on the surface of the sheets, it is not possible to observe the conformation of the CPAM and SEM cannot be used as a tool to characterize the internal structure of NP - CPAM complexes or to quantify the structural assembly of NPs under the influence of CPAM. Therefore, the next two chapters used complementary scattering techniques to characterize the internal nanoscale structure.

In Chapter 3, two different scattering techniques were used to analyse 22 nm SiO₂ NP-CPAM systems. Dynamic light scattering (DLS) was used to characterize NP-CPAM suspensions with different CPAM dosages (0.03-0.09 mg CPAM/m² SiO₂). Here, the formation of aggregate sizes were quantified. At higher dosage of CPAM, the size of the NP aggregates increases due to a more stretched out configuration of CPAM increasing the probability of adhering further SiO₂ NPs to the cluster. However, the DLS scattering technique does not give reliable results at higher CPAM dosages. At higher dosages, without a fibre matrix, NPs agglomerate into much bigger clusters

when compared to being in the sheet form. When NP-CPAM complexes are added to a fibre matrix, fibres have an influence on the size of NP-CPAM aggregation. Therefore, small angle X-ray scattering (SAXS) technique was used to analyse the 22 nm SiO₂ – CPAM – nanocellulose structure.

SAXS was used to obtain the structural assembly model of 22 nm SiO₂ NPs under the influence of CPAM with 13 MDa and 40% charge (radius of gyration of ~37 nm). Here, the SAXS curve fitted well with a spherical core shell model (SiO₂ coated in a layer of CPAM) and sphere model (pure SiO₂). The interaction between particles did not vary significantly with CPAM dosage as indicated by the structure factor peaks. With increasing CPAM dosage, the number of structures increase but the structure size remained the same.

In Chapter 4, SAXS was used for composites made with 8 nm SiO₂ NPs instead of 22 nm SiO₂ NPs. Here, the aim was to observe if different sizes of NPs behave differently with CPAM. 8 nm is considerably smaller in size than the radius of gyration of the CPAM used. After analysis, the data was best fitted by a bimodal distribution of NPs with smaller particles of diameter 8 nm and bigger particles of diameter between 15-20 nm. Transmission electron microscopy (TEM) also revealed the bimodal distribution. Here, the structure factor sharpness increased and peak shifted to lower values at low CPAM dosage. This means that structure size changes with higher CPAM dosage.

Chapter 3 and 4 concluded that the interaction of NPs and polyelectrolytes is highly dependent on the size and that SAXS is a powerful tool in characterizing such systems to better engineer properties of these composites to develop nanocellulose-NP composites for high end applications.

7.1.3 Produce functional NP-nanocellulose composites targeted towards specific applications.

The last two chapters of this thesis provide two application chapters based on the knowledge and expertise obtained through the preceding chapters investigating the fundamentals. Here, nano-montmorillonite (MMT) was used to produce nanocellulose – MMT composites for water barrier applications, and nano-titanium dioxide (TiO₂) was used to produce nanocellulose – TiO₂ composites for photocatalytic applications.

7.1.3.1 Nanocellulose - MMT composites for barrier applications.

Composites were made with varying MMT content (9.1-37.5 wt%). Three different preparation methods were used to engineer the internal structure. In the first preparation method, MMT was added to nanocellulose and then composites were formed using filtration. As MMT content increased, WVP initially decreased due to tortuous path created by MMT, reached a minimum and increased again. It was hypothesized that MMT forms stacks when highly loading and breaking down stacks could improve WVP even further. Therefore, the effect on the composite suspensions of sonication and homogenization before filtration was tested. Sonication worsened the results as it fractured individual MMT platelets into fragments. Homogenization improved the results even further by breaking down the larger stacks into smaller stacks, maximising the surface area available by MMT to create an effective tortuous path. The lowest WVP achieved of $6.3 \pm 1.5 \text{ g}\cdot\mu\text{m}/\text{m}^2\cdot\text{day}\cdot\text{kPa}$ at 23.1 wt% loading was the lowest reported for nanocellulose-clay composites in literature. In addition, this material is cheap, strong, flexible, recyclable, biodegradable, recyclable and easy to scale up.

7.1.3.2 Nanocellulose - TiO₂ composites for photocatalytic applications.

Nanocellulose - TiO₂ – polyamide amine epichlorohydrin (PAE) composites were made with varying TiO₂ content (0.5-80 wt%) and also with two different PAE dosages (10 and 50 mg PAE/ g nanocellulose). The composites were tested for photocatalytic activity using methyl orange (MO) as a model dye pollutant. PAE was used here as a wet strengthening agent to hold the nanocellulose structure together when it is wet. PAE was also acting as a weak retention aid to retain TiO₂ in nanocellulose matrix. Here, the effect of PAE dosage and TiO₂ loading on photocatalytic activity was studied. SEM, adsorption isotherm measurements obtained through polyelectrolyte titration and SAXS were used to characterize the internal structure. With low PAE dosage (10 mg/g), photocatalytic activity of composites saturated at 2 wt% TiO₂ loading and 80% of MO was degraded in ~120 minutes. With high PAE dosage (50 mg/g), photocatalytic activity of composites saturated at 20 wt% TiO₂ loading and 80 % of MO was degraded in ~90 minutes. The composites prepared were reusable and reproducible. The composite material produced is effective in photocatalysis, strong, flexible, holds its structure without falling apart in wet conditions, cheap, easy to make and scalable. This material has wide uses as a portable photocatalytic material.

7.2 PERSPECTIVE

While the characterisation of nanocellulose-inorganic NP composites through various techniques such as SEM, TEM, XRD, DLS and SAXS has given good insight into production of engineered nanocellulose based composites for high end applications, the study was only performed under one type of CPAM (13 MDa and 40% charge). Therefore, it is worthwhile to investigate how the CPAMs with other molecular weights and charges affect the structure, final film properties and also the structural assembly of NPs.

In addition, with the functional NPs (MMT and TiO₂), it has been proven through this thesis that well performing materials can be made and they are easy to make, flexible, strong and scalable. However, the preparation time via filtration could still be quite slow. Our research group recently discovered a spraying system to spray nanocellulose films. Therefore, next step would be to expand the work of spraying nanocellulose films to spraying nanocellulose-NP composites. This is easier to scale up at a pilot scale for manufacture of nanocomposites. This would then be the first step towards the commercialization of hierarchically engineered nanocellulose-inorganic NP composites for desired applications.

THIS PAGE HAS BEEN INTENTIONALLY LEFT BLANK

APPENDIX I

SUPPLEMENTARY INFORMATION

THIS PAGE HAS BEEN INTENTIONALLY LEFT BLANK

STRONG CELLULOSE NANOFIBRE – NANOSILICA COMPOSITES OF CONTROLLABLE PORE STRUCTURE

Uthpala M Garusinghe, Swambabu Varanasi, Gil Garnier, Warren Batchelor.

BioResource Processing Research Institute of Australia (BioPRIA), Department of Chemical Engineering, Monash University, Clayton 3800, VIC, Australia.

*Corresponding author: warren.batchelor@monash.edu

A1: Diameter distribution

The silica nanoparticle (NP) diameter distributions were measured at 0.1 wt% by dynamic light scattering (DLS) using nanobrook omni brookhaven. Size distributions were also measured from SEM using image J software. NP diameter was sorted to bins and normalized to counts/m², by dividing by image area (Figure A1) The colloidal silica are not monodispersed as indicated two distinctive populated areas for both the NexSil 85-40 and NexSil 125-40 samples. The peaks of each distribution were 30 nm and 70 nm from Image J, and 35 nm and 78 nm from DLS for the NexSil 85-40 sample. While it was 60 nm and 130 nm from Image J, and 46 nm and 113 nm from DLS for the NexSil 125-40 sample.

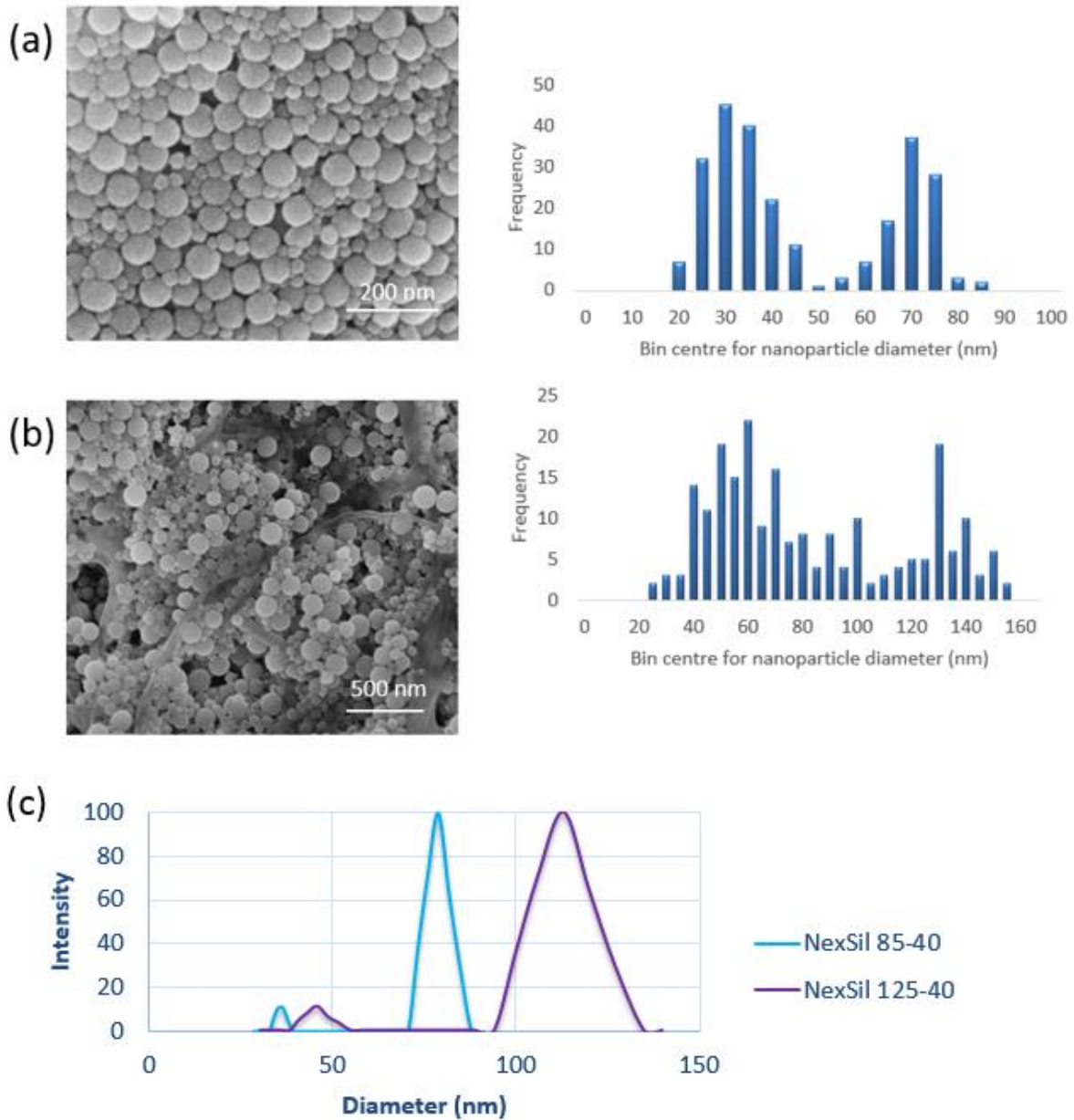


Figure A1. Particle diameter distribution. (a) and (b) are SEM with image analysis (analysed via image J) for size distribution of NexSil 85-40 and NexSil 125-40 respectively. (c) Size distribution obtained from DLS analysis

A2: SEM images for V/S composites with different nanoparticle loadings

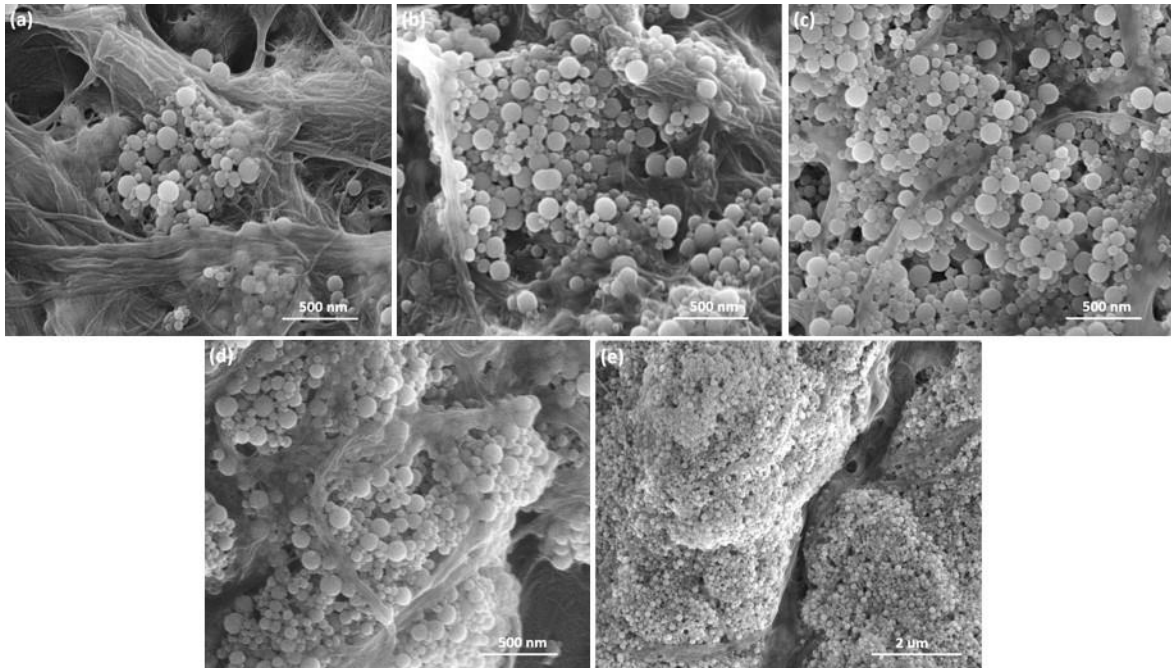


Figure A2. SEM images of composite (V/L). a, b, c and d refers to 5 wt%, 10 wt%, 40 wt% and 50 wt% NP, respectively, all at 100,000 magnifications. e refers to 60 wt% at 30,000 magnifications.

THIS PAGE HAS BEEN INTENTIONALLY LEFT BLANK

ASSEMBLY OF NANOPARTICLES-POLYELECTROLYTE COMPLEXES IN NANOFIBER CELLULOSE STRUCTURES

Uthpala Garusinghe^{1,#}, Vikram. S. Raghuwanshi^{1,#,*}, Christopher J. Garvey³, Swambabu Varanasi¹, Christopher. R. Hutchinson², Warren Batchelor¹ and Gil Garnier^{1,*}

BioResource Processing Research Institute of Australia (BioPRIA), Department of Chemical Engineering, Monash University, VIC-3800, Australia

²Department of Materials Science and Engineering, Monash University, VIC-3800, Australia

³ANSTO, Locked Bag 2001, Kirrawee DC NSW 2232, Australia

*Corresponding authors: vikram.raghuwanshi@monash.edu

gil.garnier@monash.edu

Equal contributors as first authors

B1: SAXS Theory

SAXS experiments were performed to reveal the distribution of SiO₂ nanoparticles to estimate quantitatively the structure parameters [1, 2]. SAXS experiments are sensitive to the spatial correlation in the electron scattering densities present in the samples. In SAXS, the differential scattering cross section of a system of particles can be given as [3]:

$$\frac{d\sigma}{d\Omega}(\vec{q}) = \int_0^{\infty} N(r) V_p(r)^2 |F(q, r, \Delta\eta)|^2 S(q, r) dr + cq^{-\alpha} \quad (1)$$

Where, $N(r)$ is the number density distribution, $V_p(r)$ is the volume of the particle. $|\vec{q}|$ is the transferred momentum, which is related with the scattering angle of ϑ as:

$$|\vec{q}| = q = \frac{4\pi \sin \vartheta}{\lambda} \quad (2)$$

Here, λ is the wavelength of the X-rays. In equation (1), $F(q, r, \Delta\eta)$ is the form factor that accounts for the shape and the size of particles. For a homogeneous sphere with radius r , the form factor is given as:

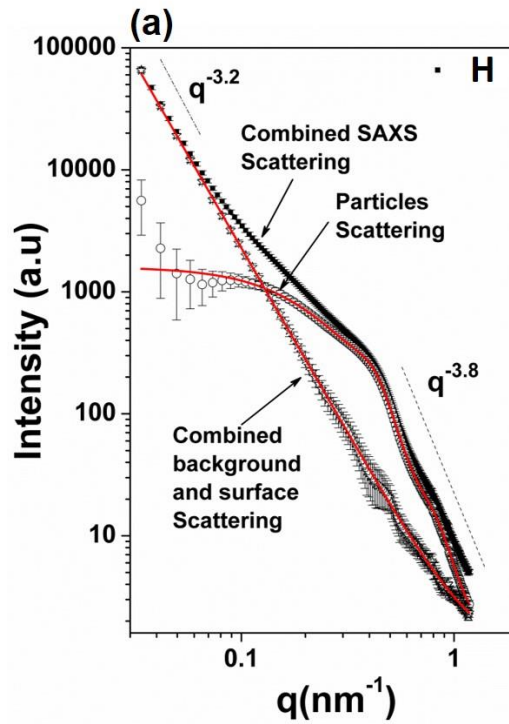
$$F(q, r, \Delta\eta) = 3\Delta\eta \frac{\sin(qr) - (qr)\cos(qr)}{(qr)^3} \quad (3)$$

where, $\Delta\eta = \eta_{particle} - \eta_{matrix}$ is the electron density difference between the particles and the remaining matrix. $S(q)$ is the structure factor which reveals the interaction between the particles. Additionally, in equation (1), a constant background is included from parasitic scattering. Moreover, the term $cq^{-\alpha}$ reveals the smoothness of the particle surface. For a smooth surface the value of $\alpha=4$.

B2: SAXS Curve fitting in SASfit

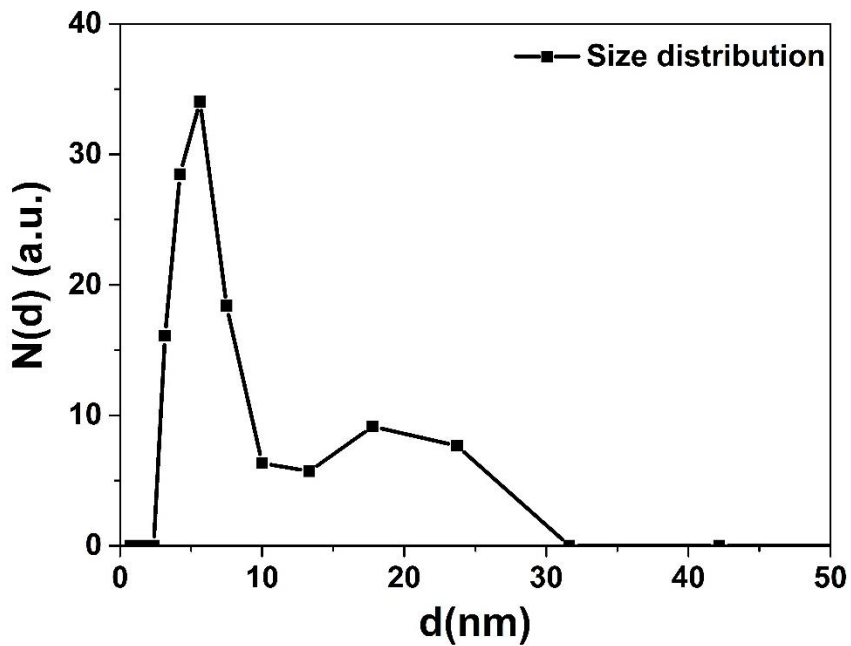
To fit any SAS scattering curves, SASFit requires a predefined shape of particles and shape of the distribution of particles. Here, a bimodal distribution of spherical particles with lognormal distribution of particles was used. A structure factor of hard spheres with local monodisperse approximation was included and found to be appropriate to fit the respective SAXS curves [4-6]. When scattering occurs from the surface of particles, a surface scattering constant that reveals the smoothness of the particle surface is considered during SAXS curves fitting.

The figure below (B2) shows the detailed fit of the SAXS curves for the sample having high dosage of CPAM. It displays individually fitted SAXS scattering curves from the bimodal distribution of spheres, a surface scattering term combined with the constant background. Moreover, the slope at the lower and higher q values of 3.2 and 3.8 indicates that the surface of particles is smooth.



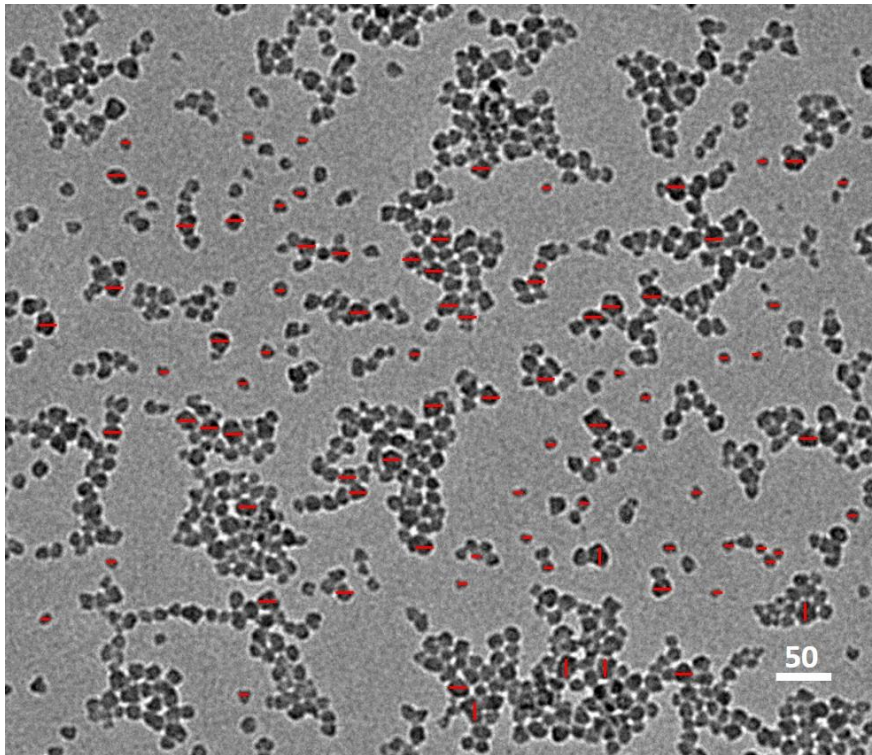
B3: Dynamic light scattering (DLS)

Dynamic light scattering (DLS) measurement on the initial SiO₂ nanoparticle suspension which shows bimodal size distribution of NPs. Here, d is the diameter of the nanoparticle.



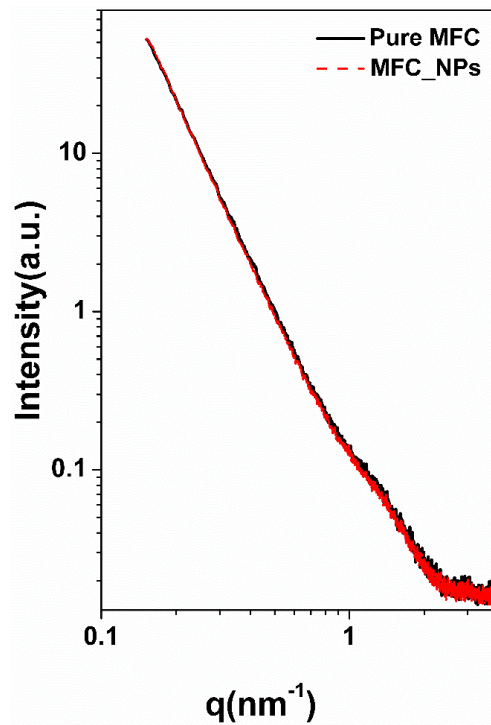
B3: Bimodal distribution by TEM micrograph

Two different size of SiO₂ nanoparticles are shown by two different sized red lines (8 nm and 15-20 nm).



B4: SAXS measurement on MFC and MFC with NP without CPAM

SAXS curves for the pure MFC sheet (black solid line) and for the MFC sheet with the SiO₂ nanoparticles without CPAM (red dashed line). It is seen that both SAXS curves are similar and that no SiO₂ nanoparticles were retained without addition of CPAM.



B5 References

1. Small-Angle X-ray scattering, by O. Glatter, O. Kratky, (Academic Press, New York, 1982).
2. Small Angle Scattering of X-ray, by A. Guinier, G. Fournet, (Wiley, New York, 1955).
3. J. Kohlbrecher, I. Bressler, SASfit, Software package for fitting small-angle scattering curves. <http://kur.web.psi.ch/sans1/SANSSoft/sasfit.html>.
4. J. Haug et al, Nanotechnology 2009, **20**, 505705.
5. S. Pedersen. *Determination of size distributions from small-angle scattering data for systems with effective hard-sphere interactions*. J. Appl. Cryst. 1994, **27**, 595-608.
6. J. K. Percus and G. J. Yevick. *Analysis of classical statistical mechanics by means of collective coordinates*. Phys. Rev. 1958, **110**, 1-13.

THIS PAGE HAS BEEN INTENTIONALLY LEFT BLANK

NANOCELLULOSE – MONTMORILLONITE COMPOSITES OF LOW WATER VAPOUR PERMEABILITY

Uthpala M. Garusinghe, Swambabu Varanasi, Vikram. S. Raghuwanshi, Gil Garnier* and
Warren Batchelor*

BioResource Processing Research Institute of Australia (BioPRIA), Department of Chemical
Engineering, Monash University, VIC-3800, Australia

*Corresponding authors: warren.batchelor@monash.edu

gil.garnier@monash.edu

C1: Nanofibre diameter calculation

Nanofibre suspension was casted on a silica plate, coated with Iridium, and viewed under FEI Magellan 400 FEGSEM for the fibre diameters. Images were taken at the magnification of 150,000. Following shows the images used in the diameter distribution calculations.

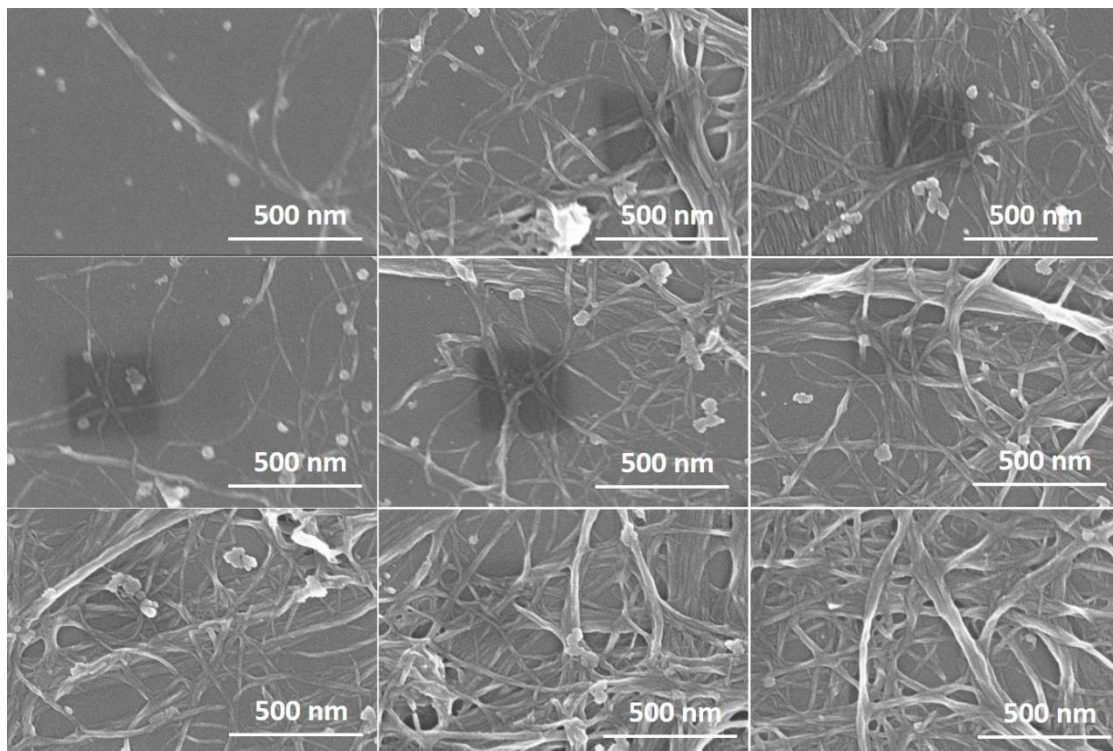


Figure C1: SEM images of nanocellulose at 150,000 magnifications

Diameters of the visible nanofibre in the above images are then measured using ImageJ software and following histogram was obtained.

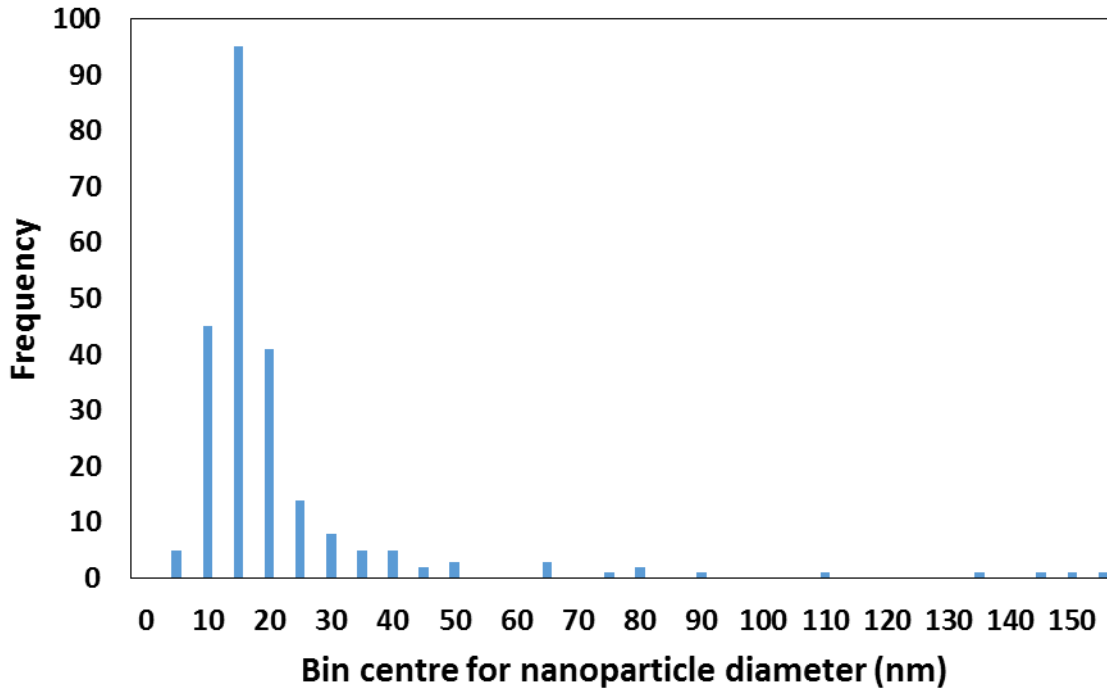


Figure C2: Frequency histogram of fibre diameter distribution

The average diameter from the above graph was **20 nm**.

C2: Aspect ratio calculation

Aspect ratio was calculated using gel point. Gel point is the lowest solids concentration where the fibres can form a continuous network in the suspension. The gel point calculations were first developed by Martinez et al [1] for the wood fibres, and then the method was adapted to use on nanocellulose suspensions by Zhang et al [2]. The measurement and analysis method used to calculate gel point and aspect ratio in this study is explained in a previous study conducted by Raj et al [3].

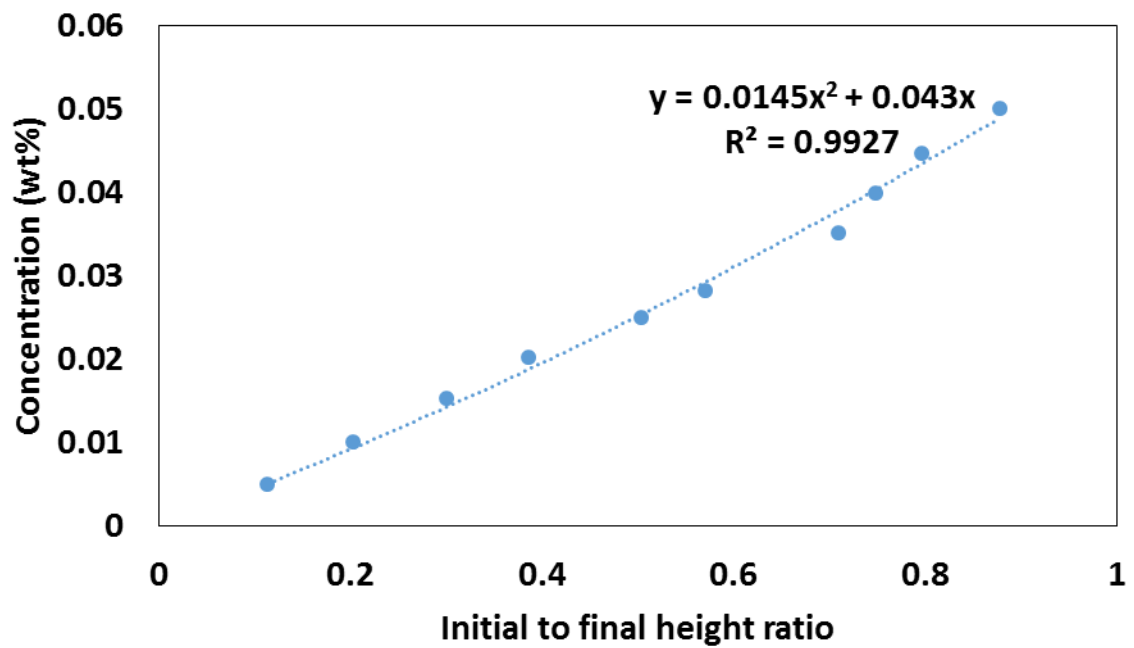


Figure C3: Experimental gel point curve to measure the aspect ratio

The gel point in the above graph is 0.043 wt%.

From this, the aspect ratio was calculated to be **286**.

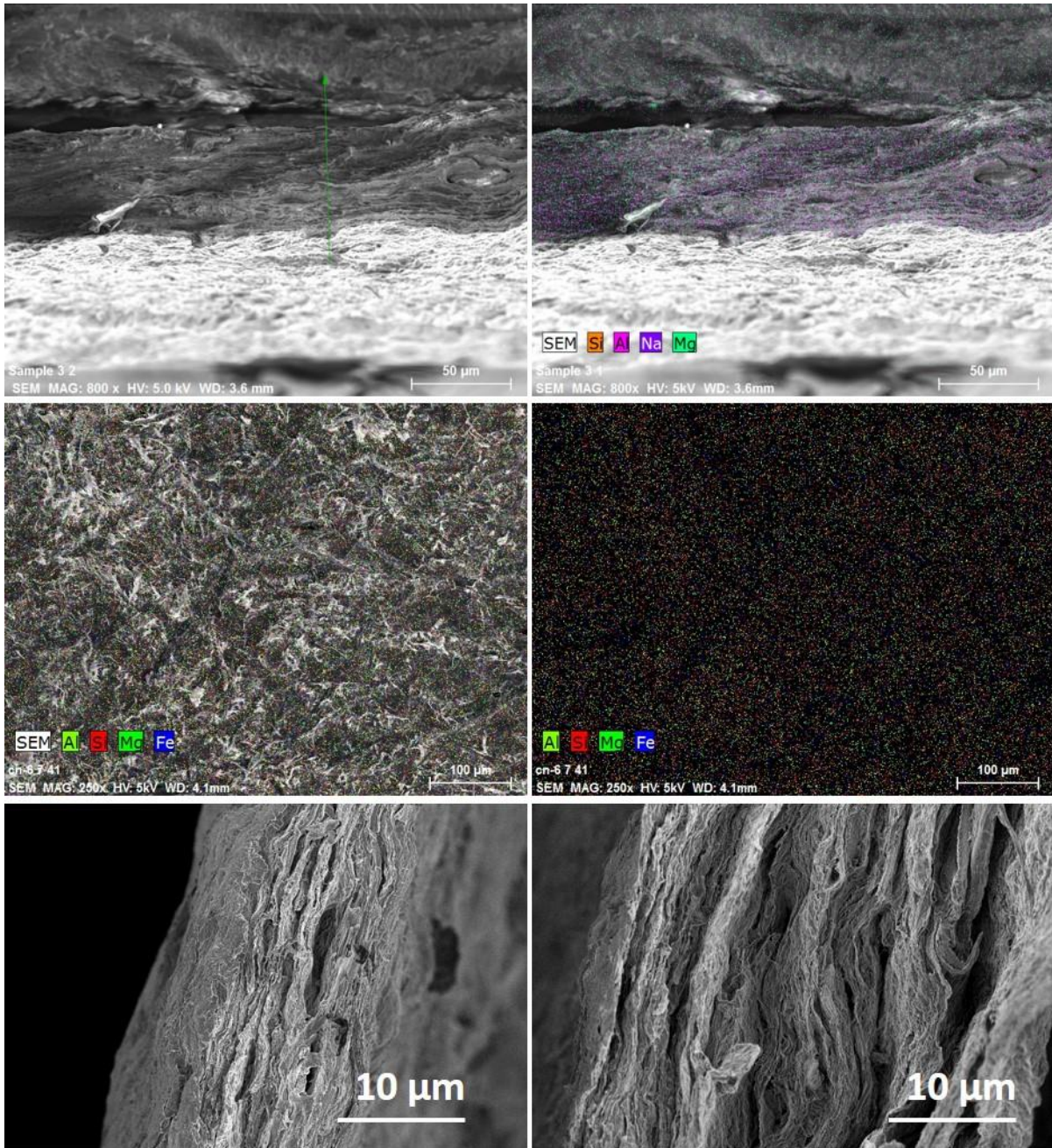
C3: EDX study on morphology on clay hybrids

Figure C4: EDX and SEM images of the original composite sheets with various compositions. Elemental mapping over the cross section and top down view for 28.1 wt% MMT revealing a homogeneous composite formation. Cross section of 9.1 and 28.6 wt% at low magnification.

C4: XRD pattern for composites with homogenization step

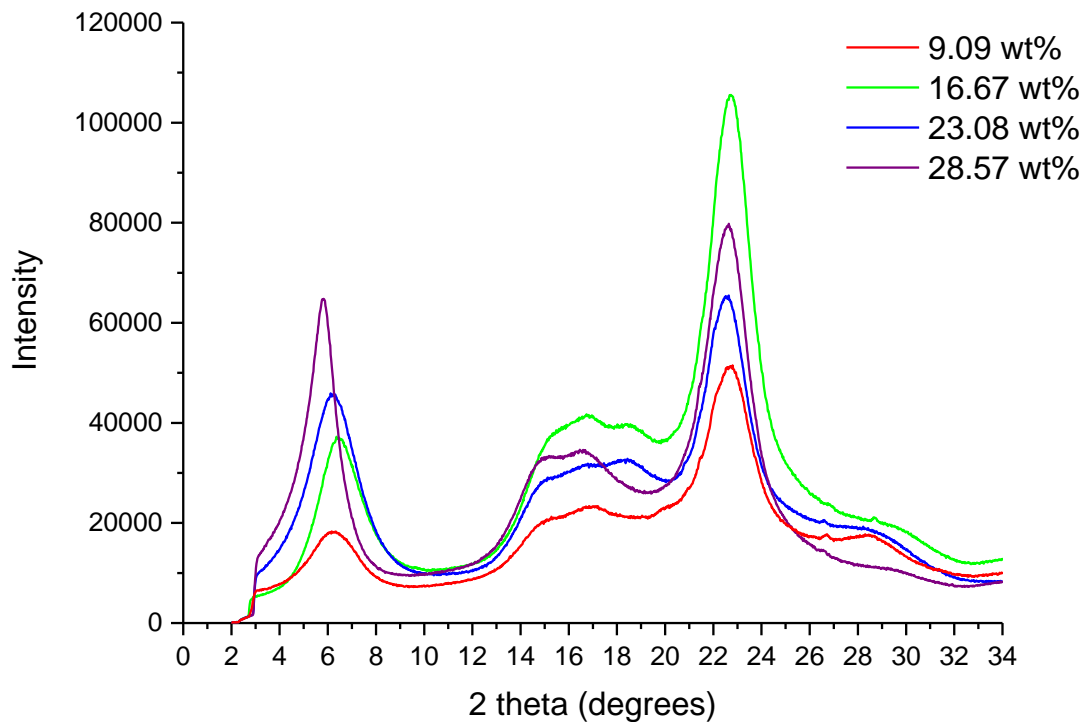


Figure C5: XRD patterns for composite sheets with homogenization step.

C5: References

1. Martinez, D., et al. *Characterizing the mobility of papermaking fibres during sedimentation*. in *The science of papermaking: transactions of the 12th fundamental research symposium*, Oxford. The Pulp and Paper Fundamental Research Society, Bury, UK. 2001.
2. Zhang, L., et al., *Effect of cellulose nanofiber dimensions on sheet forming through filtration*. *Cellulose*, 2012. **19**(2): p. 561-574.
3. Raj, P., et al., *Effect of cationic polyacrylamide on the processing and properties of nanocellulose films*. *Journal of colloid and interface science*, 2015. **447**: p. 113-119.

THIS PAGE HAS BEEN INTENTIONALLY LEFT BLANK

WATER RESISTANT CELLULOSE – TITANIUM DIOXIDE COMPOSITES FOR PHOTOCATALYSIS

Uthpala M. Garusinghe, Vikram. S. Raghuwanshi, Warren Batchelor* and Gil Garnier*

BioResource Processing Research Institute of Australia (BioPRIA), Department of Chemical
Engineering, Monash University, VIC-3800, Australia

*Corresponding authors: [REDACTED]

[REDACTED]

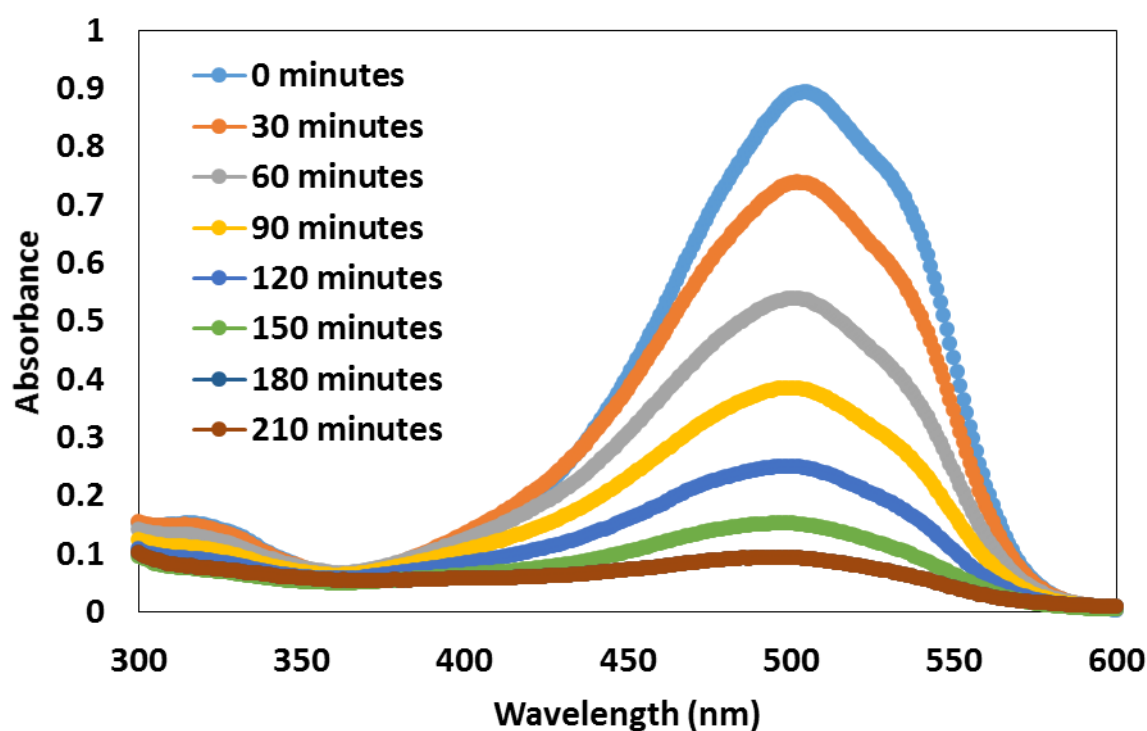


Figure D1: Effect of UV exposure time on adsorption spectra for the composite with 1 wt% TiO₂ loading and with 10 mg PAE/g MFC (second repeat of the same composite test sample).

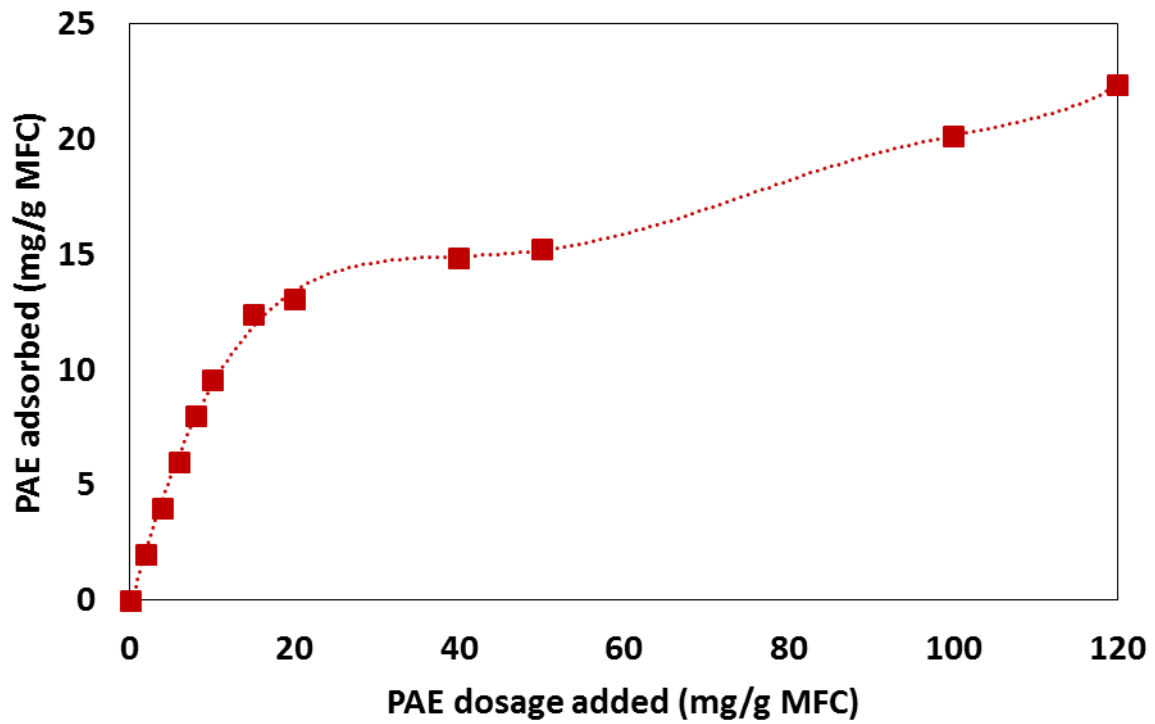


Figure D2: PAE Adsorption isotherm on MFC for extreme PAE dosages.

APPENDIX II

PUBLICATIONS INCLUDED IN THESIS IN THEIR

PUBLISHED FORMAT

THIS PAGE HAS BEEN INTENTIONALLY LEFT BLANK

Strong cellulose nanofibre–nanosilica composites with controllable pore structure

Uthpala M. Garusinghe · Swambabu Varanasi · Gil Garnier · Warren Batchelor 

Received: 9 January 2017 / Accepted: 21 March 2017 / Published online: 27 March 2017
© Springer Science+Business Media Dordrecht 2017

Abstract Flexible nanocellulose composites with silica nanoparticle loading from 5 to 77 wt% and tunable pore size were made and characterised. The pore structure of the new composites can be controlled (100–1000 nm to 10–60 nm) by adjusting the silica nanoparticle content. Composites were prepared by first complexing nanoparticles with a cationic dimethylaminoethyl methacrylate polyacrylamide, followed by retaining this complex in a nanocellulose fibre network. High retention of nanoparticles resulted. The structural changes and pore size distribution of the composites were characterised through scanning electron microscopy (SEM) and mercury porosimetry analysis, respectively. The heavily loaded composites formed packed bed structures of nanoparticles. Film thickness was approximately constant for composites with low loading, indicating that nanoparticles filled gaps created by nanocellulose fibres without altering their structure. Film thickness increased drastically for high loading because of the new packed bed structure. Unexpectedly, within the

investigated loading range, the level of the tensile index on nanocellulose mass basis remained constant, showing that the silica nanoparticles did not significantly interfere with the bonding between the cellulose nanofibres. This hierarchically engineered material remains flexible at all loadings, and its unique packing enables use in applications requiring nanocellulose composites with controlled pore structure and high surface area.

Keywords Nanocellulose · Nanoparticles · Composites · Porosity · Structure · Strength

Introduction

Work aimed at development of novel nanoparticle (NP) structures is ever increasing because of their excellent properties, e.g. large surface area. NPs can be selected for their chemical composition, but also tailored in terms of size (scale), shape (cylindrical, planar and spherical) and surface properties (surface area, bonding type and charge distribution) (Schaefer and Justice 2007; Winey and Vaia 2007; Kausch and Michler 2007). Although NPs have versatile properties and can self-aggregate, their use raises important issues concerning uncontrolled release into air when dry, which may limit their applications. To prevent such release, NPs can be dispersed in a supporting

Electronic supplementary material The online version of this article (doi:10.1007/s10570-017-1265-2) contains supplementary material, which is available to authorized users.

U. M. Garusinghe · S. Varanasi · G. Garnier ·
W. Batchelor (✉)

Department of Chemical Engineering, BioResource
Processing Research Institute of Australia (BioPRIA),
Monash University, Clayton, VIC 3800, Australia
e-mail: 

matrix or sintered to form films. Embedding NPs in a continuous polymer matrix limits the availability of their surface. Sintering keeps NPs together by forming a composite film, which is typically brittle and weak, also limiting applications. An ideal NP embedding matrix would be strong, flexible and durable, able to retain NPs, while allowing the surface of the NPs to be readily available; achieving these requirements simultaneously remains a significant challenge.

Using nanocellulose as the structural component/binder to hold NPs in the matrix opens up a new route to tailor high-performance nanoparticulate composites. The porous fibre structure allows access to the NPs in the material. Nanocellulose is a renewable and sustainable nanomaterial which is biodegradable, recyclable and readily available (Oksman et al. 2006; Kim et al. 2006). Nanocellulose has great potential for use in many applications due to its high mechanical strength, low thermal expansion, large surface area, broad capacity for chemical modification and flexibility (Sehaqui et al. 2010; Klemm et al. 2006). While the diameter of nanocellulose ranges from 1 to 100 nm (Farhang 2007), its length is on micron scale, giving nanocellulose fibres high aspect ratio, which allows formation of highly entangled networks when transformed into nonwoven materials (Sehaqui et al. 2014). As a result, nanocellulose can form aerogels (Korhonen et al. 2011), strong films (Sehaqui et al. 2010), membranes (Sehaqui et al. 2012), bio-composites (Tingaut et al. 2009), hydrogels etc. Each of these high-porosity substrates can serve as a flexible template or carrier for NPs, enabling production of nanocomposites that combine the advantages of both constituents (Varanasi et al. 2015; Krol et al. 2015).

Even though progress has been made on developing nanocellulose–NP composites, the role played by the NPs in the composite structure is poorly understood. In particular, the performance of the material at very high NP loading and the variation in performance, surface area and pore size with the NP loading are not well understood. Nanocomposites with very high NP loading have been created by mixing cellulose nanofibrils and montmorillonite together with 90 wt% clay loading, which helped improve the tortuosity of the composite to lower its oxygen permeability (Liu et al. 2011). However, a combination of features of the clay, such as its shape, size and cationic charge, facilitates its binding to the nanofibril

network. On the other hand, it is far more difficult to retain anionic and spherical NPs of materials such as SiO₂ with dimensions in the same range as the nanofibre diameter in a fibrous cellulose matrix.

In this work, we focus on composites made of nanocellulose and silica NPs. Materials including silica NPs have widespread applications in drug delivery (Slowing et al. 2007; Lu et al. 2007) and separators in Li-ion batteries (Krol et al. 2015; Kim et al. 2013), and while silica NPs have been used at low levels in nanocellulose membranes (Garusinghe et al. 2017; Varanasi et al. 2015), there has been no systematic study of silica NP–nanocellulose composites across the range of composition. Therefore, the aim of this work is to produce flexible, strong and pore-size-controllable nanocellulose composites using a solution/filtration process to provide high retention of the NPs in the structure while retaining the availability of their surface.

Experimental

Materials

Microfibrillated cellulose (MFC) was purchased from DAICEL Chemical Industries Limited, Japan (grade Celish KY-100G). MFC was supplied at 25 % solids content and stored at 5 °C as received. MFC has mean diameter of 73 nm and aspect ratio between 100 to 150 (Varanasi et al. 2013).

Cationic dimethylaminoethyl methacrylate polyacrylamide (CPAM) polymer with high molecular weight (13 MDa) and charge density of 40 wt% (F1, SnowFlake Cationics) was kindly supplied by AQUA + TECH, Switzerland. This CPAM can flocculate nanofibres (Li et al. 2016) and NPs.

NexSil 85-40 and NexSil 125-40 aqueous colloidal silica with surface area of 55 and 35 m²/g, respectively, were provided by IMCD Australia Ltd. as 40 wt% suspensions. Their diameter distributions are summarised in Table 1.

Methods

Preparation of MFC, CPAM and NP suspensions

A 3L Mavis Engineering (model no. 8522) disintegrator was used to disperse 0.2 wt% nanofibres in

Table 1 Diameter distribution of NPs (see Fig. S1 in Supplementary Information for details)

	ImageJ using SEM images	Dynamic light scattering (DLS)
NexSil 85-40 (Small)	30 and 70 nm	35 and 78 nm
NexSil 125-40 (Large)	60 and 130 nm	46 and 113 nm

deionised water uniformly using 15,000 propeller revolutions. CPAM solutions (0.01 wt%) were prepared by mixing CPAM powder in deionised water using a magnetic stirrer for 8 h prior to the experiment to ensure full solubilisation (Ngo et al. 2013). Silica NP suspensions (0.1 wt%) were prepared by diluting 40 wt% silica NP suspension using deionised water and mixing using a magnetic stirrer for 10 min prior to use. All suspensions were prepared at room temperature.

MFC sheet preparation

Nanofibre sheets were prepared using a standard British hand sheet maker (model T205). The hand sheet maker was equipped with a woven filter with average openings of 74 microns. MFC suspension (0.2 wt% solids) was poured into the hand sheet maker and allowed to drain under gravity. After the water had drained, the formed film was removed from the filter using blotting papers, then dried at 105 °C using a sheet drier.

MFC–NP composite preparation

Preparation of composite suspension involved mixing nanofibres (0.2 wt%), colloidal silica (0.1 wt%) and CPAM (0.01 wt%) suspensions together (Fig. 1a) by double controlled simultaneous addition (CSA) method (Varanasi et al. 2015; Bringley et al. 2006). Firstly, CPAM and NP suspensions were mixed together; secondly, the NP-CPAM and nanofibre suspensions were mixed to obtain the final suspension of 0.15 wt%. To facilitate mixing in both stages, a small amount of deionised water (50 mL) was initially added to both beakers. In the composite suspensions, the silica weight fraction was varied from 5 to 77 wt%. As composites with higher NP content have more solution to be mixed, the flow rate was varied. The CPAM flow rate ranged from 2.1 to 165 mL/min, the NP suspension flow rate was varied from 5.2 to

397 mL/min, while nanofibres were mixed at 75 mL/min. Flow rates were adjusted to keep the mixing time in each step at 8 min. The final suspension was poured into the British hand sheet maker for composite processing as described above. The NP–CPAM ratio was kept constant at 0.5 mg CPAM/1 m² NP surface for all composites because complete retention was achieved at this ratio.

The nanofibre mass was fixed at 1.2 g, while NPs were added as a percentage of nanofibre mass. Therefore, the composite's final mass varied. Two sets of composites were prepared using two different NP sizes, denoted as “composite V/S” for variable total grammage and small NP size, and “composite V/L” for variable total grammage and large NP size.

Characterisation

Structure and morphology study

SEM was performed using an FEI Nova NanoSEM 450 FEG SEM on nanofibres, composites and cast silica NPs to investigate their structure and morphology. To prepare samples for SEM study, a 3 mm × 3 mm square sample was mounted onto a metal substrate using carbon tape and coated with a thin layer of iridium.

Thickness and density measurements

The thickness of the composites was measured using an L&W thickness tester (model no. 222) as the average value at ten points. The theoretical density of silica NPs and nanofibres was taken as 2400 and 1500 kg/m³, respectively (Varanasi et al. 2013). The composite density was calculated after the sample had been oven dried for 4 h at 105 °C; the volume was calculated from the area and thickness of the composite after oven drying. The minimum thickness, t_m was calculated as

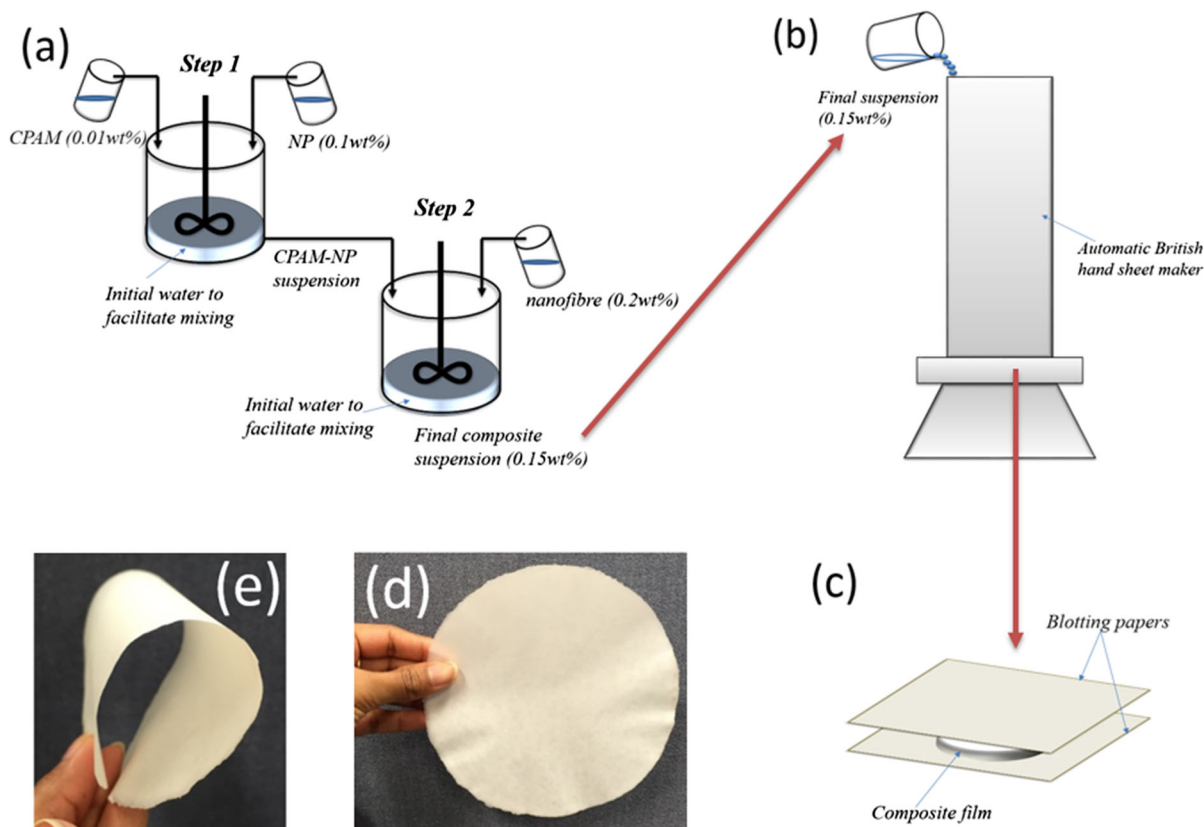


Fig. 1 Preparation of nanocomposite: **a** controlled simultaneous addition (CSA) method, **b** preparation of composite sheet by filtration method, **c** composite sheet processed using blotting

papers, **d** free-standing 77 wt% V/S composite sheet, and **e** illustration of flexibility of 77 wt% V/S sheet

$$t_m = \frac{g_f}{\rho_f} + \frac{g_s}{\rho_s}, \quad (1)$$

where g_f and g_s are the grammage (g/m^2) of nanofibres and NPs, respectively, and ρ_f and ρ_s are the density of nanofibres and NPs, respectively. The maximum density of the composites was calculated as

$$\rho_m = \frac{g_f + g_s}{t_m}. \quad (2)$$

The fractional density ratio was calculated as the density of the composite divided by the theoretical maximum density.

Pore size distribution measurements

The pore size distribution and surface area of the composites were measured using mercury porosimetry (Micromeritics' AutoPore IV 9500 series). The sheets

were cut into $5 \text{ mm} \times 5 \text{ mm}$ pieces and placed in the sample holder, then degassed overnight at $105 \text{ }^\circ\text{C}$. Samples were then transferred into a penetrometer (0.412 stem, solid) for analysis. The minimum pore size that can be measured using mercury porosimetry is 3 nm.

Particle and colloid charge

Zeta potential measurements of MFC and SiO_2 NPs were performed using a Nanobrook Omni (Brookhaven Instruments) in a cuvette cell at $25 \text{ }^\circ\text{C}$. Using the supplied software, the zeta potential was calculated by determining the electrophoretic mobility in an electrophoresis experiment using laser Doppler velocimetry and applying the Smoluchowski equation. MFC suspension (0.2 wt%) was centrifuged at 4400 rpm for 20 min to remove large aggregates, then the supernatant containing colloidal nanocellulose was used to

measure the zeta potential. SiO₂ suspension (0.1 wt%) was used as is for the measurements.

Mechanical strength

An Instron tensile tester (model 5566) was used to record the tensile strength based on Australian/New Zealand Standard Methods 448s and 437s. Composites were cut into 120 mm × 15 mm strips and equilibrated at 23 °C and 50 % relative humidity for a minimum of 24 h prior to dry tensile testing. The span tested was 100 mm, and the elongation was 10 mm/min. For each sample, a mean value was obtained from 20 valid tests.

Results and discussion

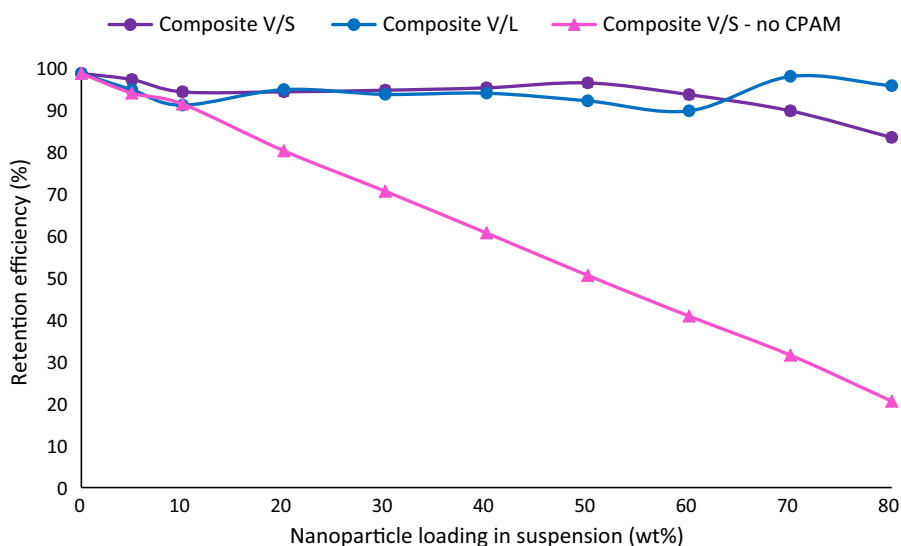
Two series of composites, viz. V/S and V/L, were prepared with small (S) and large (L) NPs, respectively. The nanofibre grammage was fixed at 60 gsm to allow good retention of NPs in the nanocellulose matrix at all NP loadings in both composites. The basis weight of the films varied as the NP loading was increased (denoted by “V” for variable). The properties of the composites were evaluated as a function of the SiO₂ loading and are discussed below in terms of the composite structure. The retention efficiency in the composites with both small and large NPs with and without CPAM is shown in Fig. 2. The retention efficiency is the ratio of the total solid content retained

after the filtration process to the initial solid content added to the suspension. The sheet preparation technique used resulted in high retention efficiency for both series. Nanofibre sheets alone showed 98 % fibre retention with 0.2 wt% fibre concentration because the highly entangled network of fibres prevented fibre loss during the filtering process. The composites achieved high loadings (up to 77 wt%), as the majority of the NPs were strongly bound to the interconnecting cellulose fibres which provide a flexible material (Fig. 1e).

Both MFC and SiO₂ are negatively charged with zeta potential of −26 and −29 mV, respectively. Retention of SiO₂ in an anionic matrix is unfavourable, particularly when using the filtration method. However, some methods such as spray coating (Krol et al. 2015) or layer-by-layer techniques (Li et al. 2013) can force adhesion of NPs onto the cellulose surface irrespective of charge. In such cases, retention is not an issue. Without a retention aid such as CPAM, the retention is very low (Fig. 2, triangles), but still remained at around 20 % at 77 wt% loading.

SEM images of V/S composites with progressively increasing SiO₂ content are shown in Fig. 3. These results indicate that, in the absence of NPs, nanofibres formed a highly interconnected, reasonably dense film with pores of irregular shape (Fig. 3a). The density without NP addition was 750 kg/m³, which is consistent with previous data (783 kg/m³) obtained on sheets of these fibres (Varanasi et al. 2012). As the NP content was progressively increased, the nanofibres’

Fig. 2 Retention of nanofibres and NPs in the composite as function of initial NP loading



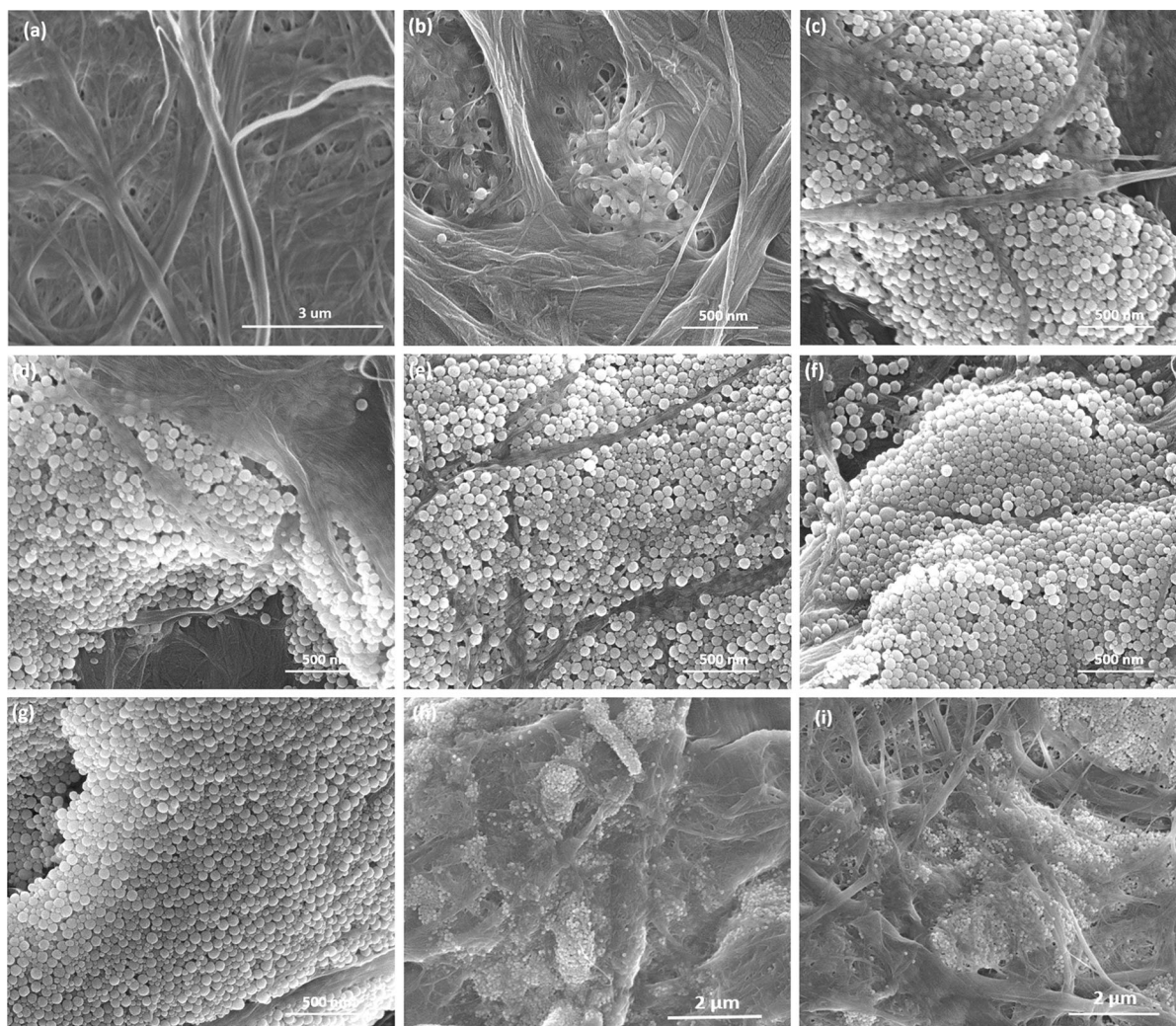


Fig. 3 SEM images of nanofiber composite (V/S) with **a** nanofiber sheet alone and **b** 20 wt%, **c** 30 wt%, **d** 40 wt%, **e** 50 wt%, and **f** 60 wt%, **g** 77 wt% NPs at high magnification, and **h** 60 wt% and **i** 77 wt% NPs at low magnification

porous structure was filled up by NPs (Fig. 3b–d). High NP content results in formation of large NP–CPAM clusters, which remained intact since no nanofibres were seen between the clusters (Fig. 3e). The aggregates were distributed uniformly in the nanofiber matrix. Beyond a certain NP content, the aggregates became larger than the inter-fibrous pores, thus embedding into the nanofiber matrix caused nanofibres to be pushed apart, de-structuring the nanofiber matrix into a packed bed structure. Hence, NP content between 5 and 40 wt% (low loading) represents one regime where the role of NPs is to fill gaps in the nanofiber network, whereas NP content between 50 and 77 wt% (high loading) represents

another regime where NP clusters form a much tighter, controlled pore structure (Fig. 3e–g). This behaviour is illustrated schematically in Fig. 4. Figure 3h, i shows SEM images for 60 and 77 wt%, respectively, at low magnification. SEM images of the V/L composites can be found in Fig. S2 in the Supplementary Information. The transition point from one regime to the other differed for the V/S and V/L composites, probably due to the different NP size. These images are significant as they show a new packing arrangement of SiO₂ in the nanofiber matrix. SEM demonstrated that incorporation of silica NPs as complexes is an effective way to control the pore structure and achieve high surface area using NPs. At very high NP

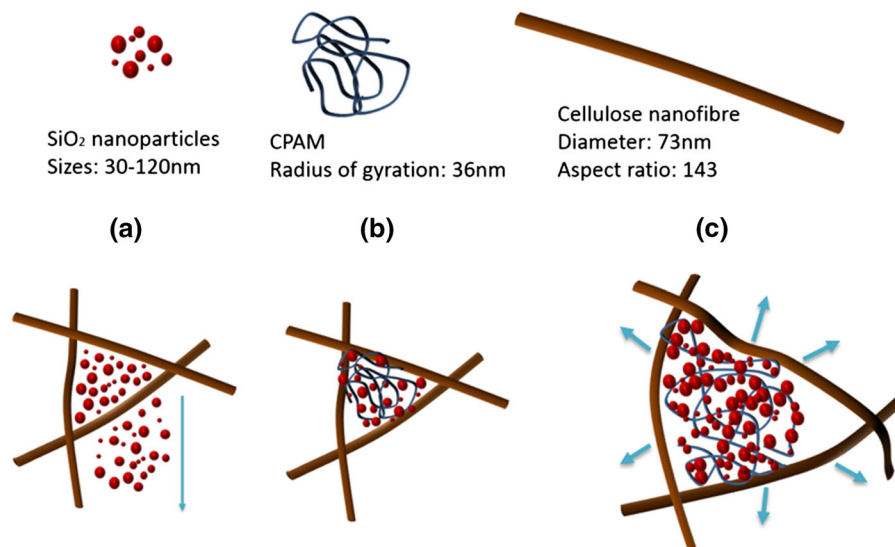


Fig. 4 Schematic mechanism of NP and CPAM hetero-coagulation with nanocellulose (not to scale): **a** no CPAM: NPs flow through the gap (indicated by *arrow*); **b** with CPAM at low NP loading: CPAM bridges NPs with cellulose nanofibres

(NPs retained in gap); **c** with CPAM at high NP loading: large NP–CPAM structure pushes nanofibres to fit in the gap, creating a packed bed structure. *Arrows* indicate movement of fibres from initial position

content, the surface area of the composite as determined by mercury porosimetry analysis almost doubled ($33 \text{ m}^2/\text{g}$ for pure nanofibre sheet versus 80 and $70 \text{ m}^2/\text{g}$ for $70 \text{ wt}\%$ V/S and V/L composites, respectively).

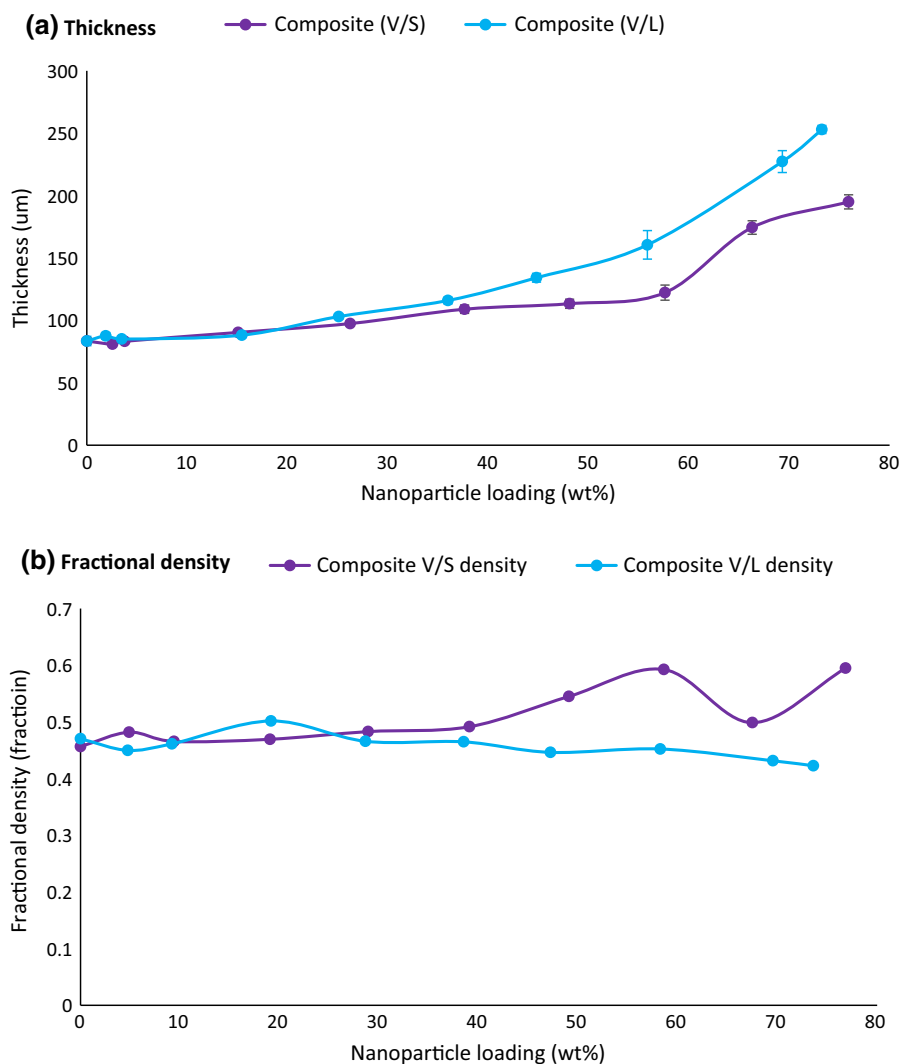
The thickness variation (Fig. 5a) also supported the de-structuring described based on the SEM images. Initially, the thickness increased slowly with NP addition level for V/S and V/L, but both series showed a transition point where the slope of the data increased. This happened at $50 \text{ wt}\%$ for V/L and $60 \text{ wt}\%$ for V/S composites, due to deformation of the structure. In previous work, we used small-angle X-ray scattering (SAXS) analysis to quantify the structure of the silica NP/MFC/CPAM system; this allowed statistical measurements on the structure (Garusinghe et al. 2017), revealing that higher CPAM dosage results in larger/bulk NP clusters. Therefore, high CPAM dosage ($0.5 \text{ mg}/\text{m}^2$) was used in this study, resulting in large clusters of SiO₂ NPs that were retained in the structure, which contributed to the almost twofold increase in thickness compared with pure nanofibre sheet. The fractional density data are shown in Fig. 5b. The fractional density is the fraction of the maximum density achievable if all the pores were to be removed. The constant fractional density across the investigated NP loading range indicates that the structure had

constant void volume, although the nature of the volume changed.

The pore structure results obtained by mercury porosimetry showed that pure nanofibre sheet had a broad pore range between 100 and 1000 nm , arising from the pores within the nonwoven fibre structure (Fig. 6). However, a significant change in pore structure was observed with SiO₂ NP addition. With subsequent increase in the NP content, not only did the broad peak from nanofibres reduce in width, but also the pore size range shifted to smaller values. In addition, a new peak was observed between 10 and 60 nm , increasing continuously in size with higher NP content, because these represent pores present within NP clusters, the number of which increased with the NP content. The pore volume in this figure represents the number of pores present with given pore diameter. Plotting this for lower (3 – 100 nm) and higher (100 – 1000 nm) diameter ranges indicates that the number of pores in the smaller pore range increased with the SiO₂ loading while the number of pores in the larger pore range decreased (Fig. 7). This signifies that the large pore size range is controlled by SiO₂, whose addition to the nanocellulose composite results in a more developed pore structure.

The pore size distribution patterns for V/L (Fig. 6b) and V/S (Fig. 6a) differed. At low loading for the V/L

Fig. 5 **a** Thickness and **b** fractional density of composites as function of NP loading. *Error bars* in thickness graph indicate standard deviations



series ($\text{SiO}_2 = 10 \text{ wt}\%$), the overall pore structure did not deviate much from that of pure nanofibres. However, at high loading, the V/L series showed lower pore size by almost an order of magnitude compared with V/S. The bimodal structure changed to a single peak at low pore size, indicating a more compact and more tightly controlled pore size distribution. It is not clear why these two composites behaved differently; it may be due to the different NP size. A drawback of the mercury porosimetry method is that it only measures pores with size larger than 3 nm. However, this is of little consequence as the target application of these composites is for separation of larger particles—especially bacteria and food-

based colloids—which are orders of magnitude larger than this 3 nm detection limit.

The strength of the composite is a significant factor, because composites with very high loading and retention are useless if their strength is poor. The silica NPs are not expected to contribute significantly to the strength. Indeed, for sheets made from conventional cellulose fibres, addition of inorganic filler particles significantly reduces the strength, as the particles interfere with the bonding between fibres.

Figure 8 shows the curves of tensile index (TI) versus strain for the V/S composites with different nanofibre grammages. Here, the tensile index is calculated as $\text{TI} = F/(w \times G)$, where F is the breaking

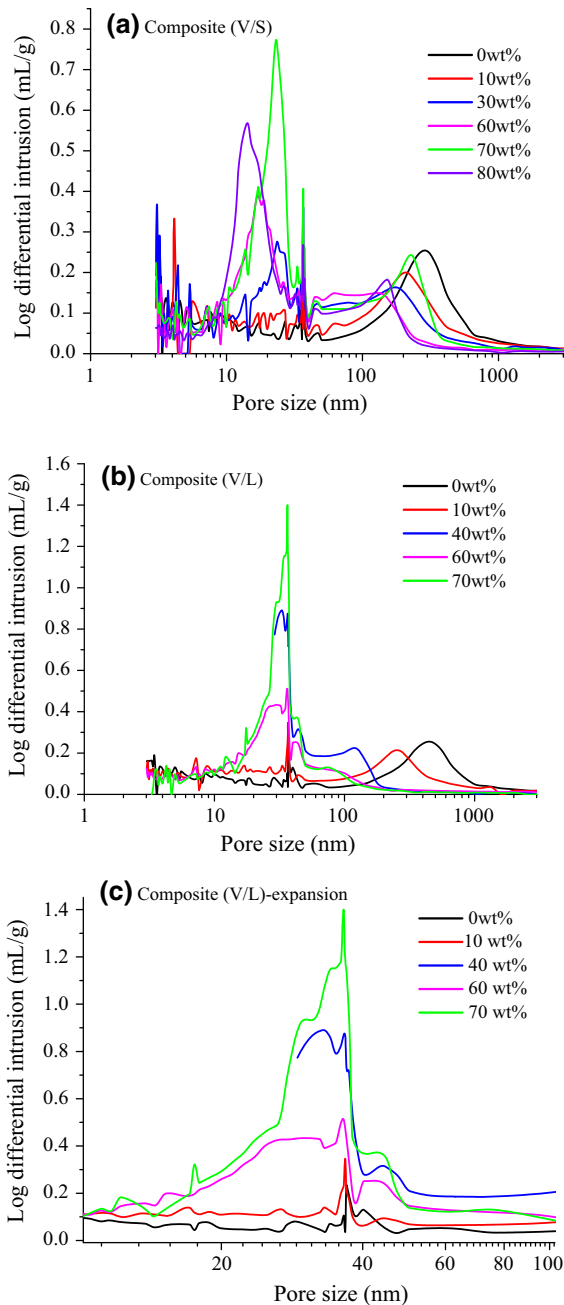


Fig. 6 Pore size distribution for nanocellulose–SiO₂ composite sheets as function of silica content: **a** V/S (with smaller NPs), **b** V/L (with larger NPs), **c** enlarged graph for V/L composite between 10 and 100 nm. The legend indicates the NP loading added in the suspension

force, w is the test specimen width of 15 mm, and G is the nanofibre grammage in g/m². Since the mass of nanofibres used was the same for all the composites

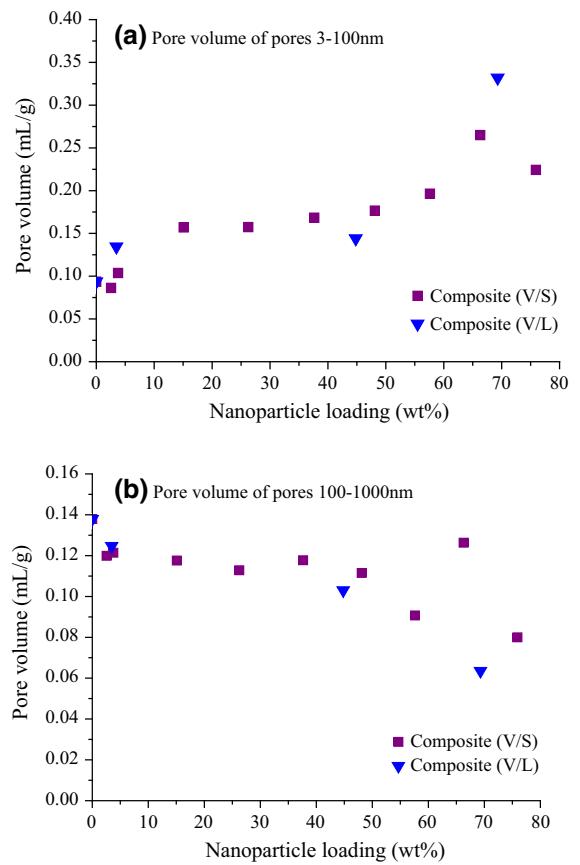


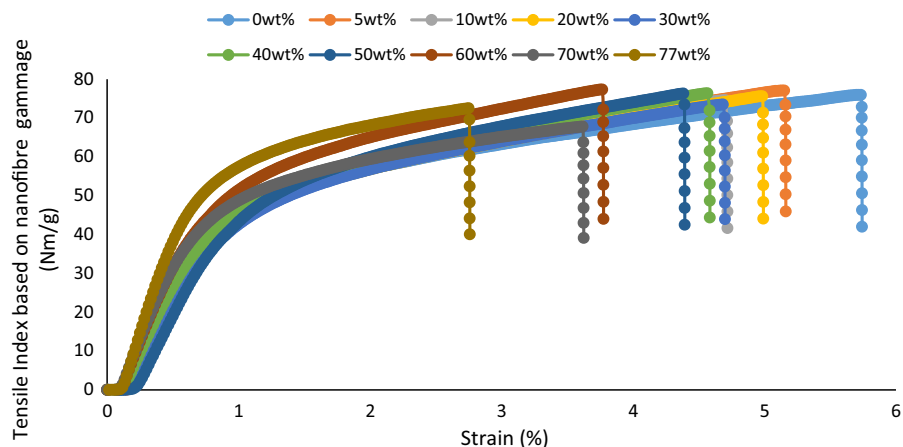
Fig. 7 Composite pore volume as function of NP loading: **a** total pore volume for small pores (3–100 nm) and **b** total pore volume for large pores (100–1000 nm)

(1.2 g, 60 g/m²), the force versus strain graph is identical except for a scaling factor.

The results in Fig. 8 are extremely interesting. While the strain at break reduced from 5.8 % for the unloaded sample to 2.8 % at 77 wt% loading, there was very little dependence of the tensile index on the nanofibre grammage, remaining in the range of 70–80 Nm/g.

It is likely that the strain at break is reduced because, at high loadings, the fibres are completely surrounded by NPs and are not free to rearrange themselves to accommodate an applied load, thus significantly reducing the plastic deformation occurring just before fracture. The fact that all the composites showed the same breaking load indicates, firstly, that the NPs do not contribute to the strength and are only filling the gaps between fibres, but also surprisingly, that the NPs do not interfere with the bonding

Fig. 8 Tensile index versus strain for V/S composites with different nanofibre grammages



between the fibres. This is an extremely interesting finding, and the corresponding mechanisms should be explored further. The initial slope, in the elastic region, was similar for all the loadings except for 60 wt% onwards. This is the point at which the fibre structure changed, as mentioned above. The measured mean elastic modulus and tensile stiffness index for nanofibre sheet alone were 4.8 GPa and 4582 Nm/g, respectively, while for 77 wt% sheet they were 3.8 GPa and 6130 Nm/g, respectively. Thus, the novel composites maintained their strength even at high loading, highlighting promising mechanical properties.

SEM and structure analysis demonstrated that the produced MFC–SiO₂ composites represent a new type of fibrous composite with very high NP loading and unique packing arrangement. Based on their good strength, flexibility and tunable pore structure, this new material is promising for use in membranes for applications such as pasteurisation and other food processes, separators in batteries (Krol et al. 2015; Kim et al. 2013) and water treatment (Varanasi et al. 2015).

Conclusions

New flexible MFC–SiO₂ composite films with high surface area and tunable pore structure were developed using a process combining controlled simultaneous addition (CSA) with standard filtration. This process is easily scalable for industrial applications. Anionic NP loading up to 77 wt% was achieved with high nanoparticle (NP) retention by forming NP–

polyelectrolyte complexes. For low levels of NP loading, NP clusters simply filled the gaps created by the nanofibre porous structure. At this point, no significant change in the thickness of the composite film was observed. At high levels of NP loading, the NP clusters became too large for the available pores and the nanofibre matrix de-structured to accommodate the clusters by pushing fibres apart, resulting in composites with a packed bed-type structure. The thickness of the composite films with higher NP loadings therefore increased significantly. Analysis of the pore size distribution of the composites revealed that the material had tunable pore structure (100–1000 nm to 10–60 nm), controlled by the NP content. At higher loadings, much tighter and well-controlled pore structure could be obtained. The tensile index of all the composites remained between 70 and 80 Nm/g even at higher loadings, suggesting that NPs did not affect the strength.

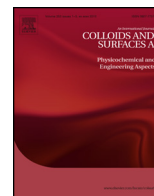
New, well-developed and highly flexible nanocellulose composite materials with high NP loading distributed in a unique packing arrangement were produced using a process that ensured high NP retention. This composite process is scalable to develop a platform for preparation of very high surface area, functionalised porous materials with industrial applications as filters, absorbents and catalysts.

Acknowledgments We thank MCEM for scanning electron microscopy and Scot Sharman for technical help. The authors acknowledge financial support from the Australian Research Council, Australian Paper, Carter Holt Harvey, Circa, Norske Skog and Visy through Industry Transformation Research Hub

Grant IH130100016. U.M.G. thanks Monash University for MGS and FEIPRS scholarships.

References

- Bringley JF, Wunder A, Howe AM, Wesley RD, Qiao TA, Liebert NB et al (2006) Controlled, simultaneous assembly of polyethylenimine onto nanoparticle silica colloids. *Langmuir* 22(9):4198–4207
- Farhang B (2007) Nanotechnology and lipids. *Lipid Technol* 19(6):132–135
- Garusinghe UM, Raghuvanshi VS, Garvey CJ, Varanasi S, Hutchinson CR, Batchelor W et al (2017) Assembly of nanoparticles–polyelectrolyte complexes in nanofiber cellulose structures. *Colloids Surf A* 513:373–379
- Kausch H, Michler G (2007) Effect of nanoparticle size and size-distribution on mechanical behavior of filled amorphous thermoplastic polymers. *J Appl Polym Sci* 105(5):2577–2587
- Kim J, Yun S, Ounaies Z (2006) Discovery of cellulose as a smart material. *Macromolecules* 39(12):4202–4206
- Kim J-H, Kim J-H, Choi E-S, Yu HK, Kim JH, Wu Q et al (2013) Colloidal silica nanoparticle-assisted structural control of cellulose nanofiber paper separators for lithium-ion batteries. *J Power Sour* 242:533–540
- Klemm D, Schumann D, Kramer F, Heßler N, Hornung M, Schmauder H-P et al (2006) Nanocelluloses as innovative polymers in research and application. *Polysaccharides II*. Springer, New York, pp 49–96
- Korhonen JT, Kettunen M, Ras RH, Ikkala O (2011) Hydrophobic nanocellulose aerogels as floating, sustainable, reusable, and recyclable oil absorbents. *ACS Appl Mater Interfaces* 3(6):1813–1816
- Krol LF, Beneventi D, Alloin F, Chaussy D (2015) Microfibrillated cellulose-SiO₂ composite nanopapers produced by spray deposition. *J Mater Sci* 50(11):4095–4103
- Li H, Fu S, Peng L (2013) Surface modification of cellulose fibers by layer-by-layer self-assembly of lignosulfonates and TiO₂ nanoparticles: effect on photocatalytic abilities and paper properties. *Fibers Polym* 14(11):1794–1802
- Li Q, Raj P, Husain FA, Varanasi S, Rainey T, Garnier G et al (2016) Engineering cellulose nanofibre suspensions to control filtration resistance and sheet permeability. *Cellulose* 23(1):391–402
- Liu A, Walther A, Ikkala O, Belova L, Berglund LA (2011) Clay nanopaper with tough cellulose nanofiber matrix for fire retardancy and gas barrier functions. *Biomacromolecules* 12(3):633–641
- Lu J, Liong M, Zink JJ, Tamanoi F (2007) Mesoporous silica nanoparticles as a delivery system for hydrophobic anti-cancer drugs. *Small* 3(8):1341–1346
- Ngo YH, Li D, Simon GP, Garnier G (2013) Effect of cationic polyacrylamide dissolution on the adsorption state of gold nanoparticles on paper and their surface enhanced Raman scattering properties. *Colloids Surf A* 420:46–52
- Oksman K, Mathew A, Bondeson D, Kvien I (2006) Manufacturing process of cellulose whiskers/poly(lactic acid) nanocomposites. *Compos Sci Technol* 66(15):2776–2784
- Schaefer DW, Justice RS (2007) How nano are nanocomposites? *Macromolecules* 40(24):8501–8517
- Sehaqui H, Liu A, Zhou Q, Berglund LA (2010) Fast preparation procedure for large, flat cellulose and cellulose/inorganic nanopaper structures. *Biomacromolecules* 11(9):2195–2198
- Sehaqui H, Morimune S, Nishino T, Berglund LA (2012) Stretchable and strong cellulose nanopaper structures based on polymer-coated nanofiber networks: an alternative to nonwoven porous membranes from electrospinning. *Biomacromolecules* 13(11):3661–3667
- Sehaqui H, Zimmermann T, Tingaut P (2014) Hydrophobic cellulose nanopaper through a mild esterification procedure. *Cellulose* 21(1):367–382
- Slowing II, Trewyn BG, Giri S, Lin VY (2007) Mesoporous silica nanoparticles for drug delivery and biosensing applications. *Adv Funct Mater* 17(8):1225–1236
- Tingaut P, Zimmermann T, Lopez-Suevos F (2009) Synthesis and characterization of bionanocomposites with tunable properties from poly (lactic acid) and acetylated microfibrillated cellulose. *Biomacromolecules* 11(2):454–464
- Varanasi S, Chiam HH, Batchelor W (2012) Application and interpretation of zero and short-span testing on nanofibre sheet materials. *Nord Pulp Pap Res J* 27(2):343
- Varanasi S, He R, Batchelor W (2013) Estimation of cellulose nanofibre aspect ratio from measurements of fibre suspension gel point. *Cellulose* 20(4):1885–1896
- Varanasi S, Low Z-X, Batchelor W (2015) Cellulose nanofibre composite membranes—biodegradable and recyclable UF membranes. *Chem Eng J* 265:138–146
- Winey KI, Vaia RA (2007) Polymer nanocomposites. *MRS Bull* 32(04):314–322



Assembly of nanoparticles–polyelectrolyte complexes in nanofiber cellulose structures



Uthpala M. Garusinghe^{a,1}, Vikram S. Raghuvanshi^{a,*,1}, Christopher J. Garvey^c, Swambabu Varanasi^a, Christopher R. Hutchinson^b, Warren Batchelor^a, Gil Garnier^{a,*}

^a BioResource Processing Research Institute of Australia (BioPRIA), Department of Chemical Engineering, Monash University, VIC-3800, Australia

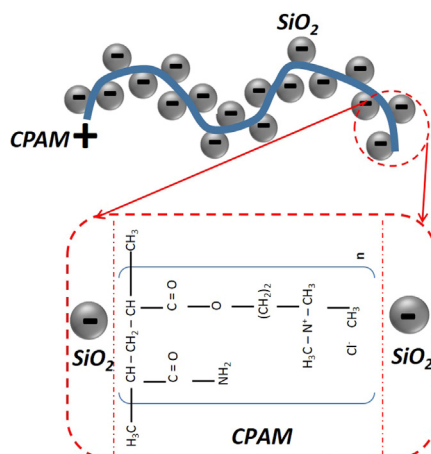
^b Department of Materials Science and Engineering, Monash University, VIC-3800, Australia

^c Australian Nuclear Science and Technology Organisation (ANSTO), Locked Bag 2001, Kirrawee DC, NSW 2232, Australia

HIGHLIGHTS

- We quantify the effect of cationic polyacrylamide (CPAM) dosage on the assembly of silica nanoparticles (NPs) within a nanocellulose composite.
- Increasing CPAM dosage increases retention of NPs within the cellulose matrix with stronger interparticle interactions.
- Small angle X-ray scattering (SAXS) and microscopic reveal that CPAM concentration affects the aggregates size of SiO₂ NPs within the composite.
- We show a bimodal distribution of spherical particles (8–20 nm in diameter) in nanocellulose composites by modelling the SAXS curves.
- Data analysis allow understanding interparticle interactions within assemblies of SiO₂ NPs at the nanometer scale with different dosage of CPAM.

GRAPHICAL ABSTRACT



ARTICLE INFO

Article history:

Received 14 September 2016

Received in revised form 23 October 2016

Accepted 30 October 2016

Available online 1 November 2016

Keywords:

Small angle X-ray scattering (SAXS)

TEM

Silica nanoparticles (NPs)

Cationic polyacrylamide (CPAM)

ABSTRACT

We report the effect of cationic polyacrylamide (CPAM) addition on the structural assembly of silica nanoparticles (NPs) within a nanocellulose fibre matrix. Paper like composites are fabricated by first forming complexes of NPs with CPAM, then adding those to a suspension of nanocellulose fibres; followed by filtration, pressing and drying of the final suspension. Complementary small angle X-ray scattering (SAXS) and microscopy (SEM, TEM) investigations of these composites showed a lognormal bimodal distribution of NP sizes. Data analysis allows understanding interparticle interactions within assemblies of SiO₂ NPs at the nanometer scale with respect to different dosage of CPAM. Increasing CPAM dosage increases retention of NPs within the cellulose matrix with stronger interparticle interactions and produces composites with smaller pores. The correlation length of NPs, indicative of the size of the NP clusters increased from 30 to 70 nm as the CPAM dosage increased from 16.5 to 330 mg/g NPs. Retention

* Corresponding authors.

E-mail addresses: V.S.Raghuvanshi@monash.edu (V.S. Raghuvanshi), G.Garnier@monash.edu (G. Garnier).

¹ Equal contributors as first authors.

1. Introduction

Cellulose nanofibres are fast becoming widely available low-cost organic nanomaterials with specific properties such as tuneable opacity, low thermal expansion, high stiffness, high strength and flexibility. Cellulose is the most abundant, renewable and biodegradable biopolymer, efficiently produced by well-established manufacturing processes and infrastructures [1–3]. Nanocellulose fibres result from the intense fiberizing of cellulose pulp fibres. Cellulose nanofibres “paper” composites have exciting prospects and emerging applications such as smart clothing [4], transparent conductive films for electronics [5,6], tissue engineering [7] and barriers [8]. Even though the full commercial scale production of cellulose nanofibres has not yet been fully achieved, the wide availability of cellulose is promoting the production of new materials with cellulose nanofibres as the main component [9].

Nanocomposites are usually two phase materials consisting of a continuous polymeric phase reinforced by a discontinuous phase consisting of high surface area nanofillers [10]. When the size of fillers shrinks from microscale to nanoscale, the resulting composite develops unusual properties primarily due to the concomitant increase in interfacial area [11]. The properties of nanocomposites depend not only on the properties of their individual components but also on the morphological and interfacial characteristics arising from assembling the individual constituents [12]. In the materials investigated here, nanocellulose is the semi-continuous or connecting phase where silica nanoparticles (NPs) are linked through a retention aid to provide a new structure with voids, in which porosity and pore structure are dependent on NPs. The terms “cellulose nanofibres” and “nanocellulose” are used interchangeably in this paper and nanosilica was selected as model of functional NP.

Since both silica NPs and nanocellulose are negatively charged, an electrostatic repulsion is opposing the retention of NP's in the composite. In such cases, cationic polyelectrolytes are widely used in paper industries as retention aids [13,14]. Common industrial cationic polyelectrolytes include: cationic dimethylamino-ethyl-methacrylate polyacrylamide (CPAM), polyethylenimine (PEI), Polydiallyldimethylammonium chloride (polyDADMAC) and polyamide-amine-epichlorohydrin (PAE). Among those, CPAM is the most prevalent in industry for its low cost, high performance, and wide range of morphologies available. Also, it has the ability to strongly adsorb onto the negatively charged cellulose fibres [15,16] and is a stable polymer soluble in water and many organic solvents [17]. Important industrial applications for CPAM include water treatment, oil well stimulation and mineral processing [17]. Previously, we used CPAM to coagulate and retain NPs into nanocellulose and demonstrated that composite pore structure can be controlled [18]. However, the interaction of the CPAM with NPs and the mechanism of structural formation by CPAM induced NPs assembling within the composite at nanoscale have not been explored and there are no good methodology available to quantify NP aggregate at the critical length scale ranging from 1 nm to 1 μ m.

Generally, for characterization, direct methods such as scanning electron microscopy (SEM) and transmission electron microscopy (TEM) are used, but they evaluate a limited area of the composite and it is difficult to measure interparticle interactions between NPs

[19,20]. Indirect inverse space techniques such as X-ray, neutrons or light scattering provide a complementary statistical perspective on the internal structure of the material. Small angle X-ray scattering (SAXS) is a powerful method to characterize particle or structure size in ranges from \sim 1 to 100 nm [21,22].

In this study, a novel structural characterization approach is developed to elucidate NPs interactions within the respective formed assemblies dispersed in the cellulose matrix. We prepared nanocellulose/SiO₂ nanocomposites using CPAM as a retention aid. SAXS, TEM and SEM were used to quantify and optimize the interaction within silica NP assemblies with respect to different dosage of CPAM and distribution of assemblies within the cellulose matrix. Results from this study will contribute to engineer nanocomposites efficiently with polyelectrolytes. It is the objective of the study to characterize the structure of novel inorganic NP –organic fibre composites at the critical length scale affecting catalysis, permeability and biocompatibility.

2. Experiments

2.1. Materials

Microfibrillated cellulose (MFC) was purchased from DAICEL Chemical Industries Limited, Japan (grade Celish KY-100G). The MFC was supplied at 25% solids content and stored at 5 °C as received. The surface area of MFC is 31.1 m²/g [22,23]. Cationic dimethylamino-ethyl-methacrylate polyacrylamide (CPAM) polymer of high molecular weight (13 MDa) and with a charge density of 40 wt% (F1, SnowFlake Cationics) was graciously supplied by AQUA + TECH, Switzerland. NexSil 8 Aqueous Colloidal Silica was provided by IMCD Australia Ltd as 30 wt% suspensions. The manufacturer reported a colloidal silica average diameter of 8 nm and a specific surface area of 330 m²/g.

2.2. Method

2.2.1. Preparation of MFC, CPAM and NP suspensions

MFC suspensions (0.2 wt%) were prepared by dispersing fibres in deionized water uniformly using a disintegrator equipped with a 3 L vessel at 15000 propeller revolutions. CPAM solutions (0.01 wt%) were prepared by dissolving CPAM powder in deionized water for 8 h using a magnetic stirrer prior to nanocomposite fabrication. SiO₂ NP (0.1 wt%) suspensions were prepared by diluting 30 wt% original silica NP suspension using deionized water, and the suspension was stirred using a magnetic stirrer for 10 min before use. Mixing time is important in both cases to obtain homogenous suspensions. All suspensions were prepared at room temperature. The pH of final solutions is about 8 and does not vary significantly with different dosage of CPAM.

2.2.2. MFC sheet preparation

MFC sheets were prepared [24], using a standard British hand sheet maker (model T205). Concentrated MFC suspension (0.2 wt%) was poured into the hand sheet maker column and allowed to drain under gravity. After the water drained, the formed film was

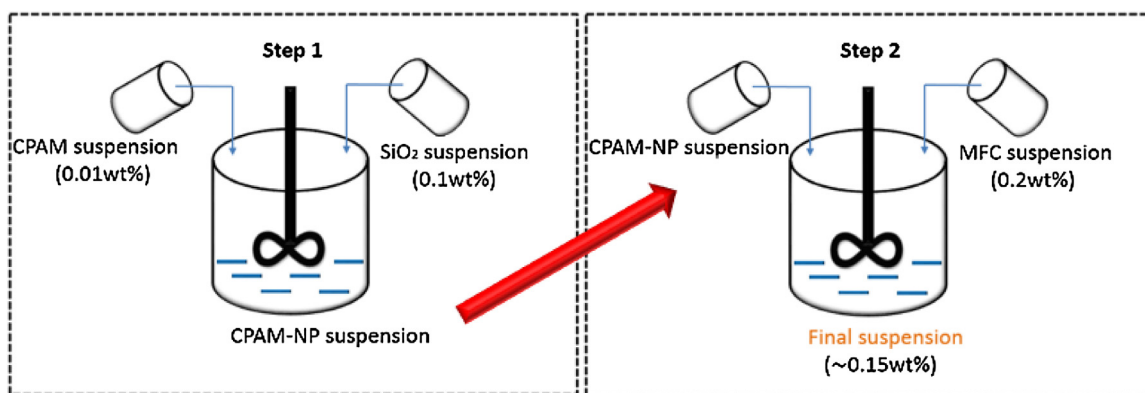


Fig. 1. NP-CPAM complexes are first formed (step 1) and then mixed with a cellulose nanofiber suspension (step 2).

removed from the mesh using blotting papers, then pressed and dried using a sheet drier at 100 °C.

2.2.3. MFC-NP composite preparation

Composite preparation involves a two-step method (Fig. 1). Firstly, CPAM (0.01 wt%) and SiO₂ (0.1 wt%) suspensions were mixed simultaneously together using a hand stirrer (model: HB968NSSJH, 600 W). Secondly, prepared CPAM-SiO₂ suspension was mixed with MFC (0.2 wt%) suspension to obtain the final suspension of the mixture close to 0.15 wt%. This method was adopted from the controlled simultaneous assembly (CSA) of Bringley et al. [25] where he mixed silica colloids and polyethylenimine together.

MFC and SiO₂ masses were kept constant at 1.2 g and 0.12 g, respectively for all composites. Three different CPAM dosages (1.98 mg, 3.96 mg and 39.6 mg) were used. The mixing time in each step was set to a total of 8 min. The flowrate at which CPAM was mixed varied from 2.5 mL/min to 49.5 mL/min. MFC and SiO₂ suspensions were mixed at 75 mL/min and 84 mL/min respectively. The final suspension was poured into the British hand sheet maker and the composite film was prepared as described above (MFC sheet preparation). Table 1 summarizes the type of composites prepared.

2.3. Characterization

2.3.1. Small angle X-ray scattering (SAXS)

Two instruments were used for SAXS measurements. SAXS analyses were first made on a Laboratory Bruker N8 Horizon using a CuK α ($\lambda = 0.154$ nm) micro-source. The scattered photons were collected using a 2D Vantec-500 detector with a pixel size of $\sim 70 \mu\text{m} \times 70 \mu\text{m}$. The scattered photons were collected at the sample to detector distance of 0.6 m which covers the q range from ~ 0.15 to 3.7 nm^{-1} . Radial averaging was used to obtain the final scattering curves. For data reduction, Bruker EVA software was used. Data analysis was performed using SASFit software [26,43,44].

SAXS measurements were also made in a transmission mode on a Pilatus 1 M detector (Dectris, Baden, Switzerland) at the Australian Synchrotron's SAXS/WAXS beamline [27] with a sample to detector distance of 7.2 m. The isotropic raw detector images were

converted to intensity versus q , where $q = 4\pi\sin(\theta)/\lambda$ defined by $\theta/2$ the scattering angle and λ the wavelength (0.113 nm) of the incident x-rays and q range between 0.01 – 1 nm^{-1} . The scattered intensity is plotted as a function of the momentum transfer vector q . Specific macros written [28] for the program IgorPro [29] accounted for the measurement geometry, masking dead pixels and the beam stop and a subtraction of air scatter.

2.3.2. Scanning electron microscopy (SEM)

SEM was performed using a FEI Nova NanoSEM 450 FEG. Secondary electron images were captured. This mode produces high-resolution images and avoids any problems associated with sample charging. A small square (3×3 mm) of composite was mounted onto a metal substrate with a carbon tape. The sample was then coated with a thin layer of Iridium. The accelerating voltage was 5 kV and images were captured at 30,000 to 100,000 magnifications.

2.3.3. Transmission electron microscopy (TEM)

TEM was performed using FEI Tecnai G2 T20 TWIN. For sample preparation, copper grid of 3 mm with a thin carbon layer was dipped into a NP-CPAM suspension and dried. The accelerating voltage was 200 kV and images were captured at 250,000 magnifications at 100 nm scale.

2.3.4. Particle and colloid charge

The zeta potentials were determined by performing measurement using a Nanobrook Omni (Brookhaven Instruments) in a cuvette cell at 25 °C. The software determines the electrophoretic mobility from an electrophoresis experiment by laser Doppler velocimetry and applying Smoluchowski equation to calculate zeta potential. CPAM and SiO₂ NP concentrations were used at 0.5 mg/mL and 0.01 wt% respectively.

3. Results

SAXS measurements were performed to determine the statistical description of the internal composite structure of SiO₂ NPs dispersed in a cellulose matrix [30–36]. Fig. 2a shows the SAXS measurements of a MFC sheet. The SAXS curve for the pure MFC sample shows a weak correlation peak at $q = 1.3 \text{ nm}^{-1}$ indicating the presence of weakly correlated small heterogeneities at length-scales of about 3–5 nm. This weak correlation peak is superimposed upon a broader signal, which is indicative of a broad distribution of length-scales, for example a fibre network. The characteristic size of the elementary fibres is between 3 and 5 nm, and the major contribution to the scattering is from the fibre/nanofiber surface [37,38].

Table 1

Composition of SiO₂-nanocellulose composites, High (H), Medium (M) and Low (L) denote the CPAM dosage.

Samples	MFC (g)	SiO ₂ (mg)	CPAM (mg)
Pure MFC	1.2	–	–
High (H)	1.2	120 (10 wt%)	39.6
Medium (M)	1.2	120 (10 wt%)	3.96
Low (L)	1.2	120 (10 wt%)	1.98

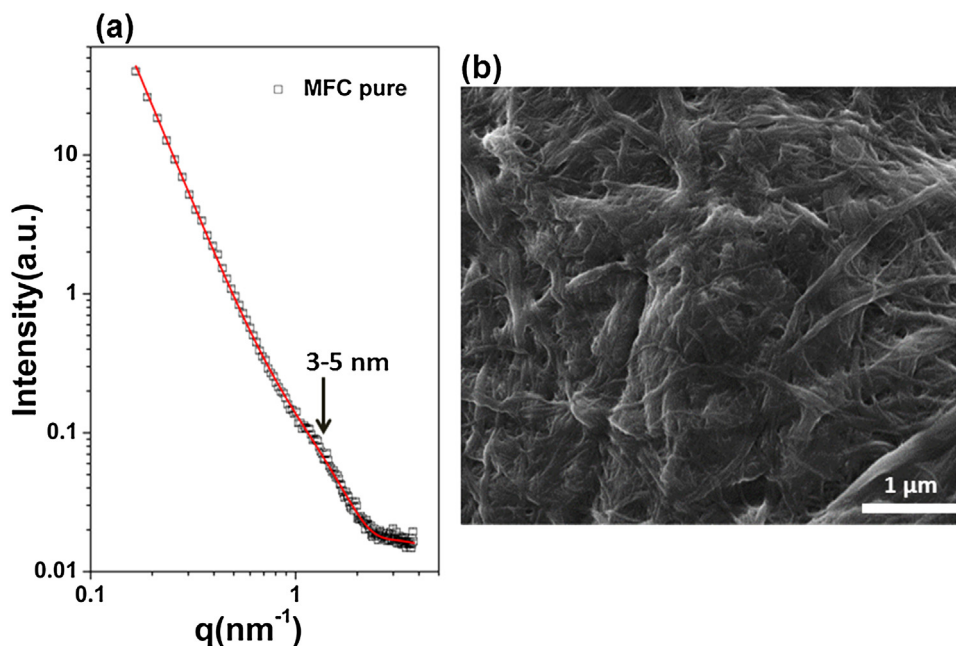


Fig. 2. (a) SAXS curve of the pure MFC sheet. The solid line shows the modelled fit. Arrow shows the diameter of the sample for a peak obtained at a particular q value. (b) SEM image of the MFC sheet at 50,000 magnification.

Fig. 2(b) displays the SEM micrograph of the pure MFC sheet. The micrograph shows that the fibres are isotropically oriented to form a highly entangled network with a wide distribution of pore sizes. This is consistent with the view obtained from SAXS measurements. The average diameter of the fibres was found to be 73 nm [39]. These microfibrils are bundles of elementary nanofibers which are responsible for the weak SAXS correlation peak.

SAXS measurements with a synchrotron can probe a wide structure size range at a high resolution and statistics, which is unachievable with a laboratory SAXS instrument. Fig. 3(a) shows the synchrotron SAXS curves of the MFC-SiO₂ NP composites at

different CPAM dosages. All the SAXS curves show two maxima at fixed q positions of $q = 0.4 \text{ nm}^{-1}$ and 0.2 nm^{-1} which indicates the existence of two kinds of size distributions and volume fractions in the composite. As the CPAM dosage increases, the SAXS peak at $q = 0.4 \text{ nm}^{-1}$ becomes more pronounced and broader for the q ranging between $0.0\text{--}0.7 \text{ nm}^{-1}$. The peaks at $q = 0.8 \text{ nm}^{-1}$ indicate the formation of structures of about 8 nm and the peaks at $q = 0.4 \text{ nm}^{-1}$ reveal the formation of larger structures of about 15–20 nm; these are shown by the arrows in Fig. 3(a).

The quantitative analysis of size, size distribution and number density of the particles was evaluated by non-linear fitting of the

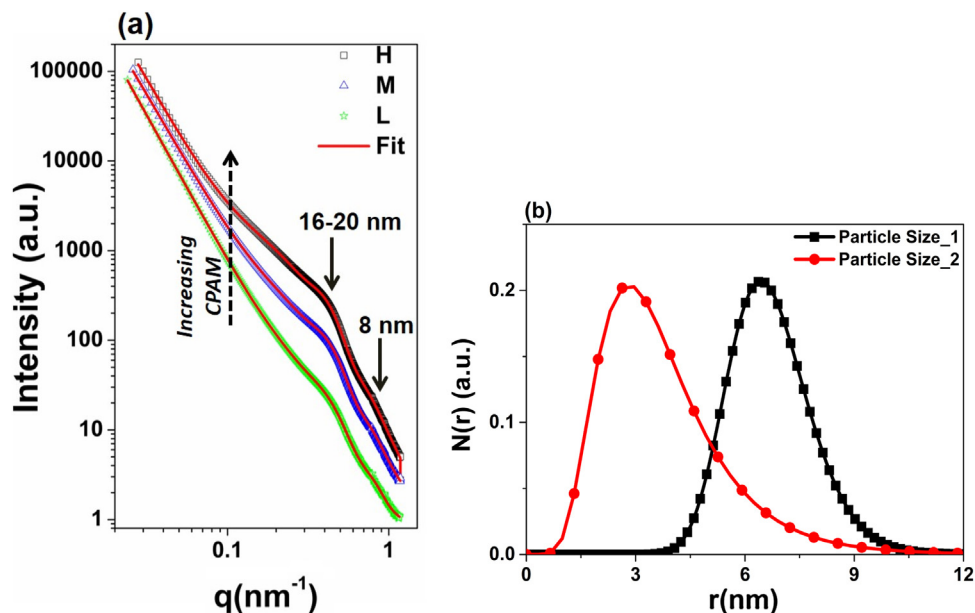


Fig. 3. (a) SAXS curves fitted with the bimodal distribution of the particles with different CPAM dosages; Sample H (High CPAM dosage), Sample M (Medium CPAM dosage), and Sample L (low CPAM dosage). The solid red line shows the fit and the arrows show the diameter obtained from the particular peak position. (b) Lognormal size distribution curves for the sample with the high dosage of CPAM (H). (For interpretation of the references to colour in this figure legend, the reader is referred to the web version of this article).

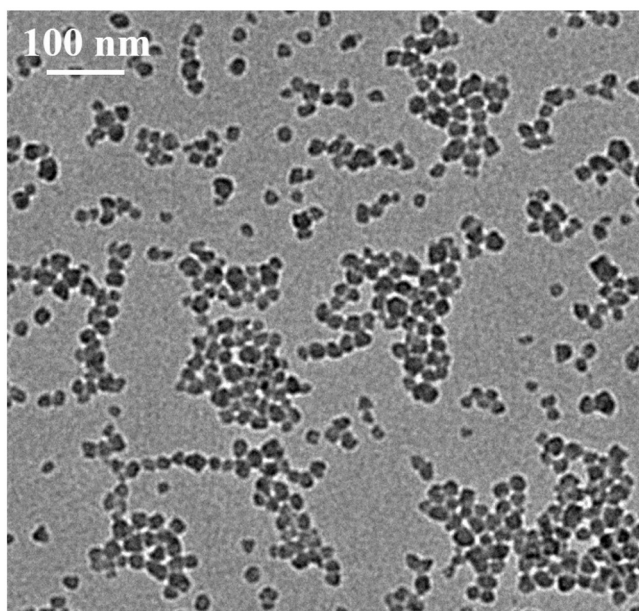


Fig. 4. TEM micrograph for the SiO₂/CPAM complexes at high CPAM dosage prior to the addition of MFC suspension.

curves by using the software SASFit [30–33]. Here, a model for bimodal distribution of spheres and a structure factor for hard spheres with a local monodisperse approximation was fitted to the SAXS curves [45–47]. Details on the modelling of the SAXS curves are given in the Supporting information (S1, S2). Fig. 3(b) shows the lognormal bimodal distribution of spherical shape particles obtained after model fitting of the scattering curves. The size parameters reveal that the smaller particle diameter is about 8 nm and the larger particle diameter is between 15 and 20 nm. The average diameter of 8 nm for smaller structure and 15–20 nm for the bigger structure were determined after fitting the respective SAXS curves. Dynamic light scattering (DLS) measurements on the initial nanoparticle suspension also shows the corresponding bimodal size distribution, which is in agreement with the SAXS results (Supporting information S3).

Evidence on the assemblies of SiO₂-CPAM complexes before addition to the MFC suspension were obtained by the TEM measurements. Fig. 4 shows the TEM micrograph on solution of SiO₂/CPAM at high CPAM dosage and prior to the addition of the MFC. In the TEM micrograph, two different kinds of particle sizes and assemblies of NPs are clearly observed (Supporting information

S4). The results obtained from TEM analysis are in good agreement with the SAXS results.

The structure factor calculated from the SAXS curves accounts for the correlation between the NPs and interparticle interactions [19]. Fig. 5(a) shows the hard sphere structure factor for SiO₂ NPs with local monodisperse approximation used to fit the respective SAXS curves [30,33]. Fig. 5(a) indicates that the clusters of SiO₂ NPs formed in the cellulose fibre matrix are a direct function of the CPAM dosage. As CPAM amount increases, the sharpness of the structure factor peak increases and the peak shifts towards higher q values with respect to the sample with low CPAM dosage. This indicates increase in the volume fraction of NPs and decrease in interparticle separation with increase in CPAM dosage. Fig. 5(b) shows the correlation length obtained from the structure factor, which reveals an increase in interaction between SiO₂ NPs at the high dosage of CPAM.

SEM images of the SiO₂ composites are shown in Fig. 6(a) and (b) for low and high CPAM loadings, respectively. For the composite with low CPAM dosage, the SiO₂ NPs cluster size is smaller and less particles are retained in the cellulose fibre matrix. NPs and small NP clusters accommodate themselves randomly within the fibre matrix without changing any fibre position. Fig. 6(a) is similar to Fig. 2(b) but with bigger pores within the fibre network filled up by NPs. At high CPAM dosage, more and more NPs come into contact and bound with each other, resulting in larger clusters or assemblies with high retention. When the fibre gaps within the structure are not sufficiently large to accommodate the big NPs clusters, the fibres expand to make space. This changes the structure of the composite: volume increases and density decreases, as clearly seen in Fig. 6(b).

4. Discussion

We combined SAXS and microscopic (TEM, SEM) methods to characterize at the nanoscale the structural assemblies/aggregates formed by SiO₂ NPs within a cellulose fibre matrix; CPAM concentration was used to vary the fraction and size of NP aggregation. From our measurement, SiO₂ NPs are negatively charged and form stable aqueous suspensions due to a high zeta potential of -30 mV. On the other hand, CPAM in suspension is positively and strongly charged with a zeta potential for the polymer coil of $+76$ mV and a charge density of 10^{-3} eq/g. Both SiO₂ and cellulose are negatively charged and therefore SiO₂ NPs do not readily adsorb onto the surface of cellulose. This is consistent with the interpretation of SAXS measurements conducted on the composite without any CPAM (Supporting information S5). There is a little difference between this material and the structure characterized with the pure MFC sheet with SAXS. A small amount of CPAM has a significant effect

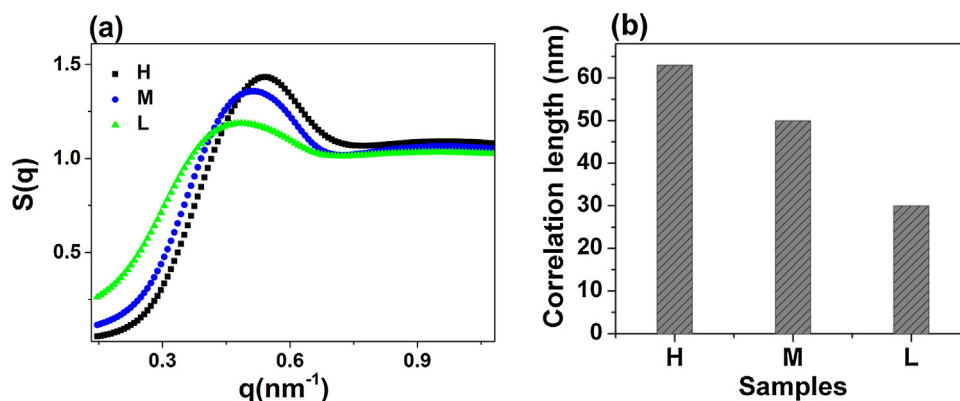


Fig. 5. (a): Evaluated structure factor $S(q)$ for the samples with different CPAM dosages; sample H has high CPAM, M medium and sample L has low CPAM. (b) Correlation length obtained from the SAXS data analysis.

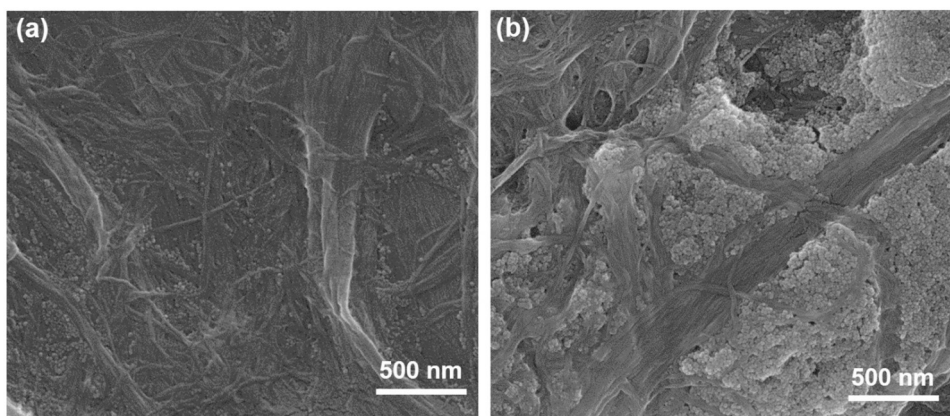


Fig. 6. SEM micrograph of the MFC sheet containing SiO₂ nanoparticles with (a) low (L) CPAM dosage and (b) high (H) CPAM dosage.

on the interactions between SiO₂ NPs and cellulose fibres. CPAM acts as a retention aid for NPs.

SAXS and TEM data analysis corroborate the formation of different size of aggregates of SiO₂ NPs in cellulose matrix at the different CPAM dosages. TEM micrographs (Fig. 4) of the SiO₂/CPAM complexes prior to the addition of MFC suspension reveals that in the presence of CPAM, the SiO₂ NPs aggregate and form assemblies. These assemblies are consisting of two size of NPs (8 and 20 nm) as shown in the Supporting information S4. After addition of SiO₂/CPAM suspension into MFC suspension (step 2), it is hard to obtain TEM micrograph due to difficulty in sample preparation and to get reliable results. Therefore, SAXS measurements were made to obtain much better average information on interparticle spacing within the assemblies of SiO₂ NPs at the nanometer scale.

SAXS data analysis show that these assemblies of SiO₂ NPs consist of NPs structures of diameter ranging between 8 and 20 nm (Fig. 3b). The diameter of NPs is about two to four times smaller than the expected radius of gyration of a CPAM molecule ($R_g = 30\text{--}35\text{ nm}$) assuming random coil at theta conditions (more if electrostatic forces are involved). Therefore, the SiO₂ NPs can easily adsorb onto the CPAM surface or even diffuse within the coil structure to interact directly with the CPAM cations. It is expected that the large CPAM coils are decorated with the SiO₂ NPs and form assemblies by electrostatic interactions and CPAM conformations [40].

Structure factor analysis reveal the information on the correlation between the aggregated SiO₂ NPs assemblies. In Fig. 5a, it is seen that for the high dosage of CPAM the structure factor peak is sharper and shifts towards high q values as compared to the structure factor peak for low CPAM dosage, which indicates narrow distribution of inter-particle separations with high volume fractions. Moreover, increase in the amplitude of structure factor peak reveals the strong interparticle interactions within the assemblies of SiO₂ NPs. This is because at the high CPAM dosage more polyelectrolyte is available to neutralize the NPs surface and overcome the electrostatic repulsion between the particles, resulting in an increase in contact aggregation between the SiO₂ NPs. This results in the formation of large size assemblies having a higher correlation length of about 70 nm and with high volume fraction of NPs within the assemblies. This is in agreement with the TEM measurements shown in Fig. 4. Recently, Ganesan et al. also reported the aggregation of charged NPs in the surrounding of oppositely charged polymers by using mean field self-consistent theory model [41,42]. They described that at low polymer concentration, the charged NPs form polymer-bridged clusters and by increasing the polymer concentration, clusters are formed by inter-particle bridging.

However, at the low CPAM dosage, the structure factor peak is broad, lower in amplitude and shifts towards lower q values which

resembles the loosen SiO₂ NPs aggregates structure with smaller volume fraction and wider distributions. At low CPAM dosage and for a fixed SiO₂ NPs concentration, the tendency to form aggregates/assemblies decreases. This is due to the low density of CPAM available to neutralize the SiO₂ NPs; hence, an electrostatic repulsion between the SiO₂ NPs dominates and leads to the formation of polymer-bridged aggregates of loosely bounded SiO₂ NPs.

Surface coverage of NPs by CPAM directly depends upon the conformation CPAM adopts on the surface of the spherical NPs upon adsorption. The total specific surface area of SiO₂ NPs ($r = 4\text{ nm}$) is 330 m²/g. There are two extreme cases of CPAM adsorption conformation of interest. Should the CPAM remains coiled to adsorb in the form of a blob/sphere of radius 30 nm, it can then cover about 15% of the surface area of SiO₂ NPs. However, should CPAM stretch and adsorb as an extended chain wire of length 22,744 nm (end to end distance; contour length), then it will fully saturate the available surface area of the NPs. Precise estimate of CPAM surface coverage requires measurement as the exact CPAM adsorption conformation which remains undetermined.

5. Conclusion

A series of novel SiO₂-nanocellulose composites of different structures was developed and characterized. SiO₂ nanoparticle (NP) assemblies of different sizes were formed by varying the dosage of CPAM in a nanocellulose matrix. Small angle X-ray scattering (SAXS) and transmission electron microscopy (TEM) measurements reveal the formation of NPs assemblies consisting of bimodal distribution of NPs with smaller particle diameter of 8 nm and large particle diameter of 15–20 nm, respectively. Structure factor obtained from SAXS data analysis shows that at high dosage of CPAM, the assemblies of NPs formed within the cellulose matrix have high volume fraction. Moreover, the NPs in the assemblies have a lower interparticle distance, are strongly bounded, and have larger correlation length. An increase in CPAM dosage increases the retention of NPs assemblies within the cellulose matrix. However, at low dosage of CPAM, the retention of NPs within the cellulose matrix is low (smaller volume fraction) and the assemblies have a loosen structure with weak interparticle interaction. Characterizing and controlling NPs assemblies dispersed in a nanocellulose matrix allows tailoring a novel generation of sustainable composites for applications requiring selected catalytical, permeability or biocompatibility properties.

Acknowledgments

Financial support is from Australian Research Council (ARC), Australian paper, Carter Holt Harvey, Circa, Norske Skog, Orora

and Visy through the Industry Transformation Research Hub grant IH130100016. Thanks to MCEM for scanning electron microscopy, Australian Synchrotron for SAXS measurements and Praveena Raj for discussions. The authors gratefully acknowledge using the Bruker N8 Horizon SAXS funded from ARC LIEF LE130100072

Supporting information Available: Theory of the SAXS method and the equations used for a non-linear fitting procedure of the measured SAXS curves. Moreover, the TEM image of bimodal distribution.

Appendix A. Supplementary data

Supplementary data associated with this article can be found, in the online version, at <http://dx.doi.org/10.1016/j.colsurfa.2016.10.068>.

References

- [1] I. Siró, D. Plackett, *Cellulose* 17 (2010) 459.
- [2] D. Klemm, B. Heublein, H.P. Fink, A. Bohn, *Angew. Chem. Int. Ed.* 44 (2005) 3358.
- [3] D. Klemm, H.P. Schmauder, T. Heinze, *Biopolym. Online* (2005).
- [4] K. Gao, Z. Shao, X. Wu, X. Wang, J. Li, Y. Zhang, W. Wang, F. Wang, *Carbohydr. Polym.* 97 (2013) 243.
- [5] H. Zhu, Z. Fang, C. Preston, Y. Li, L. Hu, *Energy Environ. Sci.* 7 (2014) 269.
- [6] M. Nogi, S. Iwamoto, A.N. Nakagaito, H. Yano, *Adv. Mater.* 21 (2009) 1595.
- [7] Q.P. Pham, U. Sharma, A.G. Mikos, *Tissue Eng.* 12 (2006) 1197.
- [8] C. Aulin, M. Gällstedt, T. Lindström, *Cellulose* 17 (2010) 559.
- [9] L.F. Krol, D. Beneventi, F. Alloin, D. Chaussy, *J. Mater. Sci.* 50 (2015) 4095.
- [10] R.A. Vaia, E.P. Giannelis, *MRS Bull.* 26 (2001) 394.
- [11] K.I. Winey, R.A. Vaia, *MRS Bull.* 32 (2007) 314.
- [12] C. Sanchez, L. Rozes, F. Ribot, C. Laberty-Robert, D. Grosso, C. Sasseo, C. Boissiere, L. Nicole, *C.R. Chim.* 13 (2010) 3.
- [13] T. Asselman, G. Garnier, *Colloids Surf. A: Physicochem. Eng. Asp.* 170 (2000) 79.
- [14] T. Asselman, G. Garnier, *Langmuir* 16 (2000) 4871.
- [15] T. Lindström, C. Söremark, *J. Colloid Interface Sci.* 55 (1976) 305.
- [16] H. Tanaka, A. Swerin, L. Ödberg, S.-B. Park, *J. Pulp Pap. Sci.* 25 (1999) 283.
- [17] N.M. Bikales (Ed.), *Water-Soluble Polymers*, Springer, 1973, p. 213.
- [18] S. Varanasi, Z.-X. Low, W. Batchelor, *Chem. Eng. J.* 265 (2015) 138.
- [19] D. Qiu, T. Cosgrove, A.M. Howe, C.A. Dreiss, *Langmuir* 22 (2006) 546.
- [20] R.H. Ottewill, *J. Colloid Interface Sci.* 58 (1977) 357.
- [21] H. Schnablegger, Y. Singh, Anton Paar, Graz, Austria (2006).
- [22] P. Raj, S. Varanasi, W. Batchelor, G. Garnier, *J. Colloid Interface Sci.* 447 (2015) 113.
- [23] H. Sehaqui, M. Salajkova, Q. Zhou, L.A. Berglund, in: (Eds.) ICCM-17 17th International Conference on Composite Materials, Edinburgh, United Kingdom, 2009.
- [24] S. Varanasi, W.J. Batchelor, *Cellulose* 20 (2013) 211.
- [25] J.F. Bringley, A. Wunder, A.M. Howe, R.D. Wesley, T.A. Qiao, N.B. Liebert, B. Kelley, J. Minter, B. Antalek, J.M. Hewitt, *Langmuir* 22 (2006) 4198.
- [26] J. Kohlbrecher, I. Bressler, URL: <http://kur.web.psi.ch/sans1/SANSSoft/sasfit.html>.
- [27] N.M. Kirby, S.T. Mudie, A.M. Hawley, D.J. Cookson, H.D. Mertens, N. Cowieson, V. Samardzic-Boban, *J. Appl. Crystallogr.* 46 (2013) 1670.
- [28] J. Ilavsky, *J. Appl. Crystallogr.* 45 (2012) 324.
- [29] I. WaveMetrics, WaveMetrics, Inc. PO Box 2088, Lake Oswego, OR 97035 USA 6 (2011).
- [30] V. Raghuvanshi, M. Ochmann, F. Polzer, A. Hoell, K. Rademann, *Chem. Commun.* 50 (2014) 8693.
- [31] V.S. Raghuvanshi, R. Harizanova, D. Tatchev, A. Hoell, C. Rüssel, *J. Solid State Chem.* 222 (2015) 103.
- [32] V.S. Raghuvanshi, A. Hoell, C. Bocker, C. Rüssel, *CrystEngComm* 14 (2012) 5215.
- [33] V.S. Raghuvanshi, M. Ochmann, A. Hoell, F. Polzer, K. Rademann, *Langmuir* 30 (2014) 6038.
- [34] V.S. Raghuvanshi, C. Rüssel, A. Hoell, *Cryst. Growth Des.* 14 (2014) 2838.
- [35] V.S. Raghuvanshi, D. Tatchev, S. Haas, R. Harizanova, I. Gugov, C. Rüssel, A. Hoell, *Appl. Crystallogr.* 45 (2012) 644.
- [36] A. Hoell, Z. Varga, V.S. Raghuvanshi, M. Krumrey, C. Bocker, C. Rüssel, *J. Appl. Crystallogr.* 47 (2014) 60.
- [37] H.F. Jakob, P. Fratzl, S.E. Tschegg, *J. Struct. Biol.* 113 (1994) 13.
- [38] H.F. Jakob, S.E. Tschegg, P. Fratzl, *Macromolecules* 29 (1996) 8435.
- [39] S. Varanasi, R. He, W. Batchelor, *Cellulose* 20 (2013) 1885.
- [40] D. Solberg, L. Wågberg, *Colloids Surf. A: Physicochem. Eng. Aspects* 219 (2003) 161.
- [41] V. Pryamitsyn, V. Ganesan, *Macromolecules* 47 (2014) 6095.
- [42] G. Pandav, V. Pryamitsyn, J. Errington, V. Ganesan, *J. Phys. Chem. B* 119 (2015) 14536.
- [43] I. Breßler, J. Kohlbrecher, A.F. Thünemann, *J. App. Cryst.* 48 (2015) 1587–1598.
- [44] J.S. Pedersen, *Adv. Colloid Interface Sci.* 70 (1997) 171–210.
- [45] A. Vrij, *J. Chem. Phys.* 71 (1979) 3267–3270.
- [46] J.S. Pedersen, *J. Appl. Cryst.* 27 (1994) 595–608.
- [47] J.K. Percus, G.J. Yevick, *Phys. Rev.* 110 (1958) 1–13.

INVESTIGATING SILICA NANOPARTICLE-POLYELECTROLYTE STRUCTURES IN MICROFIBRILLATED CELLULOSE FILMS BY SCATTERING TECHNIQUES

*Uthpala Garusinghe, Vikram Singh Raghuwanshi,
Praveena Raj, Gil Garnier* and Warren Batchelor*

Bioresource Processing Research Institute of Australia (BioPRIA), Department
of Chemical Engineering, Monash University, Clayton 3800, VIC, Australia

ABSTRACT

We report the cationic polyelectrolyte (CPAM)-SiO₂ nanoparticle (NP) interactions in suspension and in a sheet form, when mixed with microfibrillated cellulose (MFC), using dynamic light scattering (DLS) and small angle X-ray scattering (SAXS) techniques. The CPAM-SiO₂ NP suspensions were prepared by adding NPs into CPAM drop wise and composites were prepared by adding CPAM-SiO₂ suspension into MFC and through standard paper making procedure. DLS revealed that increase in CPAM dosage creates larger sized CPAM-NP aggregates because more NPs can be picked up by stretched CPAM chains. SAXS study revealed that CPAM-SiO₂ NP assembly in the formed nanopaper fits well with a spherical core shell model (with SiO₂ partially covered with CPAM) and sphere model (SiO₂ alone) combined together. Understanding the interaction between polyelectrolyte-NP system through such scattering techniques enables us to engineer novel cellulose based composites for specific applications.

* Corresponding author: XXXXXXXXXX

Keywords: Dynamic light scattering (DLS), Small angle X-ray scattering (SAXS), Scanning electron microscopy (SEM), Structure, Polyelectrolyte-nanoparticle system, Cellulose.

1 INTRODUCTION

Nanotechnology involves the manipulation or self-assembly of individual particles or their aggregates into desired configurations, to create materials and devices with new or vastly different properties and functions [1]. Nanoparticles (NPs) take an important role in nanotechnology because of their unique properties and can be selected for their chemical composition, but also can be tailored for their sizes, shape and surface properties [2]. NPs on their own cannot be used as they self-aggregate or pose the danger of uncontrolled release to the environment when dry. Therefore, ideally NPs need to be embedded into a matrix that is strong, flexible, and durable and also allows the surface area of NPs to be readily available.

Using nanocellulose as a supporting matrix combines the advantage of two constituents to give new composite materials with superior properties. Nanocellulose fibres are a new class of material that has received significant attention over the past decade. This material is of technological interest as it is renewable, biodegradable, exhibits excellent mechanical strength and superior barrier properties, while remaining fully compatible with conventional wood fibres [3]. However, embedding NPs into a nanocellulose matrix at times is difficult, especially when both materials are of same charge. In such cases, polyelectrolytes play an important role for the fixation of NPs onto surfaces in charged systems [4].

Polyelectrolytes play an important role in many industrial applications such as wastewater treatment[5], gene and drug delivery[6], [7], flocculation in paper making[5], [8], sensor development [9], [10], mineral processing [5] and coating processes [11]. This is due to their ability to adsorb at solid-liquid interfaces, thus, modifying surface properties and the interactions between particles and their environment [12]. The understanding of the interaction between polyelectrolytes and surfaces are crucial to optimise surface properties for a specific application. Polyelectrolytes and NPs are used in the papermaking industry as they act as retention aids, adhering fines and mineral fillers on the fibre surface [12]–[14], while at the laboratory scale polyelectrolytes have been shown to strongly interact with cellulose nanofibres, lowering the gel-point by bridging between fibres and increasing the flow through the fibre network during filtration [15]. Despite the numerous studies concerning the adsorption of polyelectrolytes onto charged NP surfaces which has been studied in the past using both theoretical [16]–[18] and experimental [4], [11], [12], [19] methods, their modes of action are poorly understood as they depend greatly on the type of polymer and particles in the system

[20]. The conformation of the adsorbed polyelectrolyte on the NP surface is still a largely unexplored subject.

In this paper we quantify the interaction between cationic polyacrylamide – SiO₂ NPs using two complimentary scattering techniques in order to engineer specific structures in the composite. Understanding on the behaviour of cationic dimethylamino-ethyl-methacrylate (CPAM) in SiO₂ nanoparticle (NP) suspension is crucial in production of cellulose-polyelectrolyte-NP based composite films for different applications. Dynamic light scattering (DLS) technique is used to investigate the conformation and changes in hydrodynamic radius of cationic polyacrylamide adsorbed on the surface of SiO₂ NPs. Small angle X-ray scattering (SAXS) technique is used to investigate the effect of CPAM concentration on the SiO₂ NP assemblies formed within the MFC matrix.

2 EXPERIMENTAL METHOD

2.1 Material

Microfibrillated cellulose (MFC) was purchased from DAICEL Chemical Industries Limited, Japan (Grade Celish KY-100G). MFC was supplied at 25 wt% solids content and stored at 5 °C. MFC has a mean diameter of 73 nm and the aspect ratio of 142 [21]. Cationic dimethylamino-ethyl-methacrylate (CPAM) polymer with molecular weight 13 MDa and charge density 50% was kindly provided by AQUA+TECH, Switzerland from their SnowFlake Cationics range. 22 nm colloidal silica with surface area 220 m²/g was purchased from Sigma Aldrich at 30 wt% suspension.

2.2 Method

2.2.1 Preparation of MFC, CPAM and silica NP suspensions

A 3 L disintegrator (Mavis Engineering Model No. 8522) was used to disperse 0.2 wt% MFC in deionized water at 15,000 propeller revolutions. 0.01 wt% CPAM suspension was prepared by mixing CPAM with deionized water for minimum of 8 hours prior to the experiments. SiO₂ NPs were diluted to 0.5 wt% from the stock solution using deionized water. The CPAM and SiO₂ NP solutions were sonicated for 2 minutes at 100% amplitude to ensure evenly distribution.

2.2.2 Preparation of pure MFC sheet

Sheets were prepared using a British handsheet maker (model T205) which is equipped with a woven filter with an average opening of 74 microns. 0.2 wt%

pure MFC suspension was poured into the column and allowed water to drain under gravity. When the film was formed, it was taken out using blotting papers and dried at 105 °C using a sheet drier.

2.2.3 Preparation of CPAM-silica NP suspension for DLS

0.5 wt% sonicated SiO₂ NP suspension was added through a peristaltic pump at 10 mL/min into the sonicated 0.01 wt% CPAM solution which was stirred at 200 rpm/min with a magnetic stirrer. Amount of SiO₂ NPs in the suspension was fixed at 0.3 g. The mixing process was repeated for three different surface coverages of CPAM to NPs (0.03, 0.05 and 0.09 mg CPAM/m² surface area of SiO₂ NPs). The concentration of the final suspension changes from 0.38–0.26 wt% depending upon CPAM dosage. This method of addition allowed SiO₂ NP suspension to be added drop by drop into the sonicated CPAM solution. Dynamic Light Scattering (DLS) was then used to measure the size of the NPs with adsorbed CPAM on its surface.

2.2.4 Preparation of MFC-CPAM- SiO₂ NP composite for SAXS

Preparation of composite sheets involved mixing MFC (1.2 g at 0.2 wt%), SiO₂ NPs (25 wt% of the total composite at 0.1 wt%) and CPAM (different ratios at 0.01 wt%) suspensions together simultaneously. While SiO₂ NPs and MFC used in composite sheets was fixed, four different CPAM dosages were used (0.07, 0.14, 0.2 and 0.5 mg CPAM/m² surface area of SiO₂ NPs). Firstly, CPAM and SiO₂ NP suspensions were mixed together into a beaker through simultaneous addition with two peristaltic pumps. Secondly, CPAM-SiO₂ NP suspension and MFC suspension was mixed again into a beaker through simultaneous addition with two peristaltic pumps to make the final composite suspension. Total mixing time was set to 8 minutes in each step. CPAM was added at different speeds (7.7–55 mL/min) depending on the dosage, SiO₂ was added at 50 mL/min and MFC was added at 75 mL/min. The final concentration of the suspension varied between 0.15–0.11 wt% depending on the CPAM dosage. Final suspension was poured into British handsheet maker for composite processing as mentioned above.

2.3 Characterization

2.3.1 Dynamic light scattering (DLS)

CPAM-SiO₂ NP suspensions prepared above for DLS analysis were used as prepared to measure DLS with a Nanobrook Omni (Brookhaven Instruments) using a cuvette cell at 25 °C. Diameter distribution of the clusters were calculated using the supplied software.

2.3.2 Small angle X-ray scattering (SAXS)

SAXS measurements were conducted at the SAXS/WAXS beamline at the Australian Synchrotron, Melbourne [22]. Measurements were made in a transmission mode with the X-ray energy of 11 keV. Scattered photons were collected at detector distance of 7.2 m using the Pilatus 1 M detector (Dectris, Baden, Switzerland). The isotropic raw detector images were converted to intensity versus q ,

$$|\vec{q}| = q = \frac{4\pi \sin \theta}{\lambda}$$

where θ is the scattering angle and λ is the wavelength (0.113 nm) of incident X-rays. Data reduction with respect to the measurement geometry, masking dead pixels and the beam stop and a subtraction of air scatter were conducted using IDL based ScatterBrain software [23]. The scattered intensity is plotted as a function of the momentum transfer vector q . Data analysis was conducted by fitting the SAXS curves using the SASfit software.

2.3.3 Scanning electron microscopy (SEM)

SEM analysis was performed using FEI Magellan 400 FEGSEM on the composites. Each sample was cut to 3 mm by 3 mm pieces and mounted onto a metal sample holder, coated with a thin layer of Iridium prior to imaging. Accelerating voltage was 3kV and current was 6.3 pA. The images were taken at 30,000 \times and 100,000 \times magnifications.

3 RESULTS AND DISCUSSION

3.1 Scanning Electron Microscopy (SEM) of MFC-SiO₂-CPAM composite sheets

Figure 1(a) shows a SEM image of a pure MFC sheet. A wide distribution of pore sizes can be observed. Figure 1(b) shows SEM images of a MFC with 0.5 mg/m² CPAM dosage on 22 nm SiO₂ NPs respectively. NPs seem to accommodate themselves to the gaps created by the MFC fibres and fill up without altering the fibre network. While qualitative information can be obtained from SEM, it is difficult to fully characterise the samples with SEM alone as (1) SEM images are from a selected area and it does not give enough information about the local distribution of NPs in the matrix, (2) SEM only show the NPs which are on the surface, (3) the interaction or the type of distribution between CPAM-SiO₂ NPs cannot be properly understood or seen. Therefore, SEM alone is not good enough to properly investigate a polyelectrolyte-NP system to optimise performance. Scattering

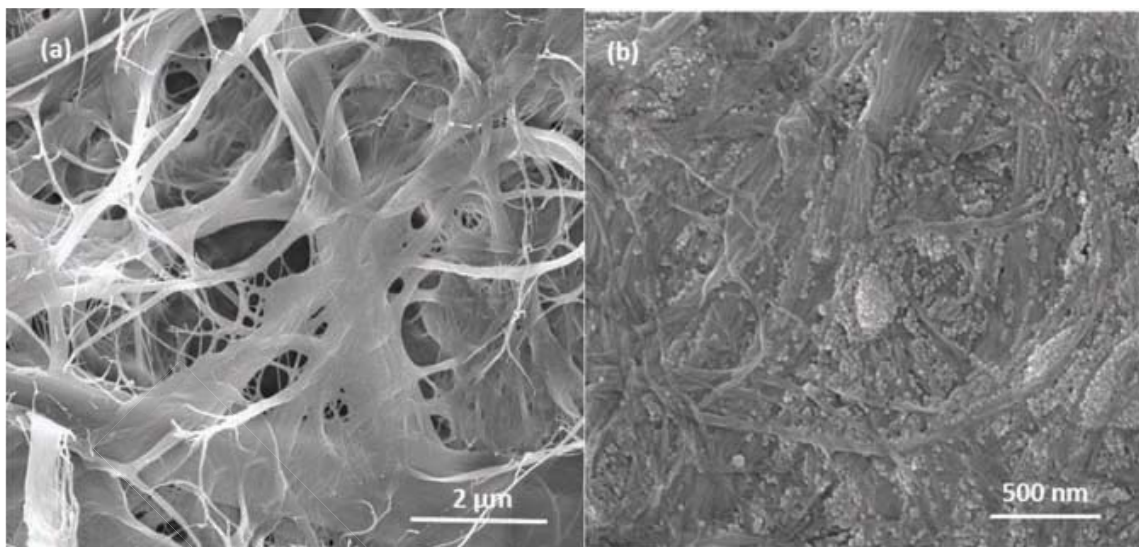


Figure 1. Scanning electron microscopy (SEM) images: (a) pure MFC sheet, and (b) MFC–22 nm SiO₂ NPs–0.5 mg/m² CPAM composite at high magnification.

techniques such as DLS and SAXS are useful in obtaining further information on the internal structure of the material in the 1 to 100 nm length scale.

3.2 Dynamic Light Scattering (DLS) on CPAM-NP suspensions

DLS experiments were conducted to reveal the interaction between SiO₂ NPs and CPAM with respect to different dosages of CPAM. Figure 2(a) shows the correlation curves for pure SiO₂ NPs and NPs with two different dosages of CPAM (0.03 mg/m² and 0.05 mg/m²). The correlation curve decays at a slower rate with increase in CPAM dosages. For pure NPs the correlation curve decays at around 200 μsec while for the higher CPAM dosage (0.05 mg/m²) the correlation curve decays at 3000 μsec. This corresponds to CPAM adsorption onto the SiO₂ NPs which results in formation of aggregates and reduce the diffusion rate of aggregated particles. Distribution of the NPs and NP aggregates obtained from DLS are shown in the Figure 2(b).

The radius of gyration of CPAM with 13 MDa, without accounting for the charged groups is 38 nm when calculated theoretically using the random walk model [24]. Polyelectrolytes with a low charged density have a coiled conformation in solution with smaller diameters which is characterised by a random walk much the same as non-charged polymers in a solvent [25], [26]. Highly charged polymers have stretched out or extended conformations in solution which is due to the closely spaced charged sites resulting in larger diameters [25], [26]. Thus, the actual radius of gyration of CPAM that when stretched out due to repulsion between charged groups on the polymer segment is much larger. In this work, we

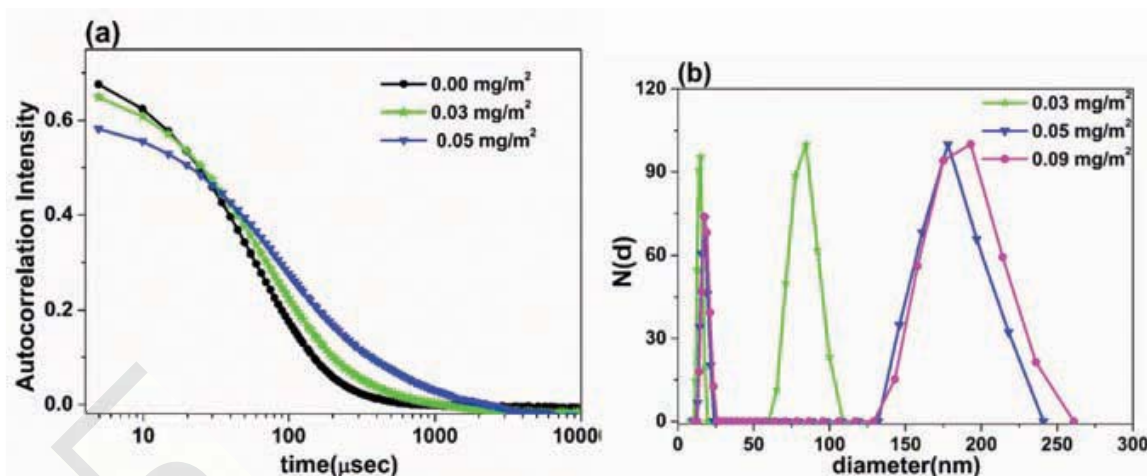


Figure 2. (a) Auto correlation curves of Pure SiO₂ NPs and SiO₂ with CPAM concentration of 0.03 mg/m² and 0.05 mg/m². (b) Diameter distribution obtained from DLS for SiO₂ NPs with CPAM concentration of 0.03 mg/m², 0.05 mg/m² and 0.09 mg/m².

have used 50% charge density and that is considered fairly high. Therefore, CPAM used in this work is expected to be stretched out and have a more extended conformation on the surface.

Two distinct peaks are seen for each dosage of CPAM in Figure 2(b). There is no significant difference in the diameter with increase in CPAM dosage for Peak 1, which has a maximum in the range 19 nm to 23 nm, consistent with measurements of single particles. However, the intensity of Peak 1 reduces when CPAM dosage increased from 0.05 mg/m² onwards, suggesting that number of single SiO₂ NPs that have not formed agglomerates are reducing as the dosage of CPAM increases. With increasing CPAM dosage, the second peak shifted to higher diameters. At 0.003 mg/m² (lower dosage), Peak 2 appeared at 85 nm. This peak shifted to 178 nm and 193 nm with 0.05 mg/m² and 0.09 mg/m² (higher dosages), respectively. This could be due to more stretched out configuration of the polymer causing a high probability of SiO₂ NPs to be picked up and forming larger agglomerates.

However, using DLS as a scattering technique is difficult for higher dosages of CPAM as DLS does not give reliable results when higher amount of polymer is added. At higher doses without a fibre matrix, isolated particles tend to agglomerate into much bigger clusters when compared to being in the sheet form. This is because when CPAM-NP is mixed with MFC to form sheets, fibres has an influence on the size of aggregations and stop bigger agglomerations from forming. Therefore, SAXS is a more suitable scattering technique to measure the particle interactions at higher CPAM dosages.

3.3 Small Angle X-ray Scattering (SAXS) on MFC-NP-CPAM composite sheets

Small Angle X-ray Scattering (SAXS) is a powerful method to give information on the shape, size, distribution of NPs in different kind of matrices [27]–[31]. SAXS experiments were performed to investigate the effect of CPAM on the dispersion of SiO₂ NPs in the MFC fibre matrix. Figure 3(a) shows the SAXS curve from the MFC sheet. No features were observed in SAXS curve which is due to the presence of large structure of MFC fibres with large pore sizes as seen in Figure 1(a). Figure 3(b) shows the fitted SAXS curves for the SiO₂ NPs with different dosages of CPAM (0.07–0.50 mg/m²: a higher range than the dosages used in DLS).

Further information from the SAXS curves (Figure 3(b)) were extracted by nonlinear fitting using combination of different form factor and structure factor using the software SASfit [32]. The total SAXS scattering intensity can be given as:

$$I_{SAXS}(\vec{q}) = \int_0^\infty N(r) |F(q, r, \Delta\eta)|^2 S(q, r, \Delta\eta) dr + Bkg + Cq^{-\alpha} \quad (1)$$

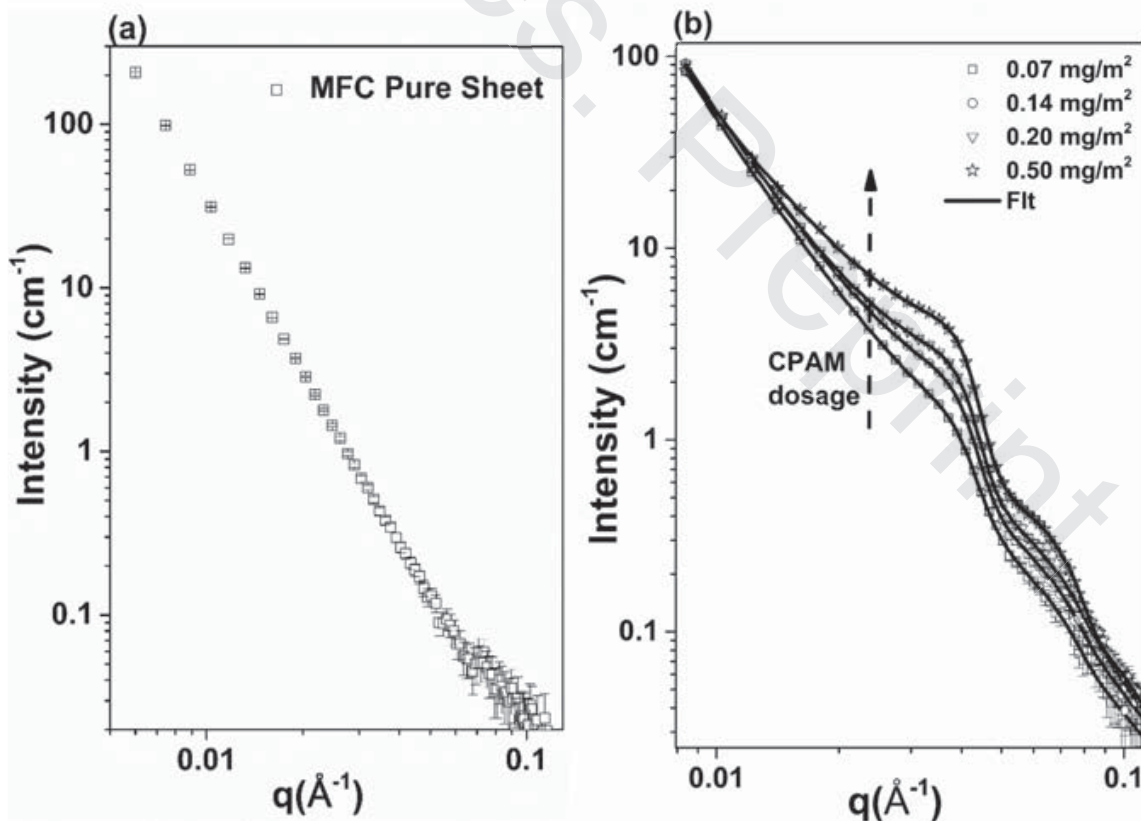


Figure 3. (a) SAXS curve for pure MFC sheet. (b) SAXS curves fitted with the core-shell and spherical models with different CPAM dosages.

Where, $N(r)$ is the particle number distribution, $F(q, r, \Delta\eta)$ is the structure model which contains information about shape and size of the particles. In the structure model, $\Delta\eta$ is the effective electron density difference between the particle and the remaining matrix, q is the transferred momentum, $S(q, r)$ is the structure factor contains information on the interaction between the particle and Bkg is the background with the surface scattering term.

The form factor with the combination of the spherical core shell particle and the spherical particle with the lognormal size distribution fits well for all the scattering curves (Figure 3b). The form factor is defined as:

$$F(q, r, \Delta\eta) = F_{sphere\ shell}(q, r_p, \Delta\eta_s) + F_{sphere}(q, r_p, \Delta\eta_s) \quad (2)$$

where the F_{sphere} is the form factor of sphere as:

$$F_{sphere}(q, r, \Delta\eta) = 3\Delta\eta \frac{\sin qr - qr \cos qr}{(qr)^3} \quad (3)$$

and $F_{sphere\ shell}$ is the form factor for spherical core shell particles and given as:

$$F_{sphere\ shell}(q, r_p, \Delta\eta_s, v, \mu) = F_{sphere}(q, r_p, \Delta\eta_s) - F_{sphere}(q, vr_p, \Delta\eta_s(1 - \mu)) \quad (4)$$

where, r_t is the radius of the core (SiO₂) + shell (CPAM), which is related to the core radius as $r = vr_t$ ($0 < v < 1$), $\Delta\eta_s = \eta_{shell} - \eta_{matrix}$ is the effective electron density difference between shell and matrix and $\mu\Delta\eta_s$ is the effective electron density difference between the core and the matrix. Additionally, the structure factor was included into the fitting procedure [33], [34]. While fitting a SAXS curve, all the structure determining parameters, size distribution parameters, structure factor parameters and the contrast of the particles were free fitting variables.

The obtained parameters show the average SiO₂ particle diameter of 22 ± 3 nm and thickness of the CPAM layer adsorbed onto the SiO₂ NPs is about 5 ± 0.5 nm. The schematic of the electron density profile for the spherical core shell particle is given in the Figure 4(a). It is found that the effective electron density of the core (SiO₂; density 2.4 g/cm³) is larger than the cellulose matrix (C₆H₁₀O₅; density 1.5 g/cm³). Moreover, the effective electron density of shell (CPAM, density: 1.1 g/cm³) is smaller than the cellulose matrix.

The evaluated resultant structure factor for the two dosages of CPAM (0.07 mg/m² and 0.5 mg/m²) obtained after fitting the SAXS curve is given in Figure 4(b). There is a small shift in the structure factor peak of high CPAM dosage (0.5 mg/m²) towards the higher q values with respect to the small CPAM dosage (0.07 mg/m²). The shift towards higher q values indicates a decrease in the inter-particle distance between the particles with the high dosage of CPAM. However, the

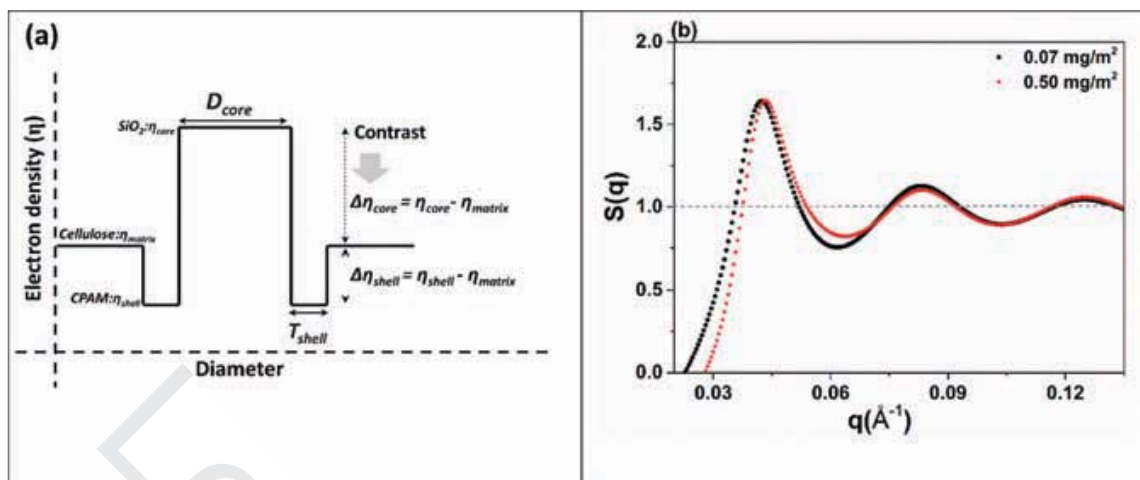


Figure 4. (a) Electron density variation profile for the spherical core shell particle with SiO₂ core, CPAM shell and cellulose matrix, (b) Structure factor obtained after fitting of the SAXS curve for the CPAM dosages of 0.07 mg/m² and 0.5 mg/m².

difference is not significant and peak sharpness is also almost the same. This result reveals that with increase in CPAM dosage, the interaction between 22 nm SiO₂ NPs does not vary strongly.

Both SiO₂ NPs and MFC are negatively charged and therefore is difficult for SiO₂ to directly adsorb onto/within the cellulose matrix. CPAM is a positively charged polymer with the radius of gyration of 38 nm. CPAM acts as a bridge for SiO₂ NPs to be retained within the cellulose matrix. At low CPAM dosage, the CPAM adsorb onto the SiO₂ NPs surface and spread over the NP surface. It is difficult to identify whether CPAM totally covers the surface of NPs or partially cover the surface. In the case when the CPAM covers the surface of NPs completely, then the CPAM forms a positive shell like region over NPs surface. This will not allow NPs to form aggregates due to the electrostatic repulsion between NPs. In the DLS investigation, it was observed that even at the lowest CPAM dosage the NPs form aggregates. Therefore, it is expected that the CPAM partially covers the NPs surface. This results in distribution of both partly CPAM coated NPs and NPs without any CPAM. SAXS curves fits well with the proposed model of distribution of spherical shell (SiO₂ coated in a layer of CPAM) and sphere model (pure SiO₂). Increase in CPAM dosage results in increasing the number of SiO₂ NP aggregates. However, the interaction within the particles does not vary significantly and remain the same as observed by the variation in structure factor peak (Figure 4(b)).

22 nm SiO₂ NP behaves differently with CPAM compared to 8 nm SiO₂ NPs with CPAM which was published previously [14]. This could probably be due to the size difference between SiO₂ NPs. The structure factor reported for 8 nm SiO₂

NPs with increase in CPAM showed that structure factor sharpness increased and the peak shifted towards lower value with respect to low CPAM dosage. This suggests that at low CPAM dosages, loosely bounded NP aggregates in the CPAM chain is formed because of the electrostatic repulsion between NPs, therefore the correlation length of the aggregates were about 25–30 nm in size. At high CPAM dosages, more CPAM is available to neutralize the NPs surface and overcome the electrostatic repulsion between NPs, therefore a strong aggregations between NPs were obtained with a bigger correlation length of about 70 nm [14]. For 22 nm particles used in this study, with increase in CPAM dosages, only the number of structures increases and not the structure size. This proves that different length scales of NPs react differently in a polyelectrolyte system.

We conclude that SAXS technique is a better tool in investigating the polyelectrolyte-NP interactions when the polyelectrolyte concentration is higher. Overall, scattering techniques are essential tools in understanding the behavior of a polyelectrolyte-NP systems to better engineer the properties to develop nanocellulose-NP composites for varies applications.

4 CONCLUSION

Interaction between cationic dimethylamino-ethyl-methacrylate (CPAM) and SiO₂ nanoparticles (NPs) in suspension and in a microfibrillated cellulose (MFC) matrix was investigated using scattering methods. This study is beneficial in understanding a polyelectrolyte-NP system with respect to interactions between them, which cannot be obtained from techniques such as scanning electron microscopy (SEM).

Dynamic light scattering (DLS) shows aggregates of NPs at low dosage of CPAM (0.03 mg/m²) and aggregate size increased to larger sizes with increase in CPAM dosage further (0.05–0.09 mg/m²). It was noted that DLS results become unreliable when higher amount of polymer is added as DLS technique is sensitive to charge. Therefore, small angle X-ray (SAXS) techniques as well was used to characterize the system.

SAXS investigation revealed that the distribution of CPAM-NP system fits well with a distribution of spherical shell (from SiO₂ coated in 5 nm layer CPAM around) model and a sphere model (SiO₂ alone) combined, and the number of such systems increase with increase in CPAM dosage. Structure factor obtained from SAXS curves reveals the interaction between NPs does not have a significant effect with respect to the dosage of CPAM.

Overall, this study proves that complimentary scattering techniques are essential in understanding a polyelectrolyte-NP system better to develop nanocellulose based composite material targeted for specific applications.

ACKNOWLEDGEMENT

Thanks to MCEM for scanning electron microscopy. The financial support from Australian research council, Australian paper, Carter Holt Harvey, Circa, Norske Skog, and Visy through the Industry Transformation Research Hub grant IH130100016 is acknowledged. Thanks Monash University for MGS and FEIPRS scholarships. The authors would like to thank to Dr. Tim Ryan, Dr. Nigel Kirby, Dr. Adrian Hawley and Dr. Chris Garvey for assistance during SAXS measurements at SAXS/WAXS beamline in Australian Synchrotron.

REFERENCES

1. B. Farhang. Nanotechnology and lipids. *Lipid Technology* **19**(6):132–135, 2007.
2. K. I. Winey and R. A. Vaia. Polymer nanocomposites. *MRS bulletin* **32**(04):314–322, 2007.
3. J. Kim, S. Yun and Z. Ounaies. Discovery of cellulose as a smart material. *Macromolecules* **39**(12):4202–4206, 2006.
4. L.-E. Enarsson and L. Wågberg. Conformation of preadsorbed polyelectrolyte layers on silica studied by secondary adsorption of colloidal silica. *Journal of Colloid and Interface Science* **325**(1):84–92, 2008.
5. G.M. Moody (ed.). Polymeric flocculants. In *Handbook of Industrial Water Soluble Polymers*, Blackwell Publishing Ltd, pp. 134–173, 2007.
6. M. Dimitrova, Y. Arntz, P. Lavalle, F. Meyer, M. Wolf, C. Schuster, Y. Haïkel, J. C. Voegel and J. Ogier. Adenoviral gene delivery from multilayered polyelectrolyte architectures. *Advanced Functional Materials* **17**(2):233–245, 2007.
7. N. Benkirane-Jessel, P. Schwinté, P. Falvey, R. Darcy, Y. Haïkel, P. Schaaf, J. C. Voegel and J. Ogier. Build-up of polypeptide multilayer coatings with anti-inflammatory properties based on the embedding of piroxicam–cyclodextrin complexes. *Advanced Functional Materials* **14**(2):174–182, 2004.
8. L. Wågberg, L. Winter, L. Ödberg and T. Lindström. On the charge stoichiometry upon adsorption of a cationic polyelectrolyte on cellulosic materials. *Colloids and Surfaces* **27**(4):163–173, 1987.
9. F. Caruso, K. Niikura, D.N. Furlong and Y. Okahata. 1. Ultrathin multilayer polyelectrolyte films on gold: Construction and thickness determination. *Langmuir* **13**(13):3422–3426, 1997.
10. F. Caruso, K. Niikura, D. N. Furlong and Y. Okahata. 2. Assembly of alternating polyelectrolyte and protein multilayer films for immunosensing. *Langmuir* **13**(13):3427–3433, 1997.
11. D. L. Elbert, C. B. Herbert and J. A. Hubbell. Thin polymer layers formed by polyelectrolyte multilayer techniques on biological surfaces. *Langmuir* **15**(16):5355–5362, 1999.
12. S.-C. Liufu, H.-N. Xiao and Y.-P. Li. Adsorption of cationic polyelectrolyte at the solid/liquid interface and dispersion of nanosized silica in water. *Journal of Colloid and Interface Science* **285**(1):33–40, 2005.

13. M. Cadotte, M.-E. Tellier, A. Blanco, E. Fuente, T. G. M. van de Ven and P. Paris. Flocculation, retention and drainage in papermaking: A comparative study of polymeric additives. *Canadian Journal of Chemical Engineering* **85**:240, 2007.
14. U. M. Garusinghe, V. S. Raghuvanshi, C. J. Garvey, S. Varanasi, C. R. Hutchinson, W. Batchelor and G. Garnier. Assembly of Nanoparticles-polyelectrolyte complexes in nanofiber cellulose structures. *Colloids and Surfaces A: Physicochemical and Engineering Aspects* **513**:373–379, 2017.
15. Q. Li, P. Raj, F. A. Husain, S. Varanasi, T. Rainey, G. Garnier and W. Batchelor. Engineering cellulose nanofibre suspensions to control filtration resistance and sheet permeability. *Cellulose* **23**(1):391–402, 2016.
16. F. W. Wiegel. Adsorption of a macromolecule to a charged surface. *Journal of Physics A: Mathematical and General* **10**(2):299, 1977.
17. J.-M. Y. Carrillo and A. V. Dobrynin. Molecular dynamics simulations of polyelectrolyte adsorption. *Langmuir* **23**(5):2472–2482, 2007.
18. M. Turesson, C. Labbez and A. Nonat. Calcium Mediated polyelectrolyte adsorption on like-charged surfaces. *Langmuir* **27**(22):13572–13581, 2011.
19. F. T. Hesselink. On the theory of polyelectrolyte adsorption. *Journal of Colloid and Interface Science* **60**(3):448–466, 1977.
20. J. Gregory and S. Barany. Adsorption and flocculation by polymers and polymer mixtures. *Advances in Colloid and Interface Science* **169**(1):1–12, 2011.
21. S. Varanasi, R. He and W. Batchelor. Estimation of cellulose nanofibre aspect ratio from measurements of fibre suspension gel point. *Cellulose* **20**(4):1885–1896, 2013.
22. N. M. Kirby, S. T. Mudie, A. M. Hawley, D. J. Cookson, H. D. Mertens, N. Cowieson and V. Samardzic-Boban. A low-background-intensity focusing Small-Angle X-Ray Scattering undulator beamline. *Journal of Applied Crystallography* **46**(6):1670–1680, 2013.
23. <http://www.synchrotron.org.au/aussyncbeamlines/saxswaxs/software-saxswaxs>. SAXS Software ScatterBrain.
24. P. Raj, S. Varanasi, W. Batchelor and G. Garnier. Effect of cationic polyacrylamide on the processing and properties of nanocellulose films. *Journal of Colloid and Interface Science* **447**:113–119, 2015.
25. L. A. Connal, Q. Li, J. F. Quinn, E. Tjipto, F. Caruso and G. G. Qiao. Ph-Responsive poly(acrylic acid) core cross-linked star polymers: Morphology transitions in solution and multilayer thin films. *Macromolecules* **41**(7):2620–2626, 2008.
26. Y. Zhou, G. J. Jameson and G. V. Franks. Influence of polymer charge on the compressive yield stress of silica aggregated with adsorbed cationic polymers. *Colloids and Surfaces A: Physicochemical and Engineering Aspects* **331**(3):183–194, 2008.
27. V. Raghuvanshi, M. Ochmann, F. Polzer, A. Hoell and K. Rademann. Self-assembly of gold nanoparticles on Deep Eutectic Solvent (DES) surfaces. *Chem. Commun.* **50**(63):8693–8696, 2014.
28. V. S. Raghuvanshi, R. Harizanova, D. Tatchev, A. Hoell and C. Rüssel. Structural analysis of Fe–Mn–O nanoparticles in glass ceramics by small angle scattering. *Journal of Solid State Chemistry* **222**:103–110, 2015.
29. V. S. Raghuvanshi, A. Hoell, C. Bocker and C. Rüssel. Experimental evidence of a diffusion barrier around Baf 2 nanocrystals in a silicate glass system by ASAXS. *CrystEngComm* **14**(16):5215–5223, 2012.

30. V. S. Raghuvanshi, C. Russel and A. Hoell. Crystallization of ZrTiO₄ nanocrystals in lithium-alumino-silicate glass ceramics: Anomalous Small-Angle X-Ray Scattering investigation. *Crystal Growth & Design* **14**(6):2838–2845, 2014.
31. V. S. Raghuvanshi, D. Tatchev, S. Haas, R. Harizanova, I. Gugov, C. Rüssel and A. Hoell. Structural analysis of magnetic nanocrystals embedded in silicate glasses by anomalous Small-Angle X-Ray Scattering. *Applied Crystallography* **45**(4):644–651, 2012.
32. I. Breßler, J. Kohlbrecher and A. F. Thünemann. SASfit: A tool for Small-Angle Scattering data analysis using a library of analytical expressions. *Journal of Applied Crystallography* **48**(5):1587–1598, 2015.
33. J. B. Hayter and J. Penfold. An analytic structure factor for macroion solutions. *Molecular Physics* **42**(1):109–118, 1981.
34. J.-P. Hansen and J.B. Hayter. A Rescaled Msa Structure Factor for Dilute Charged Colloidal Dispersions. *Molecular Physics* **46**(3):651–656, 1982.

■